Contribution to the detection of exoplanets transiting nearby stars by the mission TESS

A dissertation presented by

Mourad GHACHOUI

on October 18, 2024

in fulfillment of the requirements for the degree of
Doctor of Philosophy in Science

Specialization in Space Sciences

Thesis Supervisors:

Dr. Michaël Gillon (University of Liege)
Prof. Zouhair Benkhaldoun (University Cadi Ayyad)

Jury Members:

President :	**Prof. Abdelhadi Jabiri**	University Cadi Ayyad,
Members:	**Prof. Michaël De Becker**	University of Liege,
	Dr. Emmanuël Jehin	University of Liege,
	Prof. Abdelmajid Benhida	University Cadi Ayyad,
	Prof. Thami Elhalkouj	CRMEF-Marrakech,
	Prof. Zouhair Benkhaldoun	University Cadi Ayyad,
	Dr. Michaël Gillon	University of Liege,
	Prof. Monika Lendl	University of Geneva

Academic year 2023-2024

Ghachoui Mourad
mr.ghachoui@gmail.com

ACKNOWLEDGMENTS

This thesis summarizes extensive research work conducted between two institutions: Cadi Ayyad University in Morocco and the University of Liège in Belgium, as part of the TRAPPIST project at the Oukaimeden Observatory.

I could not have completed this thesis without the support of many people, foremost among them my supervisors and my family.

My deepest gratitude goes to my thesis directors *Michaël Gillon* and *Zouhair Benkhaldoun*, under whose supervision I had the honor of conducting both my master's research and this thesis. Thank you for your super nice supervision and your contribution. Thank you also for all your nice guidance during my thesis and for the heartwarming welcome in both institutes.

I would also like to sincerely thank my *parents* and *siblings*, especially *Younes*, for their unwavering support throughout my studies. My thesis could not have been completed without your assistance. You have never been stingy whenever I needed your help and I am very grateful for that.

Many thanks to *Karen Collins, Jon Jenkins, Avi Shporer, David Latham, Jason Eastman* and all the architects of the NASA TESS mission, for their active collaboration and their help during my thesis.

I would also like to thank all the members of the TRAPPIST and SPECULOOS teams, for their valuable scientific exchanges. Special thanks go to *Mathilde Timmermans, Francisco Pozuelos, Laetitia Delrez, Emmanuel Jehin, Benjamin Rackham, Daniel Sébastian, Sandrine Sohy, Amaury Triaud and Brice-Olivier Demory.*

I dedicate my warm thanks to all the reviewers and members of my thesis jury: *Prof. Abdelahdi Jabiri, Prof. Michaël De Becker, Dr. Emmanuël Jehin, Prof. Abdelmajid Benhida, Prof. Thami Elhalkouj, Prof. Monika Lendl, and Prof. Abdelfattah Habib* for agreeing to read, comment and evaluate my thesis work.

I would also like to thank all the members of the High Energy Physics and Astrophysics Laboratory (LPHEA) and the Oukaimeden observatory for their support and encouragements. Special thanks go to *Khalid Barkaoui, Jamila Chouqar, Said Hmiddouch, Abderrahman Soubkiou, Omar Ouchaou and Jamal Chafi.*

I sincerely thank all my professors, especially *Said Sabor, Abdessalam Jdaa, Ahmed Aamouch, Abdelmajid Benhida, Fouad Sefyani, and Mohamed Sabil.*

I would also like to extend my gratitude to all my friends, especially *Anass Yarroudh, Zakaria Seddad, Khaoula Mzioui, Kaoutar Elhabbari and Naïma Rharnit.* Thank you all for your support during the nice moments we spent together in Liege.

ABSTRACT

Since the first discovery in 1995 of a planet in orbit around a main-sequence star other than our Sun (i.e., an exoplanet), the study of exoplanets has become one of the most dynamical scientific fields. Since then, various space- and ground-based missions have been funded specifically to detect and characterize these exotic worlds, leading to the discovery of more than 5500 of them known to date. Most of these exoplanets are formally known as '*transiting planets*' as they transit periodically in front of their host stars for observers on Earth. When a planet passes in front of its host star, it causes a drop, known as a *transit*, in its brightness as a quantity of the starlight is blocked by the planetary disc. Photometric monitoring of stars, which aims at measuring the evolution of the brightness of stars, can detect *transit* signals, revealing the existence of *transiting exoplanets*. This is the principle of the '*transit method*' used in the detection of most of the exoplanets known to date. The space mission TESS, launched by NASA in 2018, is rapidly increasing the number of *transiting planets* with a special focus on exoplanets sized between Earth and Neptune and orbiting nearby bright stars. This focus on bright nearby stars is motivated by the easier detailed characterization of the planets' physical parameters, such as radius and mass, as well as their atmospheres. TESS has already detected transit-like signals for thousands of exoplanet candidates. However, many of these transit-like signals are due to other astrophysical phenomena such as eclipsing binaries, blended eclipsing binaries or to the activity of the stars. Some signals might even be due to instrumental artifacts of the spacecraft. Thus, these signals still need validation of their planetary nature using higher photometric precision measurements from ground-based facilities.

During my thesis, I contributed to the photometric follow-up of more than 257 *TESS* planet candidates, known as TESS Object of Interest (TOIs), to confirm those that are indeed due to transiting exoplanets and discard those due to astrophysical or instrumental phenomena. Most of these TOIs were observed with the TRAPPIST-North telescope. My work contributed to the *'validation'* of 9 transiting exoplanets, In this context, the *'validation'* of exoplanets is a process to confirm the planetary nature of the transit signals through multi-color photometric observations of the transit signal, adaptive optic observation to confirm that the host stars are single, spectroscopic observations to further characterize the host stars (e.g. spectral type, metallicity), as well as statistical validation checking that the transits present a significantly higher probability to be produced by transiting planets than by other astrophysical phenomena. In addition to their *'validation'*, 11 other exoplanets have received radial velocity measurements, where their masses have been found consistent with planetary companions. These planets are classified as *'confirmed'* planets. Both *'validated'* and *'confirmed'* planets were presented in peer-reviewed publications. 198 TOIs (out of the 257 TOIs) have been found to present signals consistent with *transiting planets* using only

multi-color photometric observations. Such cases are called *'verified planet candidates'* (VPC). I also participated in the identification of 2 nearby planet candidates (NPC, i.e planets transiting stars close to the targeted stars), 4 eclipsing binaries (EB/SEB1), 10 nearby eclipsing binaries (NEB), 9 blended eclipsing binaries (BEB/SEB2) and 4 false alarm (FA) detections. $\sim$ 10 TOIs remain as planet candidates that need more photometric follow-up observations.

I led the *'validation'* paper for the planet TOI-1680 b. It is a super-Earth planet observed by the TRAPPIST-North telescope beside many other facilities. It has a radius of $1.460^{+0.063}_{-0.049}\,R_\oplus$ and is on 4.8-days orbit around a nearby (37.14 parsecs away) mid-type M dwarf star (TOI-1680, V = 15.87 mag and J = 11.63 mag). Given that all known planets with similar radius are rocky, TOI-1680 b is presumed to be a rocky planet. This supposition will be confirmed with the planetary mass measurements from radial velocity observations. I also investigated its potential for atmospheric characterization, where I found it could be a promising candidate for these studies with the *JWST*. This conclusion is strengthened by the location of this planet near the continuous viewing zone of *JWST*.

I also led the *'validation'* paper of two other super-Earths: TOI-6002 b and TOI-5713 b. The first planet, TOI-6002 b, has a radius of $1.65^{+0.22}_{-0.19}\,R_\oplus$ and is on a 10.9 days orbit around a mid-type M dwarf star (TOI-6002, V = 14.6 mag and J = 11 mag) located at 32.04 pc from the Sun. The second planet (TOI-5713 b) has a radius of $1.77^{+0.13}_{-0.11}\,R_\oplus$ and is on a 10.44 days orbit around an active mid-type M dwarf star (TOI-5713, V = 15.35 mag and J = 11.07 mag) 40.95 pc away. Given their location in the radii distribution corresponding to the *density valley*, both TOI-6002 b and TOI-5713 b can be either of rocky or water-rich compositions. As for their location in the *radius valley*, it is not clear whether they saved their atmospheres or not. Theses findings classify them as important targets for determining their masses via radial velocity observations. When it is done, both planets will be added to the sample of exoplanets on which in-depth statistical inferences will be conducted to understand how super-Earths and sub-Neptunes form and evolve around M dwarf stars. Interestingly, both planets are located near the inner edge of the habitable zone of their host stars, which also make them intriguing targets for future atmospheric studies to expand our understanding of the potential habitability of M-dwarfs' planets, and how potentially habitable planets transition to Venus-like planets as it happened for Venus in our solar system.

RÉSUMÉ

Depuis la première découverte en 1995 d'une planète en orbite autour d'une étoile de la séquence principale autre que notre Soleil (c'est-à-dire une exoplanète), l'étude des exoplanètes est devenue l'un des domaines scientifiques les plus dynamiques. Depuis lors, diverses missions spatiales et terrestres ont été financées spécifiquement pour détecter et caractériser ces mondes exotiques, conduisant à la découverte de plus de 5 500 d'entre eux à ce jour. La plupart transitaient leurs étoiles hôtes. Lorsqu'une planète passe devant son étoile hôte, son disque planétaire occulte une partie du disque de l'étoile hôte, ce qui entraîne une baisse de sa brillance apparente. Ce phénomène se nomme "transit". Le suivi photométrique des étoiles, qui vise à surveiller la luminosité des étoiles en fonction du temps, peut détecter les signaux de transit, conduisant ainsi à la détection d'exoplanètes. C'est le principe de la *méthode des transits* utilisée pour détecter la plupart des exoplanètes connues à ce jour. La mission spatiale TESS, lancée par la NASA en 2018, augmente rapidement le nombre de planètes en transit avec un accent particulier sur les exoplanètes de taille comprise entre la Terre et Neptune et en orbite autour d'étoiles brillantes et proches de notre système solaire. Ce concept rend plus facile la caracterisation détaillées des paramètres physiques des planètes détectees, tels que leurs rayons et masses, ainsi que leurs atmosphères. TESS a déjà détecté des signaux de type transit pour des milliers de candidats exoplanètes. Cependant, des signaux pourraient être dûs à d'autres phénomènes astrophysiques. tels que les binaires à éclipses, les binaires à éclipses blindées ou à l'activité des étoiles. Certains signaux pourraient même être dûs à des artefacts instrumentaux du satellite. Ainsi, ces signaux doivent encore être re-observés pour confirmer leurs origines planétaires, en utilisant des mesures photométriques de plus grande précision à partir d'installations au sol.

Au cours de ma thèse, j'ai contribué au suivi photométrique de plus de 257 planètes candidates TESS, connues sous le nom d'objets d'intérêt TESS (TOI, TESS Object of Interest), pour confirmer celles qui sont bien dues à des exoplanètes en transit et écarter celles dues à d'autres phénomènes astrophysiques ou instrumentaux. La plupart de ces TOIs ont été observés avec le télescope TRAPPIST-North. Mon travail a contribué à la *'validation'* de 9 exoplanètes en transit. Dans ce contexte, la *'validation'* des exoplanètes est un processus visant à confirmer la nature planétaire des signaux de transit grâce à des observations photométriques multi-couleur du signal de transit, des observations d'optique adaptative pour confirmer que les étoiles hôtes sont isolées et des observations spectroscopiques pour mieux caractériser les étoiles hôtes (par exemple, type spectral, métallicité), ainsi qu'une validation statistique pour vérifier que les transits présentent une probabilité significativement plus élevée d'être produits par des planètes en transit que par d'autres phénomènes astrophysiques. En plus de leur *'validation'*, 11 autres exoplanètes ont été découvertes avec des masses compatibles avec celles des compagnons planétaires grâce à des mesures de vitesse

radiale. Ces planètes sont classées comme planètes *'confirmées'*. 198 TOI (sur les 257 TOI) se sont avérés présenter des signaux compatibles avec des planètes en transit en utilisant uniquement des observations photométriques multi-couleur. De tels cas sont appelés *'planètes candidates vérifiées'* (VPC). J'ai également participé à l'identification de 2 planètes candidates proches (NPC, c'est-à-dire planètes transitant par des étoiles proches des étoiles ciblées), 4 binaires à éclipses (EB/SEB1), 10 binaires à éclipses proches (NEB), 9 binaires à éclipses blindées (BEB/SEB2).) et 4 détections de fausses alarmes (FA). ∼10 TOI restent des planètes candidates qui nécessitent davantage d'observations de suivi photométrique.

J'ai dirigé l'article de *'validation'* pour la planète TOI-1680 b. Il s'agit d'une planète de type super-Terre observée par le télescope TRAPPIST-Nord ainsi que par de nombreux autres instruments. Elle a un rayon de $1.460^{+0.063}_{-0.049}\,R_\oplus$ et se situe sur une orbite de 4.8 jours autour d'une étoile naine de type M proche (à 37.14 parsecs) (TOI-1680, V = 15.87 mag et J = 11.63 mag). Étant donné que toutes les planètes connues ayant un rayon similaire à celui de TOI-1680 b sont rocheuses, cette planète est censée être une planète rocheuse. Cette supposition sera confirmée par les mesures de masse planétaire issues des observations de vitesse radiale. J'ai également évaluer son potentiel pour la caractérisation atmosphérique, où j'ai découvert qu'elle pourrait être une candidate prometteuse pour ces études avec le *JWST*, d'autant plus que ce système se trouve à proximité de la zone d'observation continue de *JWST*.

Je dirige également l'article de *'validation'* de deux autres super-Terres : TOI-6002 b et TOI-5713 b. La première planète, TOI-6002 b, a un rayon de $1.65^{+0.22}_{-0.19}\,R_\oplus$ et est sur une orbite de 10.90 jours autour d'une étoile naine de type M moyen (TOI-6002, V = 14.6 mag et J = 11 mag) située à 32.04 pc du Soleil. La deuxième planète (TOI-5713 b) a un rayon de $1.77^{+0.13}_{-0.11}\,R_\oplus$ et est sur une orbite de 10.44 jours autour d'une étoile naine active de type M (TOI-5713, V = 15.35 mag et J = 11.07 mag) située à 40.95 pc du Soleil. Compte tenu de leur emplacement dans la distribution des rayons correspondant à la *vallée de densité*, TOI-6002 b et TOI-5713 b peuvent être soit de compositions rocheuses ou riches en eau. Au vu de leur emplacement dans la *vallée de rayon*, il n'est pas clair si elle ont conservé leur atmosphère ou non. Ces résultats les classent comme des cibles importantes pour déterminer leurs masses via des observations de vitesse radiale. Lorsque cela sera fait, les deux planètes seront ajoutées à l'échantillon d'exoplanètes sur lequel des inférences statistiques approfondies seront menées pour comprendre comment les super-Terres et les sous-Neptunes se forment et évoluent autour de étoiles naines de type M. Il est intéressant de noter que les deux planètes sont situées près du bord intérieur de la zone habitable de leurs étoiles hôtes, ce qui en fait également des cibles intrigantes pour de futures études atmosphériques visant à élargir notre compréhension de l'habitabilité potentielle autour des étoiles de type M et comment des planètes potentiellement habitables deviennent des planètes semblables à Vénus.

ملخص

منذ اكتشاف أول كوكب يدور حول نجم من النسق الرئيسي غير الشمس لأول مرة في عام 1995 (أي، كوكب خارج المجموعة الشمسية)، أصبحت دراسة الكواكب خارج المجموعة الشمسية واحدة من أكثر المجالات العلمية ديناميكية. منذ ذلك الحين، تم تمويل مهمات مختلفة في الفضاء وعلى الأرض بشكل خاص لاكتشاف وتوصيف هذه العوالم الغريبة، مما أدى إلى اكتشاف أكثر من 5500 منها حتى الآن. معظم هذه الكواكب خارج المجموعة الشمسية تُعرف رسميًا باسم "الكواكب العابرة" لأنها تمر بانتظام أمام نجومها المضيفة بالنسبة للمراقبين على الأرض. عندما يمر كوكب أمام نجمه المضيف، يتسبب في انخفاض، المعروف باسم الترانزيت، في سطوعه لان كمية من ضوء النجم يحجبها القرص الكوكبي. يمكن للمتابعة الفوتومترية للنجوم، التي تهدف إلى مراقبة تغيرات سطوع النجوم عبر الزمن، اكتشاف إشارات الترانزيتات، مما يكشف عن وجود كوكب يدور حول النجم المستهدف. هذا هو مبدأ "طريقة العبور" المستخدمة في اكتشاف معظم الكواكب خارج المجموعة الشمسية المعروفة حتى الآن. تزيد المهمة الفضائية TESS، التي أطلقتها وكالة ناسا في عام 2018، بسرعة من عدد الكواكب العابرة مع التركيز بشكل خاص على الكواكب البالغة احجامها بين الأرض ونبتون والتي تدور حول نجوم لامعة وفلكيا قريبة من مجموعتنا الشمسية. يعود ذلك إلى التوصيف المفصل لمعاييرها الفيزيائية، مثل نصف القطر والكتلة، وغلافها الجوي. لقد كشفت TESS بالفعل عن إشارات شبيهة بالعبور لآلاف الكواكب الخارجية, الا ان العديد من هذه الإشارات يعود سببها إلى ظواهر فلكية أخرى مثل النجوم المزدوجة، والنجوم المزدوجة المختلطة أو نشاط النجوم. قد تكون بعض الإشارات ناتجة عن الأدوات الاصطناعية للمركبة الفضائية. وبالتالي، لا تزال هذه الإشارات بحاجة إلى التحقق من طبيعتها الكوكبية باستخدام قياسات فوتومترية بواسطة تلسكوبات دات دقة اعلى من دقة TESS.

خلال أطروحتي، ساهمت في المتابعة الضوئية لأكثر من 257من الكواكب المرشحة التي إكتشفها TESS، والمعروفة باسم TOIs، لتأكيد الكواكب الخارجية الحقيقية وتجاهل تلك الناتجة عن الظواهر الفلكية أو الآلية. تمت المتابعة الضوئية لمعظم هذه الأهداف باستخدام التلسكوب TRAPPIST-North. ساهم عملي في "تصديق" 9 كواكب خارجية عابرة، وفي هذا السياق، يعد "تصديق" الكواكب الخارجية عملية لتأكيد الطبيعة الكوكبية لترانزيتاتها من خلال عمليات الرصد الضوئية متعددة الألوان، والمراقبة البصرية التكيفية للتأكد من أن النجوم المضيفة عبارة عن نجوم منفردة, بالاضافة الى عمليات رصد طيفية لتوصيف أكثر للنجوم المضيفة (على سبيل المثال، النوع الطيفي واالمعدنية)، بالإضافة إلى التحقق الإحصائي حيث تمثل إشارات العبور احتمالًا كبيرًا أن تنتج عن طريق الكواكب العابرة أكثر من الظواهر الفيزيائية الفلكية الأخرى. بالإضافة إلى "تصديقها"، تلقى 11 كوكبًا خارجيًا آخر قياسات للسرعة الشعاعية لنجومها، حيث وجدت كتلها متوافقة مع كتل الكواكب المرافقة. يتم تصنيف هذه الكواكب على أنها كواكب "مؤكدة". تم تقديم كل من الكواكب "المصدقة" و"المؤكدة" في منشورات على مجلات علمية. تم كذلك التأكد من إشارات 198 كوكب باستخدام عمليات رصد بصرية متعددة الألوان فقط (Verified Planet Candidates). شاركت أيضًا في تحديد كوكبين

قريبين مرشحين NPC، (أي كواكب تمر بنجوم قريبة من النجوم المستهدفة)، وأربعة ثنائيات كسوفية (EB/SEB1)، و10 ثنائيات كسوفية قريبة (NEB)، و9 ثنائيات كسوفية ممزوجة (BEB/SEB2).) و4إندارات كاذبة (FA). حوالي عشرة TOIs تبقى كواكب مرشحة تحتاج لمزيد من عمليات الرصد.

لقد قدت ورقة اكتشاف الكوكب TOI-1680 b. وهو كوكب تمت مراقبته بواسطة تلسكوب TRAPPIST-North بجانب العديد من التلسكوبات الأرض الأخرى. يبلغ نصف قطره $1.46^{+0.063}_{-0.049}$ نصف قطر كوكب الأرض في مدار يبلغ 4.8 يومًا حول نجم قزم متوسط من نوع M قريب (يبعد ب 37.14 فرسخًا فلكيًا) (TOI-1680, V = 15.87 mag and J = 11.63 mag)). نظرًا لنصف قطره، من المفترض أن يكون TOI-1680 b كوكبًا صخريًا. سيتم تأكيد هذا الافتراض من خلال قياسات كتلة الكوكب بواسطة عمليات رصد السرعة الشعاعية.

كما أقوم أيضًا بقيادة ورقة اكتشاف كوكبين آخرين: TOI-6002 b وTOI-5713 b. الكوكب الأول (TOI-6002 b) يبلغ نصف قطره $1.65^{+0.22}_{-0.19}$ نصف قطر الأرض ومداره 10.90 يومًا حول نجم قزم متوسط من نوع M قريب (TOI-6002, V= 14.6 mag J = 11 mag) يقع على بعد 32.038 فرسخًا فلكيًا من الشمس. الكوكب الثاني (TOI-5713 b) يبلغ نصف قطره $1.77^{+0.13}_{-0.11}$ نصف قطر الأرض وهو في مدار 10.44 يومًا حول نجم قزم نشط من نوع M قريب كذلك (TOI-5713, V= 15.35 mag J = 11.07 mag) يقع على بعد 40.946 فرسخًا فلكيًا. نظرًا لأن كتل الكواكب غير محددة بعد، فليس من الواضح ما إذا كانت عوالم صخرية أم غنية بالمياه كما أنها ليس من الواضح إذا كانت تمتلك غلاف جوي أم لا. المعرفة الدقيقة لطبيعة هذه الكواكب ستكون ممكنة عندما يتم تحديد كتلتها عبر مراقبة السرعة الشعاعية. ومن المثير للاهتمام أن كلا الكوكبين يقعان بالقرب من الحافة الداخلية للمنطقة الصالحة للسكن لنجومهما المضيفة، مما يجعلهما أهدافًا مثيرة للاهتمام للدراسات المستقبلية لتوسيع فهمنا للمنطقة الصالحة للسكن المحيطة بالنجوم الأقزام من نوع M. و لفهم كيفية تحول الكواكب القابلة للسكن الى كواكب شبيهة بكوكب الزهرة

Contents

List of Figures

List of Tables

" There are countless suns and countless earths all rotating around their suns in exactly the same way as the seven planets of our system... The countless worlds in the universe are no worse and no less inhabited than our earth"

–Giordano Bruno, 1584 A.D

Chapter 1

Introduction

1.1 Exoplanets: historical context

Are we alone in this Universe? Is Earth the only planet home to life? Or more generally, is there any form of life elsewhere in the universe? These questions, which have been posed for millennia by philosophers and thinkers, are currently being asked by everyone. From centuries before our era to this day, man never stopped contemplating the Universe and being fascinated by its mysteries. The Universe contains hundreds of billions of Galaxies, each composed of hundreds of billions of stars bound together by gravitation. The Sun around which the Earth where we live orbits is one of the stars in our galaxy, the "*Milky Way*".

Throughout history, there was a large debate between contradicting philosophical trends about the existence of other worlds like ours elsewhere in the universe. In fact, they where divided in two groups: philosophers believing in the uniqueness of our world and others believing in the plurality of worlds. For example, four centuries Before Christ (BC), *Platon*[1] wrote: *"So that our world would be similar in unity to the perfect animal, the author did not create two, nor an infinite number; only this unique sky was born, and no other will be born"*. On the other hand, Epicurus[2] imagined the plurality of worlds and wrote in his *Letter to Herodotus*: *"It is not only the number of atoms, it is the number of worlds that is infinite in the universe. There are an infinite number of worlds similar to ours and an infinite number of different worlds"*. Centuries after, the possible existence of other worlds turned out to be one of the core questions raised by the Copernican revolution. We cite for instance the Italian philosopher *Giordano Bruno*[3] (1548-1600) who said: *"There are countless Suns and countless Earths all rotating around their suns in exactly the same way as the seven planets of our system... The countless worlds in the universe are no worse and no less inhabited than our Earth"*. Some years after, *Isaac Newton*[4] (1643-1727) supported the idea of *Giordano Bruno* and stated that: *"And if the fixed stars are the centers of similar systems, they will all be constructed according to a similar design and subject to the dominion of One."* Since the mid-last-century, the idea of extraterrestrial life existence became most popular with the era

[1] 428/427-348/347 BC in Athens. He is an ancient Greek philosopher, considered one of the most influential thinkers in the history of Western philosophy. He was a student of Socrates and the founder of the Academy, the first institution of higher learning in Europe.

[2] Epicurus is a Greek philosopher, born at the end of 342 BC. or early 341 BC and died in 270 BC. He is the founder of Epicureanism, one of the most important philosophical schools of Antiquity

[3] Giordano Bruno (1548-1600) was an Italian philosopher and cosmologist known for defending a heliocentric, infinite universe. He was accused of heresy by the Inquisition and burned alive on February 17, 1600 in Rome.

[4] Isaac Newton (1643-1727) was British philosopher, mathematician, physicist, alchemist, astronomer and theologian. He is the founder of classical mechanics.

of space exploration and popularization of space science. As an example, let's cite, *Carl Sagan*[5] (1934-1996) who emphasized and popularized the vastness of the universe and the possibility of life beyond Earth in his book *"Cosmos"*. More recently, *Didier Queloz*, the co-discoverer of the first ever exoplanet around a main-sequence star and co-winner of Nobel Prize, stated[6]: "*I can't believe we are the only living entity in the whole Universe. There's just way too many planets, way too many stars... the chemistry that led to life has to happen elsewhere. So, I am a strong believer that there must be life elsewhere*".

The oldest exoplanet discovery claim was in 1855 by *William Stephen Jacob* (1813–1862) (Jacob, 1855) who carried out studies of the star *70 Ophiuchi*, a binary star located at 16.6 light years from the Sun in the *Ophiuchus* constellation. Jacob (1855) performed measurements on the position of the star and found some anomalies that he interpreted as positive hints in favor of the existence of a planetary companion in connection with the system. In 1896, *Thomas Jefferson Jackson* (Jackson, 1896) emphasized this finding and announced that these anomalies should be caused by a third object of planetary mass with an orbital period of 36 years around one of the two stars. However, Moulton (1899) subsequently refuted that discovery by demonstrating that a three-bodies system in such configuration cannot be stable. That discovery was refuted but it led to strong speculations on the possibility of the existence and detection of exoplanets

In 1952, Otto Struve (1897-1963) proposed the first ever proposal (*Proposal for a project of high-precision stellar radial velocity work observatory*, Struve (1952)) for a project to detect exoplanets in short orbits using radial velocity and transit methods. In his proposal, *Struve* had many comments that seem to be prescient. For example, he stated that *"It is not unreasonable that a planet might exist at a distance of 0.02 au, or about 3,000,000 km. Its period around a star of solar mass would be then about 1 day"*. In 1963 and after extensive observations, the Dutch astronomer *Peter van de Kamp* announced the discovery of an exoplanet in orbit around the *Barnard's star* after detecting peculiar anomalies in its proper motion (van de Kamp, 1963). *Barnard's star* is an M dwarf and it is the fourth closer star to our solar system. In 1969, *P. van de Kamp* declared the finding of a second companion around the same star (van de Kamp, 1969). These discoveries induced a large and lengthy controversy within the scientific community (van de Kamp (1982), Gatewood & Eichhorn (1973), Croswell (1988)). This controversy led to the invalidation of these discoveries be revealing that they originated from instrumental effects. It was a disappointment not only for astrophysicists but for all the scientific community, but it triggered strong speculations on the existence of exo-worlds.

The first confirmed discovery of an exoplanet was announced in 1992. It was a multiple system of two planets with masses comparable to that of Earth in orbit around a pulsar[7] named PSR1257+12 (Wolszczan, 1992). Regular variations in the period of the pulsar had as only plausible explanation the existence of two Earth-mass planets orbiting around it. It was the first demonstration that exoplanets do exist. Yet, instead of exoplanets orbiting main sequence stars as anticipated by the

[5]Carl Sagan (1934-1996) Is an American astrophysicist and science vulgarization and communication.

[6]https://unescoalfozanprize.org/professor-didier-queloz/

[7]A pulsar is an extremely dense neutron star, the residue of a massive star supernova, which rotates very quickly around itself and emits electromagnetic radiation parallel to its magnetic axis.

scientific community, these planets were space oddities in orbits around stellar corpse.

The first detection of an exoplanet in orbit around a 'normal' main-sequence star came three years later, in 1995. Two Swiss astrophysicists *Michel Mayor* and his then PhD student *Didier Queloz* announced the discovery of a planet, named *51 Pegasi b*, around a solar-type star *51 Pegasi* (Mayor & Queloz, 1995). *51 Pegasi* b is a giant hot-Jupiter planet, analogue to Jupiter in our solar system, but its orbit is at only 0.05 *au* from its host star. This discovery marked a pioneering achievement in the field of astrophysics. It demonstrated that other main sequence stars also possess planetary systems and proved the detectability of exoplanets. In this context, *Michel Mayor* and *Didier Queloz* were awarded a Nobel Prize in 2019.

Since 1995, the science of exoplanets, exoplanetology, has known a great revolution. That first discovery has driven significant improvements in the observation instrumentation and the detection techniques, notably the radial velocity and transit techniques described later in this chapter. To date, a total of more than 5500 exoplanet have been detected and confirmed according to the NASA Exoplanet Archive[8]. Thanks to this large sample and its diversity in terms of planets' sizes, masses, and orbits, our understanding of the planetary systems formation and evolution has also significantly revolutionized. This expanded thematics like exobiology, that was focusing only on planets of the solar system, with the goal of detecting life signatures (biosignatures) on exoplanets orbiting their stars within the so called *habitable zone*, an annular region around the star where temperature can allow the water to exist in its liquid state. Since then, many ground-based and space missions have been deployed. We cite for example the space missions *Kepler* (Borucki et al., 2010) and the Transiting Exoplanet Survey Satellite (*TESS*: Ricker et al., 2015) that were responsible for detecting most of the exoplanets known today, and CHaracterizing ExOPlanet Satellite (*CHEOPS:* Isaak, 2015). *Kepler* was launched in 2009 by NASA and was the most successful exoplanet search project in terms of sheet number of detections. It observed a fixed field of view in the *Cygnus* and *Lyra* constellations. It monitored over 150,000 stars and detected more than 2778 exoplanets of different sizes. *TESS* (described in detail hereafter) is a space mission that was launched in 2018. It is performing an all-sky survey focused on nearby stars. It has detected more than 400 confirmed exoplanets at the time of writing, and thousands of exoplanet candidates. *CHEOPS* is a mission of the European Space Agency (ESA), launched in 2019 one year after the *TESS* launch. It is the first mission to study already known exoplanets transiting around bright stars. *CHEOPS* performs high-precision photometric observations of transiting planets to precisely improve their parameters. It focuses on small planets with sizes smaller than Neptune, with the goal to investigate their internal structures and compositions.

The science of exoplanets seems to have a bright future and the ceiling of ambitions is rising. The James Webb Space Telescope (*JWST*: Greene et al., 2016), launched in December 2021, is going to help the scientific community to dive deeper in the atmospheres characterization of exoplanets. In addition, two other space missions are scheduled for launch in the next few years by ESA,

[8] https://exoplanetarchive.ipac.caltech.edu/

PLATO[9] (PLAnetary Transits and Oscillation of stars, (Rauer et al., 2022)) in 2026 and *ARIEL*[10] (Atmospheric Remote-sensing Infrared Exoplanet Large-survey, (Haswell, 2021)) in 2029. *PLATO* is a space mission that will focus on detecting temperate rocky planets transiting bright Sun-like stars, and to bring a strong constraint on the frequency of 'Earth-twins', something that Kepler failed to achieve. Using asteroseismology, *PLATO* will also be able to study radii, masses and ages of the host stars with unprecedented precision and provide precise planet parameters. On its side, *ARIEL* will focus on studying the atmospheric properties of a large sample of transiting exoplanets. It will use both visible and infrared wavelengths to study a sample of ∼1000 exoplanets

1.2 Search for extraterrestrial life

One of the most important aims of detecting and characterizing exoplanets is to answer the *old-new* questions on extraterrestrial life existence. Scientists have defined the so-called *Habitable Zone* (*HZ*: Kopparapu et al., 2013) as the area around the star in which large amount of water could exist in liquid form at the surface of a rocky planet, as water is the key chemical element for any form of life to exist and develop. The location of the *HZ* is contingent on the size and the luminosity (or mass as well) of stars. It also depends on the atmospheric composition of the planet (whether it contains green-house effect gases or not). The fainter the star is, the closer the *HZ* is (see Figure 1.1). Our planet Earth, is located at one astronomical unit (au[11]) where the equilibrium temperature is theoretically determined to be 255 K (considerably lower than the freezing point of water at 273.15 K). However, the greenhouse effect elevates it to be approximately 288 K. It is worth noting planets orbiting in the *HZ* is a necessary but not sufficient condition for a planet to be habitable. It of course needs to have water on its surface, but also to have an atmosphere sustaining the right surface conditions (pressure and temperature) to maintain a part of this water in liquid form. The *HZ* is thus nothing more than a simple concept used to identify and prioritize potentially habitable exoplanets.

As of today, thousands of exoplanets have been confirmed. These planets, displaying a large diversity, orbit around stars of different spectral types. As our Sun is just a star among billions of stars in the universe, it is very natural (in my point of view) for extraterrestrial lives to have evolved on exoplanets that are more or less similar to our Earth, and orbiting stars more or less similar to our Sun. The first step to search for exoplanet habitability is to consider only rocky planets orbiting in the *HZ* of their stars, where they could have liquid water (if any) on their solid surface. It is also important for the considered planets to have moderate surface gravity (that depends on the planetary mass and radius) enough to retain their atmospheres (if any) but not as high as it can make dense atmospheres optically thick to the stellar light (Robinson, 2019). It is important for parent stars to have a long enough lifetime for life on their hosted planets to develop. Most of the planets considered today in the search for extraterrestrial life are hosted by M dwarf stars, whose advantages are explained later in this chapter. From their names, M dwarfs are the

[9] https://platomission.com/
[10] https://arielmission.space/
[11] 1 au = 149 597 870.7 km

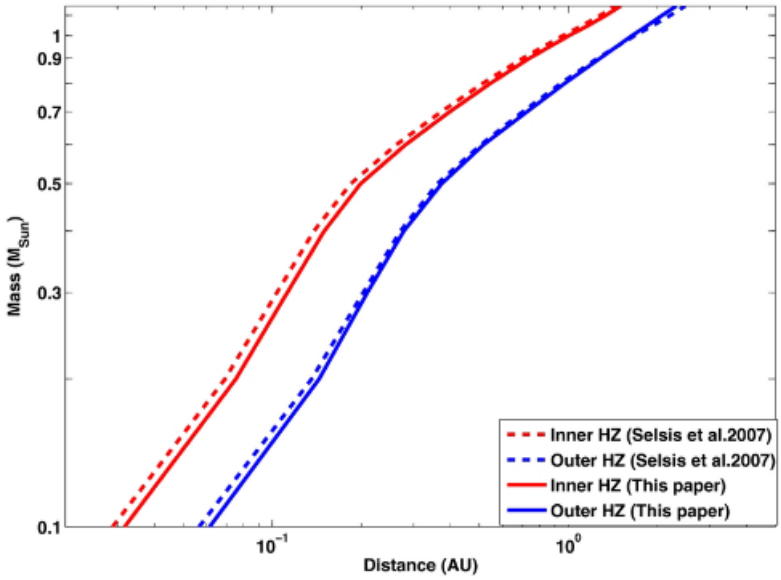

Figure 1.1: Habitable zone with interior and exterior limits as function of the stellar mass. Credit: Figure adapted from Kopparapu et al. (2013).

smallest, lightest and coolest stars in the main-sequence. They have radii from 0.1 to 0.6 $R_{\odot}$, masses from 0.08 to 0.6 $M_{\odot}$, and effective temperatures from 2700 to 3750 K. With these effective temperatures, are given the spectral type "M". Some of these planets orbit closely to their stars, which might make them to be tidally-locked with endless day/night-sides (Mazeh, 2008; Guillot et al., 1996; Matsumura et al., 2010). Such case may lead to atmospheric collapse as gases would condense in the dark (cold) hemisphere unless there is an efficient heat redistribution (Joshi et al., 1997; Williams & Pollard, 2002; Wordsworth, 2015; Tasker et al., 2017). Additionally, M dwarf stars have been found emitters of high-energetic X-ray and Ultra-Violet (XUV) radiations during their long pre-main sequence phase (the phase before settling the main-sequence when hydrogen start fusing in their cores) (see e.g. do Nascimento et al., 2016; Driscoll, 2018; Robinson, 2019). This could be very challenging for the close orbiting planets, as XUV may trigger atmospheric erosion, runaway greenhouse effect and hydrodynamic escape, especially for planets without magnetic fields. This might even make the planets lose oceans of water to space, making them voided from surface life conditions (see e.g Shields et al. (2016) and references therein).

The major question is *how to detect any potential life on exoplanets that are light-years away from us?* As introduced earlier, *exobiology* has a special focus on this topic. This field of science consists of detecting biosignatures, which are indirect evidences of the existence of life as known on Earth. For example, a measured atmospheric composition reflecting a strong chemical disequilibrium that could not be explained by any abiotic process. For instance, an atmosphere rich in CO_2 and CH_4 (Tasker et al., 2017) would be hard to be explained without biology, as CH_4 has a very short lifetime in an oxygenic atmosphere and as abiotic sources of CH_4 are rare.

Another trending subject among scientists is about the existence of any intelligence extraterrestrial civilization elsewhere in the universe. Scientists try to deal with this subject following a step-by-step scientific approach. It is the approach of Drake (1961) who formulated, in 1961, an

equation (usually known as *Drake equation*) that estimates the number of technological, and then communicative, civilizations *now* existing in the Milky Way galaxy. It is written as follows:

$$N_{civilizations} = R_* f_p n_e f_e f_i f_c L \tag{1.2.1}$$

where R_* is the rate of stars' formation in our galaxy, f_p is the fraction of those stars hosting planetary systems, n_e is the mean number of planets per star with the potential to support life, f_e is the fraction of suitable planets on which life actually appears, f_i is the fraction of life-bearing planets on which intelligent life emerges, f_c is the fraction of civilizations that build technology emitting detectable signs of their existence into space and L is the duration of time for which such civilization releases detectable signals into space. There are two approaches to deal with Drake equation: we either try to directly detect technological civilization, it is the SETI (Search for Extra Terrestrial Intelligence) approach, or try to determine the different terms of the equation step-by-step. The SETI project is "listening to" the universe to detect coherent electromagnetic radiations that could have been emitted by alien civilizations, assuming generally that these civilizations have detected our existence and are trying to communicate with us. This is an attractive project because in case of any positive detection, this will settle the question of the possible existence of extraterrestrial life, while demonstrating that we are not the most technologically advanced species in our vast Universe. Given the advance in exoplanets researches since 1995, astrobiologits have many constraints at their disposal such as how many exoplanets exists and how many of them lie in the *HZ*. This pushed Frank & Sullivan (2016) to develop a new form, called "Archaeological-form", of the *Drake equation* where they eliminate the need for L. This new form defines A as the "number of technological species that have *ever* formed over the history of the observable Universe" and it is written as:

$$A = [N_* f_p n_p][f_l f_i f_t] \tag{1.2.2}$$

where N_* represents the total number of stars, f_p the fraction of those stars that hots planets, n_p the mean number of planets within the habitable zone around a star with planets, f_l the probability that a planet within the habitable zone develops life, f_i the probability that a planet with life develops intelligence, and f_t the likelihood that a planet with intelligent life advance technology. Under their selected assumptions, Frank & Sullivan (2016) inferred that we are probably not the only advanced civilization that *has* evolved in Universe.

It is important to note that, given the vast distance between stars, any communication with another civilization could be frustratingly slow and difficult. First, it would require that two species, having evolved totally independently, find a common set of concepts and methods (i.e. a 'language') to exchange information. Secondly, given the vast distance between stars and the finite value of the speed of light, getting an answer to any message would take at least several decades, if not centuries or even much more.

1.3 Methods of detection of exoplanets

In this section I will introduce the different techniques used to detect exoplanets. There are two main families of detection methods of exoplanets: direct and indirect methods. The first family is founded on the direct imaging of exoplanet systems and the second aims to observing and analyzing different types of interactions between the star and its hosted planet. In this section I introduce all these methods and I will insist on the transit method used in this thesis.

1.3.1 Direct methods

Direct methods for exoplanets detection are one of the most significant challenges of modern astronomical instrumentation to date. Generally, the host stars are at least billion times brighter than the planets orbiting around them. The direct imaging methods must therefore be based on high-resolution and high-contrast imaging using techniques like e.g. adaptive optics, chronography and image processing.

Detecting an exoplanet via direct methods requires the improvement of some essential parameters, namely the angular resolution. In the sense of the Rayleigh criterion, the angular resolution limit is obtained by the diffraction limit of the telescopes being used:

$$\theta = 1.22 \times \frac{\lambda}{D}$$

with λ being the observational wavelength and D the aperture diameter of the telescope.

To perform direct imaging of an exoplanetary system, it is first necessary to achieve a good adjustment between the angular resolution of the instrument and the spectral domaine of observation. Let us now see some of the main techniques used for direct detection of exoplanets.

Nulling interferometry

The nulling interferometry method allows the direct detection of exoplanets using at least two telescopes. It consists of canceling the luminous flux coming from the star and allowing only the planetary flux to amplify. For simple explanation, let's consider the case of two telescopes. The light from a distant star reaches the two telescopes simultaneously. The beam from one telescope is π phase-shifted with respect to the beam reaching the second telescope. When the two beams are combined together, they experience a destructive interferometry and so are canceled out. Light from the planet (generally in IR or mid-IR), around the star, reaches the two telescopes at a certain angle. This causes a delay in the light reaching the second telescope. Thus, even after the π phase shift in one of the beams, when the rays (from the planet) are combined, they are amplified and not destructed. In short, the nulling interferometry technique cancels out the light coming from the host star and amplifies the light coming from its planet (see e.g. Bracewell, 1978).

An ambitious space mission called Large Interferometer For Exoplanets (LIFE: see e.g. Quanz et al., 2022) will be based on the nulling interferometry. It is a constellation of five satellites, one space telescope with four independent mirrors (see Figure 1.2). It is still in its early preparation stage and it will likely take decades to be built. The main goal of this mission is to detect directly

exoplanets and traces of life (biosignatures) on them.

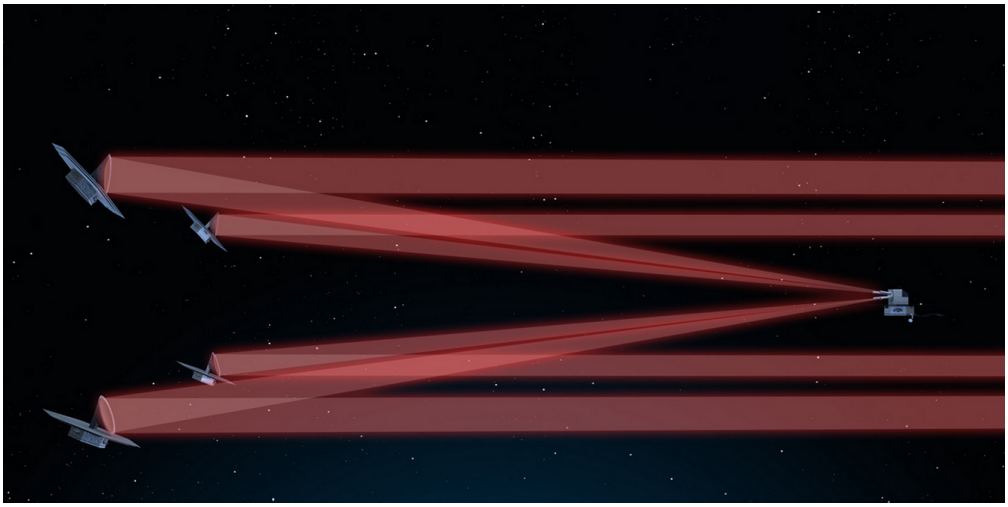

Figure 1.2: Illustration of the LIFE mission's five satellites, connected to form a large space telescope. Credit: https://ethz.ch/en/news-and-events/eth-news/news/2023/04/a-key-experiment-for-the-life-space-mission.html.

Coronagraphy

Planets are generally drowned in the starlight due to the tiny angular separation between the two objects and to the huge star/planet contrast. The coronagraph method is used to block the light from the star and let only the light from the planet. Such direct imaging observations are generally performed in the mid-IR where the contrast between the planet and star is minimal, especially for cold planets like Earth and Jupiter. This method was first invented by Lyot (1932) for solar observation. Figure 1.3 shows the standard *Lyot* coronagraph. This technique consists of placing a mask in the optical system to block the starlight in order to distinguish the planet. However, the diffraction created by the mask located in the primary focal plane reduces the performance of the optical system. To solve this problem, Lyot (1932) proposed to re-image the primary image focal plane and to obscure the edges of the pupil with a diaphragm in order to eliminate as much as possible the stellar residues. With the coronagraphy, we can therefore reduce the contrast and increase the chance of distinguishing the companion from its parent star.

This technique can be affected by some spurious fluxes and noises that make the detection of telluric-type planets difficult. These parasites are of various origins, such as a possible residue of the stellar flux, thermal emission of the telescope optics and the flux emitted by the zodiacal and/or exo-zodiacal cloud.

Coronagraph technique has been employed in many projects, in particular in the recent *JWST* to directly detect gas giant exoplanet. In their work, Carter et al. (2023) presented the first observations by such technique on *JWST*. It was for the super-Jupiter exoplanet HIP 65426, previously detected by (Chauvin et al., 2017). They used the high-contrast imaging modes of *JWST* instruments, NIRCam from 2–5 μm and MIRI from 11–16 μm.

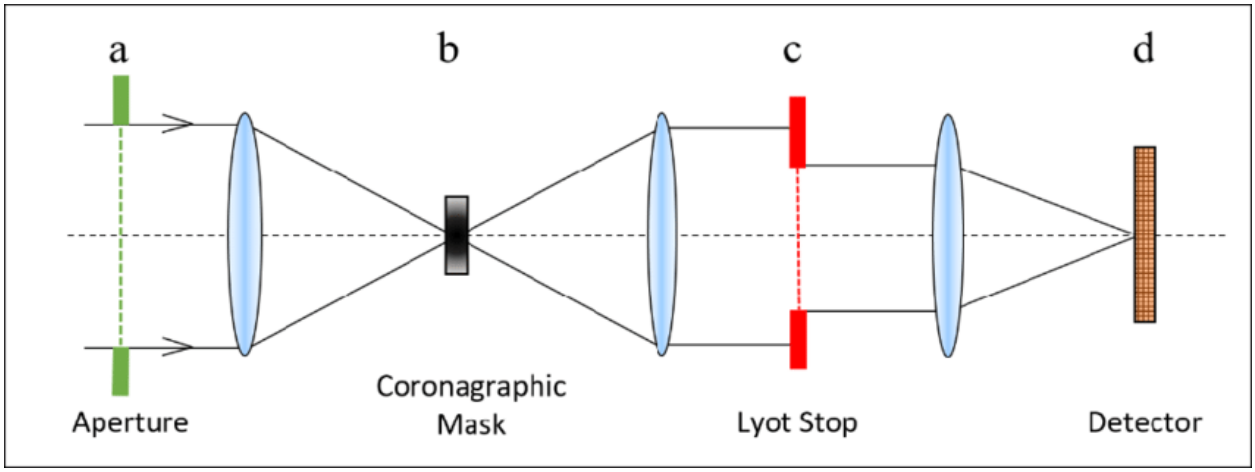

Figure 1.3: Standard *Lyot* coronagraph. a: entrance pupil plane, b: coronagraphic plane, c: Lyot stop plane, d: plane of detection (Valle et al., 2019).

Adaptive optic

The major challenge for ground observations of exoplanetary systems is atmospheric turbulence. The troposphere, which is the closest atmospheric layer to the ground is not homogeneous but it consists of multiple bubbles of different temperatures and humidity. These bubbles are not static; they move with the speed of the wind through convection, with the warmer ones rising and the colder ones sinking. This is what we call *atmospheric turbulence*. This leads to random variations of refractive index of these bubbles, causing light rays from a star to undergo different and random refractions depending on the atmospheric zone they pass through. When we observe a star with a large-diameter, single-pupil terrestrial telescope, the angular resolution is not solely limited by the telescope's diameter (Fusco et al., 2006). The *atmospheric turbulence* also disturbs the incident wavefront and degrades the angular resolution of the image, reducing the telescope's performance to that of a small telescope with a low diameter (see right panel of Figure 1.5).

The adaptive optics is a technique that allows partial real-time correction of evolving and non-predictive wavefront deformations using a deformable mirror. As shown in Figure 1.4, the adaptive optics system consists of three main components that work simultaneously in perfect harmony as follows:

- The wavefront sensor (WFS): it measures and analyzes the deformations of the incident wavefront after passing through atmospheric turbulence. The sensor must be robust to noise and capable of measuring the wavefront's phase in real-time.
- The deformable mirror: after each analysis of the incident wavefront, the mirror changes its shape using a system of pistons installed beneath its deformable surface to compensate for these deformations. This process occurs continuously in real-time. As a result, the mirror shape is adapted so that the obtained wavefront is more or less identical to the one obtained above atmospheric turbulence.
- The controller: the controller drives the mirror based on the measurements provided by the

wavefront sensor.

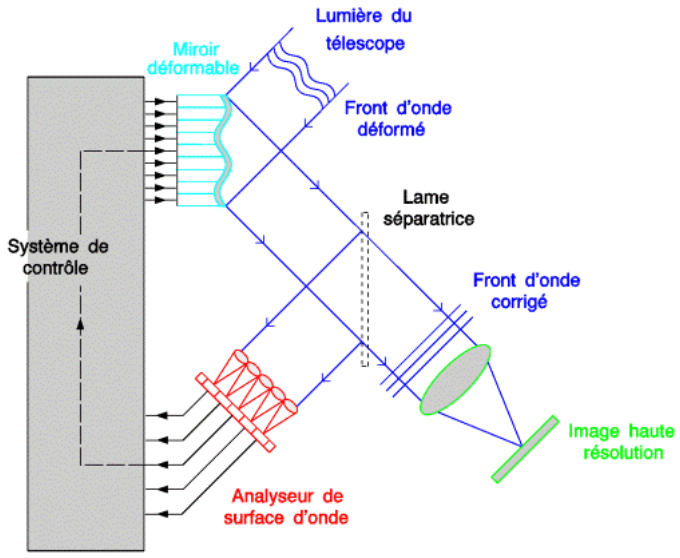

Figure 1.4: Different components of adaptive optic system. Credit: Observatory of Paris/LESIA.

The adaptive optic technique allows the elimination of atmospheric turbulence to obtain a resolution close to be limited by diffraction. This technique was first ever successfully used to discover the planetary mass brown dwarf companion 2M1207b (see left panel of Figure 1.5) in 2004 using the Very Large Telescope (VLT) of the European Southern Observatory (ESO) (Chauvin et al., 2004).

Advantages of direct imaging

The direct methods have the advantages to detect exoplanets relatively far from their parent stars, which rend them complementary to the indirect methods (i.e. transit and radial velocity methods) as we will see later. This may be the only way to detect and study in detail an Earth-like planet orbiting around a solar-type star, including searching for spectroscopic traces of life from the planet's spectrum.

Limits of direct imaging

In addition to the challenge of the high host star/planet contrast, and the atmospheric turbulence, the *zodiacal dust* (resulting from collisions between asteroids and from evaporation of comets in the solar system) and *exozodiacal dust*(resulting from collisions between planetesimals) can limit the detection potential of direct imaging, especially for faint, faraway systems. Thus, these methods are better applied only for stars in the solar neighborhood and do not have direct access to the size and mass of the detected companions, but these important parameters can still be inferred with the help of theoretical models complementing the observations.

1.3.2 Indirect methods

Nowadays, more than 5500 planets have been discovered, with the vast majority of them with indirect detection methods. These methods aim to observe and study the various types of perturbations that a planetary companion exerts on its host star. In this part of chapter, I will discuss the main

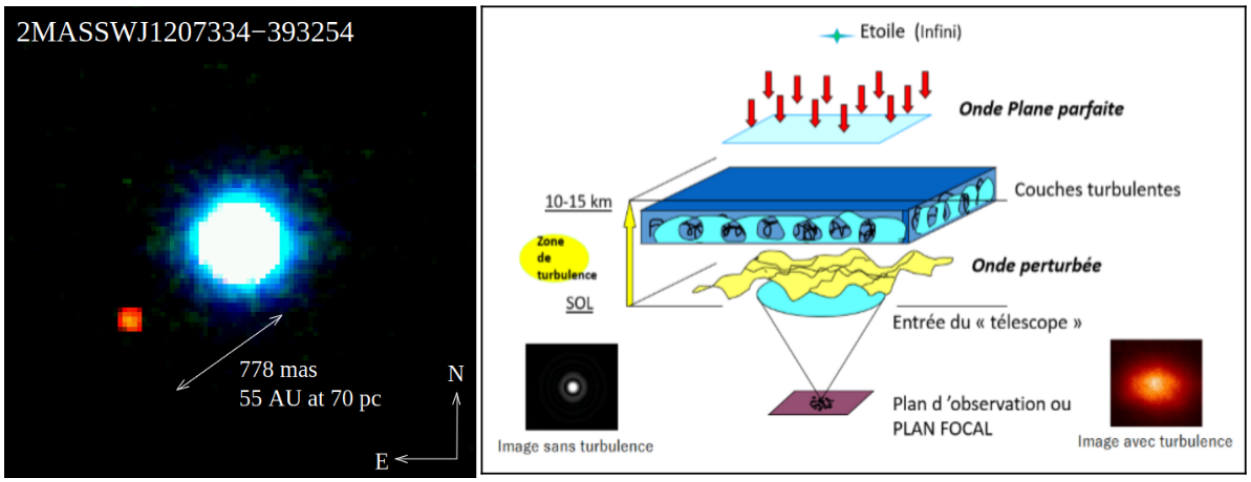

Figure 1.5: *Left*: Composite image of brown dwarf 2M1207 and its giant planet candidate companion. The companion is easily distinguishable, in term of its color, from the brown dwarf 2M1207 (Chauvin et al., 2004). *Right*: Effect of atmospheric turbulence on the wave front. Before passing through the turbulent layer, the wave fronts are flat, but after passing, the wave front is disturbed which affect the image of the object. Credit: http://physique.unice.fr/sem6/2015-2016/PagesWeb/PT/Turbulence/introduction.html

indirect detection methods, with a particular focus on the transit method used at the core of this thesis work.

Gravitational microlensing

This method is based on the principle of gravitational lenses described by *Einstein*, in 1936, in his general relativity theory (Einstein, 1936). If a foreground star passes through or approaches the line of sight of a background star, the gravitational field of the foreground star will act as a converging lens, bending the light coming from the background star and amplifying it.

If the foreground star harbors an orbiting planet, the planet cause a disturbance in the light of the single-lens indicating its presence (Mao & Paczynski, 1991; Gould & Loeb, 1992). This tool is capable of detecting planets with masses ranging from those of giant planets to those of terrestrial planets. The method of gravitational microlensing is capable of detecting exoplanets with orbits at any inclination with respect to the observer. However, due to the low probability of geometric alignment between the observer, the lens, and the source, this method needs simultaneous observation of a high number of distant stars. Figure 1.6 presents an example of a light curve of a gravitational microlensing effect observed by Beaulieu et al. (2006) for the exoplanet OGLE-2005-BLG-390.

Astrometry

This method was first expounded by Gatewood (1987) in 1987. It aims at studying the gravitational interaction between a star and its hosted planet. It consists of accurately determining the position of the star in the plane of sky perpendicular to the line of sight. The host star perturbed by its planet's gravitational force, will orbit around the barycenter of the system describing an ellipse (in the sky plane). Such movement is superposed to the proper motion of the star (see Figure 1.7).

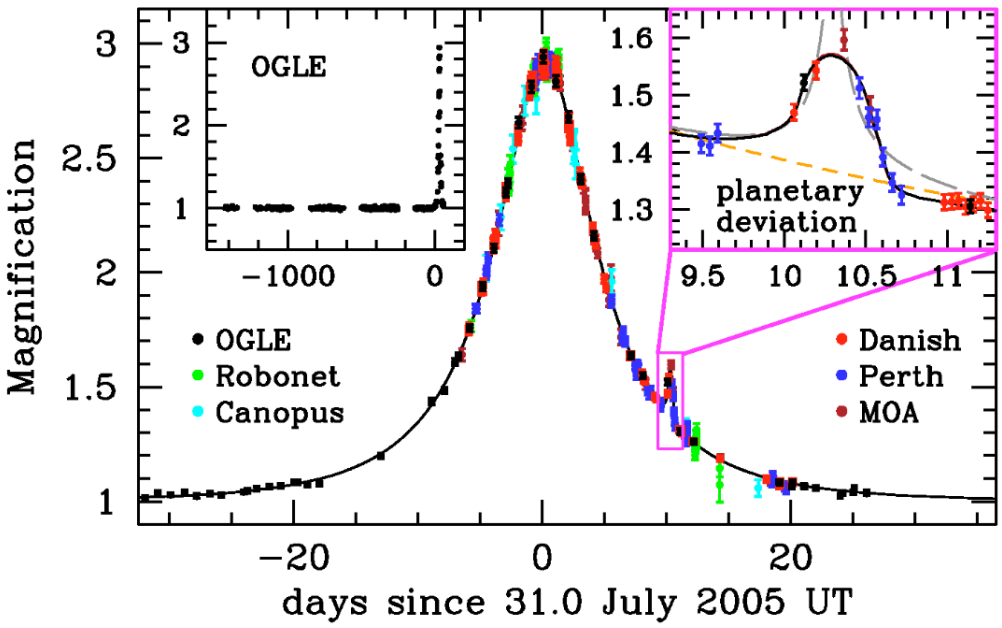

Figure 1.6: Light curve of the microlensing event of OGLE-2005-BLG-390 plotted as a function of time. The black line is the best fit model. Credit: (Beaulieu et al., 2006)

The angular semi-major axis α of the ellipse is expressed as:

$$\alpha = \left(\frac{M_p}{M_* + M_p}\right)\left(\frac{a}{1AU}\right)\left(\frac{d}{1pc}\right)^{-1} arcsecond \tag{1.3.1}$$

with a and d are the semi-major axis of the planetary orbit and the distance from the observed system, respectively. The significant advantage of this method is that it allows the detection of planets in wide and low-inclination orbits and can determine precisely the planet's mass and its orbital inclination. The first successful use of this tool to detect an exoplanet was in 2010 by Muterspaugh et al. (2010) to detect the exoplanet HD 176051 b in a double star system, where it is not yet known around which star the planet orbits. Astrometry requires extremely precise optics and is especially hard to use it from the Earth's surface because our atmosphere distorts and bends light. This limitation does not apply to space-based telescopes, and it is expected that the ESA Gaia mission (Gaia Collaboration et al., 2016) will eventually detect hundreds of giant planets with orbital periods of few years (see e.g. Panahi et al., 2022).

Pulsar timing

Pulsars are neutron stars remnant from the death as *supernova* explosion of massive ($M > 8M_{sun}$) stars. They are extremely dense, highly magnetized and rapidly rotating objects. Their rotational periods range from seconds to milliseconds. They emit intense electromagnetic radiation (radio waves) in the direction parallel to their magnetic dipole axis which is not perfectly aligned with their rotational axis. As pulsars spin, regular and precisely timed pulses of their magnetic radiation can be detected from Earth if it crosses the emission beam. If a pulsar has a planet, it will be orbiting the center of mass of the system under the planetary gravitational influence. This results

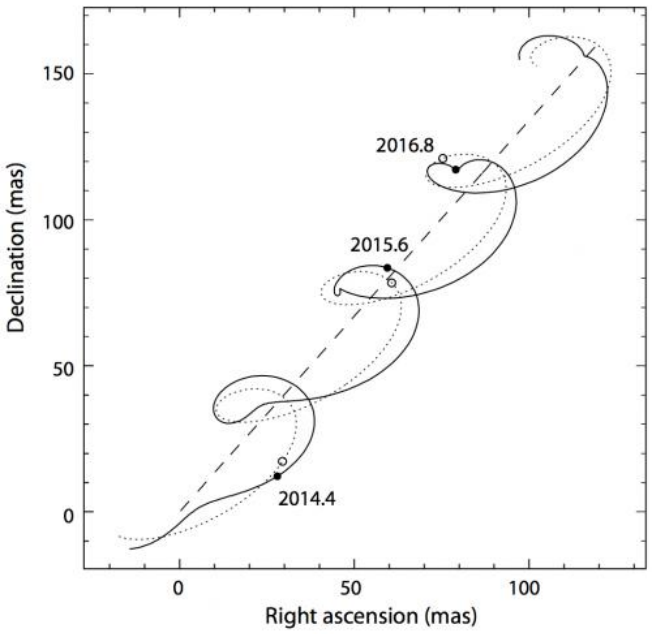

Figure 1.7: Modeled position of a star on the sky plane. The star is supposed to be at 50 pc, to have a proper motion of 50 mas.year^{-1}, and to orbited by a planet with = 15 M_J , e = 0.2, and a = 0.6 *au*. The straight dashed line represents the path of the motion of system's barycenter as seen from the solar system' barycenter. The dotted curve shows the effect of parallax on top of the system's proper motion. The solid curve includes the apparent motion of the star due to the gravitational interaction with the planet. Credit: Figure adapted from Perryman (2000).

in a back and forth movement of the pulsar on the observer's line of sight, which causes slight regular variations in the frequencies. Thus, this method can constrain precisely the orbit and the mass of the planetary companion.

The first exoplanetary system discovered using this method was PSR 1257+12 system, for which three planets with masses comparable to that of Earth (two planets) and the Moon (one planet) were detected in 1992 by Wolszczan (1992). As of today, seven exoplanets have been detected to orbit pulsars according to the NASA Exoplanet Archive.

Radial Velocity

The radial velocity is one of the most efficient methods used for the detection and characterization of exoplanets. It was credited with discovering the first ever exoplanet in orbit around a Sun-like star by Mayor & Queloz (1995). This technique is based on the famous *Doppler* effect. When a light source is moving in a given direction, an observer who sees the source approaching does not perceive the same wavelength as an observer who sees the same source moving away. When the light source approaches the observer, the wavelengths will appear shorter, resulting in a "Blueshift". Conversely, when the source moves away, the wavelengths are perceived longer, causing a "Redshift" (see Figure 1.8). The wavelength shift is given by the following relativistic formula:

$$\lambda = \lambda_0 \left[1 - \frac{V_s}{c} \times \sin(i)\right] \tag{1.3.2}$$

With c is the speed of light in vacuum, V_s is the magnitude of the velocity vector of the source

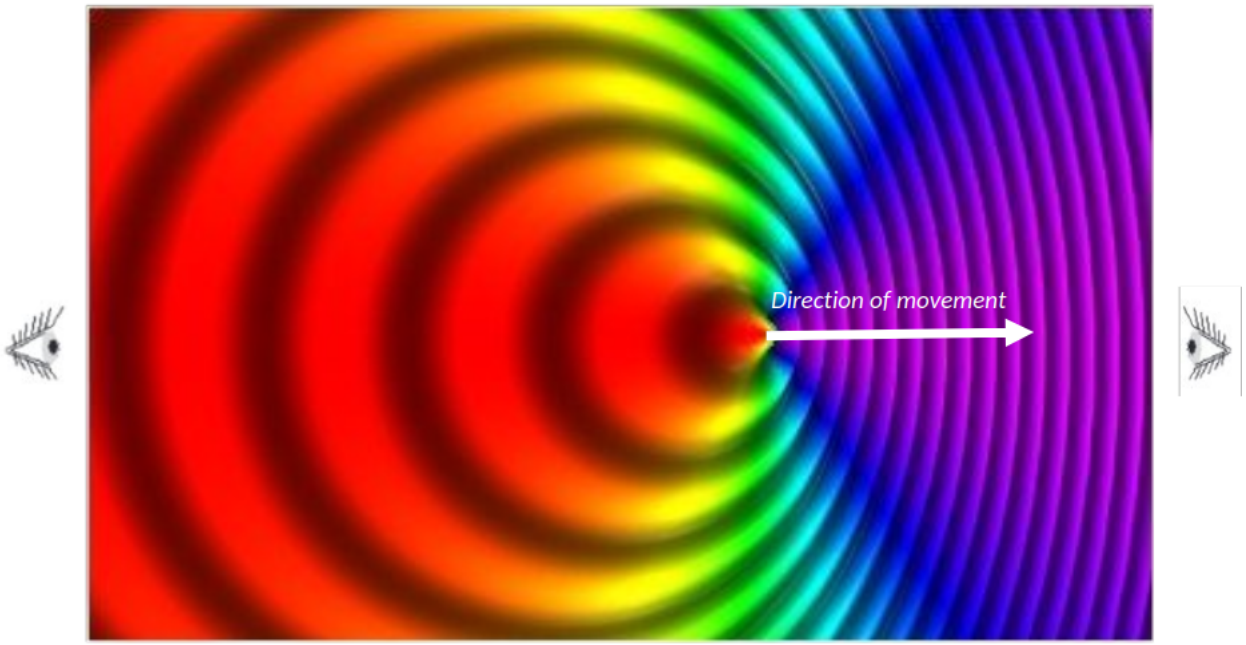

Figure 1.8: Hypothetical source of light moving to the right at a speed of $0.7c$. The wavelengths are perceived shorter by the observer in the right and longer by the observer in the left the left. Credit: https://fr.wikipedia.org/wiki/Effet_Doppler_relativiste#/media/Fichier:Velocity0_70c.jpg

relative in the observer's referential system, and i is the angle between the line of sight directed towards the observer and the normal on the speed vector (it is also called the "orbit inclination", see right panel of Figure 1.9). The *radial velocity*, expressed as $V_r = V_s \sin(i)$, is defined as the component of the velocity vector of the light source in the radial direction, i.e. along the line connecting the observer and the source. If $V_r > 0$ the source approaches the observer and if it is < 0 the source moves away.

Let's apply this effect on a system of two bodies, a star and a planet (see left panel of Figure 1.9). Because of the gravitational interaction between the two bodies, the star is also in orbit around the common barycenter of the system. Therefore, there is a back-and-forth motion of the star along the observer's line of sight, which results in a "Redshift" when the star moves away and a "Blueshift" when it approaches (see e.g. Marcy & Butler, 1992).

By measuring the wavelength shift of the source's spectrum using a spectrograph, one can determine the radial velocity by applying the following formula:

$$\frac{\Delta\lambda}{\lambda_0} = \frac{V_r}{c} \tag{1.3.3}$$

$\Delta\lambda$ is the the shift on the observation wavelength λ_0. Likewise, the radial velocity of the star as being orbited by a planetary companion is expressed as (see e.g. Murray & Correia, 2010a; Wright & Gaudi, 2013):

$$V_r = V_0 + K\left[\cos(\omega + \nu) + e\cos(\omega)\right] \tag{1.3.4}$$

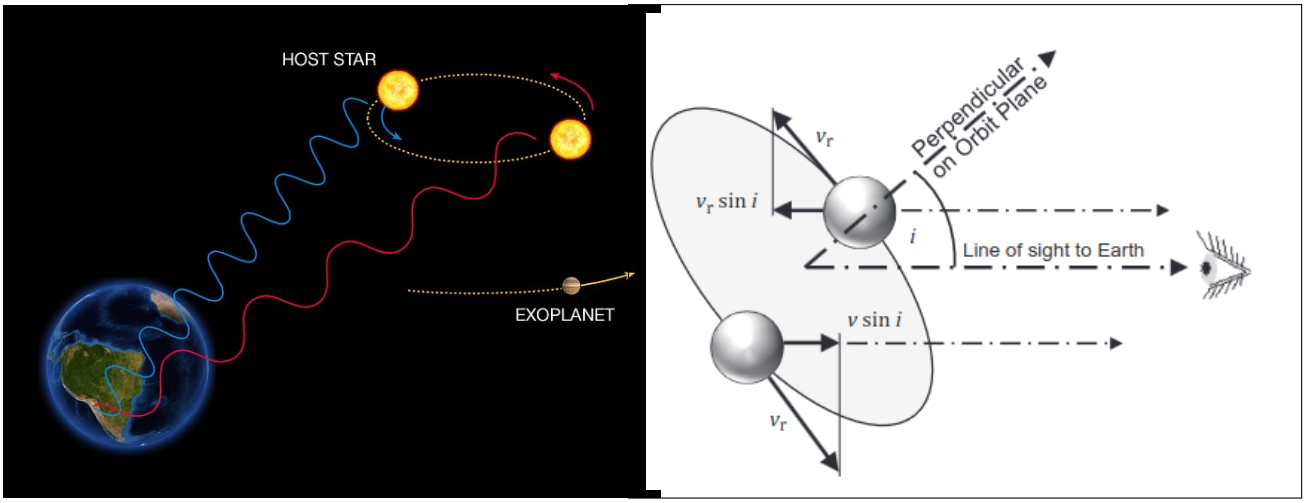

Figure 1.9: *Left*: Imaginary "star-planet" system in orbit around the common center of gravity (blue represents the Blueshift, and red represents the Redshift), Credit: ESO . *Right*: Spatial orientation of the orbit plane of a star and its movement component on the line of sight directed towards the observer. Credit: Cambridge (2017).

where V_0 is the constant systematic velocity of the system's barycenter, ω is the argument of periastron (the position where the planet is at the closest distance to its host star), e the eccentricity of the planetary orbit, ν is the true anomalie[12]. ω and ν are shown on Figure 1.12 in the next section. K is the RV semi-amplitude, expressed as:

$$K = \frac{M_p \sin(i)}{(M_p + M_*)^{\frac{2}{3}} \sqrt{1 - e^2}} \left(\frac{2\pi G}{P}\right)^{\frac{1}{3}} \tag{1.3.5}$$

Generally, $M_p << M_*$, which lead to constrain the quantity:

$$\frac{M_p \sin(i)}{M_*^{\frac{2}{3}}} = K \sqrt{1 - e^2} \left(\frac{P}{2\pi G}\right) \tag{1.3.6}$$

If the variation of the radial velocity as function of time is periodic, it indicates the existence of at least one exoplanet orbiting around the star. A model is then fitted to the RV data to constrain K, e and P. Thus, the RV provides the minimum planetary mass $M_p \sin(i)$. It is worthy to note that the mass of the star M_* can be determined from independent analyses. The orbital period of the planet is the same as that of the radial velocity variation. However, it is crucial to verify that the star is not a binary star system, and the variation in radial velocity is not caused by its rotation or magnetic cycle. Figure 1.10 presents an example of a radial velocity curve of the first exoplanet detected around a Sun-like star in 1995 by *Michel Mayor* and *Didier Queloz* from the Geneva Observatory (Mayor & Queloz, 1995).

RV method is more effective for giant (massive) planets in short and inclined orbits (relative to the plane of the sky) around low mass stars. This is because low mass stars are more affected by

[12]The true anomaly is the angle between the periapsis direction and position of the planet along its Keplerian orbit around its host star

the gravitational interaction induced by the planet. In summary, the radial velocity method allows for the determination of the following parameters:

- orbital period (and then semi-major axis)
- periastron time
- orbital eccentricity
- argument of periastron
- minimum planetary mass

The radial velocity tool is usually used in complementary with transit method. The inclination i determined by means of transits is used to break the $M_p \sin(i)$ degeneracy to determine the exact planetary mass. Importantly, the RV method can determine the eccentricity of the orbit, which offers valuable insights into the dynamical history of the system.

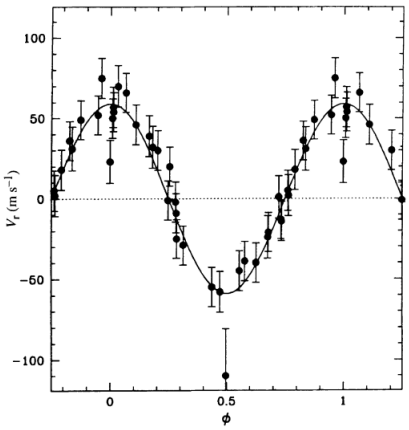

Figure 1.10: Radial velocity curve of *51 Pegasi* obtained by Mayor & Queloz (1995).

Thanks to technological advances, the RV method has known a significant improvement in the last two decades. It is now capable of detecting terrestrial planets orbiting M dwarf stars. Current spectrographs used in radial velocity can detect RV changes less than 1m/s. For instance, the Echelle SPectrograph for Rocky Exoplanets and Stable Spectroscopic Observations (ESPRESSO: Pepe et al., 2021) at VLT can reach a precision of 10 cm/s. One of the main goals of ESPRESSO is to search and characterize Earth-size planets orbiting solar-type stars in the *HZ*. Besides of that, the MAROON-X[13] instrument, operated by the University of Chicago, should be able to detect Earth-size planets in the habitable zones of mid- to late-M dwarfs (Seifahrt et al., 2020, 2022). It is a high-resolution (R≈80,000) optical (500-920nm), designed to reach out 1 m/s radial velocity precision for M dwarfs down to and beyond Vmag = 16. This instrument has already determined the masses of many small planets planets, such as TOI-561b (Brinkman et al., 2023), TOI-732 b and c (Bonfanti et al., 2024) and TOI-4481b (Palle et al., 2023).

[13] https://gemini.edu/instrumentation/maroon-x

1.4 Transiting exoplanets

In this section I will present the transit method. I will notably detail its theoretical foundations and its use to study the atmospheres of the transiting exoplanets.

1.4.1 Theoretical foundation

The transit method is a photometric method for exoplanet detection and characterization. Thanks to its ease of use and the wealth of information it can provide for both planet and its host star, it is the most widely used method in both ground-based and space facilities to detect and characterize transiting exoplanets. It is simply based on the astronomic eclipse phenomenon when an observer, a star and an eclipsing object are aligned. It aims at measuring the light intensity of the targeted star over time (Figure 1.11). If the star shows a temporary and periodic decrement in its brightness, this means that an object is obscuring a part of the stellar disk. This signal is called *transit*. I will explain hereafter how this signal is exploited to characterize the planetary system. However, a periodic decrement is not always due to a planet, but it might originate from other sources like, e.g. a bound or background eclipsing binary. I will explain these false positives in details in Chapter 2.

The first successful use of the transit method was the detection in 1999 of the transits of the giant exoplanet HD209458b, previously detected with the radial velocity method, by Henry et al. (2000) and Charbonneau et al. (2000). The first exoplanet discovered with the transit technique was OGLE-TR-56b by Konacki et al. (2003) in 2003. Since then, the transit method started to be the most widely used technique to detect and characterize exoplanets. Interestingly, many ground-based projects (e.g. WASP: Pollacco et al., 2006)) and space missions (e.g. *Kepler*: Borucki et al., 2010) and TESS (Ricker et al., 2015)) have used this technique to detect thousands of transiting exoplanets.

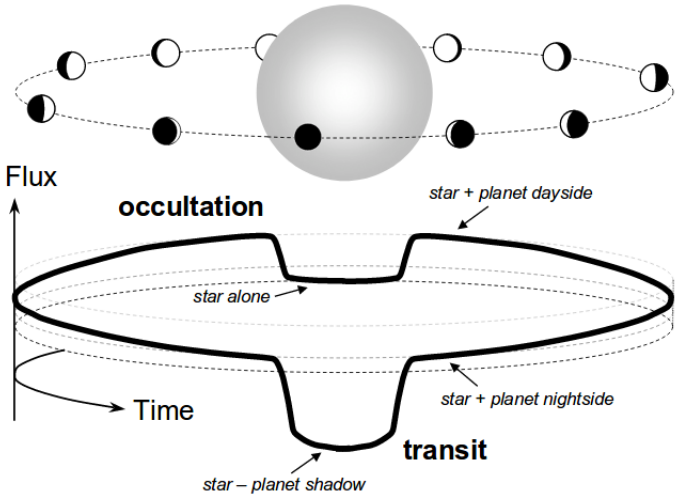

Figure 1.11: Illustration of transit-occultation. The transit corresponds to the crossing of the planet in front of the star and the occultation corresponds to the crossing of the planet behind the star. The flux curve represents the combined fluxes of the star and planet as the planets orbits around the star. This figure is taken from (Winn, 2010).

Let's consider a two-bodies system consisting of a planet with radius R_p and mass M_p orbiting

around a star with radius R_* and mass M_*. To study this system it is convenient to choose a cartesian coordinate system of center O coincident with the center of the star, with the plane xOy parallel to the plane of the sky and with the Oz axis pointing towards the observer. The distance from the center of the star to the center of the planet is given by the equation 20 of Murray & Correia (2010a):

$$r = \frac{a(1-e^2)}{1+e\cos(\nu)}$$

where a is the semi-major axis, e is the orbit eccentricity and ν[14] is the true anomaly. Based on Figure 1.12, we can easily express x, y and z coordinates as functions of the orbital parameters. We obtain the following expressions (Murray & Correia, 2010b):

$$x = r\left[\cos(\Omega)\cos(\omega+\nu) - \sin(\Omega)\sin(\omega+\nu)\cos(i)\right] \tag{1.4.1}$$

$$y = r\left[\sin(\Omega)\cos(\omega+\nu) + \cos(\Omega)\sin(\omega+\nu)\cos(i)\right] \tag{1.4.2}$$

$$z = r\sin(\omega+\nu)\sin(i) \tag{1.4.3}$$

where Ω is the longitude of ascending node (the angle from the reference direction axis Ox to

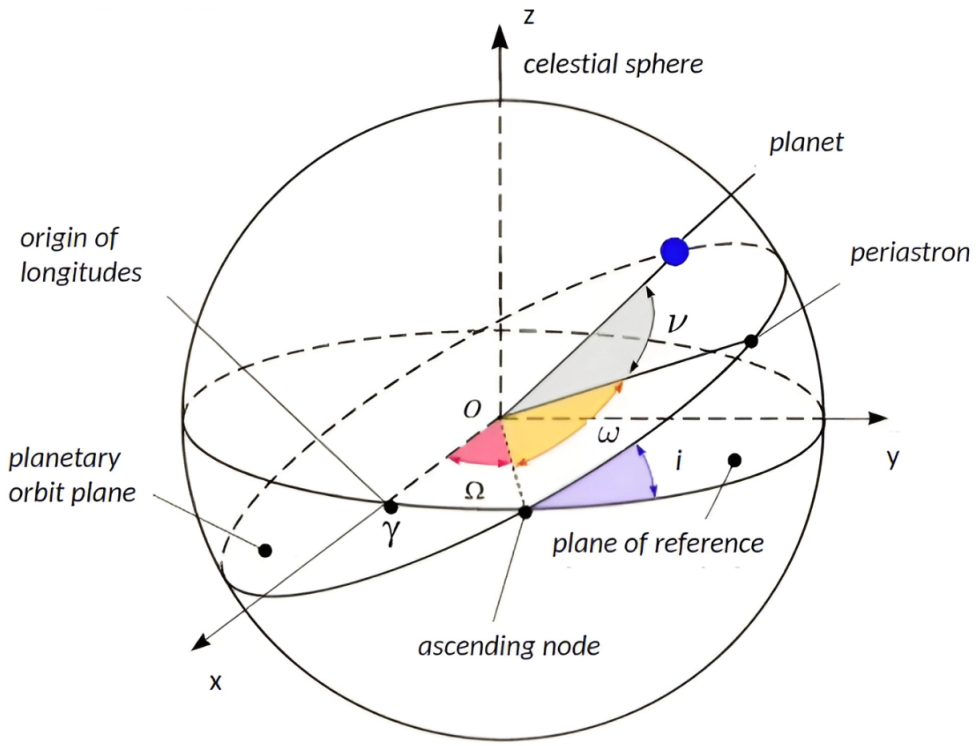

Figure 1.12: Illustration of orbital parameters for two-bodies system. +z axis is pointing towards the observer. Credit: https://drillaudweb.files.wordpress.com/2014/01/orbit.png

the direction of the ascending node γ, which is the point where the orbiting object moves north through the reference plane), ω is the argument of periastron, i is the inclination of the orbit plane

[14]The true anomaly is the angle between the periapsis direction and position of the planet along its Keplerian orbit around its host star

with respect to the reference plane (sky plane) and ν is the true anomaly. Usually the longitude of ascending node Ω is unknown (in other word, the orientation of the nodes axis is unknown) neither from transits nor from RV. Thus, Ω can be set to 180 °, aligning the Ox with nodes axis, with ascending node placed on $-x$. This does not change any other orbital parameter. In this simplified case we obtain:

$$x = -r\,[\cos(\omega + \nu)] \tag{1.4.4}$$

$$y = -r\,[\sin(\omega + \nu)\cos(i)] \tag{1.4.5}$$

$$z = r\sin(\omega + \nu)\sin(i) \tag{1.4.6}$$

Geometric condition to observe a transit

Observing a transit is not always possible for every planetary system, as an important condition should be verified: the observer, planet and its host star must be (or nearly) aligned. We can express this condition mathematically considering the Figure 1.13 below. A planet transit can be seen only if $a\cos(i) < (R_* - R_p)$. If $(R_* - R_p) < a\cos(i) < (R_* + R_p)$, then we observe a grazing transit. In the final case where $a\cos(i) > (R_* + R_p)$ we observe no transit. It is worth noting that this condition is built on the simple supposition that the planet's orbit is circular. Meanwhile, for planets that have a very elliptical orbit and depending on the system configuration with respect to the observer, we can observe a transit without occultation.

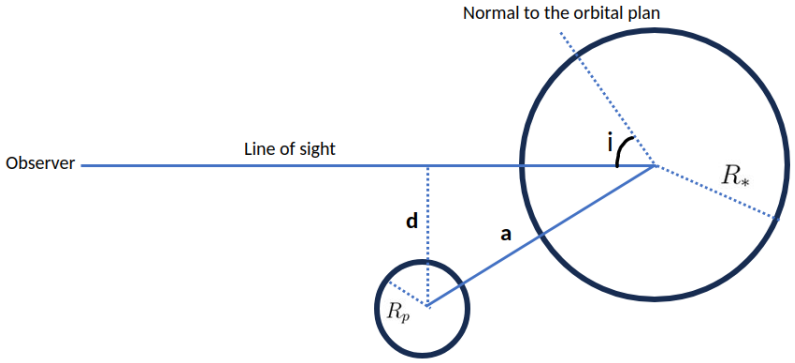

Figure 1.13: Illustration of the geometric condition for a transit to occur for an observer. Credit: Ghachoui Mourad.

Impact parameter

Let us note by r_{sky} the projection of the orbital radius r on the sky plan (xOy). Using expression 1.4.4 and 1.4.5 we obtain:

$$r_{sky} = \frac{a(1-e^2)}{1 + e\cos(\nu)}\sqrt{1 - \sin^2(\omega + \nu)\sin^2(i)} \tag{1.4.7}$$

as we are interested in the transit signal, let's consider the case where the center of planet is at the moment of inferior conjunction (planet between the host star and the observer). In this case we

have $x = 0$ which gives:

$$\nu_{tra} = \frac{\pi}{2} - \omega \qquad\qquad \nu_{occ} = -\frac{\pi}{2} - \omega \tag{1.4.8}$$

ν_{tra} is the true anomaly for the transit at inferior conjunction and ν_{occ} is the true anomaly for the occultation at superior conjunction (host star between the planet and the observer). The impact parameter is the sky-projected r distance at conjunctions, in units of stellar radius.

$$b_{tra} = \frac{a\cos(i)}{R_*}\left(\frac{1-e^2}{1+e\sin(\omega)}\right) \qquad\qquad b_{occ} = \frac{a\cos(i)}{R_*}\left(\frac{1-e^2}{1-e\sin(\omega)}\right) \tag{1.4.9}$$

We can also use the impact parameter to express the geometrical condition to observe the transit. A transit is observable if $b_{tra} < 1 - \frac{R_p}{R_*}$. If $1 - \frac{R_p}{R_*} < b_{tra} < 1 + \frac{R_p}{R_*}$ we observe a grazing transit. In the final case where $b_{tra} > 1 + \frac{R_p}{R_*}$ no transit is observable.

Limb-darkening

Real stellar disks are not of uniform brightness. In addition to spots and flares (whose intensity change from a star to another), stellar discs are brighter at the center and become gradually dimmer towards the limbs. This phenomenon is known as the *limb-darkening effect*. To explain this phenomenon we resort to the radiative transfer in the stellar atmosphere. The light from an object is mostly emitted by its layers of optical depth $\tau \approx 1$. At the center of a stellar disc, where light travels radially, this optical depth corresponds to deeper and then hotter and brighter layers. On the contrary, light emerging from the limbs, travels through the stellar atmosphere with an angle ν (see Figure 1.14), which makes $\tau \approx 1$ corresponds to lower and then colder and dimmer atmospheric layers. Figure 1.14 shows a real optic image of the Sun where the solar disc appears brighter at the center and becomes increasingly dimmer and then redder as we approach the edge. The LD profile of stars depends on their composition and spectral type. It is difficult to observe the LD profile for other stars than the Sun but we can observe only its effect on the transits. When a planetary disc transits near the center of the stellar disc, it blocks more light than when it is near the limbs. Consequently, real transits are not flat-bottomed but U-shaped at the center and softened in the extremities. They are deeper (shallower) than $(\frac{R_p}{R_*})^2$ at the center (near the extremities).

Several analytical relationships have been proposed to represent the LD profile of stars. The first law that was proposed is a linear law that is written as follows:

$$\frac{I(\mu)}{I(1)} = 1 - u_0(1-\mu) \tag{1.4.10}$$

Where I is the intensity of the stellar disk, u_0 is the linear LD coefficient and $\mu = \cos(\theta_*)$, with θ_* being the angle between the observer and the normal vector on the surface of star. μ is equal to 1 at the center of the stellar disk and 0 at the limbs, thus $I(1)$ is the intensity at the center stellar disk. This law can be sufficient for transits observed with limited precision, but light curves from

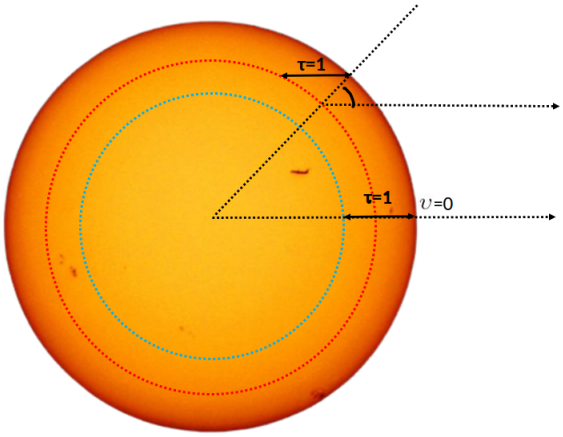

Figure 1.14: An optical image of Sun, taken by the SOHO mission, showing the limb-darkening effect. The center of the solar disk appears clearly brighter than the edge. Credit: adopted from https://soho.nascom.nasa.gov/gallery/images/mdi20031028.html

the *Hubble Space Telescope* for HD 209458b have shown that it is insufficient to adequately model high precision transits (Brown et al., 2001). A more complex analytical formula is thus generally preferred, such as the quadratic LD law (Mandel & Agol, 2002) that is describe as follows:

$$\frac{I(\mu)}{I(1)} = 1 - u_1(1-\mu) - u_2(1-\mu)^2 \tag{1.4.11}$$

where u_1 and u_2 are the two quadratic LD coefficients. Theoretical values of u_1 and u_2 can be computed either from stellar-atmosphere models or measured from transit high-precision light curves. For example, Claret & Bloemen (2011) presented tables that can be interpolated based on T_{eff}, $[Fe/H]$ and $\log(g)$ parameters that are determined from independent spectroscopic analyses, to compute theoretical values of u_1 and u_2. This must take into account the filter being used in the observations due to the dependence of the LD effect to the wavelengths as I will explain hereafter. The tables of Claret & Bloemen (2011) have been updated to cover *TESS* bands by Claret (2017).

The LD effect is wavelength-dependent. It tends to be stronger towards shorter wavelengths (Knutson et al., 2007a). This can mathematically be demonstrated by the temperature derivative of the function of Planck:

$$B(\lambda, T) = \frac{2hc^2}{\lambda^5} \frac{1}{\exp(\frac{hc}{\lambda k_B T}) - 1}$$

When using the Rayleigh-Jean approximation ($hc << \lambda k_B T$) and deriving with respect to the temperature, we obtain:

$$\frac{dB(\lambda, T)}{dT} = \frac{2k_B c}{\lambda^4}$$

This varies as λ^{-4}, which means that the LD effect is more intense at shorter wavelengths than it is at longer wavelengths. This affects directly the transit depth and the planetary radius. It is therefore important to take it into account in the transit modeling to get the planetary parameters. Mandel & Agol (2002) presented analytical formulae for modeling transits for stars described by quadratic or nonlinear LD laws. Figure 1.15 shows the 10 transits observed with Hubble space

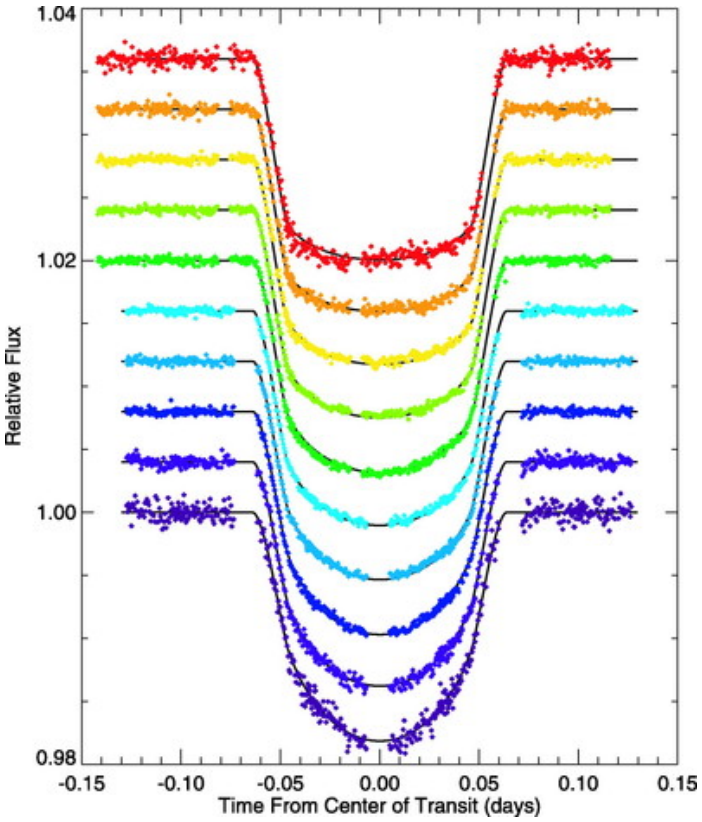

Figure 1.15: Transits of HD 209458b observed by the space telescope Hubble at wavelengths ranging from 0.32 μm (upper transit) to 0.97 μm (lower transit). The transit depths of the same planet becomes a little bit deeper towards shorter wavelengths. This figure is taken from Knutson et al. (2007a).

telescope for the planet HD 209458b obtained at 10 different pass-band filters. It should also be noted that the shape of the transit is not affected by only the LD effect but also by stellar spots or flares that differ from a star to another.

1.4.2 Measurement of the system parameters

I have presented in the first section of this chapter the theoretical foundation of the transit method. In this section, we will see how it is used to physically characterize the transiting exoplanets. The parameters we care most about are the planet radius R_p, mass M_p and equilibrium temperature T_{eq}. These parameters depend on the stellar parameters, especially the stellar radius R_* and effective temperature T_{eff}. Thus, the stellar characterization is an important step before any transit science. For example, this can be done by spectroscopic observations, stellar evolution models, empirical laws calibrated on eclipsing binaries, etc.

Parameters measured from the transit

The transit carries behind its shape a wealth of information on the physical and orbital parameters of the planet, and also on the host star. Here I describe how a transit signal is exploited to extract physical information on the system. To simplify the calculations, we will consider a transit light curve, with neglected LD effect (uniform brightness of the stellar disc), of a planet in circular orbit

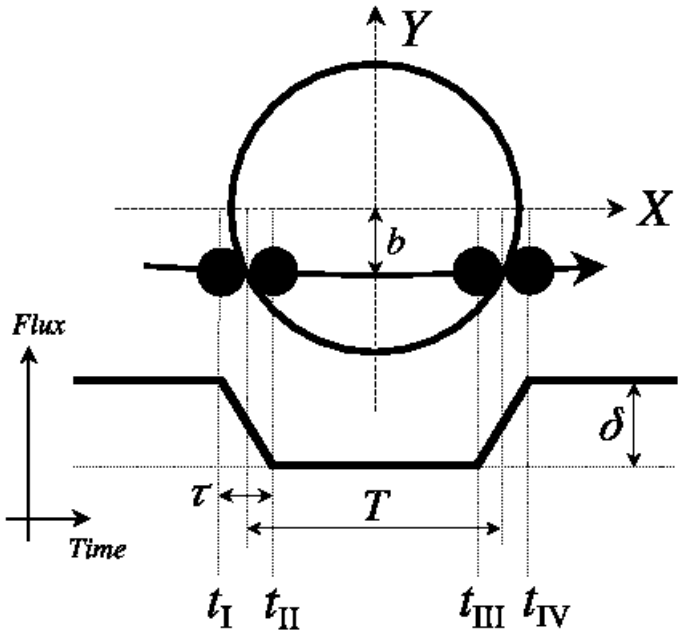

Figure 1.16: Illustration of a transit with neglected limb-darkening effect (Winn, 2010).

($e = 0$).

Transit depth

The transit depth is the very first parameter one can extract directly from the transit light curve. It represents the amplitude of the apparent variation of the star brightness during transit relative to its base value outside transit. This parameter is given as:

$$\delta = \frac{F_{out} - F_{int}}{F_{out}} \tag{1.4.12}$$

With F_{out} and F_{int} being the flux of the star out of and during the transit, respectively. Analytically, the transit depth is the surface of the planetary disc divided by the surface of the stellar disc. Based on these last simplifications and according to the last equation, we can write (Seager & Mallén-Ornelas, 2003):

$$\delta = \frac{\pi R_*^2 - \pi(R_*^2 - R_p^2)}{\pi R_*^2} \approx \left(\frac{R_p}{R_*}\right)^2 \tag{1.4.13}$$

With R_* and R_p are the radii of the host star and the planet, respectively. It is important to note that the formula 1.4.13 is just an approximation of the transit depth since it does not take into account the LD effect. Finally the transit depth allows to determine the ratio $\frac{R_p}{R_*}$.

The transit depth is proportional to the square of the planet radius and inversely proportional to the square of the stellar radius. This means that the signal is deeper for giant planets orbiting small stars.

Transit durations

Other important parameters that can be measured directly from the transit signal are transits durations. As we can see on Figure 1.16 we can define: the *total* transit duration $T_{tot} = t_{IV} - t_I$

which is the duration between the forth and the first contacts, and the *full* duration $T_{full} = t_{III} - t_{II}$ (the entire planetary disc is in front of the stellar disc), the *ingress* duration $\tau_{ing} = t_{II} - t_I$ and the *egress* duration $\tau_{egr} = t_{IV} - t_{III}$. Grazing transits have only t_I and t_{IV}. It is important to sate that the orbital period of the planet is known either from follow-up (from the observation of at least two consecutive transits) or from radial velocity observations. Analytically, T_{tot} (T_{full}) can be obtained by combining Equations 14 (15) and 16 of Winn (2010), where we obtain:

$$t_{tot} = \frac{P}{\pi} \arcsin \left[\frac{R_*}{a} \frac{\sqrt{(1+k)^2 - b_{tra}^2}}{\sin(i)} \right] \frac{\sqrt{1-e^2}}{1 + e\cos(\omega)} \tag{1.4.14}$$

$$t_{full} = \frac{P}{\pi} \arcsin \left[\frac{R_*}{a} \frac{\sqrt{(1-k)^2 - b_{tra}^2}}{\sin(i)} \right] \frac{\sqrt{1-e^2}}{1 + e\cos(\omega)} \tag{1.4.15}$$

Deduced parameters

In this part we will see how to exploit the parameters deduced from transits to get more information on the system.

Impact parameter

The two expressions 1.4.14 and 1.4.15 of t_{tot} and t_{full} are written as functions of the impact parameter b_{tra} and transit depth δ with the last being directly measured from the transit light curve. We define the ratio:

$$\tau = \frac{\sin(\frac{t_{full}\pi}{P})}{\sin(\frac{t_{tot}\pi}{P})} = \sqrt{\frac{(1-\sqrt{\delta})^2 - b_{tra}^2}{(1+\sqrt{\delta})^2 - b_{tra}^2}} \tag{1.4.16}$$

The expression of the impact parameter is then given as:

$$b_{tra} = \sqrt{\frac{(1-\sqrt{\delta})^2 - \tau^2(1+\sqrt{\delta})^2}{1-\tau^2}} \tag{1.4.17}$$

for planets with orbital periods much larger than their transit durations ($\frac{\pi t_T}{P} << 1$), while $\sin(\frac{\pi t_T}{P}) \approx \frac{\pi t_T}{P}$, the expression of b_{tra} becomes:

$$b_{tra} = \sqrt{\frac{(1-\sqrt{\delta})^2 - (\frac{t_{full}}{t_{tot}})^2(1+\sqrt{\delta})^2}{1-(\frac{t_{full}}{t_{tot}})^2}} \tag{1.4.18}$$

The scale ratio $\frac{a}{R_*}$

In the transit method science, the ratio $\frac{a}{R_*}$ is an important parameter. From expressions 1.4.14, 1.4.15, **??** and the expression $b_{tra} = \frac{a}{R_*} cos(i)$ we obtain:

$$\frac{a}{R_*} = \frac{P}{\pi} \frac{2\sqrt{k}}{\sqrt{t_{tot}^2 - t_{full}^2}} \left(\frac{\sqrt{1-e^2}}{1 + e\sin(\omega)} \right) \tag{1.4.19}$$

Likewise, from the expression of b_{tra} we can determine the orbit inclination i as function of the ratio $\frac{a}{R_*}$ as follows:

$$i = \arccos(b_{tra}\frac{R_*}{a}) \tag{1.4.20}$$

Physical parameters of the planet

We have seen that the transit depth δ is determined directly from the light curve. It is simply expressed as planetary to stellar radii ratio square. Knowing the transit depth we can obtain:

$$\frac{R_p}{R_*} = \sqrt{\delta}$$

given that the stellar radius is already known from independent analyses. The planet radius is determined as:

$$R_p = R_*\sqrt{\delta}$$

If we have a measured radial velocity semi-amplitude (equation 1.3.5), the orbit inclination from the transit method can be used to remove the degeneracy from $m_p \sin(i)$ to pin down the planetary mass and thus its mean density (ρ_p) (Schmitz, 2019; Harrington, 2011). The latter is a crucial parameter to obtain a first constraint both the internal composition and structure of planets (Dorn et al., 2017). It used to distinguish between different types of planets, e.g. a rocky 'super-Earth' from a puffy 'mini-Neptune'. Additionally, this leads to determine the gravity on the planet's surface as:

$$g_p = \frac{2\pi}{P}\frac{\sqrt{1-e^2}K_*}{\left(\frac{R_p}{a}\right)^2\sin(i)}$$

This is a key parameter for a further atmospheric characterization of the planet, as it is inversely proportional to the atmosphere's extent: the larger the surface gravity, the more compact the atmosphere.

One of the most important advantages of the transit technique it that it can characterize not only the planet but also the host star. Combining the ratio a/R_* and Kepler third law, we can determine the mean stellar density (Seager & Mallén-Ornelas, 2003):

$$\rho_* = \frac{3\pi}{GP^2}\left(\frac{a}{R_*}\right)^3$$

This quantity is of particular importance. In case of high-precision photometric data and circular or near circular planetary orbit, this quantity can be combined to the stellar radius to determine the stellar mass. It can also serve as independent check that the transit signal is potentially due to a transiting planet if is consistent to its value determined independently (e.g. from stellar evolution models or empirical relations).

Now that we have the stellar density and the planetary density, we can calculate the *Roche limit*, the distance within which a secondary celestial object (planet) will disintegrate under the

tidal forces of the primary object (star) around which it is orbiting, that is given as follows:

$$d_{roche} = \left(\frac{3\rho_*}{\rho_p}\right)^{\frac{1}{3}} R_*$$

and also the *Hill radius*, the minimum distance below which another celestial body of negligible mass compared to the mass of the planet and the star can remain in orbit around the planet:

$$R_{Hill} = \left(\frac{1}{3}\frac{m_p}{M_* + m_p}\right)^{\frac{1}{3}} a$$

Transit Timing Variation

The transit of a planet in Keplerian orbit is exactly periodic. However, if another planet exists in the system, the orbit is no longer Keplerian. This is due to the gravitational interactions between the planets which causes transit timing variations (TTV: Agol et al., 2005; Holman et al., 2007). This means that the transit signals are not exactly periodic and occur either in advance or in delay to what is predicted. Interestingly, by monitoring transit signals, the detection of TTVs can reveal the presence of other planets (previously undetected) in the system. The amplitudes of TTVs depend on the planets' masses and their orbital configuration around the star (Agol & Fabrycky, 2018). These amplitudes are maximised if the planets are in (or close to) mean-motion resonances (MMRs). In such a case, the TTV technique can lead to precise measurements of the planets' masses (e.g. Agol et al. (2021)).

Some words about the host star characterization

Because the parameters we ultimately want to determine (e.g. R_p and M_p) depend strongly on the stellar parameters (notably R_* and M_*), it is crucial to have a good stellar characterization. Accurate stellar properties lead to accurate planetary properties. Here we present some of the pathways to characterize host stars. For instance, Mann et al. (2015) presented some polynomial empirical relations appropriate for M dwarfs to measure their bolometric luminosity, effective temperature, radius and mass. Mann et al. (2019) presents a revised empirical relation between M_*, M_{K_s} (absolute magnitude in the K band) and [Fe/H], spanning an order of magnitude in mass from 0.075 to 0.70 $M_\odot$. An example of use of these empirical relationships is in Ghachoui et al. (2023) presented in Chapter 4. Out of the range of M dwarfs, Torres et al. (2010) presented empirical laws calibrated on well-characterized eclipsing binaries to determine stellar mass and radius based on T_{eff}, $[Fe/H]$ and $logg_*$. In addition, a Spectral Energy Distribution (SED) fit can be performed on broadband sky photometry from catalogs (eg. APASS, WISE, 2MASS) supplied with extinction from galactic dust map (Schlafly & Finkbeiner, 2011a) and parallax from Gaia (see e.g. Gaia Collaboration et al., 2016, 2018), all to get the stellar luminosity and temperature. Then, the stellar radius can be pin down using the Stefan-Boltzmann law ($L = 4\pi R^2 \sigma T_{eff}^4$). Also, one can use stellar evolution models that takes as inputs the density of the star measured from transit light curves plus its effective temperature and metallicity determined spectroscopically, to derive stellar

mass M_* and the radius from M_* and ρ_* (see e.g. Seager & Mallén-Ornelas, 2003). As explained previously, when R_* and M_* are determined, then R_P can be determined from the transit depth, and the planetary mass via RV semi-amplitude supplied with the orbit's inclination from transit. Also, when T_{eff} of the host star is determined, one can determined the equilibrium temperature T_{eq} of the planet with the semi-major axis of the planet's orbit a determined from orbital period.

1.4.3 Rossiter-McLaughlin effect

As a star rotates, unless its spin axis points towards the observer, half of the visible photosphere moves toward the observer and the other half recedes. Because of the Doppler effect, the light emitted by the approaching part is *blue-shifted* while the light emitted by the receding part is *red-shifted*. This produces variations in the line profiles in the stellar spectrum.The *blue-* and *red-shifted* contributions are averaged out when no planet is transiting. When a planet transits, it will hide successively some parts of the stellar disk that can be blue or red-shifted, which will result in a modification in the mean spectral shift measured by the observer and then existence of anomalies on the radial velocity curve. This is called the *Rossiter-McLaughlin effect*.

To simplify the explication of this effect, let's suppose a host star with rotational spin axis in the same direction as its planet's orbit (*prograde* orbit). In this case, when a planet transits, it will start by blocking light from the approaching half which causes a deficit in the *blue-shifted* light. This is reflected in the measurement by an average spectral shift to the red and, therefore, by an increase of the measured radial velocity. When the planet crosses the mid-transit times, it will hide light emerging from the receding part of the stellar disc which will produces a deficit in the redshifted light. This is reflected in the measurement by an average spectral shift to the blue. As shown on Figure 1.17, these anomalies depend on the sky-projected obliquity β (i.e. the angle between the rotation axis of the star and the orbital axis of the planet, as projected onto the sky plane). When the orbital spin axis of the planet is parallel to the stellar spin axis ($\beta = 0°$), the anomalies on the RV curve are antisymmetric with respect to the mid-transit time. Contrarily, if the orbital axis of the planet is strongly misaligned with the stellar spin axis, the planet hides only redshifted light of the receding part of the stellar disc during transit which results in only one anomaly in the RV curve (see right panel of Figure 1.17). For $\beta = 0°$ or $\beta = 180°$, the maximum amplitude of the RV variation is given as:

$$\Delta V_r = \frac{R_p^2}{R_*^2}\sqrt{1-b^2}V_* \sin(i_*) \tag{1.4.21}$$

with $V_* \sin(i_*)$ is the projected rotational velocity (i_* is the angle between the spin of the star and the line of sight). Interestingly, by modeling the RM effect, we can get the sky-projected obliquity β.

The RM effect was introduced after its first definitive measurement for eclipsing binaries by Rossiter (1924) and McLaughlin (1924). The first exoplanetary RM effect detection was for the hot Jupiter HD 209458b by Queloz et al. (2000), who found the orbit to be *prograde*. Since then, many RM measurements have been made, revealing a broad distribution of sky-projected obliquities, from well-aligned to highly misaligned systems (see Albrecht et al., 2022, and references therein).

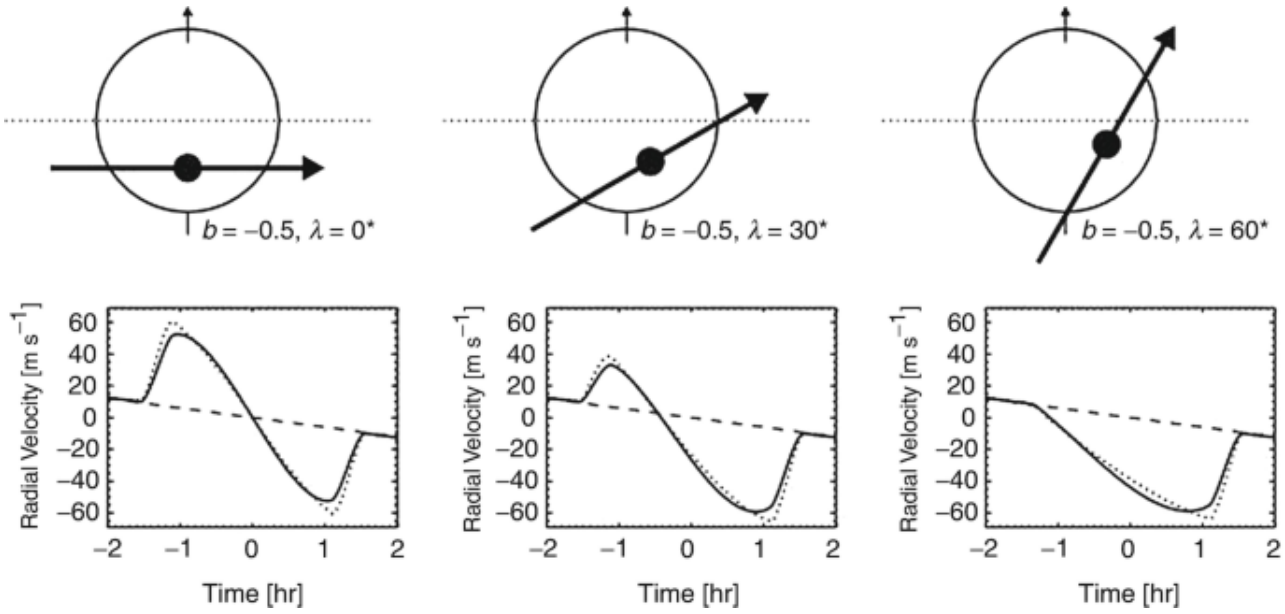

Figure 1.17: *Top*: In these three cases, the same planet is assumed to transit the same star, producing the same transit light curves, but with different projected spin-orbit angles β. *Bottom*: corresponding simulated radial velocity signals. A well-aligned orbit (left) results in a symmetric "redshift-then-blueshift" signal, a $\beta = 30°$ (*middle*) results in an asymmetric signal, and a $\beta = 60°$ (right) produces a blueshift throughout the transit. Credit: Gaudi & Winn (2007)

.

The obliquity parameter is of particular interest to shed light on the migrations and dynamical interactions of exoplanets (Winn & Fabrycky, 2015; Albrecht et al., 2022).

1.4.4 Atmospheric characterization of transiting exoplanets

We have seen previously that the transit method gives access to a treasure of information on the observed system (planet + star). It can also be used to characterize the atmosphere of the exoplanet without the need to spatially resolve it from its host star. A deep characterization of the exoplanet's atmosphere can be done in three complementary strategies whose basics are explained here after.

Transmission spectroscopy

Previously we have supposed that planets have well-defined surfaces to simplify our calculations and we have seen that the transit depth is only affected by limb-darkening effect. In fact, gaseous planets do not have a well shaped surface and even rocky planets with solid surfaces might have thick atmospheres. Each atom or molecule constituting this atmosphere has unique absorption lines/bands at specific wavelengths. As the planet transits in front of the star, light from the host star experiences attenuation through the planet's atmosphere, in the day-night terminator, due to the scattering by aerosols and absorption by the constituents of the atmosphere. This atmosphere is therefore more opaque at the wavelengths characteristic of its chemical species. This causes the transit depth, and then the effective planet radius, to be wavelength-dependent. The *transmission spectrum* is defined by measuring the transit depth (or the apparent planetary radius) as function of wavelength. An example of transmission spectrum is shown on Figure 1.18 for the hot-Jupiter

WASP-39b. From the absorption bands signatures printed on the transmission spectrum, we can then gain knowledge on the constituents of the exoplanet atmosphere. This effect was first predicted by Seager & Sasselov (2000a) and had been first successfully observed by Charbonneau et al. (2005). As an order of magnitude, the transit depth changes by $\Delta\delta$ due to an increase in the apparent planetary radius by $1H$. It is expressed as:

$$\Delta\delta = \frac{(R_p + H)^2}{R_*^2} - \frac{R_p^2}{R_*^2} \approx 2\delta\frac{H}{R_p} \tag{1.4.22}$$

where R_p and R_* are the planetary and stellar radii, respectively. H is the characteristic scale height of the atmosphere (the altitude over which the atmospheric pressure is decreased by a factor e). Its expression is:

$$H = \frac{k_B T}{\mu g_p} \tag{1.4.23}$$

with k_B being the Boltzmann's constant, T the equilibrium temperature of the planet, μ the mean molecular mass, and g_p the surface gravity. According to the expressions 1.4.22 and 1.4.23, the signal is easily detectable for giant planets with a deep transit depth, a hot extended atmosphere and a low-gravity such as hot Jupiter planets. For an Earth-sized planet orbiting a Sun-like star, $\Delta\delta$ could be at most of only few ppm, while it can be of hundreds of ppm for hot-Jupiters .

Many models have been developed to interpret the variations of $R_{p,\lambda}$ as function of wavelength (see e.g. Fortney et al. (2010)). The simpler 1D models assume temperature, pressure profiles and composition as function of altitude to produce a theoretical spectrum to compare to the observed spectrum to identify the signatures of various elements and molecules present in the exoplanet's atmosphere. More complex 3D General Circulation Models (3D GCMs) are used to simulate the atmospheric behaviors of tidally locked planets such as hot Jupiters. These models provide insights into the complex interplay between radiation, chemistry, and circulation patterns in these extreme environments. Several recent studies have reported the 3D GCMs of irradiated giant planets for which phase curve data is available to constrain the models (see e.g. Heng et al., 2011; Kataria et al., 2013). By simulating the specific conditions of planets in a tidal lock, these models reveal how extreme temperature differences can drive supersonic winds and shape climate zones (see e.g. Mendonça, 2020; Wolf et al., 2019). This detailed understanding helps in predicting weather patterns, cloud formations, and the potential for atmospheric escape, contributing to our knowledge of planetary systems beyond our own (Steinrueck et al., 2023).

In addition to its limit to constrain only the day-night terminator, the transmission spectrum is affected by many factors that reduce its effectiveness. It is also affected by high-altitude condensates (clouds and hazes) which scatter light, flattening the transmission spectrum and making it difficult to identify specific absorption features. Furthermore, as I explained previously, the transmission spectra is the measure of the transit depth (or planetary radius) as function of wavelengths. These measurements are affected by the heterogeneity of the stellar photosphere and chromosphere, such effect is usually referred to as *stellar contamination effect*. Explicitly, starspots (cool spots), faculae (hot spots) and flares contaminate the transit depth, and thus the transmission spectra. If a planet,

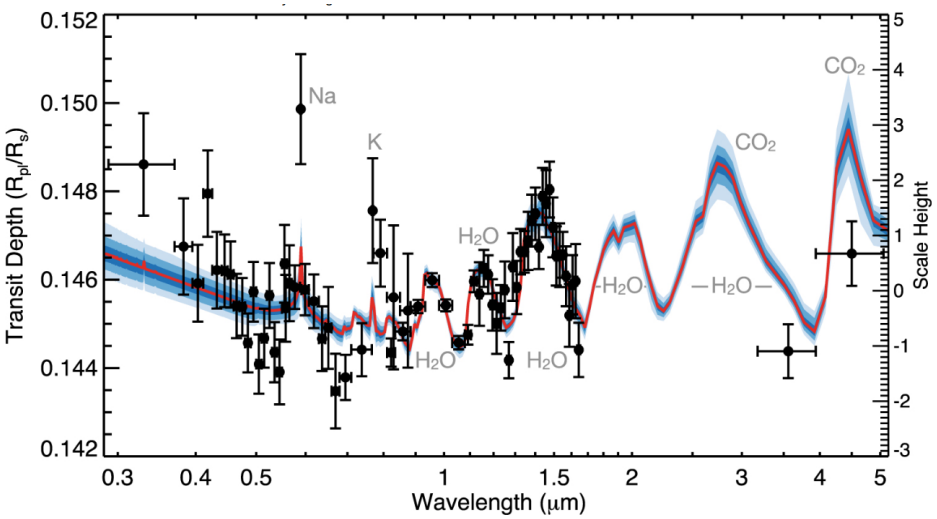

Figure 1.18: Complete transmission spectrum of WASP-39b (black points) with the best-fit atmospheric model (red). The spectrum incorporating data from HST/STIS and WFC3, *Spitzer*/RAC, and VLT/FORS2 completing the spectrum from 0.3 to 5.0 μm. Credit: Wakeford et al. (2018).

.

during its transit chord, occults starspots (faculae) this causes momentum small bumps (deeps) in the transit signal. These bumps and deeps are imprinted onto the transmission spectrum, which gives false spectral features. Yet, even not occulted starspots, faculae and flares can also affect the transmission spectra by making a slight difference between the disk-integrated and transit chord-integrated spectra, such effect is known as the Transit Light Source (TLS: Rackham et al., 2018, postfix) effect. Detailed information on the stellar contamination, TLS and how to deal with their effects can be found in e.g. Rackham et al. (2018).

The transit spectroscopy of exoplanets has significantly improved during the last two decades. The Hubble Space Telescope (HST), has gathered dozens of spectra for exoplanets of different sizes from hot-Jupiters to Earth-sized planets. Nowadays, *JWST* is taking the largest steps in characterizing exoplanets' atmospheres with its unprecedented precision. It has already revealed many discoveries. Among others, it has led to the detection of methane (CH_4) and water vapor evidences (Bell et al., 2023) in the spectra of WASP-80, a gas giant transiting a cool dwarf star.

Occultation spectroscopy

The secondary eclipse (e.g. when the planet goes behind its host star) provides an additional method, complementing the primary transit, to enhance the characterization of the atmosphere of transiting exoplanets. During transits, the light we receive is the starlight and the emission of the night-side of the hosted planet. The latter can generally be neglected in front of the star light especially at shorter wavelengths. As Figure 1.11 shows, shortly before and after the secondary eclipse, the light we perceive is the combined light of the star and the illuminated side of the planet. The contribution of the planet consists of thermal emission and reflected starlight. This contribution becomes significant and readily detectable for close-orbiting large planets, while the reflected light contribution is more challenging to be measured and can generally be neglected,

especially in the infrared. When the planet entirely disappears behind the star, no light is received from the planet which causes a small dimming in the light curve. Under the assumption that the planetary and stellar discs have uniform brightness, the occultation depth is expressed as:

$$\delta_{occ} = \frac{F_{near-occ} - F_{occ}}{F_{near-occ}} \tag{1.4.24}$$

$$= \frac{F_{p,s}\pi R_p^2}{F_{*,s}\pi R_*^2 + F_{p,s}\pi R_p^2} \tag{1.4.25}$$

$$\approx \frac{R_p^2}{R_*^2}\frac{F_p}{F_*} \tag{1.4.26}$$

with $F_{near-occ}$ is the flux of the system (star + planet day-side) just before/after the secondary eclipse and F_{occ} is the flux of the star when the entire planetary disc is behind the stellar disc. The occultation depth is the transit depth multiplied by the F_p/F_* (brightness of the day-side of the planet relative to the brightness of the host star), the latter being the relative contribution of the planet's day-side flux to the stellar flux (Charbonneau et al., 2005; Deming et al., 2005) and it is the first parameter that can be measured through occultation. It should be mentioned that the last formula considers only thermal emission.

We have seen that the planetary radiation consists of two components: emission and reflection. Figure 1.19 shows how each of the components dominates as function of wavelength range for some planets in our solar system and an hypothetical hot-Jupiter at 10 pc. The starlight reflection component dominates at short wavelengths, but its peak is much smaller than the thermal emission peak for hot Jupiters, and it has been detected only for a few exoplanets (see e.g. Knutson et al., 2007b; Sudarsky et al., 2000; Latham et al., 2010). Thus, its peak is at the same wavelength as the host star. Meanwhile, the thermal emission of the planets prevails at long wavelengths and peaks correspondingly to their effective temperatures.

To observe the occultation, one must know the range of wavelength observation. Due to the planet being generally colder than its host star, the contribution of the planet is dominated by its thermal emission at long wavelengths (i.e. typically from the near- to and mid-infrared) and it peaks at the wavelength corresponding to the effective temperatures of the planet (see Figure 1.19). In this case, under the assumption that the planet and star are radiating as blackbodies, the relative planetary flux is expressed as follows (Nikolov et al., 2017):

$$\frac{F_p}{F_*} = \left(\frac{R_p}{R_*}\right)^2 \frac{B(\lambda, T_p)}{B(\lambda, T_*)} \tag{1.4.27}$$

with λ is the wavelength of the observation, B is the blackbody spectral radiance at temperature T, and T_p and T_* are the effective temperatures of the planet and the star, respectively. Using the Rayleigh-Jeans approximation, we obtain:

$$\frac{F_p}{F_*} = \left(\frac{R_p}{R_*}\right)^2 \frac{T_p}{T_*} \tag{1.4.28}$$

It is worth to note that the effective temperature of the planet, T_P, is the temperature of a blackbody that would emit the same amount of its radiation as the planet. T_P can be estimated from its equilibrium temperature, T_{eq}, which is a theoretical value determined by equaling the energy (from its star) absorbed by the planet to the energy that it re-emits back into space. Mathematically, for a planet with radius R_p and orbital semi-major axis a in orbit around a star with radius R_* and effective temperature T_{eff}, T_{eq} is determined as follows (Seager et al., 2005):

$$\frac{4\pi R_*^2 \sigma T_{eff}^4}{4\pi a^2} \pi R_p^2 f(1 - A_B) = 4\pi R_p^2 \sigma T_{eq}^4 \tag{1.4.29}$$

$$T_{eq} = T_{eff} \left(\frac{R_*}{2a}\right)^{\frac{1}{2}} [f(1 - A_B)]^{\frac{1}{4}} \tag{1.4.30}$$

where A_B is the planetary bond albedo[15] and f is a factor heat transfer efficiency from the day-side to the night-side of the planet, and it depends on how the atmosphere (if any) is dense and rotation rate of the planet around itself (Wordsworth, 2015; Kopparapu et al., 2016).

In fact, the planet's day-side disk may not have a uniform brightness but its temperature may radially decrease from the center to the limbs, which means that it is composed of an ensemble of concentric annuli with different temperatures. In this case, it will emit as an ensemble of blackbodies with different temperatures but the obtained emission may not be a blackbody spectrum (see e.g. Seager, 2010). Nevertheless, we can still define the *brightness temperature* $T_{br,\lambda}$ of the planet's day-side as the temperature of a black body whose flux emitted at a given wavelength λ is equal to planetary flux calculated using the equation 1.4.28 at that wavelength. The emission spectrum of the planet's day-side can be obtained by observing occultation at varying wavelength in the near- and mid-infrared domains. Variations of $T_{br,\lambda}$ with wavelengths can serve constraining the planet's day-side atmosphere, particularly its chemical composition and thermal structure. The latter refers to the variation of the temperature with atmosphere altitude. If the temperature rises with altitude (i.e thermal inversion) , the bands of the molecules present in this stratosphere (the altitude range of thermal inversion) will be seen in emission. Otherwise, if the temperature decreases with altitude, all molecular bands should be seen in absorption.

Conversely, at shorter wavelength, the contribution of the planet day-side is mostly the reflected starlight. In this case, the occultation depth due to only the reflected starlight is expressed as (see e.g. Winn, 2010; Kreidberg, 2018):

$$\frac{F_p}{F_*} = A_{g,\lambda} \left(\frac{R_p}{a}\right)^2 \tag{1.4.31}$$

where A_g is the geometric albedo, the ratio between the flux reflected by the planet seen at phase angle α=0[16](i.e., when the planetary disk appears fully illuminated) and the flux reflected by a Lambertian disk of same angular size, i.e. a fully reflecting surface with an isotropic emission surface intensity.

Due to the occultation depth being shallower than the transit depth, emission spectroscopy mea-

[15]The Bond albedo A_B is the fraction of stellar incident energy that is reflected by the planet back into space ($0 \leq A_B \leq 1$).

[16]The angle at the planet subtended by its host star and the observer

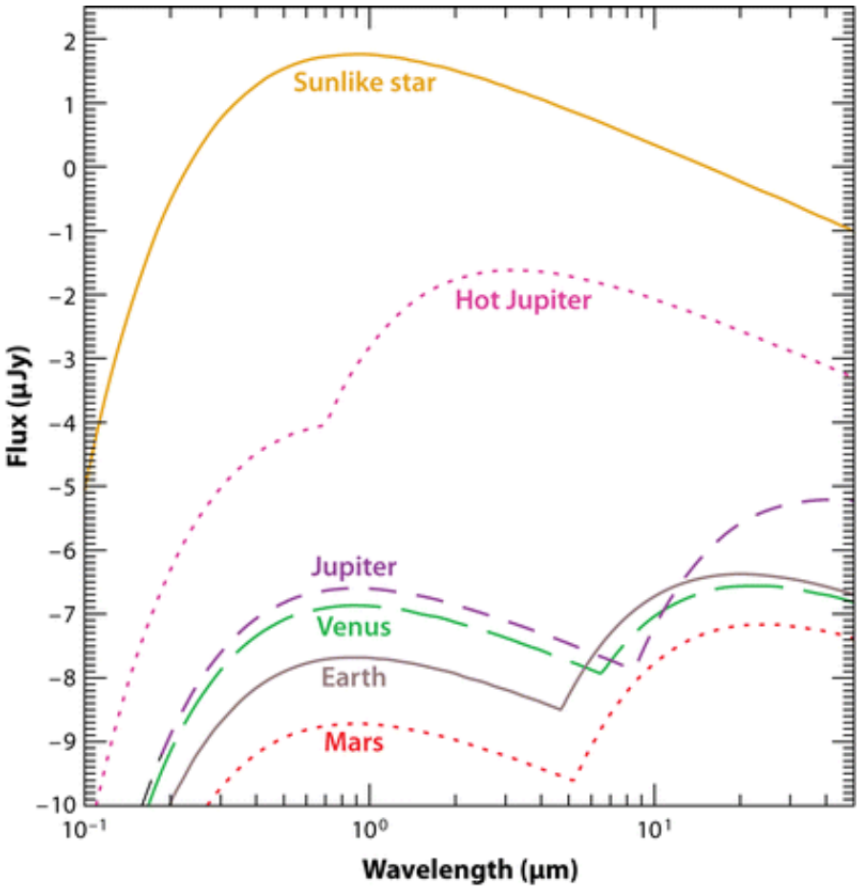

Figure 1.19: Black body flux of the Sun, some solar system planets and a theoretical hot-Jupiter supposed at 10 pc. The Sun is modeled as 5750 K black body. The planets have two peaks in their spectra: one peak in the short-wavelength range due to sunlight scattered by the planet atmosphere and computed using the planet's geometric albedo, and 2) one peak in the he long-wavelength range due the thermal emission of the planet and estimated considering a black body with the same effective temperature as the planet. The albedo and equilibrium temperature of the hot-Jupiter were supposed to be 0.05 and 1600 K, respectively. Credit: Figure adopted from Seager & Deming (2010).

surement of an exoplanet is generally harder than measuring its transit transmission spectroscopy. However, emission spectroscopy has many advantages over transmission spectroscopy. While transmission spectroscopy probes the properties of the atmosphere near the day-night terminator as explained above, emission spectroscopy offers insight on the global properties of the planet's day-side atmosphere. The difference between day-side and terminator compositions (and the night-side as well) depends on the heat transfer efficiency. If the planet has a perfect heat redistribution, then the two regions might have the same composition. Unlike transmission spectroscopy, emission spectroscopy is less sensitive to high-altitude condensates because the whole day-side atmosphere contributes to the spectrum.

The large number of exoplanets detected by *TESS* and confirmed or under confirmation by subsequent observations, led to the need of prioritizing exoplanets candidates most amenable to atmospheric characterization with *JWST*. Indeed, Kempton et al. (2018) developed a framework

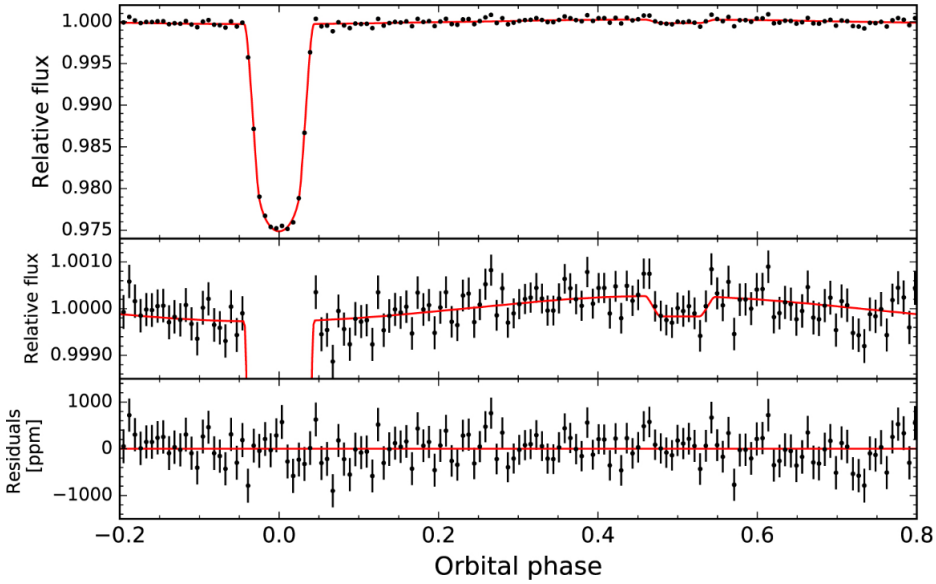

Figure 1.20: *Top*: phase-folded light curve of WASP-19 corrected for stellar variability and long-term trends, binned in 8 minute intervals (black points), with the best-fit full phase curve model (red line) overplotted. *Middle*: same as top light curve but zoomed in on the vertical axis to detail the phase curve modulation and secondary eclipse. *Bottom*: residuals from the best-fit model. Figure adapted from Wong et al. (2020)

for this purpose, based on a transmission spectroscopy metric (TSM) and an emission spectroscopy metric (ESM). The TSM and ESM metrics quantify the expected S/N in transmission and emission spectra, respectively, of the *JWST* telescope, assuming a purely white noise and neglecting practical issues like instrumental floor noises, stellar contamination effects, etc.

Phase curve

Further atmospheric characterization of exoplanets can be performed through the observation of their phase curve. The phase curve refers to the variation of the system (planet + host star) combined flux as function of the phase during a complete orbit. As for the secondary eclipse observation, the contribution of the planet flux in the phase curve is dominated by thermal emission over starlight reflection in the near- and mid-infrared and vice-versa in the optical. I will describe hereafter the fundamentals on how both cases can be utilized to extract information on the planet's atmosphere. Unlike secondary eclipse, phase curve can generally only be observed from space since the typical orbit timescale is generally longer than one night from ground. Figure 1.20 presents an example of phase curve obtained by *TESS* mission for the hot Jupiter WASP-19b.

Before detailing the use of phase curve to further characterize exoplanets' atmosphere, it is important to note that close-orbiting planets are generally tidally locked (see e.g. Mazeh, 2008; Guillot et al., 1996; Matsumura et al., 2010; Barnes, 2017) with permanent day-sides and nigh-sides, which means that their rotational periods are the same as their orbital periods (synchronized orbit). Observing the phase curve at long wavelength can help making a longitudinal brightness temperature map (i.e. variation of the brightness temperature as function of longitude) of the planet. This map provides us with information on the planetary atmospheric dynamics and en-

ergetics, which shed some light onto the atmospheric conditions throughout the planet's surface. The amplitude of the IR phase curve gives the day-night contrast temperature, which can in turn tell us about the heat transfer efficiency from the day-side to the night-side. Conversely, the amplitude of optical phase curve provides us with information about the variation of albedo, and then variation in the properties of clouds and/or hazes, or surface reflective materials, as function of longitude. Additionally, the configuration of the phase curves and the phases of their maxima and minima indicates the locations of the planet's atmosphere's hottest and coldest regions relative to the substellar meridian. If the maximum and the minimum are centered on the occultation and transit signals, respectively, then the hottest and coldest regions are located at the substellar and anti-substellar points, respectively. In the other case where the maximum and the minimum are shifted, then the location of the hottest and coldest regions are shifted correspondingly (Crossfield, 2015). This offers insight into the atmospheric circulation of the planet. More details on the phase curve are explained in Wong et al. (2020).

1.4.5 State-of-the-art

As of today, spring 2024, more than 5500 have already been confirmed according to the NASA Exoplanet Archive. This number is ever-increasing with the TESS mission, given that it still has more than seven thousands exoplanets candidates to be confirmed with subsequent observations. We have seen that there are many techniques to detect exoplanets. As Figure 1.21 shows, the cumulative number of exoplanets, detected per year and detection technique since 1995, has exponentially increased. The most fruitful methods so far has been the transit method and the radial velocity. 70% of the exoplanets are transiting according to the NASA exoplanet Archive.

The large sample of exoplanets known to date displays a great diversity not only in terms of their radii and masses, but also in terms of their orbits and types of host stars. Its large size and diversity represent key constraints on the models for the formation and evolution of planetary systems. Figure 1.22 shows the Period-Mass distribution of exoplanets known today. It labels the exoplanets detected by each detection technique. This shows clearly what I explained previously: each detection method is biased to a category of exoplanets. The RV exhibits bias towards massive planets in short orbits because their signals are readily detectable. The transit method exhibits bias towards exoplanets in short orbits because their transits occur more frequently.

1.5 TESS mission

In this section I will present the spacecraft *TESS*, its orbit and instrumentation, the scientific goals of the mission and its observing strategy.

Before introducing in details the mission *TESS*, it is important to introduce first the mission *Kepler* (Borucki et al., 2010). *Kepler* was a space mission dedicated to discover exoplanets, with the primary goal to detect Earth-sized planets transiting main-sequence stars. It was launched on Mars 7, 2009 and remained operational until October 30, 2018. The prime mission lasted from 2009 to 2013, and the extended (K2) mission from 2014 to 2018. The *Kepler* telescope had a primary mirror of 0.98m diameter. In its primary mission, *Kepler* observed a narrow unchanging field of

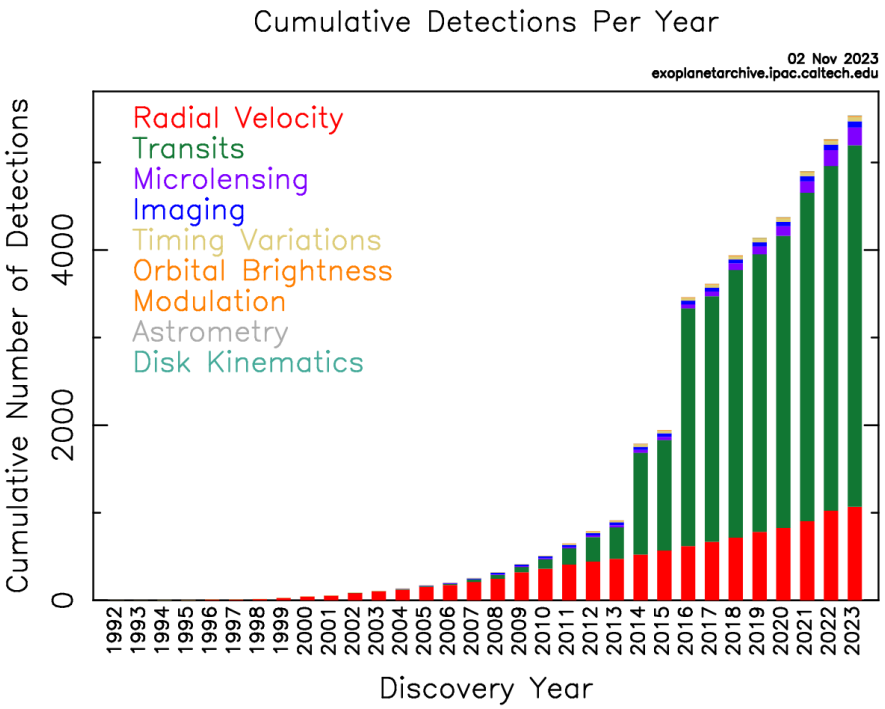

Figure 1.21: Cumulative distribution of the number of exoplanets discovered by method and by year. Most exoplanets have been detected by the transit. Figure taken from NASA Exoplanet Archive

view in the *Cygnus* constellation, a field rich of stars. It discovered 2778 transiting exoplanets by monitoring more than 150,000 stars. As I explained in the previous section, this mission had a high impact on our understanding of exoworlds. It revealed that our galaxy is teeming with exoplanets with different sizes (Borucki et al., 2011), and that terrestrial planets with sizes larger than Earth and smaller than Neptune are common in close orbits ($<$ 100 days) around other stars (Howard et al., 2012; Fressin et al., 2013). Importantly, the *Kepler* survey had a clearly-defined detection efficiency as function of period and radius, which was important to correct for the detection bias in the estimate of the occurrence rate of planets. It uncovered the intriguing radius/density valley (explained in-depth in the next chapter). To reach its goals, *Kepler* had to observe continuously a large number of stars. However, *Kepler* had a disappointing point. Most of planets that have been discovered transit stars far-away, and thus too faint for detailed follow-up measurements of the planetary masses and atmospheres. The prime mission of *Kepler* ended in 2013 because of a failure in two reaction wheels. It was then followed by the extended mission, *K2* (Howell et al., 2014), where the NASA's engineer came up with the idea to maintain its pointing using the pressure of sunlight. During *K2*, *Kepler* spacecraft observed different fields along the ecliptic plane. Despite challenges, *K2* provided valuable scientific data and expanded our understanding of the universe before *Kepler*'s official retirement in October 2018.

The Transiting Exoplanet Survey Satellite (*TESS*[17], Ricker et al., 2016) is a NASA's explorer class mission led by the Massachusetts Institute of Technology (MIT). It was launched on 18 April, 2018 aboard a SpaceX Falcon 9 rocket. *TESS* came to take over the next step of the *Kepler* mission

[17] https://tess.mit.edu/

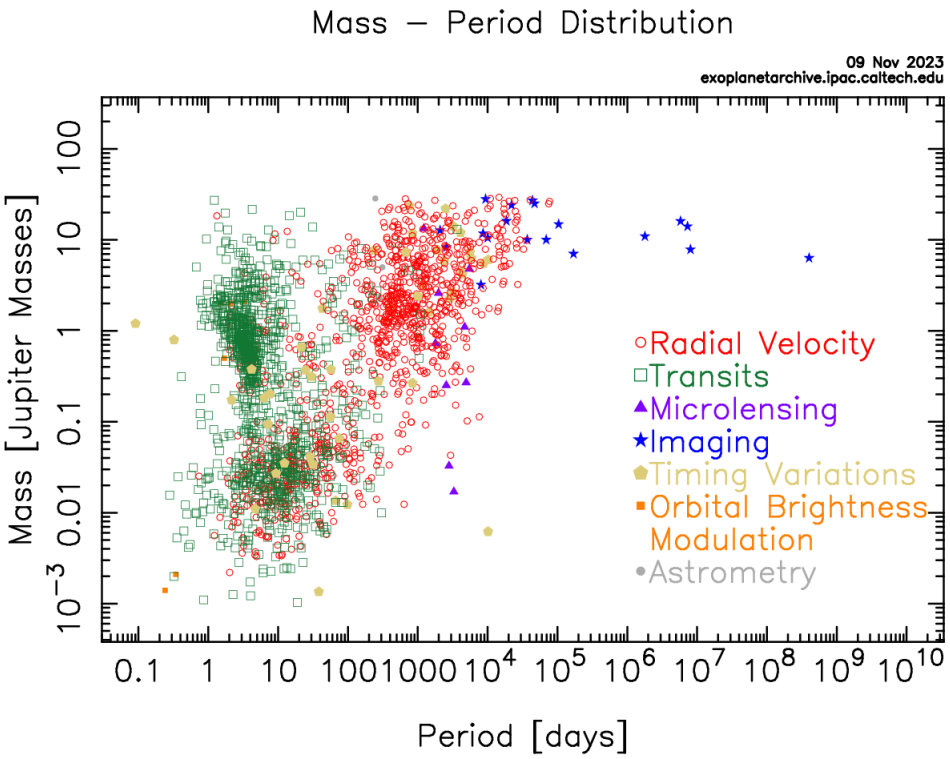

Figure 1.22: Cumulative distribution of the number of exoplanets discovered by method and by year. Most exoplanets have been detected by the transit and radial velocity methods. Figure taken from NASA Exoplanet Archive

and to overcome its limits. It was devoted to discover thousands of planets orbiting bright stars in the solar neighborhood. This strategy aimed to make possible subsequent studies on the planets' masses and atmospheric compositions with the upcoming space missions, especially with the *JWST* through transit and occultation high-precision spectroscopy. While it is important to discover all kinds of exoplanets, *TESS* and the scientific community focused on terrestrial planets with sizes between those of Earth and Neptune, often called 'super-Earths' and 'mini-Neptunes'. This is because there is no examples of these planets in our solar system which limits our understanding of their composition, formation and evolution history. To reach its goals and given that bright stars are spread all around the sky in the solar neighborhood, *TESS* was designed to perform a nearly all-sky survey, unlike its predecessor, *Kepler*, that had a narrow fixed field of view. Specifically, the primary scientific objectives of the *TESS* mission were as follows (Ricker et al., 2015):

1. Observe over 200,000 bright stars in the solar neighborhood to search for planets with periods and radii lower than 100 days and 4 $R_\oplus$, respectively.

2. Search for long-period (up to 120 days) transiting planets days among ~10,000 stars in the regions surrounding the ecliptic poles (*TESS* continuous viewing zones).

3. Detect at least 50 planets with radii ≤ 4 $R_\oplus$, whose masses will be easily measurable with RV follow-up. This is known as *TESS Level 1 Science Requirement*.

TESS focused on planets orbiting main-sequence dwarf stars with spectral types ranging from

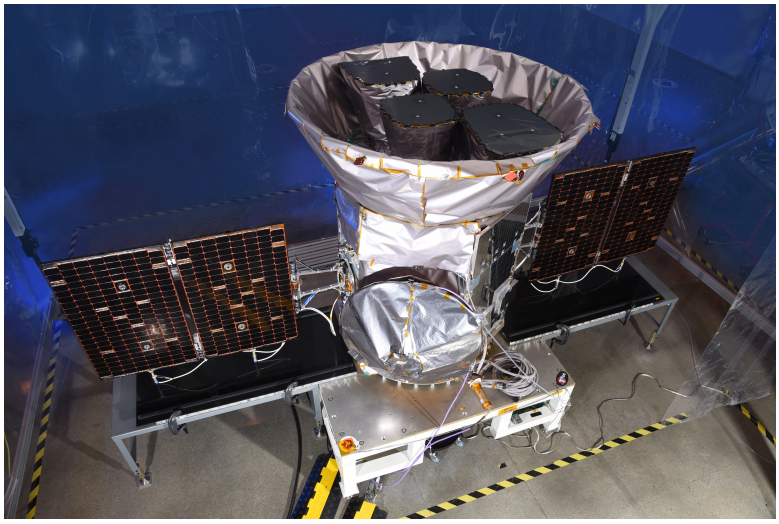

Figure 1.23: TESS spacecraft exposed to media visitors at NASA's Kennedy Space Center in Florida. Credit: NASA

F5 to M5, but with a special focus on M-dwarfs down to the M5-M6 spectral types. These M-dwarfs are the most favorable targets for the mission *TESS* because they offer many advantages such as:

1. Although they are the most abundant stars in the solar neighborhood (Henry et al., 2018; Reylé et al., 2021), they were less explored by the *Kepler* mission where they constituted only a small portion of its targets list.

2. Given their small sizes, the transit depth for a given (small) planet is deeper and then easier to detect than what it would be for larger stars (Winn, 2010). This facilitates their atmospheric studies with the present (notably with *JWST*) and near future facilities. Also, because of their low mass, M dwarfs are more influenced by gravitational interaction by their orbiting planets. This makes them favored for RV follow-up to measure the masses of the discovered planets and reach the scientific underlined goals.

3. Given their low luminosities, the habitable zone is located closer to this type of stars than it is for larger stars. Thus, planets in the habitable zone orbiting dwarf stars will have shorter orbital periods. This makes easy follow-up of these planets in a relatively short timescale. These are the most favorable targets for biosignatures detection with current technologies (Shields et al., 2016).

The discovery of TRAPPIST-1 system (Gillon et al., 2017) indicates that, despite their low mass, M dwarfs can potentially form compact system of temperate earth-sized planets in the habitable zone. TRAPPIST-1 is a system of seven Earth-sized planets all in orbit around an a very-low-mass M-dwarf star ten times smaller than our Sun. Three of these planets (TRAPPIST-1e, f, g) orbit in the habitable zone of the star. *TESS* data are also being used in astroseismology, which is the science to study the oscillations (or starquacks) of stars to probe their internal structure and properties.

1.5.1 Orbit

To accomplish its scientific objectives, *TESS* had to have a carefully selected and designed orbit for an unobstructed view of the sky. It was thus selected to have a highly elliptical high-Earth orbit (HEO) with perigee and apogee of 17 $R_\oplus$ and 59 $R_\oplus$ respectively, and a 13.7-day[18] period in 2:1 resonance with the Moon's orbit which helps stabilize the spacecraft's orbit over time. It is inclined by 40° with respect to the Moon's orbit which permits the spacecraft performed continuous monitoring by avoiding lengthy eclipses by the Earth and Moon. It also presents a relatively low radiation and nearly constant thermal environment as it is above the Earth's radiation belts[19]. This nearly constant thermal environment guarantees the CCDs operation at temperature lower than -75° C, with temperature variations < 0.1°C h^{-1} for 90% of the orbit. At apogee, observations are interrupted and the spacecraft rotates to point its antenna towards the Earth to downlink the accumulated data to the ground.

1.5.2 Cameras

TESS spacecraft is equipped with four 2k×2k Charged-Coupled Device (CCD) cameras each with a field of view 24 °× 24 °and a pixel scale of 21" per pixel. They are aligned such that they cover a strip of sky, called sector, measuring 24° width and 96° height. The detectors are deeply-depleted, a technology providing them with a wide bandpass of 400 nm from 600 to 1000 nm. This bandpass was the most convenient for *TESS* targets list where most of stars are emitting most of their light in red domaine. The sensitivity curve is shown in Figure 1.24.

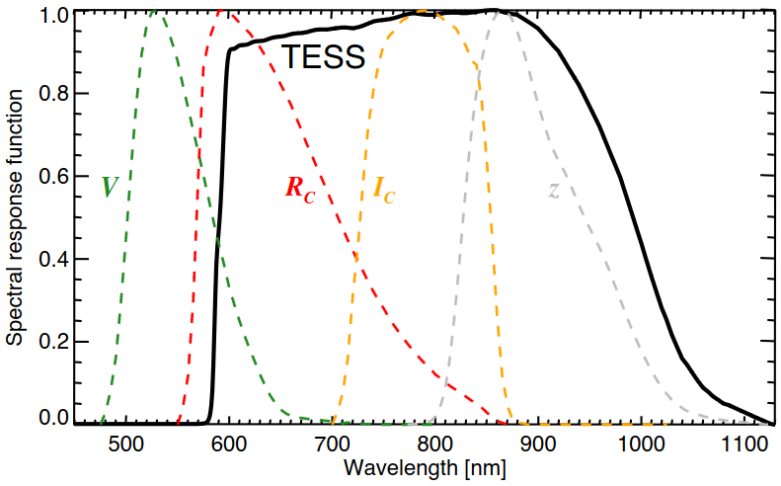

Figure 1.24: Spectral response function of *TESS* depicted as black line. It is the multiplication result of the long-pass filter transmission and the detector quantum efficiency curves. Johnson–Cousins V , R_C , and I_C filter curves and the Sloan Digital Sky Survey z filter curve are also plotted comparison. The *TESS* bandpass is equivalent the bandpass of the R_C , I_C , and z bands, each with maximum normalized to unity. Figure adopted from Ricker et al. (2015).

[18]This period is known as P/2 orbit. Which refers to the fact that *TESS* spacecraft completes an orbit in half the time that takes the moon to complete its orbit.

[19]Known as *Van Allen* belts. Two belts surrounding the Earth, held by its magnetic field and composed mainly of electrons and photons. The highest altitude is about 60000 km above the Earth.

1.5.3 Observing strategy

In its two-year prime mission, *TESS* observed the southern ecliptic hemisphere in its first year and then the northern in its second year. It performed the observation sector by sector. As I explained previously, each sector is 24° width and 96° height (left Figure 1.25). *TESS* observing strategy splits each hemisphere into 13 sectors. In the first year, the instrument boresight pointed at -54° ecliptic latitude so that the field of view covers the region from an ecliptic latitude -6° to the ecliptic pole (middle panel of Figure 1.25). In the second year, the instrument boresight pointed at an ecliptic latitude of +54° for sectors 17–23 and of +85° for sectors 14–16 and 24–26. Each sector is observed for 27.4 days during two orbits of the spacecraft, so it is sensitive to planets with orbital periods up to 13.7 days (under the requirement that at least two transits must be observed to result in a detection). When one sector's observation is completed, the instrument FOV is shifted eastward by 27°, with camera 4 being always centered on the ecliptic pole. As a result, there can be some overlap between sectors depending on the ecliptic latitute. As apparent on Figure 1.25, regions around the ecliptic poles were observed continuously for about one year. These are known as the continuous viewing zones (CVZs) (right panel of Figure 1.25) and correspond to the CVZ of *JWST*. Targets in the CVZs are highly coveted for for detecting long-period planets and extracting long-period rotational rates of the host stars. Also, planets discovered in the CVZ have a globally higher potential for detailed subsequent atmospheric studies with the *JWST*.

In the extended mission, *TESS* re-observes the sky in both hemispheres with varying boresight ecliptic latitude (Wong & Shporer, 2022). The goal of the extended mission was to increase both the observation baseline and the overall coverage of the sky observed by the satellite. This increased the number of exoplanets that could be detected by *TESS*, especially planets with long orbital periods for which only single or few transits are detected in the primary mission. This also included planets in orbits in the *HZ* of their host stars.

During operations, *TESS* four cameras take continuously images with exposure times of 2-seconds. These images are then stacked onboard (see Figure 1.26) to produce two main sets of data products in FITS extension: 1) Target Pixel files (TPFs) with a effective exposure time of 2 minutes. These are times series postage stamps prepared in a grid of 11 × 11 pixels centered on more than 200,000 preselected star of the targets list. The identification of targets appropriate for 2 minutes cadence relied on the *TESS* Input Catalog (TIC[20]: Stassun et al., 2019), that contains all needed stellar information[21]. Stars observed in more than one sector, have TPF file for each sector. The 2-minutes cadence was a strong advantage to better resolve transit shapes, especially those with short-duration; And 2) Full Frame Images (FFI) that packages a time series images across all pixels of each single CCD in every single sector with an effective exposure time of 30 min in the prime mission, and 10 min and 200 sec in the extended mission. This was motivated by the fact that *Kepler* had granted efficient discoveries of transiting planets with 30 min cadence. FFI allowed to expand the search for transiting exoplanets to any star in the FOV that is not included in

[20] https://tess.mit.edu/science/tess-input-catalogue/

[21] The latest version being used (TIC-8) is based on GAIA DR2 catalog and integrates various other photometric catalogs, including 2MASS, UCAC4, APASS, SDSS, WISE, etc.

the two-minutes-cadences TPFs, especially fainter stars. This allowed to expand the search sample beyond the bright nearby stars that are the focus of *TESS*. More detailed information on the *TESS* observations can be found on its official home page https://tess.mit.edu/observations/.

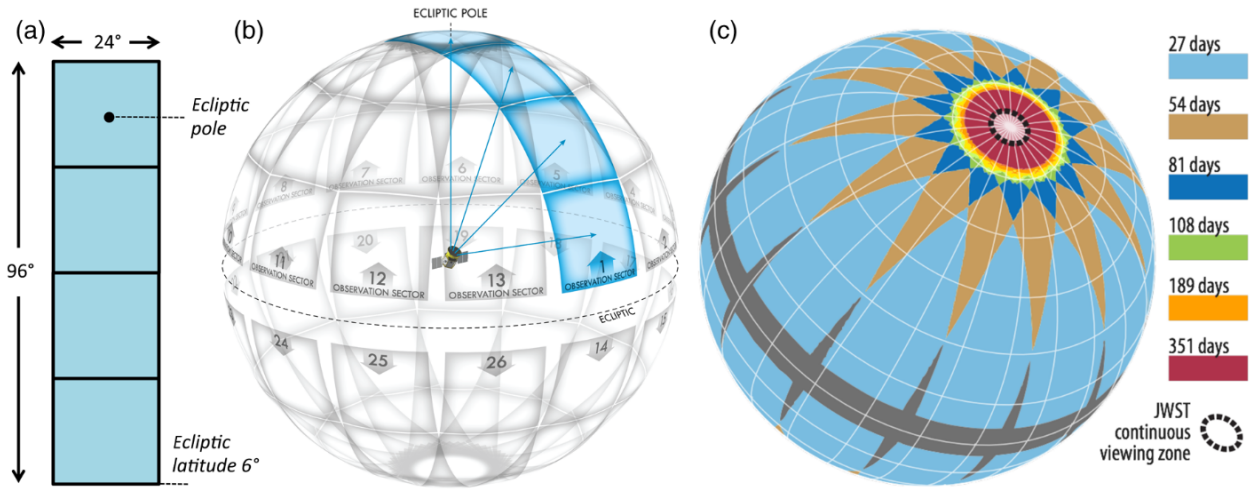

Figure 1.25: (a) The strip of sky size covered by the four TESS cameras. (b) celestial sphere divided into 26 observation sectors (13 sectors per hemisphere). (c) observation on the celestial sphere taking into account the overlap between sectors. The dashed black circle around the ecliptic pole shows the JWST CVZ. Figure taken from Ricker et al. (2015).

1.5.4 TESS data processing and data products

As explained in the previous section, at apogee, *TESS* spacecraft interrupts observation and rotates to point its antenna towards the Earth to beam the raw data (TPFs and FFIs) and engineering data to the ground. These data are then delivered to the *TESS* Science Processing Operation Center (SPOC) pipeline at NASA Ames Research Center (Jenkins et al., 2016, 2020) for processing. The SPOC pipeline is derived from the highly evaluated *Kepler* Science Operations Center (KSOC) pipeline. It calibrates the science data in two main steps, first by orbit once data transmission has been done and then by observing sector (two-orbits).

First, the data are calibrated by the Calibration (CAL) module dedicated for the removal of instrument effects and other artifacts affecting the data. This includes the correction of bias, dark current and flat fielding, in addition to pixel-level corrections that mitigates the effect of cosmic rays. These operations are performed on both 2-min cadence data and FFIs.

Then, the calibrated TPFs are transmitted to the Compute Optimal Apertures (COA) module to identify the optimum aperture pixels for extracting photometric measurements. After that, they are passed through the Simple Aperture Photometry (SAP) module to produce time-series photometry of each target star. This operation includes measurement of the brightness of each star on each frame, removal of the background flux due to zodiacal flux and the diffuse stellar background, and identification and removal of the cosmic rays from all target star apertures. It also includes the measurement of the photocenter (or centroid) of each star on each frame for the establishment of the pointing and focus of each cameras.

After that the light curves are produced, they are objected to a Presearch Data Conditioning

(PDC) module. This module carries out important corrections such as, identification and elimination of instrumental signatures induced by changes in focus and pointing, detection and removal of isolated outliers, and correction for the dilution of the target flux time series by the flux from other stars contaminating the the SPOC photometric aperture.

After each sector of data is processed through SAP and PDC, a Transiting Planet Search (TPS) is run. TPS searches for transit-like signals known as Threshold Crossing Events (TCE) in the 2-minutes cadence data. Light curves of target stars that are observed in consecutive sectors are stitched ahead before searching for planets. TCEs are then sent to the *TESS* Science Office (TSO) where they are fitted with a limb-darkened transit model and subjected, through a Data Validation (DV) module, to a suite of diagnostic tests to confirm or refute the planetary origin of the transit signals. These diagnostics include: *odd-even* test which compares the transit depths of the *odd*-numbered transits to those of the *even*-numbered transits to rule out the possibility of EB; a check for correlation between the changes in the photocenter (*centroid*) of the target star and the photometric transit signature, which might indicate the presence of a background eclipsing binary; a statistical bootstrapping test to evaluate the confidence level associated with the transit detection; a centroiding test to rule out background sources of confusion; and a ghost diagnostic test to exclude the possibility of optical ghosts of bright eclipsing binaries as the source of the transit-like signatures. Once a TCE passed successfully all the tests, the TPS is called again to search additional transiting planets. This process is repeated until TPS fails in identifying another transit signal. TCEs that passe all the tests are identified as TESS Object of Interest (TOIs hereafter) which potentially originates from transiting planets and needs confirmation with ground-based observation. Each TOI is associated to a Data Validation (DV) report that resumes the results of the diagnostics. More details on the SPOC pipeline and diagnostic tests can be found in Jenkins et al. (2016, 2020); Twicken et al. (2018).

The final products of SPOC are saved in FITS format and archived to the Mikulski Archive for Space Telescopes (MAST). These products nominally contains:

1. TPFs containing raw and calibrated pixels, masks of the pixels used for SAP and pixels used to subtract the background contribution in the SAP.

2. FFIs provided in three types: uncalibrated, calibrated, and uncertainty. The calibrated images and their uncertainties are provided in separate files.

3. Light Curves (LCs) that contain two extensions of the flux time series data at 2-minutes cadence for the preselected stars: i) SAP flux which is the flux after summing the calibrated pixels within the TESS optimal photometric aperture, and ii) Pre-search Data Conditioned Simple Aperture Photometry (PDCSAP) flux which is the SAP flux corrected for instrumental variations as I explained above. LCs contain also multiple meta data, notably the masks of the pixels used in the SAP and for background correction. As for TPFs and FFIs, one LC is provided for each target star per sector. If a star is observed in many sectors, then one LC is provided from each sector.

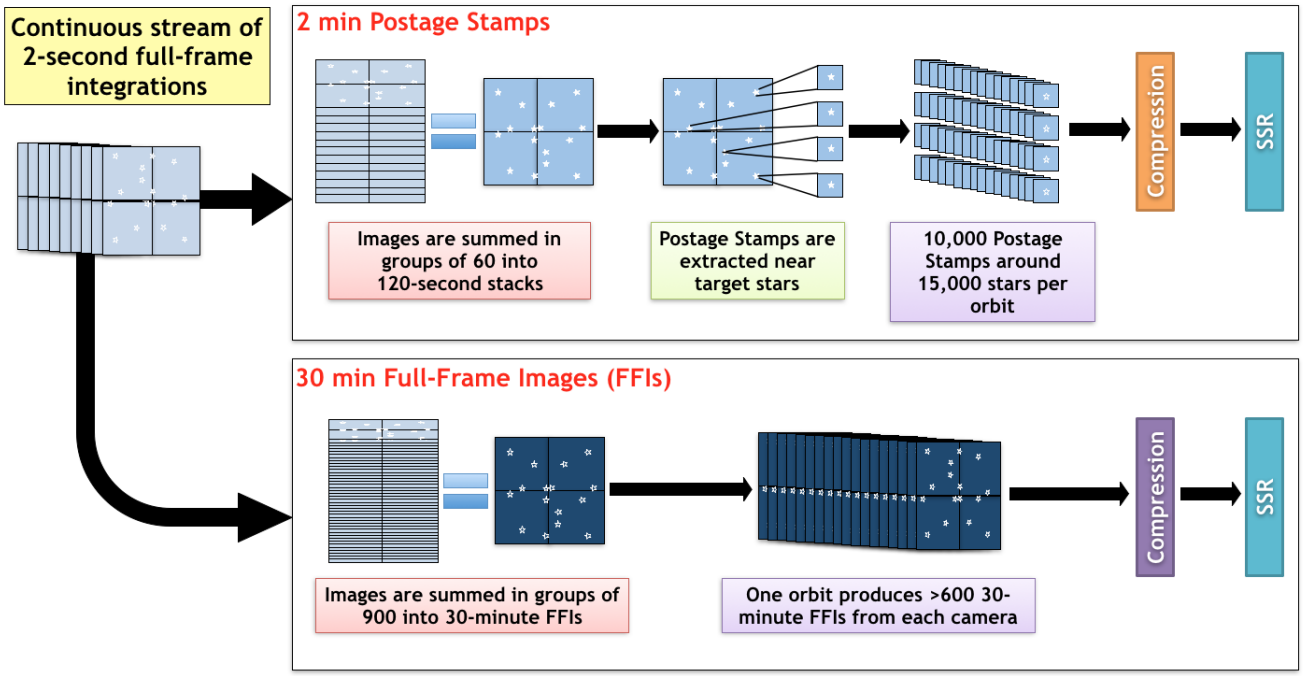

Figure 1.26: Representation of how the 2-minutes postage stamps and 30-minutes FFIs are created. Credit: NASA

For FFIs, the light curves extraction and transit search is performed by MIT's Quick Look Pipeline (QLP: Huang et al., 2020; Kunimoto et al., 2021). The QLP was developed to rapidly process *TESS* FFI data as they reach Earth. It starts by performing some necessary corrections for instrumental effects, global background subtraction and astrometric solution determination. Then, the QLP performs multi-aperture photometry to extract lightcurves for all targets captured in the FFIs with TESS magnitude brighter than T = 13.5 mag. Prior to transiting planets search, it still performs some prost-processing of the light curves. This consists of the removal of measurements outliers, stellar variability (detrending) and instrumental effects. Light curves of stars observed in more than one sectors are combined together to perform multi-sector search for transiting exoplanets. Finally, reports for the most promising candidates are compiled and then delivered to the TSO for vetting as part of the TOI alert process. More details on the QLP can be found in (Huang et al., 2020).

TOI release

As above mentioned, TSO prepares a list of TOIs deemed promising for ground-based follow-up observations by the *TESS* Follow-up Observing Program (TFOP[22]). TOI release is nominally done every four months and includes all the information needed for the follow-up, notably transit signals

[22] https://tess.mit.edu/followup/

and their ephemerides. Such information are added to the *TTF* to be used for ground-based follow-up observations.

1.5.5 TESS Follow-up Observing Program Working Group (TFOP-WG)

For *TESS* to achieve its scientific objectives, especially the Level 1 Science Requirement of providing masses for 50 transiting planets with sizes smaller than 4 $R_{\oplus}$, a *TESS* Follow-up Observing Program Working Group (TFOP-WG) was created. In this latter, a large community of astronomers is providing a variety of follow-up observations and data analyses to identify with a high confidence level TOIs that are bona fide transiting planets, and to discard those that are due to false positives. TFOP-WG promotes communication and coordination between the *TESS* Science Team and the follow-up observers to avoid redundant observations and analyses. TFOP-WG is composed of five main Sub-Groups (SG) working together:

- **SG1:** This subgroup provides Seeing-limited photometry to confirm that the transit signals detected in TESS data originate well from the targeted stars and to identify false positives due to nearby eclipsing binaries (NEBs), blended eclipsing binaries (BEBs) that contaminate the *TESS* photometry of a candidate transiting planet, or other false positives. The usual strategy of this subgroup is to use the *TESS* Transit Finder (*TTF*) to provide better photometric light curves, ephemerides, and for some cases, precise measurement of the transit timing variations (TTVs). Updated ephemerides on *TTF* are used to optimize the scheduling observations. The *TTF* tool is an adapted version of the `Tapir` (primarily developed for *Kepler* mission.) software package (Jensen, 2013) for the observability of TOIs.

- **SG2:** Provides spectroscopy observations to improve the stellar parameters (especially mass and radius) which lead to the improvement of the mass and radius of the discovered planets. This SG2 can also help in identifying eclipsing binaries and blended eclipsing binaries that masquerade as transiting planets by the detection of the composite nature of their spectra.

- **SG3:** Employs high-resolution imaging with adaptive optics, speckle imaging to detect nearby objects that remain unresolved in the *TESS* Input Catalog (TIC) or by seeing-limited photometry. This play a crucial role for the enhancement of the validation of the planets before proceeding with precise radial velocity observation for planetary mass determination, or when the dilution from a close companion affects the planetary radius determination.

- **SG4:** Specialized in precise radial velocity observations to constrain the orbits and masses (relative to the host star's mass) of the discovered planets. Generally these observations are combined with high-precision photometry to pin down the planetary mass after removing degeneracy on the orbital inclination i as I explained in Sect 1.4.2.

- **SG5:** Specialized in space-based photometry with instruments such as HST, Spitzer, MOST, CHEOPS, and *JWST*, mainly to verify and refine the ephemerides determined by *TESS*. It is also to improve light curves for transit events or even TTVs in some cases.

1.6 The photometric follow-up of TESS candidates with the TRAPPIST telescopes

As I have explained in previous section, *TESS* observes the sky and provides us with planets candidates named TOIs that need to be confirmed with ground-based observations. This is performed within TFOP-WG. This working group is made of many ground-based observers from all around the world to perform photometric time-series observation, RV observations, adaptive optic imaging and spectroscopic observations of the host stars. My thesis is implicated in the photometric time series observations (transit detection) of the planet candidates using mainly the TRAPPIST telescopes described below.

1.6.1 TRAPPIST project

TRAPPIST (**TRA**nsiting **P**lanets and **P**lanetas**I**mal **S**mall **T**elescopes) is a project led by the University of Liege, in collaboration with the Geneva Observatory. It has been funded by the Belgian Fund for Scientific Research (F.R.S.-FNRS) and the Swiss National Science Foundation (SNF). TRAPPIST is constituted of two twin robotic telescopes, each of 60cm diameter, TRAPPIST-South that is installed in the southern hemisphere at la Silla observatory (Chile) since 2010 and TRAPPIST-North that was installed in the northern hemisphere at Oukaimeden observatory (Morocco) in 2016 in collaboration with the Cadi Ayyad University in Marrakesh. The two telescopes were installed in the north and south hemispheres to have an access to the whole sky. The two telescopes, whose instrumentation will be explained in details hereafter, provide high-precision photometry to reach the scientific goals of the project that are split in two main themes, 1) search and characterize transiting exoplanets, and 2) study small bodies (e.r comets and asteroids) in our solar system (Jehin et al., 2011; Gillon et al., 2011).

Thanks to the TRAPPIST-South telescope, with the assistance of NASA's Spitzer Space Telescope, in 2017, TRAPPIST discovered an extraordinary exoplanetary system. This is the TRAPPIST-1 system (Gillon et al., 2017) with seven rocky exoplanets similar in size to Earth, all orbiting an ultra-cool dwarf star ten times smaller ($R_* = 0.121 \pm 0.003\,\mathrm{R}_\odot$ and $M_* = 0.089 \pm 0.006\,\mathrm{M}_\odot$, VanGrootel et al. (2018)) than the Sun and located in the solar neighborhood at only 40 light-years. The star was named TRAPPIST-1, while each planet was named with an additional letter from b to h in increasing order of the distance between the planet and the star. TRAPPIST-a is a moderately active star M8.0±0.5 (V=18.80, J=11.35) with effective temperature 2559±50 K. Three planets of this system (TRAPPIST-e, f and g) orbit in the *habitable zone* where water might be present in its liquid sate, which makes it a particularly important system to be studied by *JWST*. It is a compact system with the outer-most planet has a semi-major axis of only 0.06 *au*. Compared to our Solar system, this system can be placed within the Mercury orbit around the Sun. In terms of planets formation, this system is particularly important. It indicates that a fraction ultra-cool stars are potentially surrounded by a compact system of telluric temperate small planets.

It should also be noted that TRAPPIST was the prototype of SPECULOOS (**S**earch for habitable **P**lanets **EC**lipsing **UL**tra-c**OO**l **S**tars) project (Gillon, 2018; Delrez et al., 2018; Sebastian

et al., 2020; Burdanov et al., 2018), with the objective of evaluating the capacity of modest-sized robotic telescopes (up to 1m) to detect the transits of potentially habitable planets orbiting nearby ultra-cool stars. SPECULOOS aims to detect rocky exoplanets similar in size to Earth and orbiting in the habitable zone around the closest ultra-cold dwarf stars to our solar system. This project is motivated by the possibility of studying the atmosphere of these exoplanets in detail with two telescopes: The Extremely Large Telescope (ELT[23]), a terrestrial telescope equipped with a primary mirror of 39 meters in diameter, under construction by the European Southern Observatory (ESO) see its first light in 2028 and the *JWST* (Greene et al., 2016), a space telescope, equipped with a primary mirror of 6.5 meters in diameter (compared to 2.4 meters for Hubble), developed by NASA with the assistance of ESA and CSA (the Canadian Space Agency). It was launched in December 25, 2021 onboard an Ariane 5 rocket from Kourou which put it at the second Lagrange point L2 of the solar system.

As for TRAPPIST, SPECULOOS is composed of two observatories: 1) Speculoos Southern Observatory (SSO) of Paranal in the Atacama Desert, which is composed of four robotic telescopes each of 1m diameter in operation since 2019, and 2) Speculoos Northern Observatry (SNO) located at Teide Observatory in the island of Tenerife (Canaries), which constitutes of only one telescope twin of the SSO telescopes named Artemis and will soon be joined with a second telescope named "Orion". In 2022, SPECULOOS discovered a new potentially habitable planet around an M6 dwarf named SPECULOOS-2 (Delrez et al., 2022).

1.6.2 TRAPPIST telescopes

As explained previously, the TRAPPIST project is based on two twin robotic telescopes, TRAPPIST-North installed at Oukaimeden Observatory (in the northern hemisphere) and TRAPPIST-South installed at la Silla Observatory (in the southern hemisphere) in Chile. This allows an full access to the sky. The two telescopes are of type F/8 Ritchey-Chrétien and equipped with a primary mirror of 60cm. They are equipped with an equatorial mount associated with a *direct-drive* system that permits to avoid periodic errors encountered usually in the equatorial mounts of small telescopes.

Figure 1.27: Left: TRAPPIST-South telescope at la Silla observatory. Right: TRAPPIST-North telescope at Oukaimeden observatory. Credits: Jehin et al. (2011)

TRAPPIST-North is equipped with a thermoelectrically cooled Andor iKon-L BEX2-DD CCD

[23] https://elt.eso.org/science/exoplanets/

camera with an array of 2K×2K pixels and a pixel scale of 0.6" per pixel, which offer a 20' ×20' field of view. The detector has an a quantum efficiency reaching 90% between 700 and 800 nm (see top upper panel of Figure 1.28). The camera operates generally at a temperature around $-65°c$, with a mean dark current of $0.15el/pixel/s$. The camera has three reading modes. Each has its own read noise that depends on its speed: a slow mode of 1MHz with read noise of $7e/5s$, a rapid mode of 3MHz with read noise of $12e/3s$ and a very rapid mode of 5MHz with read noise $2e/1.8s$.

The CCD camera is equipped with two filters wheel each can accommodates 10 square filters of 50×50 mm with a position without filter (clear filter). One of the wheels contains 9 narrow-band filters (OH, NH, CN, C3, BC, C2, GC, RC and Hα) designed for comets observation and the second wheel contains 7 broadband filters (B, V, Rc, Ic, zp, I+z and Exo) designed for transiting exoplanets observation (see lower panel of Figure 1.28). TRAPPIST-South is equipped with a CCD camera with about of the same characteristics than TRAPPIST-North camera.

To take into consideration the weather conditions, each of the two telescopes is equipped with a weather station that records weather data, and with a system that closes the domes automatically (for the safety of the telescope) when weather conditions are not favorable during observation.

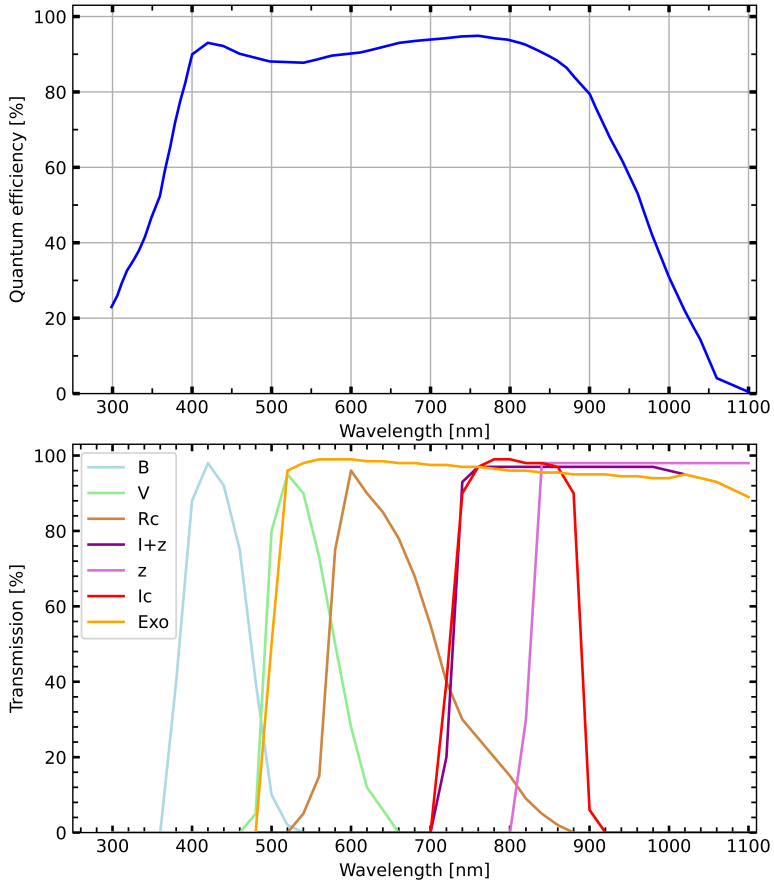

Figure 1.28: *Top*: Quantum efficiency of the TRAPPIST-North CCD camera. *Bottom*: Transmission curves of TRAPPIST-North' broad-band filters used for exoplanet photometry. The two panels were plotted taking the data files from the source code of TRAPPIST-North exposure time calculator [ETC].

1.6.3 OWL@OUKA telescope

In this thesis, it was also planned to use the OWL@OUKA telescope (see Figure 1.29), installed at Oukaimeden observatory, to follow-up *TESS* planet candidates. It is one of the five robotic telescopes, uniformly spread over the glob (Mongolia, Morocco, Israel, South Korea and USA), of the South-Korean Optical Wide-field patroL (OWL-Net, Park et al., 2017; Ghachoui et al., 2020) project. This project was designed and built by the south-Korean Astronomy and Space Science Institute (KASI) to follow-up south-Korean Low Earth Orbit (LEO) and Geostationary Earth Orbit (GEO) satellites to obtain their orbital information and maintain their orbits.

OWL@OUKA is equipped with a 0.5-m primary mirror in the Ritchey-Chretien configuration and a 0.2-m secondary mirror. It was installed in 2015 at Oukaimeden Observatory in collaboration with Cadi Ayyad University in Marrakesh (Morocco). It has an alt-azimuthal mount with a maximum speed of 10 deg/sec and an acceleration of 2 deg/sec. Given its relatively simple structure and wide field of view, a clamshell-type dome was adopted to the telescope.

OWL@OUKA has a ProLine PL 16803 CCD camera, with 4096×4096 9-μm pixels on the CCD sensor and a pixel scale of 1 arcsecond per pixel, offering a wide field of view of 1.1°×1.1°. The camera possesses a wheel of four filters (B, V, R and I) and one clear position. The CCD detector exhibits a quantum efficiency reaching a peak of 60% near 560 nm. It has two available readout modes including a low-noise mode with 10e at 1 MHz and a fast readout mode with 14e at 8 MHz. The cooling system operates at 55 degrees Celsius below ambient. Typically, during observations, the CCD detector temperature is set to -20 degrees Celsius.

While this telescope was dedicated to only track satellites, it was also tested for the follow-up of *TESS* candidates. A proceeding was published for this purpose (Ghachoui et al., 2020), reporting its capability to follow-up of hot Jupiters orbiting bright stars. For M dwarfs, this telescope shows incapability to detect small transiting planets. Given that most of our targets are of M and K spectral types, and the huge amount of data collected by both TRAPPIST-North and -South (with higher precision compared to OWL@OUKA), OWL@OUKA was no longer used in this thesis. However, four hot-Jupiters have been observed by this telescope: TOI-2146.01, TOI-2311.01, TOI-2383.01 and TOI-5152.01. The latter (TOI-5152.01) was included in a list of six short-period giant planets validated by Rodriguez et al. (2023).

1.6.4 Discarding possible false positives using TRAPPIST telescopes

Various false positives (see Figure 1.30) can masquerade as transit-like signals detected by *TESS*. Some of them are already recognized by the SPOC pipeline like some (but not all) eclipsing binaries (see Section 1.5.4) but others can remain unidentified if the signal-to-noise (SNR) and/or cadence of TESS data is too low, and can end up as TOIs. It is thus important to support *TESS* detections with high precision ground-based observations. In this section I will describe these false positives and how to rule them out:

Figure 1.29: OWL@OUKA telescope at Oukaimeden observatory. Credit: Ghachoui Mourad

Instrumental artifact:

This is the easiest possible false positive that can be ruled out. This can simply be ruled out by the detection of the transit signal with high-precision ground-based photometry.

Eclipsing binaries (EB):

It is a two-star system whose components periodically eclipse each other. When the smaller star crosses in front of the larger star, it produces a significant drop in brightness. Although both stars are emitting light, the transiting (smaller) star is still blocking light from the transited larger star. The transit shape of EBs is different from that of transiting planet. The key difference is that the transit of an EB is typically V-shaped while that of a transiting planet is U-shaped. Another clue to distinguish EBs from real transit signals is the depth of the secondary eclipse when the smaller (fainter) star passes behind the larger (brighter) star. The secondary eclipse is generally shallower than the primary eclipse. *Odd-even test* which compares the transit depths for *odd-numbered* transits to those of *even-numbered* transits, is a powerful tool to distinguish EB from planetary transits. In the *TESS* data, the SPOC performs this test and usually reports the so called *depth-sig* metric to quantify the similarity between the two depths from 0 to 100%. This test is performed for all TOIs before any data release and are reported in the data validation (DV) reports of *TESS* available on MAST.

Generally, transits of EB have typical depths of tens of percents which make them easy to be distinguished from transit depths caused by a planet. However, the extreme case is for grazing EB (see lower right corner of Figure 1.30) where the transit depths are of few percents and are then similar to those of transiting planets. These signals might be unrecognized by *TESS*, depending on the SNR and cadence. With high-cadence high-precision photometry it is possible to recognize

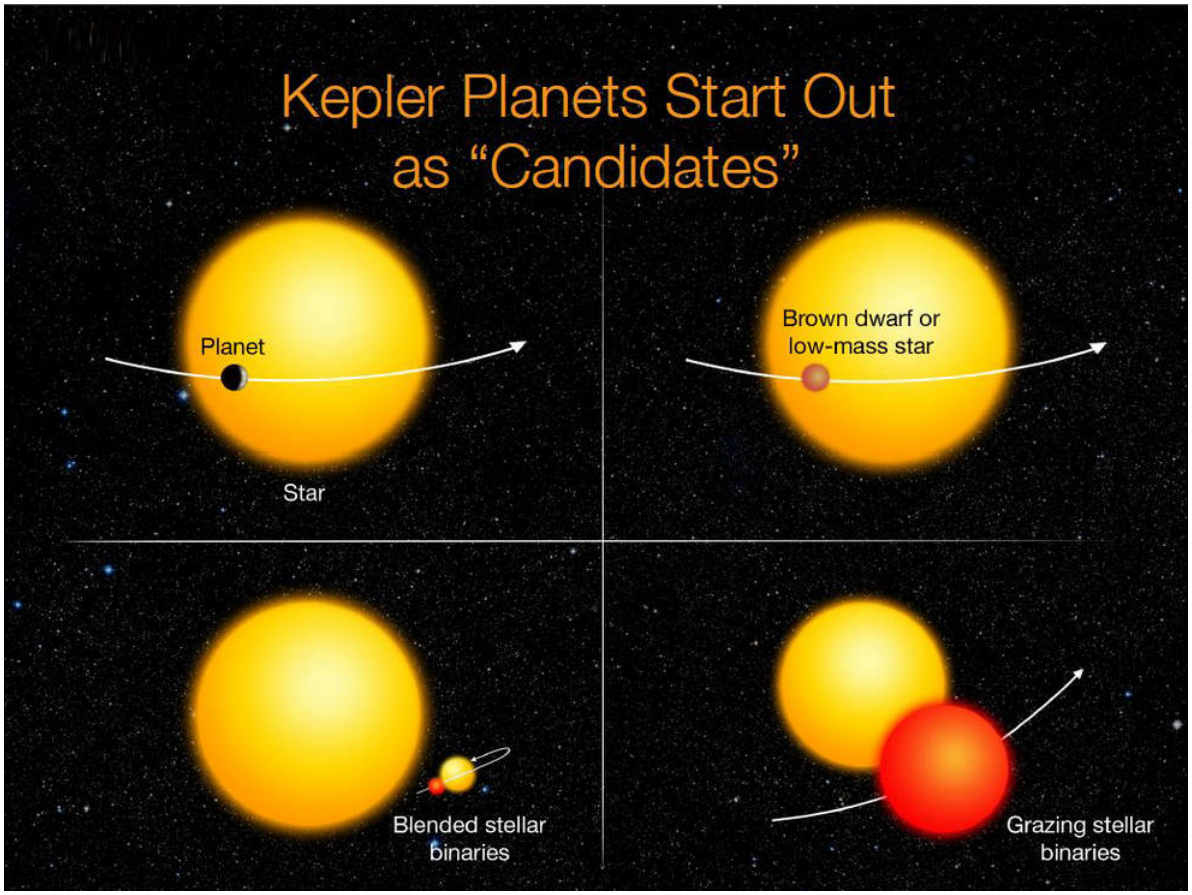

Figure 1.30: Different false positives that can masquerade as transit-like signals. The upper left corner shows transiting planets which is what *TESS* is searching for.. The upper right corner shows the very common type of false positive which is a small star, usually a brown dwarf, transiting a larger stars. The lower left corner depicts another case of false positive when a background eclipsing binary is blended with the target star. In both cases, the diluted eclipse of the EB can mimick an exoplanet transit signal. The lower right corner shows a grazing eclipsing binary. This graphic was created for the *Kepler* mission, but it can also applies to the *TESS* mission as well. Credit: https://www.nextbigfuture.com/2016/05/number-of-known-exoplanets-has.html

this false positive from a bona fide planetary transit, but with low SNR we have to resort to RV observations of the primary star. This can help determine or at least define an upper limit on the mass of the secondary object to know whether it is a planetary-mass or substellar-mass companion (i.e. a brown dwarf). For secondary companions more massive than a substellar object, the RV semi-amplitudes are typically tens of kms^{-1} while for a planetary-mass companion these are of only hundreds of ms^{-1} (Brown & Latham, 2008).

Blended eclipsing binary (BEB):

It is another case when an EB is blended with the target star (see lower left corner of Figure 1.30). This might either be an eclipsing binary in the background blended to the target star in the aperture photometry or an EB physically associated to the target star forming an hierarchical eclipsing binary (HEB). This makes distinguishing BEB from transiting planets challenging. This is a frequent case in the *TESS* photometry, escpecially because of the low angular resolution of its

cameras. As explained previously, SPOC examines the correlation between the flux-weighted center of light (*centroid*) of the stars and the transit signal time. If the *centroid* presents some anomalies at the transit time, this might indicate that the transit signal is due to a BEB. It is worth noting that transits or eclipses of the target star can still have significant centroid offsets if another bright star is blended with the target. This diagnostic is performed before data release and reported in the DV report. Of course not all false positives are ruled out by the SPOC pipeline, but many BEBs can still persist. With ground-based photometric observation, we perform a chromaticity check for the transit event by observing the predicted transits of the target star with different filters (different wavelength ranges). Here, the chromaticity refers to the variation of the transit depths from a filter color to another. In case of a transiting planet, the transit depths must be consistent across all the filters, but in case of a BEB, the transit depths will change from a filter to another. The latter is because the dilution changes from a filter to another. It is also possible to check for consistency between the stellar density from R_* and M_* (determined in independent analyses) with that determined from the transit for high precision photometric data as I explained in Section 1.4.2. If the density values are in agreement, the transit signal is likely due to a transiting planet, else, it is due to another astrophysical phenomenon.

Nearby eclipsing binary (NEB):

TESS has a pixel scale of 21" per pixel. Many nearby stars can fall within the same photometric aperture assigned by SPOC for the targeted star (see an example in Figure 1.31). These stars might be suspected as EB causing the *TESS* detection. One of the most required ground-based observation of *TESS* candidates that the signal is well on the target star and check for NEBs within 2.5′ area around the target star. The `AstroImageJ` (AIJ: Collins et al., 2017) software offers a powerful tool to check all the stars within 2.5" for NEBs. These observation are required especially when a planet candidate is observed for the first time. The *TTF* presents a `AIJ Apertures` file containing the equatorial coordinates (ra, dec) of all the nearby stars that can be the source of the detection. This file can be read by `AIJ` to identify all the nearby stars in one run (see Chapter 3).

Note: Other independent techniques can also be used to rule out the possibility of EBs and BEBs: by checking if the global spectral energy distribution and/or spectra of the target are consistent with that of a single star; by using high-resolution adaptive optic imaging to check for the presence of another source in the vicinity of the target; for stars that have high proper motion, it is also possible to rule out the possibility of BEB by searching in archival images to seek for any bright stellar object behind the target.

1.6.5 TESS discoveries

As of December 15, 2023, *TESS* is in the fourth year of its extended mission. A total of 70 sectors have been observed. It has provided the exoplanets community with 7021 TOIs (see the TOIs catalog in `https://tev.mit.edu/data/`), including more than 1386 exoplanets with radii smaller tha $4\,R_\oplus$, which are candidate planets that need validation and confirmation with ground-based observations. As of today, 410 exoplanets have been validated and more than 1701 *false positives*

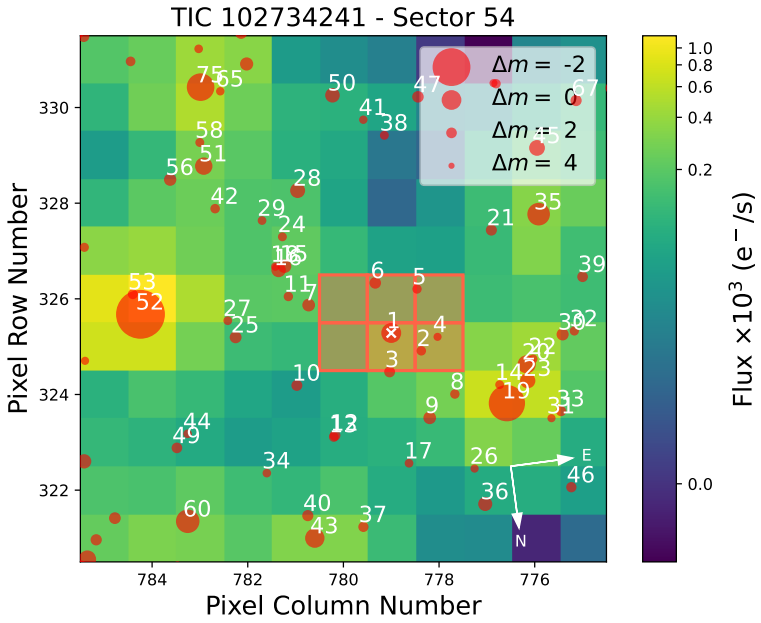

Figure 1.31: TPF of TOI-6002 (TIC 102734241) in the *TESS* Sector 54 created with `tpfplotter`(Aller et al., 2020). The pixels highlighted in orange represent the SPOC simple aperture showing clearly Gaia stars within it. The red circles represent the Gaia DR2 sources with sizes representing Δmag with respect to the targets.

have been discarded. Statistics on the TESS discoveries are usually reported and updated on the mission's website page: https://tess.mit.edu/publications/.

Chapter 2

Motivations and goals of the thesis

In this chapter, I introduce the intriguing "super-Earths" and "mini-Neptunes", two types of planets that are ubiquitous in the galaxy but absent from our solar system. I explain the uncertainty surrounding their formation and evolution mechanisms, and how my thesis aims to help constrain these mechanisms and better understand these mysterious planets.

2.1 Radius valley

The *Kepler* survey showed that our Galaxy is teeming with small exoplanets ($R_P < 4$ $R_\oplus$) orbiting close to their host stars (Howard et al., 2012; Fressin et al., 2013). Studies performed on the California–Kepler Survey exoplanets sample, a portion of transiting planets found by *Kepler* and with precise spectroscopic characterization of their host stars (CKS: Petigura et al., 2017; Johnson et al., 2017), uncovered a dichotomy in the radius distribution of transiting planets with orbits shorter than 100 days. Specifically, a dearth is observed between 1.5 and 2 $R_\oplus$ for FGK stars (see e.g. Fulton et al., 2017; Fulton & Petigura, 2018). The same feature was uncovered between 1.4 to 1.7 $R_\oplus$ for mid-K to mid-M dwarfs stars ($T_{eff} < 4700K$) (see e.g. Cloutier & Menou, 2020) based on planets from *Kepler* and K2. In the literature, this is commonly known as *radius valley* (or "*Fulton gap*"). It separates the so-called "super-Earths" and "mini-Neptunes", described as follows:

Super-Earths:

Planets below the radius valley and larger than Earth are known as super-Earths. These planets have been found to have bulk densities consistent with Earth (see e.g. Weiss & Marcy, 2014; Rogers, 2015; Dressing et al., 2015; Dorn et al., 2018; Hadden & Lithwick, 2014), especially those orbiting close to low-mass host stars, where they lose much of their atmospheres because of the intense extreme ultra-violet radiation during the long pre-main-sequence phase of their hosts (Stelzer et al., 2013). Generally, super-Earths have radii $\lesssim$ 1.6 $R_\oplus$ (Rogers, 2015). This was confirmed later by Luque & Pallé (2022) (see hereafter) who studied the demographic distribution of a well-characterized sample of exoplanets and found that planets with radii consistent with those below the radius valley have densities consistent with rocky composition. Also, all the known super-Earths with mass measurements in the NASA Exoplanet Archive are found to be rocky. Because of their small sizes and low masses, detection and characterization of these planets need an enormous amount of observations with either state-of-the-art ground- and space-based instruments, especially for large stars. However, these planets attract a great attention because we have no such example in our

solar system and studying in detail a large sample of these planets will help understanding their formation and evolution, and deeply constrain their interior compositions. Super-Earths orbiting their host stars in the habitable zones are the most targeted candidates for habitability studies by both space- and ground-based observations.

Mini-Neptunes:

Planets beyond the radius valley and smaller than Neptune (i.e. $R_p \lesssim 4\,R_\oplus$) are informally referred to as sub-Neptunes. Weiss & Marcy (2014) and Rogers (2015) showed that planets larger than 1.6 $R_\oplus$ have densities lower than Earth and consistent with Neptune-like planets, which are consistent with the presence of a H/He gaseous envelope on top of a rock or rock+ice core. Fulton et al. (2017) argued also that these planets do harbor a H/He envelope representing only a few percents of the planet's mass but accounting for a few dozens of % of its large radius, increasing significantly its observed radius as shown by i.e. Lopez & Rice (2018). Nevertheless, some of these planets could be devoid of H/He envelope, but instead could have a composition particularly rich in ices, notably in water, like the mini-Neptune GJ1214b (Charbonneau et al., 2009). Indeed, as I will explain later, Luque & Pallé (2022) observationally showed that planets with radii larger than super-Earths might be water-rich worlds ($\rho = 0.47 \pm 0.05 \rho_\oplus$ and $R_p = 1.97 \pm 0.28\,R_\oplus$) or puffy sub-Neptunes ($\rho = 0.24 \pm 0.04 \rho_\oplus$ and $R_p = 2.85 \pm 0.63\,R_\oplus$). Compared to super-Earths, sub-Neptunes are considered good targets for atmospheric studies via transmission spectroscopy thanks to their deeper transit depths and their possible extended atmospheres (high scale height H) (Brown et al., 2001; Seager & Sasselov, 2000b), especially when transiting small stars.

2.1.1 Origin of the radius valley and planets formation:

The radius valley is of central interest in the current studies to understand the formation and the evolution of small planets. In this context many high-debated theories have been proposed to understand its origin:

1) **Thermally-driven mass-loss theory:** under which it is proposed that some sub-Neptune planets, after gas accretion, may lose their atmosphere through thermally-driven mass-loss and become super-Earths. Two scenarios are acting in this theory. The first is *photoevaporation* triggered by energetic Extreme Ultra-Violet (EUV) and X-ray radiations emanating from the host stars (see e.g. Lopez & Fortney, 2013; Chen & Rogers, 2016). These radiations heat the upper atmosphere layers and cause an outflow of matter. This scenario takes place during the first ∼100 Myrs of the star's life where it is chromospherically active (Owen & Wu, 2013). The second is *core-powered mass-loss*, which is similar to the first scenario in its principle but the heating energy is remanent from the formation phase of the planet's core. This energy is transferred through the atmosphere, heating the upper layers and causing an outflow (see e.g. Ginzburg et al., 2016; Gupta & Schlichting, 2020). This happens on a timescale of Gyrs (Ginzburg et al., 2018). In regard to this theory, it

is implicitly suggested that the two planetary populations (super-Earths and sub-Neptunes) should have the same rocky core composition and that the difference in their radii is due to whether they retained their primordial atmospheres or not. Also, it should be found that sub-Neptunes hosts are globally younger than super-Earths hosts.

2) **Gas-poor formation theory:** where the formation of rocky planets is delayed in a gas-poor (but not depleted, following the terminology of Cherubim et al. (2023)) environment after dissipation of most of gas in the proto-planetary disk (Lee & Connors, 2021; Lee et al., 2022). This leads to the formation of rocky planets with small gaseous envelopes. It is worth noting that planets formed in gas-poor environment might still experience thermally-driven atmospheric escape too.

3) **Gas-depleted formation theory:** which proposes the formation of two populations in two distinct timescales. A population of rocky planets with small gaseous envelopes accreted during the first Myrs of the system, and a population of purely rocky planets formed later in a gas depleted environment (Lopez & Rice, 2018; Cloutier & Menou, 2020; Cherubim et al., 2023).

4) **Impact erosion:** where it is proposed that giant impacts of planetesimals (kilometers-sized celestial bodies formed from the dust and gas present in the proto-planetary disk around young stars) onto terrestrial planets release energy that may make them lose their primordial gaseous envelopes (see e.g Liu et al., 2015; Schlichting et al., 2015; Kegerreis et al., 2020; Wyatt et al., 2020). This mechanism is highly stochastic, thus it is doubtful that it can be alone responsible for the emergence of the radius valley. Still, the energy released by the impact can swells the gaseous envelope, which promotes thermally-driven photoevaporation (Fulton et al., 2017).

The location of the radius valley has been found to be dependent on the period of the planets and is formulated as $R_{p,valley} \propto P^{\alpha}$ with α varying from one study to the other (see Figure 2.1). Planet occurrence rate studies (see e.g. Fulton et al., 2017; VanEylen et al., 2018; Martinez et al., 2019; Affolter et al., 2023) for FGK stars found a negative slope of the radius valley where $-0.11 \leq \alpha \leq -0.09$, in alignment with the slope predicted by thermally-driven mass-loss and gas poor formation models where $-0.15 \leq \alpha \leq 0.08$ (see e.g. Lopez & Rice, 2018; Gupta & Schlichting, 2020; Lee & Connors, 2021; Rogers et al., 2021). The upper limit of the rocky planets radii decreases with the orbital period. This can be explained with the fact that thermally-driven mass-loss is more efficient at short distance from the star even for massive planets (higher surface gravity). Away from the star, only small planets are supposed to lose the gaseous envelopes because of their low surface gravities. For late-K to mid-M dwarf stars, an observational study by Cloutier & Menou (2020) found a positive slope of the radius valley where $\alpha = 0.11$, which aligns with predictions of the gas depleted model (Lopez & Rice, 2018). The upper limit of the purely rocky planets radii slightly increases towards longer periods. This can be explained with the fact that planets in long

orbits have more material to accrete along their paths, increasing their sizes.

Differences in slopes of the radius valley led to a region of opposing predictions between the different models (see Figure 2.1). Planets inside this region are expected to be purely rocky under the thermally-driven mass-loss and gas-poor formation mechanisms, and rocky with likely small gaseous envelopes under the gas depleted formation theory. These planets are considered as "*keystone objects*" and determining their densities is greatly coveted to observationally disentangle which phenomenon is more likely responsible for their formation and evolution (Cloutier & Menou, 2020; Cherubim et al., 2023). Until this day, only seven well-characterized *keystone planets* have been found around M dwarfs: TOI-1235 b (Cloutier et al., 2020), TOI-776 b (Luque et al., 2021), TOI-1634 b (Cloutier et al., 2021; Hirano et al., 2021), TOI-1685 b (Bluhm et al., 2021), G 9-40 b (Luque et al., 2022), TOI-1452 b (Cadieux et al., 2022) and TOI-1695 b (Cherubim et al., 2023). These planets have been found to possess different bulk compositions making it challenging to have firm conclusions. Thus it is important to enlarge this sample of *keystone planets* with precise density determination to put tighter constraints on the formation and evolution mechanisms.

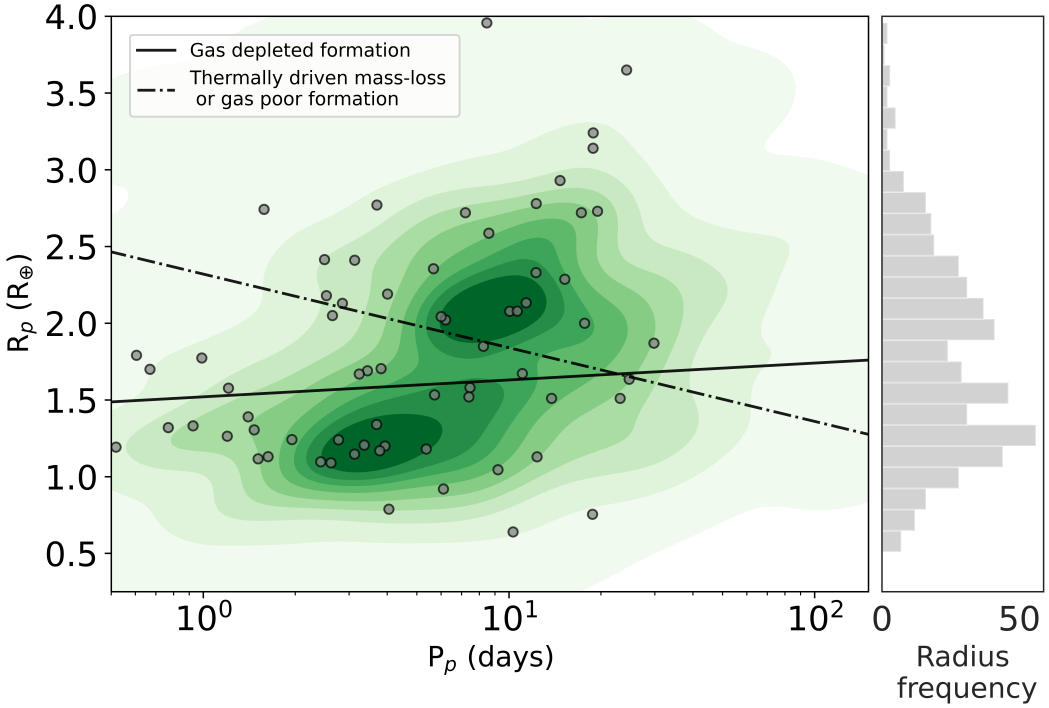

Figure 2.1: Distribution of planet radii and orbital periods for all confirmed small planets, in the Nasa Exoplanet Archive, hosted by low-mass stars ($M_* \leq 0.65\,M_\odot$). The solid line represent the empirical locations of the radius valley as given by the gas depleted formation model (Cloutier & Menou, 2020). The dashed line represent the radius valley as predicted by the thermally-driven photoevaporation and gas poor formation model (VanEylen et al., 2018). The right panel shows the 1D distribution of the planets' radii.

2.2 Density valley

The study of Luque & Pallé (2022) led to different findings and conclusions than previous statistical studies of the so-called *radius valley*. On the basis of a sample of 34 well-characterized (precisions on mass and radius better 25% and 8%, respectively) planets transiting M dwarf stars, they identified three populations of exoplanets based on their densities (see left panel of Figure 2.2): rocky planets ($\rho = 0.94 \pm 0.13\ \rho_\oplus$), water-rich planets ($\rho = 0.47 \pm 0.05\ \rho_\oplus$), and puffy sub-Neptunes ($\rho = 0.24 \pm 0.04\ \rho_\oplus$). A *density valley* is observed between rocky and water-rich planets with no intermediate composition. This favored the pebble accretion model as the main mechanism responsible for forming small planets around M dwarfs (Venturini et al., 2020; Brügger et al., 2020), where planets are formed through gradual coagulation of small solid particles known as "pebbles", sized from centimeters to meters. Luque & Pallé (2022) suggested that rocky planets are formed within the *ice line* (defined as the limit around the young star beyond which the temperature is low enough for water to exist in its solid state) and the water-rich worlds are formed beyond it and then migrate toward the star. In terms of their radii distribution, the study of Luque & Pallé (2022) is consistent with the radius valley of Fulton et al. (2017), with high dispersion in the radius distribution of puffy sub-Neptunes (see right panel of Figure 2.2). This indicates, according to the authors, that each of these planets could have its individual H/He accretion history.

It is worth noting that studies that were performed on both *radius* and *density gaps* considered small samples of exoplanets. This precludes any strong conclusions on their formation and evolution pathways. A larger sample of super-Earths and sub-Neptunes with precise radii and masses is highly needed to reach firmer statistical inferences on the *radius/density gap*, and to eventually reveal which mechanisms lie behind their formation and evolution.

2.3 Goals of the thesis

As I explained in Section 1.5, *TESS* is well on its way to discover a great number of planets of all sizes around stars of different spectral types. It has shown to be especially efficient to detect small planets around nearby early to mid-type M-dwarfs (down to spectral type M6). Many of these planets will be promising for precise density determination and detailed atmospheric characterization (especially with *JWST*). This will enlarge the sample of precisely characterized planets, making possible stronger inferences to be drawn on the mechanism(s) at the origin of the *radius* and *density valleys* (see previous section). Such studies will bring key insights on their formation and evolution history and on their interior compositions. The goal of this thesis is to bring a significant contribution to this global endeavor by participating in the photometric confirmation of a well-selected sample of sub-Neptune and super-Earths TESS candidates, mostly with TRAPPIST-north robotic telescope. This includes:

- Selection of interesting targets (TOIs) for validation from the *TESS* Transit Finder

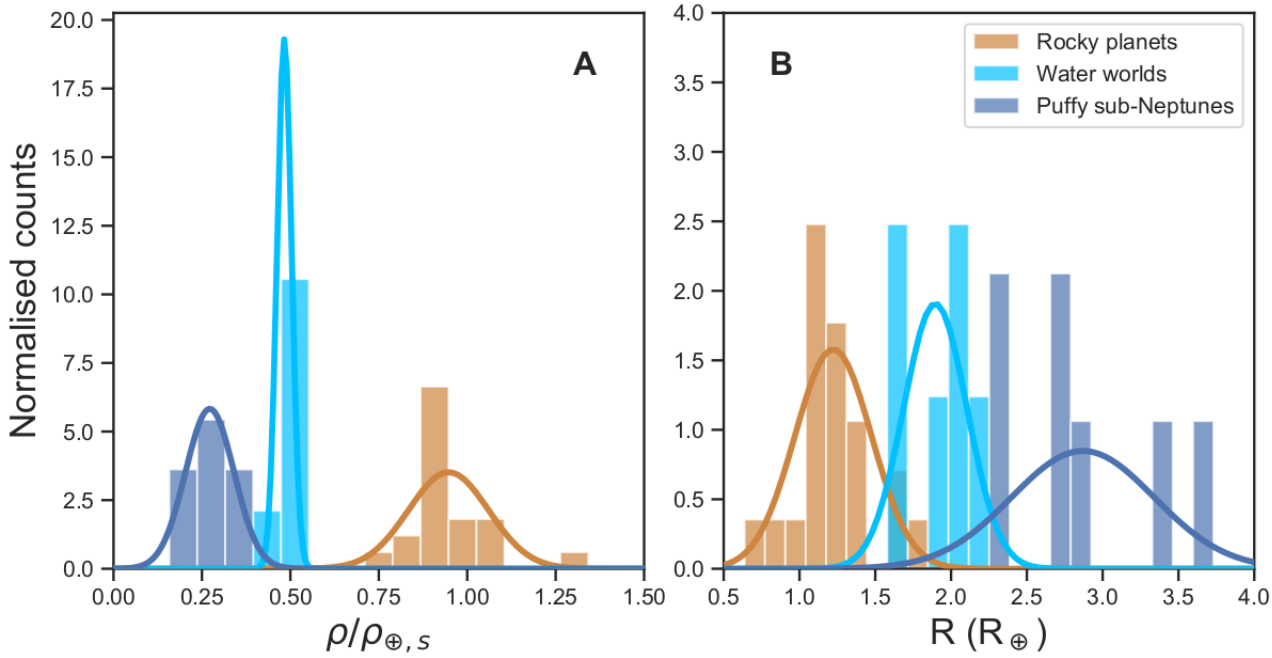

Figure 2.2: Normalised histograms of the small transiting planets around M dwarfs. (A): Distribution of the planets densities divided by an Earth-like model. (B): Distribution of the planets radii. Solid lines show Gaussian models fitted to the distribution of each planet type. Credit: Luque & Pallé (2022).

(*TTF*[1], Jensen, 2013).

- High-precision seeing-limited time-series photometric observations of potential transits of the selected *TESS* candidates, to confirm that the eclipse exists, originates well from the *TESS* target, and has the properties of an exoplanet transit signal (achromaticity, shape, depth).
- Data reduction and analyses, all in coordination with *TESS* Science Team and TFOP-WG observing members.
- Publication of the interesting results and scientific inferences in the theoretical context described above.

[1] https://astro.swarthmore.edu/telescope/tess-secure/find_tess_transits.cgi

Chapter 3

Methodology

3.1 Observation

3.1.1 Target selection

As detailed in Chapter 1, all *TESS* candidates need to be validated and confirmed using ground-based follow-up observations. The *TESS* Follow-up Observing Program Working Group (TFOP-WG) was established by *TESS* for this purpose (see Section 1.5.5). I contributed to this program, within Sub-Group 1 (SG1) with photometric time-series follow-up observations using the TRAPPIST telescopes.

For the selection of *TESS* planet candidates, I have been using the *TESS* Transit Finder (*TTF*[1]) which extracts TOIs from ExoFOP-TESS and filters them to provide a list of observable transit events for a given geographic location and for any night. All *TESS* candidates are classified on a priority scale from 1 to 5. In my thesis, I was only interested in planet candidates with priority from 1 to 3 which can be filtered by the *TTF*. When no candidates of priority 1 or 2 were available, those with priority 3 were selected. This task was performed every Monday and covered all the nights of the week, until Sunday.

For every planet candidate, *TTF* provides all the information needed for observations such as the equatorial coordinates, start/mid/end time of the predicted transit event, depth of the transit event, visibility profile curve of the host star, a link to database listing the main properties of the host star, and resuming all the previous observations (if any) and the need and goal of further observations. Below in Figure 3.1 is a screen shot from the *TTF* output for the planet candidate TOI-6717 b, as example.

Search: Show if visible transit % + baseline % > 0 V_{max}: Overlap (min.): 0 TRAPPIST-North (0.6-m)

Local evening date	Name	V mag	T mag	Start—Mid—End	Duration	BJD_{TDB} start-mid-end	Elev. at start, mid, end ±1.5 hrs	% of transit (baseline) observable, Suggested obs. start, end	Az. at start, mid, end ±1.5 hrs	HA at start, mid, end ±1.5 hrs	RA & Dec (J2000)	Depth (ppt)	Priority	R_{planet} ($R_\oplus$)	Period (days)	Comments and followup status
Wed. 2024-01-03: Nautical twilight 2024-01-03 19:37 — 2024-01-04 07:33 local time / 2024-01-03 18:37 — 2024-01-04 06:33 UTC																
Wed. 2024-01-03 (local date) Nautical twilight 18:37 – 06:33 (UTC)	☐ TIC 34986694.01 (TOI 6717.01) Add to TOC Finding charts: Annotated, Aladin; Info: ExoFOP, Simbad, Gaia, TIC, VSX, AII apertures, Vizier phot., Airmass, ACP plan	16.56 Moon 49% @28°	13.91	01:17 03:27—03:42—03:57 06:06 ±0:40	0:30 ±0:09	10313.6468 10313.6572 10313.6676	30° 50°, 52°, 53° 48°	100% (100%) 01:17—06:06	118° 152°, 157°, 163° 215°	-3.3 -1.2, -0.9, -0.7 +1.5	10:57:18.17 -04:40:24.81	5.1	2	1.9	0.47	CPC VPC? spoc-s01-s65-b02 Sectors:[36, 45, 62]: [P=0.4707476] low SNR; V-shaped; centroids centered near between target and TIC 902821804; Rick Schwarz/ LCO-CTIO-1m0 analyzed a full on 20231122 in ip and maybe detected an ~on-time 3.1 ppt (0.6x SPOC) event using an uncontaminated 5.5" target aperture and cleared 23/23 neighbors to 2.5'. An alternate analysis using detrending, different comp stars and locking a/R* and b from the SPOC s01-s65 detects a, V-shaped, ~14 min early 3.9 ppt event. [P=0.4707429]. The next observation should be a high precision (<1.0 ppt/10 min) full transit in a red (r', R, i', I, z, Y) filter to attempt a firm detection of the event on target. Multi-band or blue (U, u', B, g') filter observations even better for a simultaneous chromaticity check.

Figure 3.1: *TESS* Transit Finder output for the planet candidate TOI-6717.01.

The selection of *TESS* candidates has to respect several criteria for useful and conclusive

[1] https://astro.swarthmore.edu/telescope/tess-secure/find_tess_transits.cgi

observations:

1. the target star should not have an elevation from local horizon lower than 20° during observation to avoid the impact of high AIRMASS (see Figure 3.3) that decreases the SNR and the topography of mountains surrounding the observatory.

2. the transit depth should not be shallower than 2.5 parts per thousand (*ppt*) which has been found the detection limit of the TRAPPIST telescopes.

3. target star must be bright enough, and thus the SNR high enough, to make the observations useful. Still, it cannot be too bright, to avoid saturating the detector, even with the shortest allowed exposure time (10 seconds). Furthermore, very bright stars pose a problem of lack of comparison stars in the 'small' field of view of TRAPPIST telescopes.

3.1.2 Scheduling observations

Generally, I searched for one or two TOI per night, depending on their priorities and on the constraints of the comets program. Once a set of TOIs was selected, I put them on the TRAPPIST-North schedule. An example of schedule is presented below for TOI-3751 b, which was observed on 28 December 2023:

```
Night starting on 28 Dec 2023
From 19h10 to 00h40:  TOI-3751.01
Start:  20:05 Mid:  21:50 End:  23:30
Jmag= 12.0, SpT= F7
RA = 04:34:30.97, DEC = +32:28:35.98, filter=I+z, texp=20
```

Generally, the observation started at least 30 minutes before the predicted start time of the transit and ended at least 30 minutes after the predicted end of the transit (depending on the uncertainty on the ephemerids in the *TTF*). The *Jmag* is taken from ExoFOP database and the spectral type of the target is estimated from its effective temperature (also taken from ExoFOP) and an online table[2] of spectral types and their corresponding temperatures. These two parameters are necessary to determine the appropriate exposure time (see hereafter). The *ra* and *dec* coordinates are taken from *TTF* and the exposure time (texp) is calculated from the online Exposure Time Calculator (ETC[3]). ETC takes as inputs the *Jmag*, spectral type and *airmass* of the target star, the moon phase[4] and the filter being used, and provides the predicted target peak. Generally the best exposure time is that corresponding to a

[2] https://sites.uni.edu/morgans/astro/course/Notes/section2/spectraltemps.html
[3] http://www2.orca.ulg.ac.be/TRAPPIST/PageInterne/Prog/mourad/ProgValeur.html
[4] The moon phase takes values from 0 to 1 and it estimates the illumination of the moon. 0 means there is no moon while 1 means a full moon.

target peak from 30,000 to 40,000 ADUs[5], given that the CCD camera detectors of both TRAPPIST telescopes saturate at 64,000 ADUs (electronic saturation). An example of exposure time calculation is shown in Figure 3.2. Of course, the exposure time depends on many other parameters (like the mirror size of the telescope, the quantum efficiency of the CCCD camera, the focal ratio, etc), but they are hard-coded in the TRAPPIST ETC. The filter used for every star depends mainly on the objective of the observation as I will describe in the subsequent sections.

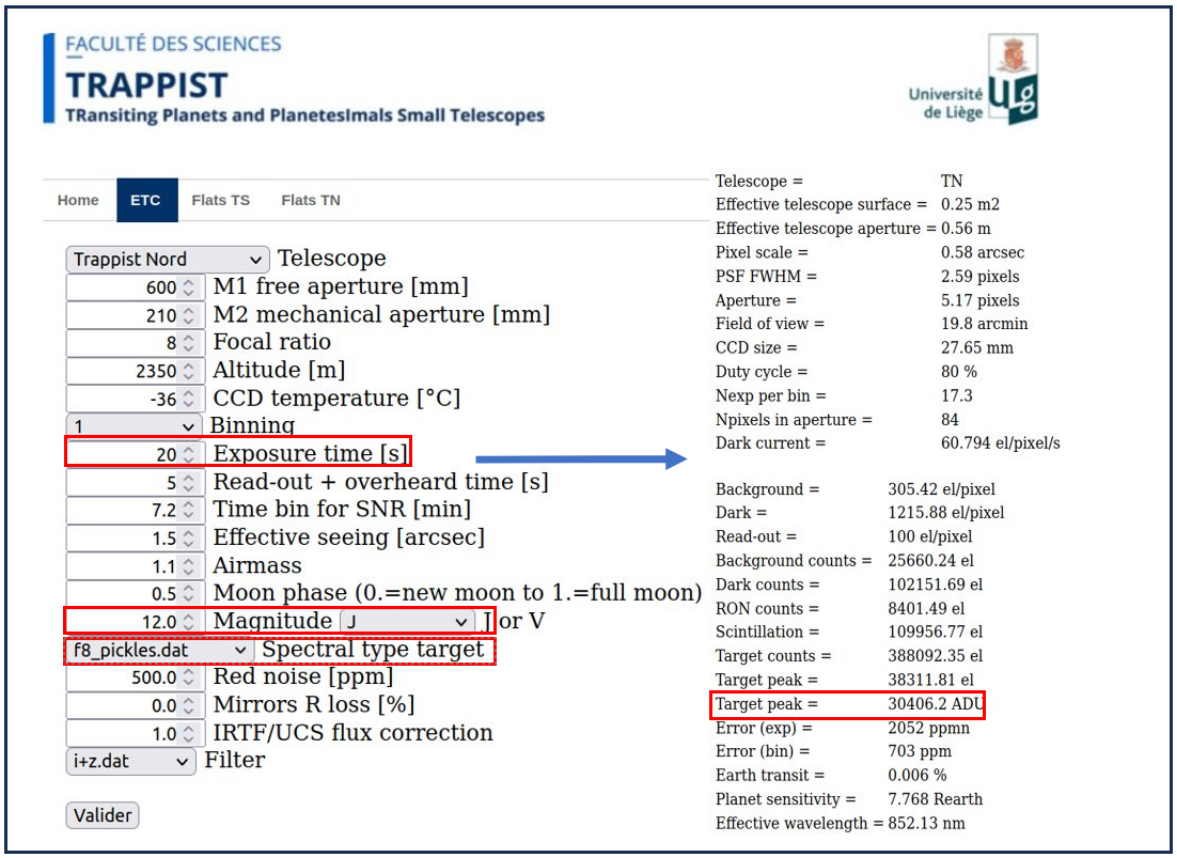

Figure 3.2: Example of exposure time calculation for the host star TOI-3751 with Jmag=12.0 and spectral type F8.

3.2 The different noises in the light curves

Several types of noise of statistical, astrophysical, atmospheric and instrumental origins can affect the accuracy of the light curves. It is important to reduce or smooth the noise as much as possible in order to accurately characterize the discovered planet. The aim of this section is to present these noises, as well as how to reduce them.

3.2.1 Photon noise

The photon noise is a statistical noise directly related to the corpuscular nature of the starlight. Even if the source of light is stable, the numbers of photons measured during equal

[5]ADU means Analogic Digital Unit, a unit to measure stars' flux.

exposure times are not equal, because photons are emitted randomly over time. The number of photons received by the CCD detector will therefore follow the *Poisson*'s law, with the standard deviation associated with this number being $\sqrt{N_{ph}}$. This noise presents a physical limit to the measurements of a light signal. It also represents the initial signal-to-noise ratio (SNR) (see e.g. Howell, 2006):

$$\frac{S}{N}(ph) = \sqrt{N_{ph}}$$

On the CCD detectors and by photoelectric effect, the absorption of some photons that have sufficient energies permits the release of an electron, with an efficiency α called quantum efficiency. For a number of electrons N_{ph}, the number of generated electrons is $N_e = \alpha N_{ph}$, with α being lower than 1. The uncertainty of this measurement is also determined by *Poisson* law.

$$\frac{S}{N}(e) = \sqrt{N_e} = \sqrt{\alpha N_{ph}} = \sqrt{\alpha}\frac{S}{N}(ph)$$

since $\alpha < 1$, then,

$$\frac{S}{N}(e) < \frac{S}{N}(ph)$$

This means that the SNR decreases when converting from photons to electrons.

3.2.2 Astrophysical noise

The astrophysical noise is due to the intrinsic properties of stars. The magnetic activity of a star induces changes in its photosphere[6]. These photosphere changes result in variations of the stellar flux over time. In addition, stars potentially exhibit dark spots and flares. Stars have angular momentum, and the rotation of these structures translates into periodic photometric modulations in the light curves.

3.2.3 Atmospheric noise

Seeing variation

The *seeing* is a physical parameter used to quantify the optical quality of the sky. It measures the atmospheric turbulence. It is defined as the full width at half maximum (FWHM) of the point spread function (PSF) (which is the response of an optical imaging system to a point source) and typically measured in *arcseconds*. Small *seeing* value indicates minimal turbulence and then the sky quality is good for observation. Adaptive optic techniques present a way of mitigating the effect of atmospheric turbulence as I explained in Section 1.3.1. Space telescopes, which operate above the Earth's atmosphere, do not experience this effect.

With a telescope of finite diameter, the image of a point source at the focus of a telescope is not a point, but an *Airy* spot. The angular radius of the *Airy* spot is given by the

[6]The photosphere is the upper gaz layer that form the visible surface of the star where the light comes from.

diffraction law:

$$\theta = 1.22(") \frac{\lambda(\mu m)}{D(m)} \tag{3.2.1}$$

where λ is the wavelength and D is the telescope diameter. θ therefore presents a physical limit of the PSF if it is subjected only to instrumental diffraction.

Atmospheric turbulence causes fluctuations in the diffraction index. These fluctuations will twist the incident wave front. Each turbulent cell will then create its own Airy spot (named *speckles*) at the focus of the telescope. These *speckles* are visible for images taken with exposure less than the *coherence time*[7]. For exposure times longer than the *coherence time*, the speckles blend to form a PSF wider than the limit of instrumental diffraction. The radius of the resulted PSF is given by replacing D (in equation 3.2.1) by r_0 (Fried, 1966):

$$\theta = 1.22 \frac{\lambda}{r_0} \tag{3.2.2}$$

with r_0 is named the Fried parameter. It represents the diameter that would be needed for a space-based telescope to have the same resolution than the considered ground-based telescope of diameter D of a ground-based telescope with diameter D. Variations in seeing often create red noise[8] in light curves.

Sky background

When observing a star, we receive not only the starlight but also contributions from the telescope and the sky through their own thermal emission/diffusion (moonlight, lamps near the observatory, etc...). Telescope's emission is more significant in the infrared, but generally remains negligible compared to the starlight. However, during the full-moon phase, the sky background could become problematic, particularly for faint target stars. In the visible, the sky background is dominated by sunlight reflected/diffused and from various artificial sources (lamps for example).

The mean signal of the sky background contribution can be corrected. Specifically, the algorithms used to extract the light curves draw a ring around the target star. The average over all pixels in the ring is subtracted from every single pixel within the circular aperture around the target star. I explained this in Section 3.3.

Atmospheric extinction

Atmospheric extinction represents the phenomenon of absorption and diffusion of the photons coming from the star by the atoms and molecules present in the Earth's atmosphere. This effect reduces the signal received from the star. Due to the diurnal movement of stars, the amount of atmosphere crossed by the light from the stars varies during observation,

[7]The coherence time characterizes the evolution time of the wavefront deformation. It depends mainly on the win speed.

[8]Red noise is the noise dominated by low-frequencies that are translated into structures in the light curves, unlike the white noise that has a flat power spectrum.

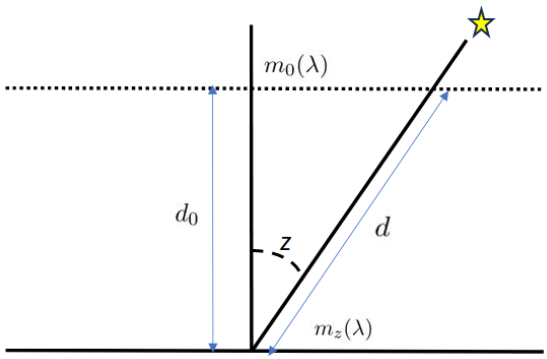

Figure 3.3: When a star has a zenithal distance z, its light crosses the distance $\frac{d_0}{\cos(z)}$. Credit: M. Ghachoui

depending mainly upon the position of the stars in the sky. This amount is minimal when the star crosses the local meridian of the observing site. In astronomy, we often use a parameter quantifying the length of atmosphere crossed, called *airmass*. Assuming a plane-parallel atmosphere (see Figure 3.3), we can express the *Airmass* as:

$$\tau = \frac{1}{\cos(z)} = \frac{d}{d_0} \tag{3.2.3}$$

with z is the zenithal distance.

When the target star passes through the local meridian, the *Airmass* is equal to 1, minimum value. During the observation, variations in the *airmass* modify the flux measured for the target and for all the stars in the field of view, causing a curvature of the light curve. Much of this effect is corrected in differential photometry by dividing the flux of the target star by the one of an ensemble of comparison stars. This correction is not total, because the atmospheric extinction in a given wavelength range varies depending on the spectral type of the target. It is thus desirable to select comparison stars with similar spectral types to the target. It is also better to pick comparison stars as close as possible to the target, to minimize the extinction effects caused by the inhomogeneity of the atmosphere.

Scintillation

Atmospheric turbulence is accompanied by pressure and temperature fluctuations, along with rapid variations in the refractive index. These variations deflect the light rays coming from the target star in random directions (Gilliland et al., 1993). This phenomenon is known as *scintillation*. Differential photometry allows us to correct for *scintillation* noise when it affects both the target and comparison stars similarly. This is typically the case for telescopes with narrow field of view like TRAPPIST-North , where the comparison stars are relatively close to the target.

3.2.4 Instrumental noise

Noise due to the telescope

The material of the telescope contribute to the noise by its thermal emission, but this emission remains insignificant. Additionally, the telescope is subjected to mechanic vibrations widening the PSF, therefore creating a noise. Stray light scattered by the telescope also increases the background noise.

CCD camera noise

The imperfections of the CCD camera detector also introduce noise that affects the precision of flux measurements. In this part of the section, I discuss these types of noises and their corresponding calibration images to correct their average signals. In the next section, I explain the algorithm for these corrections. There are three main sources of noise associated with the CCD camera (see e.g. Howell, 2006):

***Dark current*:** this noise arises from the electrons randomly generated due to the thermal vibrations (phonons) of the atoms that make up the CCD detector of the camera. This noise is as important as the temperature of the detector is high. This is why the CCD cameras are equipped with cooling systems to reduce the temperature of the detectors and then reduce their dark current. However, the mean signal (but not the random signal) of this noise can still be corrected through calibration images, called *Dark* (see right image of Figure 3.4), gathered while keeping the shutter of the camera closed, with the same exposure time as the science images.

Non-uniformity of pixels: pixels of the CCD detector do not have exactly the same quantum efficiency because of fabrication imperfections and dust on them. Because of that, if the CCD is uniformly illuminated, the responses of the pixels are not uniform. Dust typically appears as small circles on the images as shown in the left image of Figure 3.4. Practically, this noise can be corrected through calibration images, called *Flat*, gathered at Dusk (or Dawn) and with the same filter as the science images. It is crucial to periodically clean the camera to mitigate the effects of dust.

***Read noise*:** it represents the noise due to the electronic of the system when reading and saving the images after every exposure. This noise depends mainly on the reading mode as I explained in Section 1.6.2. The mean signal of this noise (but not the random signal) can be corrected through calibration images, called *Bias* images (middle image of Figure 3.4), taken while keeping the shutter of the camera closed with an exposure time as short as possible ($\sim$0 second).

3.3 Data processing and high-precision differential photometry

Having presented the different sources of noise that can affect the data, this section will detail the algorithm for data pretreatment and aperture differential photometry (see e.g. Howell,

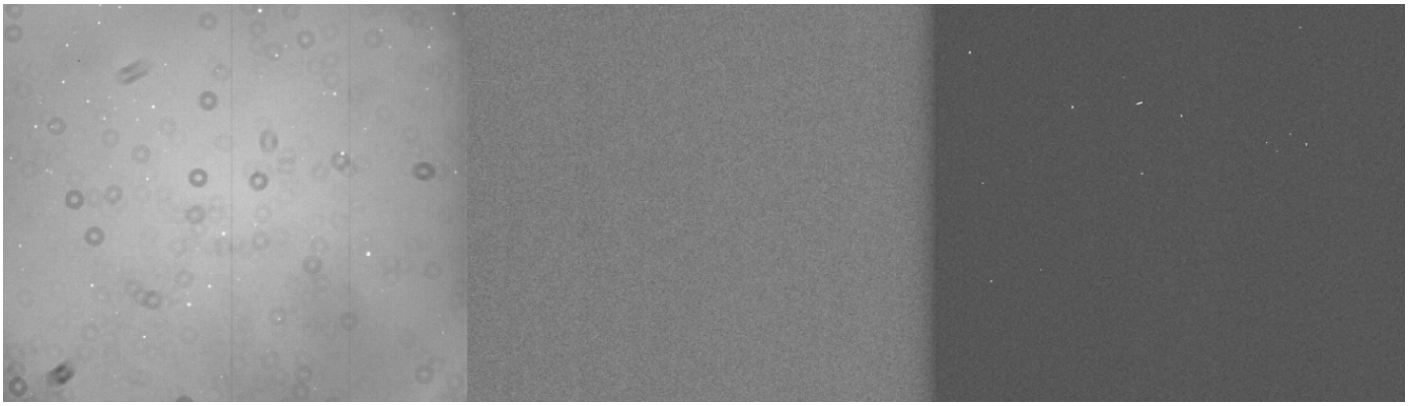

Figure 3.4: Left is the Flat, middle is the Bias and right is the Dark: Credit: Images taken by TRAPPIST-North

2006).

3.3.1 Data reduction

The pretreatment aim to remove/mitigate all correctable noises, thus preparing the data ripe for aperture differential photometry. Theoretically, every algorithm must perform the following steps:

- creation of the *MasterBias*, which is the median or the mean over all the *Bias* images:

$$MasterBias = \sum_{i=1}^{N} \frac{Bias_i}{N}$$

  this equation is applied on all pixels over N *Bias* images.

- *MasterBias* subtraction from all *Dark* images and creation of *MasterDark*.

- *MasterBias* and *MasterDark* subtraction from all *Flat* images and creation of *MasterFlat* normalized. Normalization is performed by dividing the *MasterFlat* matrix by the mean value of all its pixels.

- pretreatment of raw scientific images using the equation below:

$$Image_{Pretreated} = \frac{Image_{raw} - MasterBias - MasterDark}{MasterFlat_{Normalized}} \tag{3.3.1}$$

3.3.2 Differential aperture photometry

The principle of differential aperture photometry consists of measuring the flux in a circular aperture around a source of light. This flux is the sum over all the pixels within the circular aperture and also includes the contribution of the sky background. The latter can be removed by subtracting, from every pixel within the main aperture, a mean value over the pixels within a circular annulus placed around the main aperture (see Figure 3.5). This operation

is performed for the target star and many reference stars, usually called *comparison stars*. The flux of the target star is then divided by the sum of the fluxes from all the *comparison stars* to produce a relative flux, which is the essence of the differential aperture photometry (see e.g. Howell, 2006; Broeg et al., 2005).

The use of comparison stars is of particular importance in the search for transit events. They help to attenuate the effect of atmospheric extinction and scintillation as I explained in Section 3.2.3. The choice of comparison stars must respect several criteria: First, they should be of the same visual magnitude and spectral type as the target star, so they will experience the same atmospheric extinction. However, practically it is difficult to find stars of the same magnitudes and spectral types as the target in the field. A practical strategy is to use stars with *peaks* (i.e. the highest pixel value within the aperture, in ADU unit) similar to that of the target star. Second, it is crucial to choose as many stars as possible to minimize the photon noise, and only stars whose light curves are flat (not very active stars) and with less scatter.

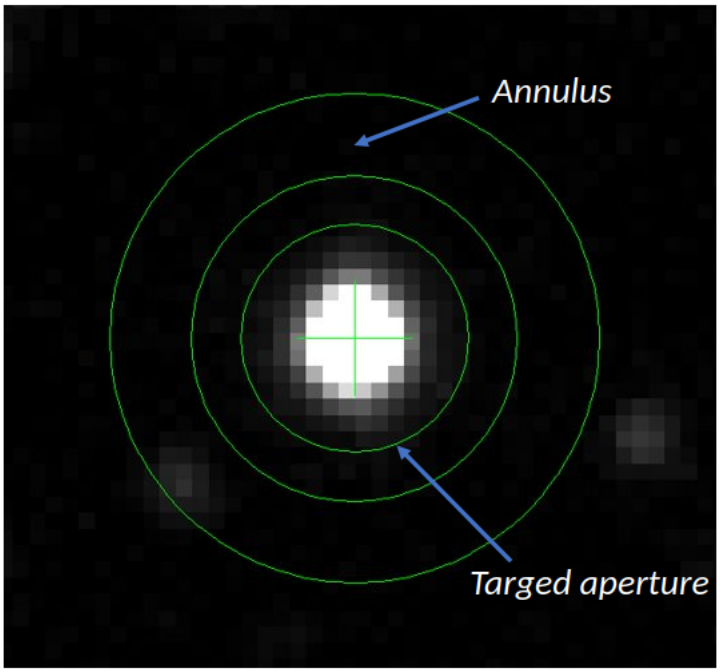

Figure 3.5: Principle of aperture photometry. the Inner circle represents the target aperture, and the middle and outer circles represents the annulus used to subtract the sky background contribution.

During my thesis, I used two softwares for the reduction and analysis of data gathered by the TRAPPIST telescopes:

Use of `AstroImageJ`

`AstroImageJ` (`AIJ`: Collins et al., 2017) is a powerful and versatile graphical user interface (GUI) based on Java and dedicated to image processing and light curves extraction in astronomy. It offers many features that made it the most used software in this work and by

most of the TFOP-SG1 members. The most important of these features include:

- read and write FITS images with standard headers. An example of a sequence of images read and displayed by `AIJ` is shown in Figure 3.6.

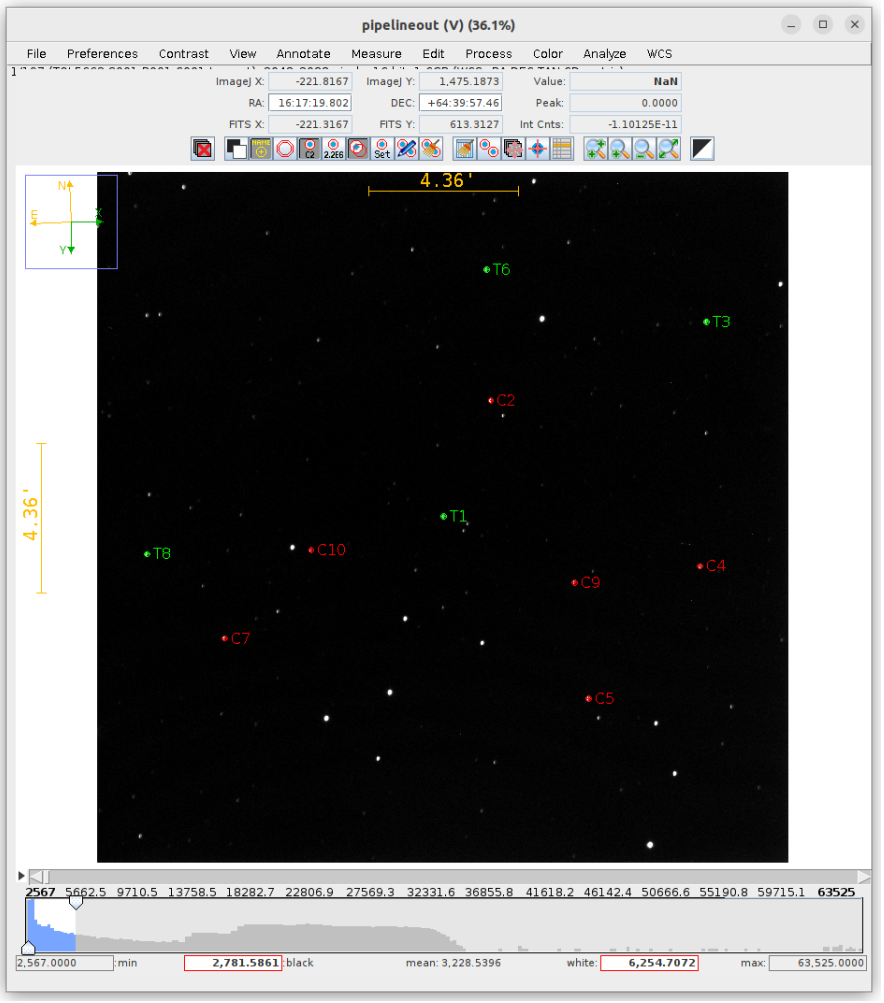

Figure 3.6: Example of a sequence of images of TOI-5663 displayed by `AIJ`The target star is usually labeled as T1 in green. In red are the comparison stars used for differential aperture photometry. Other stars in green were chosen for comparison but, afterwards, they were discarded as bad stars. Credit: made by `AIJ`.

- plate solving (i.e. determination of the right ascension and declination coordinates of all the pixels of the FITS image) FITS images on the basis of the Astrometry.net[9] web interface. This is important when the plate-solving does not work properly during observation.

- standard pretreatment of a sequence of images by *Bias* and *Dark* subtraction, and *flat-fielding*.

- graphical user interface to perform time-series differential multi-aperture photometry. It allows for easy setting of the aperture and annulus radii. The newer versions of `AIJ`

[9] http://astrometry.net/

(from v5.0 onwards) allows for the automated setting of aperture and annulus radii based on the radial profile of the target.

- user-friendly choice of comparison stars, for differential multi-aperture photometry, by simple clicks on the desired stars on the first image of the sequence displayed on the GUI. It then facilitates the selection of the optimal ensemble of comparison stars through to a box where stars can be selected (good stars) or deselected (bad stars) for comparison (see Figure 3.7). This allows for discarding bad comparison stars, that show either high variability or maximize the RMS of the target's differential light curve, without re-running photometry. The latest versions of `AIJ` allow for automated choice of comparison stars (along with the best apertures explained previously). Once the photometry is complete, it performs automated optimization by iterating over all the comparison stars to return the best sample based on the minimization of the target's light curve RMS using only the out-of-transit data to prevent erasing the transit signal.

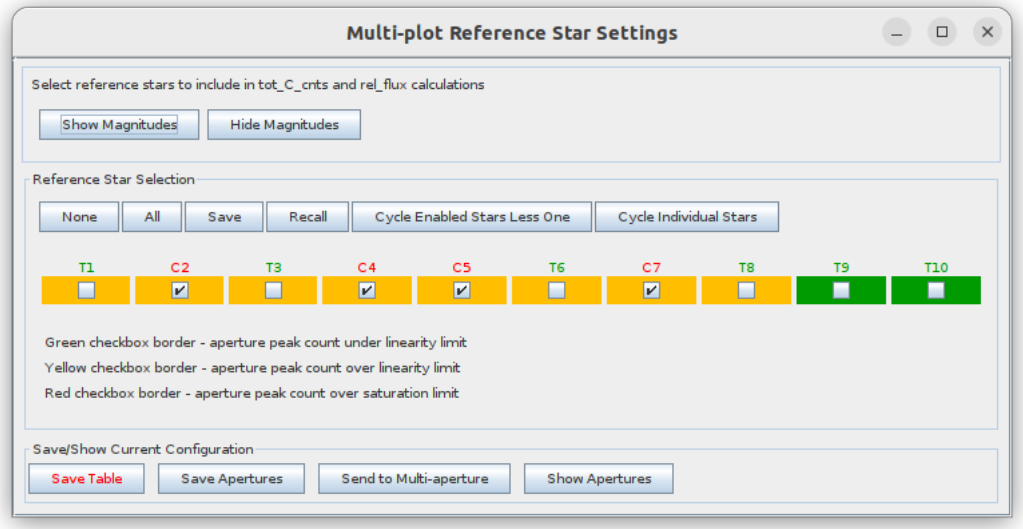

Figure 3.7: Panel where comparison stars and selected or deselected based on the minimization of RMS (see right panel of Figure 3.8). Considered comp stars are labeled as Cn in red while those that are discarded are labeled as Tn in green whith $T1$ is the target star (see also Figure 3.6). Credit: made by `AIJ`.

- provides tools for light curve fitting with simultaneous detrending. It implements the transit model of Mandel & Agol (2002) for an opaque spherical planet transiting a spherical star. The model is defined with six physical parameters (plus a baseline flux level, F_0): planetary radius in unit of stellar radius R_p/R_*, the semi-major axis of the planet in unit of stellar radius a/R_* (see Equation 1.4.19), the time of inferior conjunction T_C, the impact parameter b (see Equation 1.4.18) and the quadratic LD parameters u_1 and u_2. Transit modeling is conducted to compare with the parameters obtained by other TFOP-SG1 members or by the SPOC, though it does not account for uncertainties on the obtained fitted parameters. The best model is determined based

on the minimization of χ^2 statistic (see Equation 3.4.2). This modeling is performed for only one transit light curve, so the orbital period, along with the stellar radius, are set by the user from ExoFOP (obtained by SPOC). The latest versions of `AIJ` also perform automated optimization of the modeling by detrending the light curves by iterating over various detrending parameters and return the best sample based on the minimization of the BIC (Bayesian Information Criterion) (see details in Collins et al., 2017), a criterion that quantifies the goodness of the model fit to the detrended data. An example of the fitting panel and the obtained transit light curves are presented in Figure 3.8

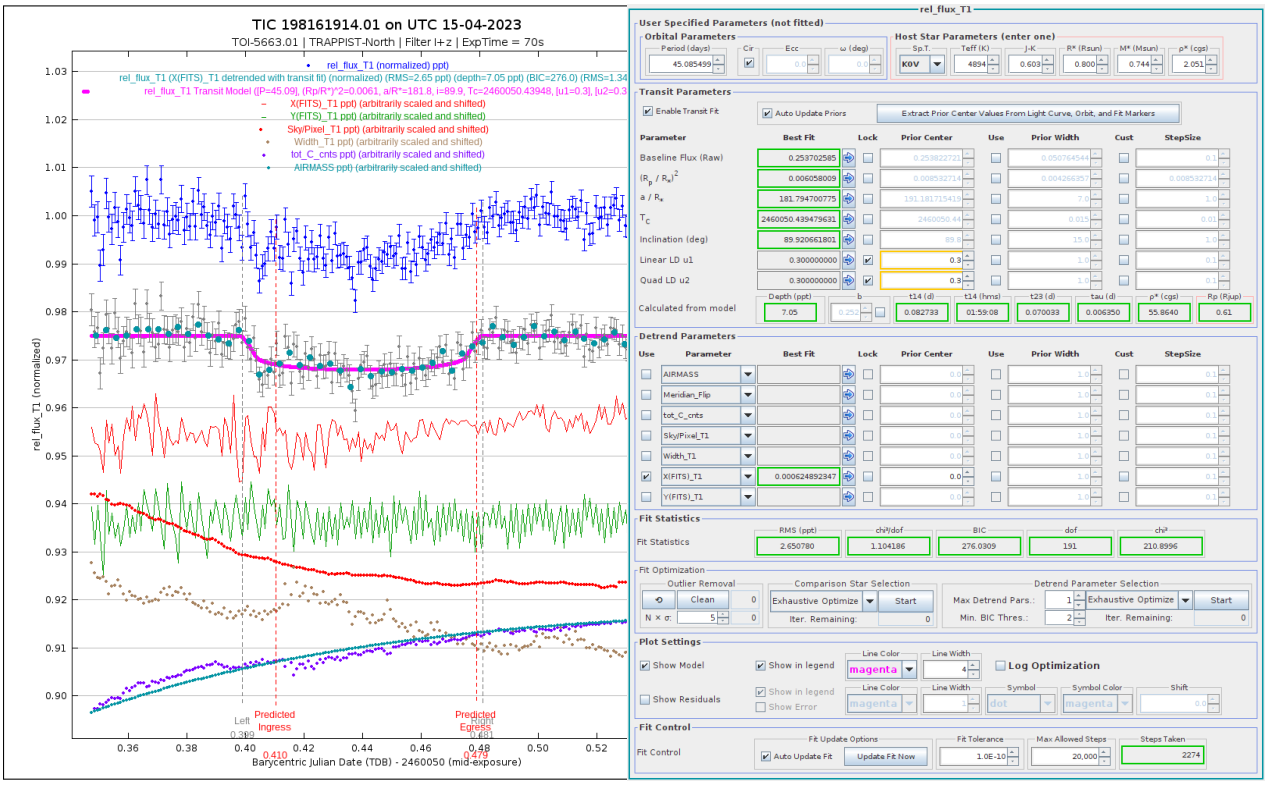

Figure 3.8: *Left*: Light curve of TOI-5663 obtained and plotted with `AIJ`. The upper light curve is the the raw one and the other just bellow is the detrended one with the best fit model inferred by `AIJ`. The other six parameters are the systematics plotted for checking if they have any correlation with the transit light curve. $X(FITS)\_T1$ and $Y(FITS)\_T1$ are the shifts of the star centroid on the CCD in pixels, $Sky/Pixel\_T1$ is the mean value of sky background over pixels within the annulus around the target T_1, $Width\_T1$ is the half width at half maximum of target's PSF, tot_C_cnts is the summation of the raw values of pixels within the target's aperture, and $AIRMASS$ as defined by Equation 3.2.3 and Figure 3.3. *Right*: Fitting panel with *User Specified Parameters* sub-panel where the orbital period and the stellar radius are set by the user, *Transit Parameters* sub-panel where the best fit parameters plus the parameters calculated from model are presented, *Detrend Parameters* sub-panel where detrending parameters can be set either manually by the user or automatically, *Fit Statistics* sub-panel presenting the statistics that quantify the goodness of the model fitting, and *Fit Optimization* sub-panel to remove the outliers and automatically optimize the comparison stars and the model fitting. Credit: made by `AIJ`.

- examines the stars near the target to search for eclipsing binaries that can be at the

origin of the *TESS* detection, and saves a summarizing report in single run. This feature is very useful for the NEB check for *TESS* candidates. An example of NEB check –for TOI-5663 b– is presented in Section 3.5.1 and further completed in Appendix A.

- saves figures and files that can be sent with the observation report to TFOP-SG1. These figures and files can also be read and replotted by `AIJ` with no need to re-run photometry. This feature is highly useful for *TESS* Science Team and TFOP observers, enabling them to check reports and access photometric data for analysis and publication.

Use of `prose`

`prose`[10] (Garcia et al., 2022) is a Python package designed to build modular image processing pipelines. It includes a default photometric reduction pipeline, which I used for reducing and analyzing the photometric data. It performs aperture photometry by applying a centroiding algorithm to accurately position apertures and annuli on the centroids of detected stars within the field. This process is repeated across a list of apertures to generate an array of light curves for all detected stars. To select suitable stars for differential photometry, `prose` includes a filtering option to retain only those stars whose median peaks are below 35K ADUs and more than three times the median background level. To perform the differential photometry in a fully automated manner for a specified target, `prose` features an option to use the Broeg et al. (2005) algorithm which selects the best comparison stars among the chosen ones. It also chooses the best aperture on the basis of minimizing the white noise of the target's light curve, estimated with the median standard deviation of data points within 5 minutes bins. The produced lightcurve can subsequently be detrended using a dedicated method that finds automatically the best detrending parameters and their polynomial orders. This detrended transit data can then be modeled using `Exoplanet`[11] (Foreman-Mackey et al., 2021). Finally, a report summarizing the observation and the obtained results can easily be created with a few simple commands. More information on this pipeline can be found in Garcia et al. (2022) and in the dedicated tutorial in `https://prose.readthedocs.io/en/latest/ipynb/casestudies/transit.html`.

3.4 Bayesian analysis

In this thesis, my analysis was limited to photometric data, specifically transits without RV data. For most of TOIs observed by TRAPPIST telescopes, I used only `AIJ` software to perform a preliminary transit fit to constrain the parameters of the planetary systems. However, it is sometimes necessary to perform tighter constraints of these parameters with their uncertainties. The *Markov Chain Monte Carlo* (*MCMC*) technique is the most widely

[10] `https://github.com/lgrcia/prose`
[11] `https://docs.exoplanet.codes/en/stable/`

used tool in exoplanets science for this purpose. *MCMC* technique is a Bayesian inference method, based on stochastic simulations, to get the posterior probability distribution functions (PDFs) of the parameters assuming a given model that is fitted to the data (here I am generally explaining the MCMC technique to properly fit any model to a given data set). It is then based on the Bayes's theorem (Bayes & Price, 1763) defined as follows (Gregory, 2005):

$$P(M|D) = \frac{P(D|M)P(M)}{P(D)} \tag{3.4.1}$$

with $P(M|D)$ is the probability that the set of model parameters' values M is correct, given the data D, $P(D|M)$ is the probability for the set of model parameters' values M to produce the data D, what is called the likelihood, $P(D)$ is the integration of the $P(D|M)$ over all values of the model parameters, what is called the marginal likelihood of the model. This is the metric used to compare the posterior probability of different models, and $P(M)$ encodes any previous beliefs about the model parameters i.e. the probability of the model. The *MCMC* technique is a powerful method for evaluating the posterior PDFs of all model parameters, allowing the determination of median values, uncertainties, and covariances of these parameters and any derived physical parameters.

The *Markov chain* is a sequence of states where a given state depends only on the state which is directly preceding it and nothing else, and the term *Monte Carlo* means that the transition from one state to another is a random process. I explain the basic of this algorithm in the following section.

3.4.1 Use of `EXOFASTv2`

Practically, in my thesis, I used the `EXOFASTv2` fitting software package (Eastman et al., 2013, 2019), which implements the *MCMC* technique for modeling exoplanetary systems (transits, eclipses, RV, SED in addition to stellar evolution models). `EXOFASTv2` is built on the IDL astronomy library (Landsman, 1993). It adopts the Metropolis-Hastings algorithm (Metropolis et al., 1953; Hastings, 1970) to sample $P(M|D)$. The code starts with a set of trial parameters (i.e. starting values) defining the model and evaluates the *'merit function'* (noted here as χ^2_{tot}) for this trial set as follows:

$$\chi^2_{tot} = \sum_{i=1}^{n} \frac{(M_i - D_i)^2}{\sigma_i^2} + \sum_{j=1}^{m} \frac{(P_j - \mu_j)^2}{\sigma_{\mu_j}^2} \tag{3.4.2}$$

with the first factor of the right term is the *chi-square*, where D_i is the data point i with an associated uncertainty σ_i, and M_i is the model on the point i. The second factor is the contribution of the parameters defining the model, on which Gaussian priors are applied where P_j is the parameter j from the model M, μ_j is the mean value of the prior and σ_{μ_j} its associated standard deviation. The smaller χ^2_{tot}, the larger the posterior probability. After that, the code randomly steps to another set of parameters, and recalculates the χ^2_{tot} for this

new set of parameters. Then, it defines the posterior probability ratio as (see demonstration in Eastman et al., 2013):

$$\tau = \frac{L_2}{L_1} = e^{[\chi^2_{tot}(M_1) - \chi^2_{tot}(M_2)]/2} \tag{3.4.3}$$

It should be noted that $P(D|M)$ is the likelihood L, it is thus proportional to $e^{(-\chi^2_{tot}/2)}$, and the parameters randomly perturbed at each step of the MCMC are called the 'jump parameters'. The acceptance or rejection of a new step is based on the *likelihood ratio*, τ. A random number uniformly distributed between 0 and 1 is drawn. If this number is larger than τ, the new step is rejected and the current set of parameters is a duplication of the previous set. In the other case, when the number is lower than τ, the new step is accepted. If τ is greater than 1, the new step is always accepted. This process is iteratively repeated until a smooth distribution of each parameter is obtained, i.e. until the chains converge to a stationary target distribution from which fitted system parameters can be inferred.

Regardless of the step size and its direction, the chains of the fitting algorithm will always converge to the target posterior probability distribution. However, the speed of convergence presents a general challenge in MCMC analyses. If the steps are too small, they are mostly accepted but this is time consuming because large number of steps are required (i.e slow convergence). This also means that many adjacent steps are accepted, leading to highly correlated chains (not well-mixed chains), inefficiently exploring the parameter space. Conversely, if the steps are too large, they are mostly rejected and lots of models are wastefully computed, which also slows down the convergence. `EXOFASTv2` comes with the Differential Evolution Markov Chain (DE-MC, see e.g. Ter Braak, 2006; Johnson et al., 2011) technique to choose the optimize step sizes and speed up the convergence. DE-MC generally runs a number of chains equal to twice the number of free parameters, i.e. parameters that are not fixed or constrained by a prior information (in the Bayes's theorem this is represented by $P(M)$), and uses the differences between parameter values of two randomly selected chains to determine the next step and direction. More details on this method can be found in Ter Braak (2006) and Eastman et al. (2013).

To ensure the convergence of the algorithm, i.e. that the chains have explored the parameter space sufficiently and are providing a representative sample from the posterior PDFs, `EXOFASTv2` uses two diagnostic parameters: the first is T_z, which is the number of independent draws (i.e uncorrelated samples) in the *MCMC* analyses. By default, T_z is set to a minimum value of 1000, meaning that each model parameter must have a minimum number of independent draws greater than 1000; the second diagnostic parameter is the Gelman Rubin statistic ($\hat{R}_\nu$, Gelman & Rubin, 1992) used to check if the chains have converged to the same target posterior distribution. $\hat{R}_\nu$ compares the variance within each chain (within-chain variance) to the variance between all chains (between-chains variance). By default, $\hat{R}_\nu$ is set to a maximum value of 1.01. Once this condition is applied (i.e.$\hat{R}_\nu < 1.01$), this indicates that the chains have converged to a stable posterior distributions. Once the two conditions

are verified ($T_z > 1000$ and $\hat{R}_\nu < 1.01$), `EXOFASTv2` stops simulations to statistically infer the fitted, and their derived, parameters of the system. Of course, the statistical inference is done after discarding the early samples (usually referred to as the "burn-in" phase) during which the code is still affected by the input values of the model's parameters and try to stabilize and adjust the structure of the parameters space.

Fitting transits

As previously noted, this thesis solely utilized photometric transit data. `EXOFASTv2` generates transit models from Mandel & Agol (2002); Agol et al. (2020) with priors on quadratic limb darkening parameters (see Section 1.4.11) by interpolating the limb darkening models of Claret & Bloemen (2011) and Claret (2017) at each step in the log_{10} of the stellar surface gravity ($logg_*$), the stellar effective temperature (T_{eff}), and metallicity of the star ($[Fe/H]$). `EXOFASTv2` fits for the transit time T_c, planet to host star radii R_p/R_*, cosine of the orbital inclination $\cos(i)$, log10 of the orbital period P, limb-darkening coefficients (u_1, u_2) and the baseline flux F_0.

Priors

In the simplest case, when fitting transits observed in different filters, priors must be applied correctly on at least the following parameters:

- upper and lower limits on the orbital period P and the transit time T_c, generally taken from ExoFOP.
- Gaussian priors on the stellar radius R_*, mass M_* and effective temperature T_{eff} from independent analyses (e.g. SED fitting, see hereafter).
- Gaussian priors on the quadratic limb-darkening parameters (u_1, u_2) for each bandpass filter.
- optional starting value on R_p/R_*.

Stellar parameters

As discussed in Section 1.4, accurate characterization of the host star is essential for precise determination of the planetary parameters. The stellar parameters most cared about are at least M_*, R_* and T_{eff}. If these parameters are unavailable or unreliable, various techniques are available for their determination. As I focused on small stars (M dwarfs), I used empirical relationships appropriate for these stars, meanly Mann et al. (2015) and Mann et al. (2019) relations to determine the stellar radius and mass, respectively, from the absolute magnitude[12] in the 2MASS K band (i.e. M_K) of the host star. Additionally, the effective temperature T_{eff} of the star can be determined from the color indexes V-J and J-H using Mann et al. (2015) relations.

[12]The absolute magnitude of a star is its visual magnitude when supposed at 10 parsecs.

Within `EXOFASTv2`, it is possible to fit for the Spectral Energy Distribution (SED) of the star separately or jointly with transits fitting. The SED is a measure of the star's bolometric flux. `EXOFASTv2` uses the *NextGen* stellar atmosphere models (Allard et al., 2012) to fit for SED. For this, different broad band photometric measurement of the host star are taken from many catalogs, such as the JHK_S magnitudes from *2MASS*, the W1–W4 magnitudes from *WISE* (Cutri et al., 2013), the $G_{\rm BP}G_{\rm RP}$ magnitudes from *Gaia* DR3 (Gaia Collaboration, 2020), and the *ugrizy* magnitudes from *Pan-STARRS* (Chambers et al., 2016). The SED provides strong constraints on T_{eff}, V-band extinction A_V and $(R_*/d)^2$, with d being the distance to the star. R_* is determined if a prior on the parallax (i.e. from *Gaia* DR3 (Gaia Collaboration, 2020)) is supplied. When fitting for SED, priors must be applied on some parameters as follows:

- starting values on T_{eff} and R_*, generally taken from the TIC catalog (Stassun et al., 2018).
- upper limit on the V-band extinction A_V, generally from the galactic dust map (Schlafly & Finkbeiner, 2011b).
- Gaussian priors on the metallicity *[Fe/H]*, determined from spectroscopic observation, and on the parallax of the star from i.e. Gaia DR3 (Gaia Collaboration, 2020).

As for the mass of the host star, it is also possible to determine this parameter within `EXOFASTv2` simultaneously with the SED and the transits fitting. `EXOFASTv2` uses the MESA Isochrones and Stellar Tracks (MIST) (see Paxton et al., 2011, 2013, 2015; Dotter, 2016) for this purpose. This parameter can even be improved if the density of the star is strongly constrained from the transits.

3.5 Observation goals

For each TOI, the observations goals are detailed in the *TTF* comment (see Figure 3.1), which summarizes all the previous observations (if any) and specifies what is needed next for every single planet candidate. In this section I will discuss the main observation cases and their goals as encountered during my thesis.

3.5.1 Confirming the on-target origin of the signal

Confirming the transit event on target and/or checking for NEBs is one of the most required observations in the *TTF* comments. This consists of confirming whether the transit event occurs on the original target star or it is coming from nearby stars (nearby eclipsing binaries) contaminating the *TESS* aperture. This is required for TOIs that are just released and have never been observed before from ground. When it is the case, I used the filter that offers the highest SNR without saturating the CCD detector. This filter depend on the spectral type of the target. As most of the targets observed by TRAPPIST telescopes are M dwarfs, the most used filter during my thesis was *I+z*.

How NEBs check is performed?

First, it must be known that if a transit occurs on a nearby star, its depth must be different from the predicted target depth in the *TTF*. This is when the magnitude of the nearby star is different from that of the target. The dimmer (higher *TESS* mag) the nearby star is, the deeper its needed transit depth in order to produce the target depth measured by *TESS*, and vice versa. The predicted nearby star depth is calculated as follows (see the *TFOP SG1 Observation Guidelines*: https://astrodennis.com/TFOP_SG1_Guidelines_Latest.pdf):

$$Depth_{NEB} = \frac{Depth_{target}}{10^{-\frac{\Delta mag}{2.5}}} \tag{3.5.1}$$

with Δmag is the magnitude of the nearby star minus that of target in the *TESS* band. It should also be known that the fainter a nearby star is, the higher the scatter (i.e RMS) in its light curve. Whether a nearby star is cleared or not, depends on the ratio $Depth_{NEB}/RMS$ (both in *ppt*). In this regard, many cases are considered and as explained bellow:

Cleared	: if $Depth_{NEB}/RMS \geq 5$
Likely cleared	: if $3 < Depth_{NEB}/RMS < 5$
Cleared-too faint	: if $Depth_{NEB}/RMS \geq 1000$. This means that the nearby star is too fain to cause the *TESS* event detection.
Not cleared-flux too low	: if there is not enough flux in the aperture.
Not cleared	: if none of the previous conditions is valid.

This operation is performed using the `AIJ` software on the basis of a "*AIJ apertures*" file (see column "name" in Figure 3.1). For each TOI, the *TTF* presents this file that contains the equatorial coordinates (*ra,dec*) of stars that are close and bright enough to cause the *TESS* detection. It also contains the *TESS* magnitudes of all these stars. `AIJ` gets the (*ra,dec*) coordinates (to place the apertures) of the nearby stars and performs simultaneous multi-aperture differential photometry for all of them. Once the photometry is complete, a NEB check can be performed by simple commands and a summary report can be saved.

Example 1: Transit event confirmed on target (TOI-5663 b)

This example considers the case where the transit event is detected on target and all the nearby stars are cleared as not being the source of the *TESS* detection. It is the *TESS* candidate TOI-5663 b (TIC 198161914.01) that was predicted to show a transit signal with a depth of 8.1 *ppt* and orbital period of 45.08 days. This target was observed by TRAPPIST-North in *I+z* filter on 15 April, 2023. Uncontaminated differential aperture photometry with `AIJ` shows an ∼9 min earlier 8 *ppt* U-shaped transit on target (see left panel of Figure 3.9). The right panel of Figure 3.9 shows the field of view of the target (labeled at the center as T1) with all the nearby stars within 2.5' radius from the target. NEBs check of this target

shows no obvious NEB as shown in Appendix A. However, it should be noted that as of this writing, this transit signal still requires confirmation of its achromatic nature to confirm its planetary origin.

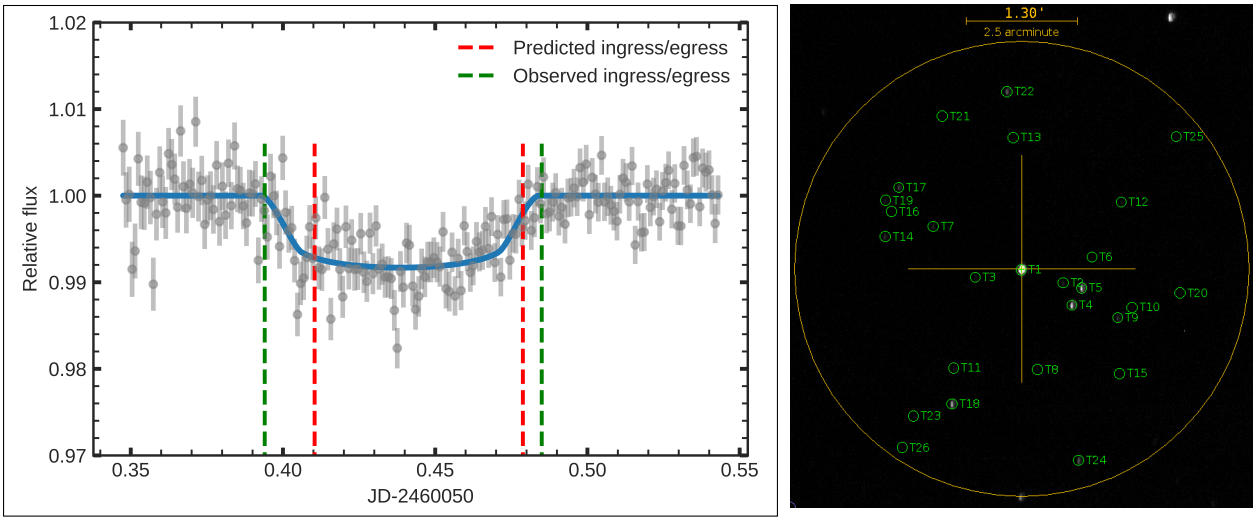

Figure 3.9: *Left*: Transit light curve of TOI-5663 b (TIC 198161914.01) observed by TRAPPIST-North on 15 April, 2023, in *I+z* filter with an exposure time of 70 seconds. The gray points show the photometric measurements. The solid blue line is a preliminary model fit of the transit with `AIJ` to extract the transit parameters. The transit was detected on target ∼9 min earlier than predicted with the same depth as was predicted. *Right*: target and nearby stars within 2.5' radius area around the target (T1). The stars are labeled as Tn, with n=1 for the target and from 2 to N for the N nearby stars.

Example 2: Identification of a NEB

Here I present an example of a NEB identification. It is for TOI-2680 b (TIC 219366908.01) that was observed by TRAPPIST-South on 23 October, 2021, in *I+z* filter. In the *TTF*, TOI-2680 was predicted to show a transit depth of 3.7 *ppt*, but TRAPPIST-South observation showed no transit event on the target. Instead, a clear V-shaped 25 *ppt* deep transit was detected at the predicted time on the nearby star T2 (TIC 219366907, at 17.44" from T1, see Figure 3.10). This TOI was then retired a NEB in the *TTF*.

3.5.2 Checking the achromatic nature of the signal

As I explained in Section 1.6.4, transits due to blended eclipsing binaries (BEB) are expected to have chromatic depths. This means that the transit depth changes from a filter color to another (see Section 1.6.4). This observation is usually required when a transit event has already been confirmed to occur on target with a determined period. The filter color to be used in this case must be different from the filters used in the previous observations.

Example: TOI-5681 b discarded as BEB

Here, I present TOI-5681 b (TIC 207439380.01), which was discarded as BEB. According to the *TTF*, this star was predicted to show a transit depth of 11.6 *ppt*. It was observed

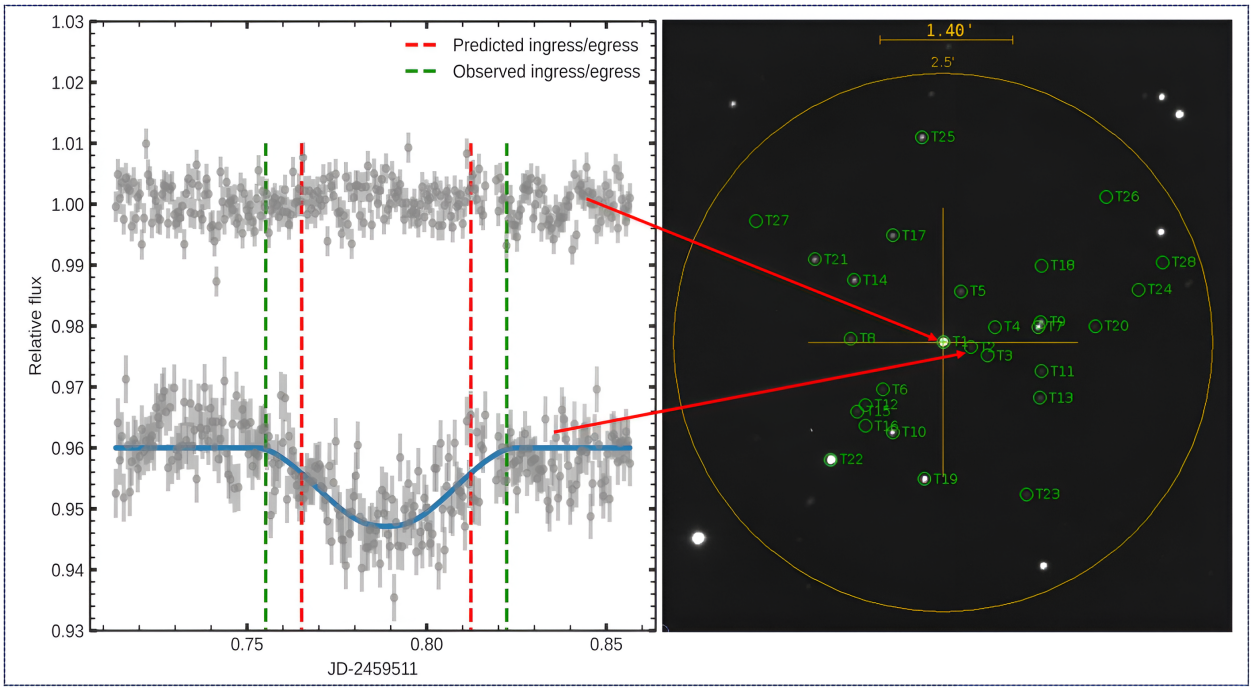

Figure 3.10: *Left*: The top light curve is for the original target TOI-2680 that was predicted to have transit depth of 3.7 *ppt*. The bottom light curve shows a clear deep transit of the nearby star T2 (TIC 219366907, at 17.44" from T1). *Right*: The field of view of the target and its nearby stars within 2.5' radius area. The data reduction, aperture photometry and NEB check were performed using `AIJ`.

by TRAPPIST-North in z' filter on 31 March, 2023. A timly V-shaped transit (see Figure 3.11) was detected with a depth of 19.1 *ppt*. As shown in Table 3.1, other observations show a strong chromaticity in different filters, especially in *gp* filter where no transit were detected. These findings serve as good hints that the transit event detected by *TESS* on the star TOI-5681 is due to BEB or HEB.

3.5.3 Searching for transit timing variations

Transit timing variations (TTVs) indicate the existence of additional planets in the system. Observations to check for TTVs are generally requested when a transit signal does not appear exactly at the predicted time. These variations are due to the fact that orbits of the planets are not exactly periodic (Section 1.4.2) because of gravitational interaction between at least two planets around the same host star. This is a powerful technique to discover additional, even not transiting, planets in the system. A best example of this case is the TOI-2015 b, which has been detected by *TESS* with a transit depth and orbital period of ∼7.2 *ppt* and ∼3.3491 days, respectively. Its transit signal has been confirmed by ground-based observations to occur on target but with large TTVs. This TOI has been classified as high priority target to observe as many as possible. It was observed in more than 32 nights by TFOP-WG members, including with TRAPPIST-North and 4 nights with TRAPPIST-South, respectively. In some observations, no transit of TOI-2015 b (with out-of-transit

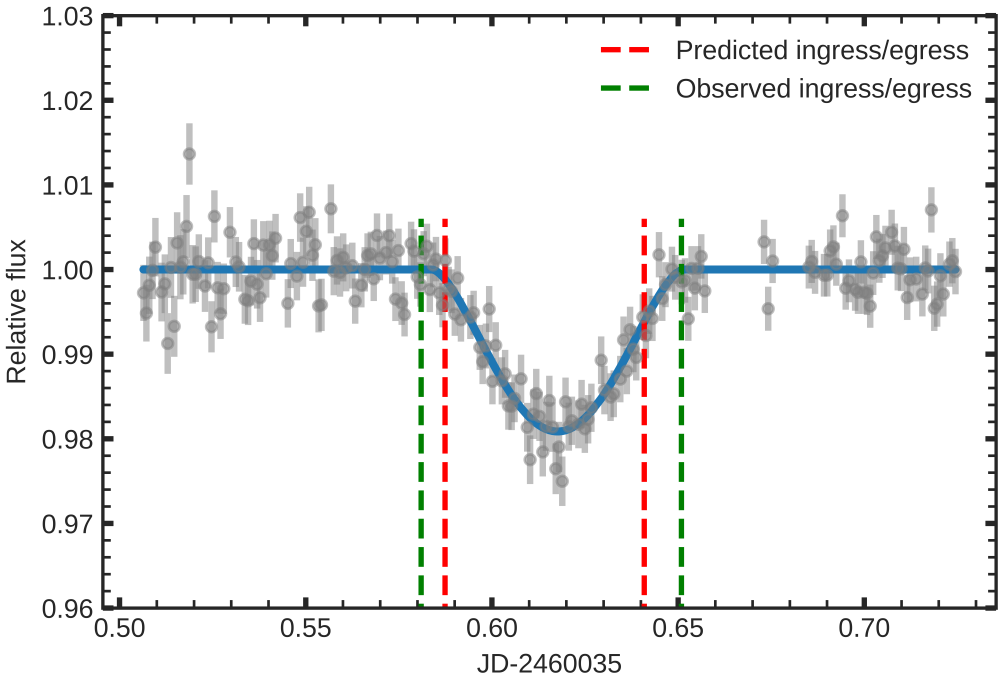

Figure 3.11: Light curve of TOI-5681 b observed by TRAPPIST-North on 31 March, 2023, in *z'* with an exposure time of 55 seconds. The blue line represents a preliminary model of the transit-like signal by `AIJ`. The transit have been found V-shaped with a depth of 19.1 *ppt* while it was predicted to be 11.6 *ppt*. Other observations in different filters showed very different depths. Giving these findings, this target was retired as BEB.

less than one hour) has been detected. In other observations, the transit was detected with variations in the transit timing between what was predicted and observed. However, intensive follow-up observations have been performed to detect the transit of the second planet, but no transit has been detected. This indicates that the second planet in the system is not transiting (low transit inclination). A discovery paper of this system is being prepared by K.Barkaoui et al. Figure 3.12 shows the light curves gathered by TRAPPIST telescopes along with other transits taken from ExoFOP, where I considered only some cases where the transit signals were detected. The corresponding TTVs are shown in Figure 3.13.

3.6 Observation statistics

3.6.1 On-sky positions

From September 20, 2019, to February 28, 2024, over than 300 TOIs have been observed (some TOIs observed on more than one night) by the TRAPPIST-North telescope. 260 reports of conclusive data were submitted to ExoFOP for 215 TOIs. The reduction and analyses of the data is a collaborative work of the TRAPPIST team members and I reduced more than 100 datasets from the TRAPPIST-North telescope, and over 43 datasets for 42 TOIs from TRAPPIST-South telescope. The list of these TOIs and their current status are presented in Appendix D.

Figure 3.14 displays a sky map showing the locations of the host stars observed by both

Date (UT)	Filter	Instrument	Transit depth (in *ppt*)
2022-07-21	i'	LCO-McD (0.4 m)	5
2022-07-21	r'	CDK700 (0.7 m)	3
2022-07-22	R	GVO-Ted14 (0.36 m)	3
2022-07-29	Ic	OAAlbanya (0.4 m)	12
2022-08-13	gp	LCO-HAL (0.4 m)	00
2022-08-08	zs	LCO-TEID (0.4 m)	15-18
2022-07-22	ip	LCO-McD (0.4m)	15

Table 3.1: Table summarizing ground-based time-series photometric observations of TOI-5681 b. The transit depth shows a very strong chromaticity, meaning that the transit event is due to a BEB or hierarchical EB. The uncertainties on the values of the transit depths are not provided because the data analyses are performed using `AIJ` which does not present them. Credit: These observations were taken from ExoFOP.

TRAPPIST-North and TRAPPIST-South. Stars observed by TRAPPIST-North are uniformly spread over the northern hemisphere. Table 3.2 presents the dispositions of these TOIs observed by both telescopes. Below is the meaning of the key words of the dispositions presented in Table 3.2:

- **VP**: *"Validated"* Planets without mass measurement from RV observations. The *validation* consists of discarding all possible false positives using multi-color photometric observations to show that the transit depths are achromatic, adaptive optic observations to confirm that the host star is single, and spectroscopic observation to further characterize the host star and also confirm that there is no secondary spectrum in its spectra. This might also include statistical *validation*, checking that the transit signals show a higher probability of being due to a transiting planet rather than false positives.
- **P**: *"Confirmed"* Planets that have been *"validated"* and subsequently received mass measurements from RV observations. This is the case where the mass was consistent with a planetary-mass companion but not stellar- or substellar-mass companion.
- **PC**: Planet Candidates that still require follow-up, as previous observations have been inconclusive.
- **VPC+**: verified planet candidates, that have been found achromatic (i.e.transit signals have been confirmed on targets with no depth chromaticity).
- **VPC-**: Verified Planet Candidates whose photometry is contaminated by nearby stars.
- **APC**: Ambiguous Planet Candidate, where initial ground-based photometry gives some evidence that the *TESS* detection might be a false positive but there is no firm conclusion.

- **PPC**: Promising Planet Candidates, where all nearby stars have not been rigorously ruled out as being the potential cause of the *TESS* detection, but that follow-up observations have found no NEBs in obvious nearby sources.
- **CPC**: Cleared Planet Candidate, where the transit depth detected by TESS is too shallow for ground-based photometry to detect, yet follow-up observations have ruled out all nearby stars as potential sources of the *TESS* detection.
- **NPC**: Nearby Planet Candidates, where transit signals are detected on a nearby star to the target, and show depths consistent with those of a transiting planet.
- **EB/SEB1**: for the TOIs that have been identified as **Eclipsing Binaries**. SEB1 is for TOIs that have subsequently been found as **Spectroscopic Binaries single-lined** by SG2 (see Section 1.5.5) whose radial velocity is too large and then not consistent with planetary companion.
- **NEB**: for Nearby Eclipsing Binaries that have been identified as the source of *TESS* detection.
- **BEB/SEB2**: for Blended Eclipsing Binaries, where transit depths have been found chromatic. SEB2 is for TOIs that have subsequently been found as '**Spectroscopic Binaries multi-lined**' by SG2.
- **FA**: means that the *TESS* detection was a **False Alarm** detection and with ground-based follow-up revealing no transit.

Telescope	P	VP	PC	VPC+	VPC-	APC	PPC	NPC	EB/SEB1	NEB	BEB/SEB2	FA
TRAPPIST-N	11	8	6	155	13	1	1	1	4	5	7	3
TRAPPIST-S	0	1	2	27	3	0	0	1	0	5	2	1
Total	11	9	8	182	16	1	1	2	4	10	9	4

Table 3.2: Status of all the TOIs observed by TRAPPIST-North and the TOIs I reduced from TRAPPIST-South. The lists of these TOIs are presented in Appendix D.

3.6.2 Stellar and planetary properties

As explained in previous chapters, *TESS* focuses on detecting small planets ($R_p \leq 4\,R_\oplus$) orbiting M type stars. The small size of these stars facilitates the detection and characterization of small transiting planets around them. When preparing the observation schedule, high priority is given to these types of stars especially if their planet candidate(s) are potentially rocky.

Figure 3.15 shows the distribution of the planets radii and the spectral types of their host stars observed by TRAPPIST-North. Out of 215 exoplanets whose observations were

conclusive, 32.7% of them (69 planets) transit stars of spectral type M, and 26.1% (55 planets) of them transit stars of spectral types K. As for the sizes of the planets, 16.7% of the planets (36 planets) have sizes smaller than $4\,R_{\oplus}$.

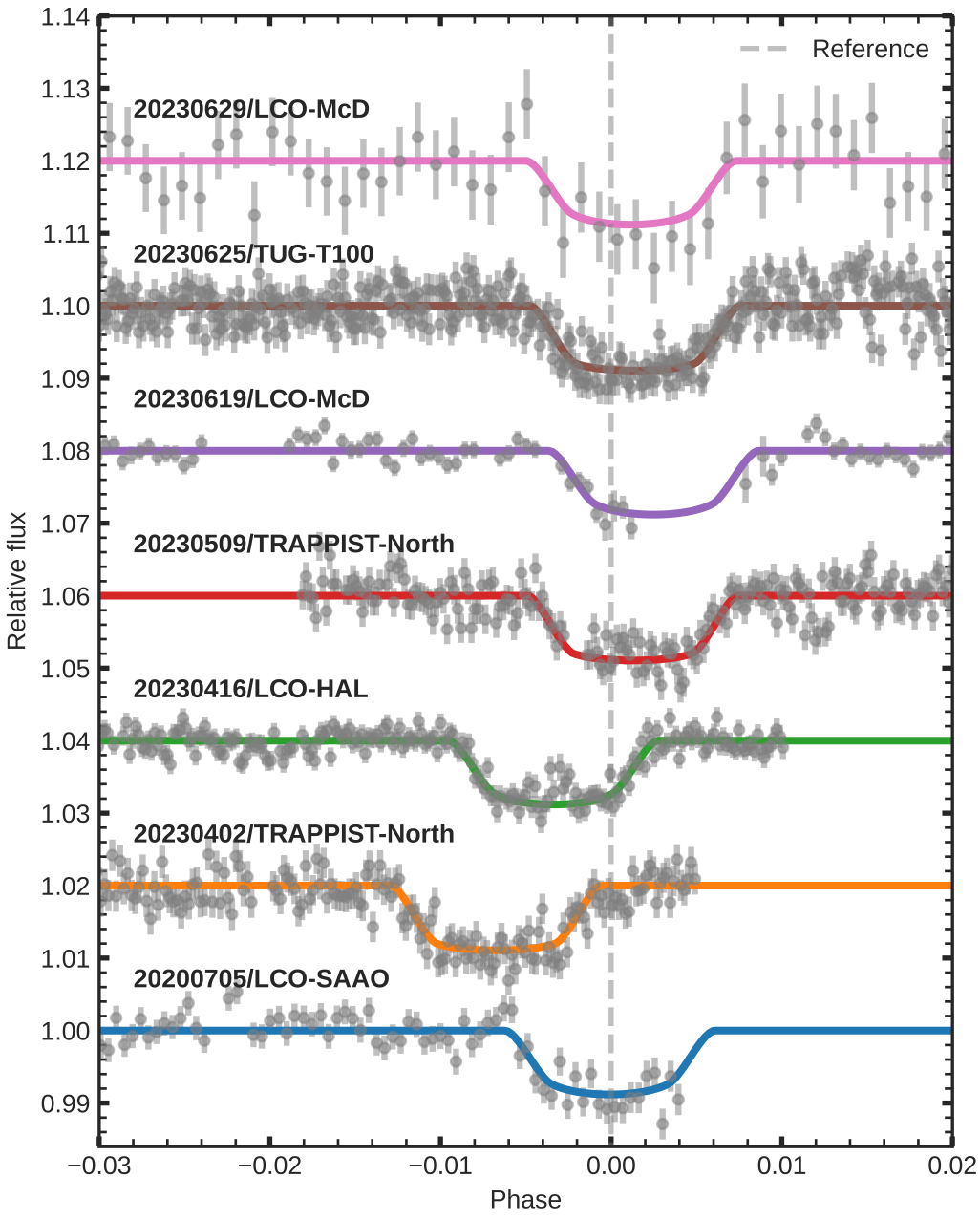

Figure 3.12: Phase-folded detrended ground-based transit light curves of TOI-2015b. The gray points show the observed data and the solid-colored lines corresponds to the best-fit transit models from `EXOFASTv2`, which gave an orbital period of 3.348894±0.000043 days. The vertical line is just to show the shift of transits with respect to the bottom transit center, showing clear TTVs.

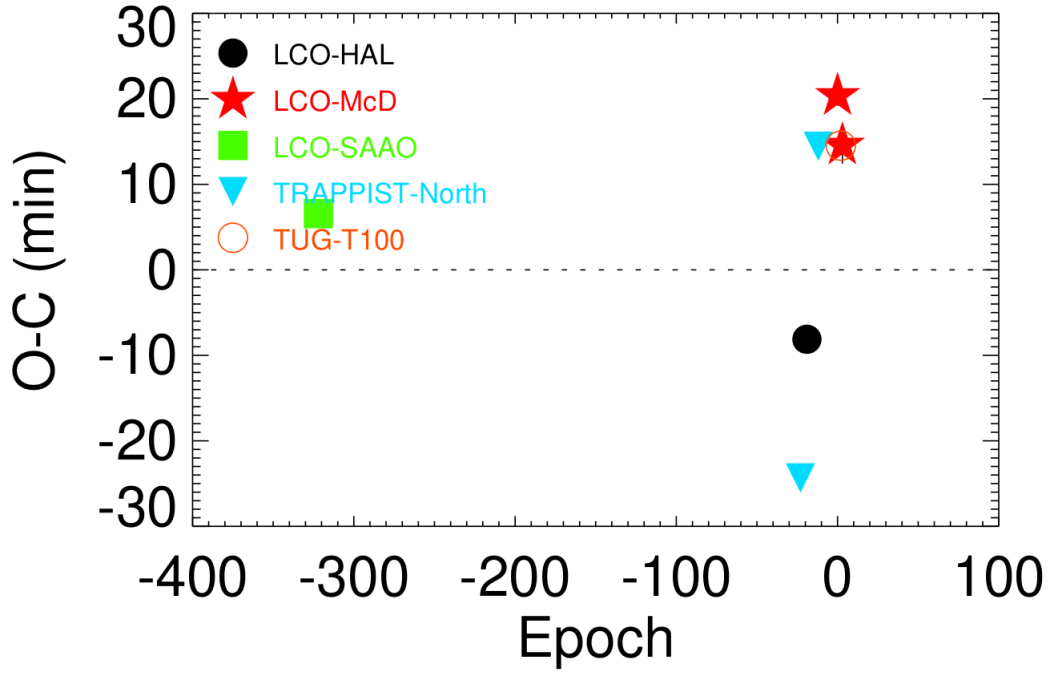

Figure 3.13: Transit Timing Variations of TOI-2015 b plotted as function of epoch number. Each symbol represents a different telescope.

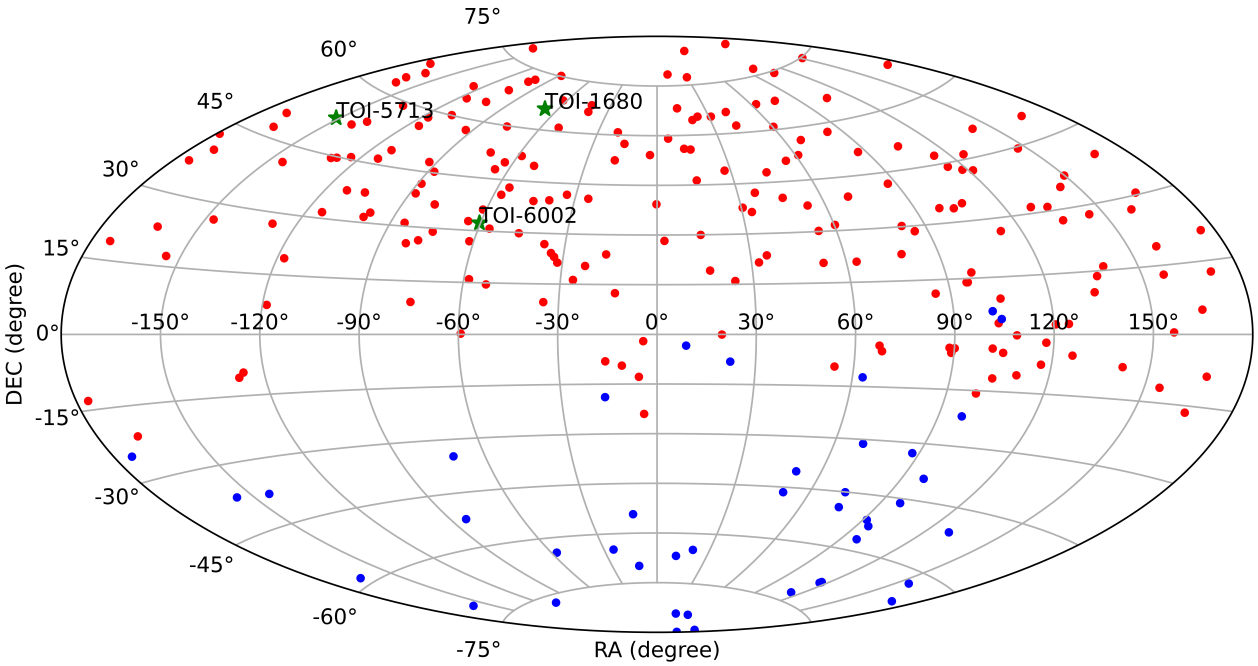

Figure 3.14: 2D sky map with the location of the stars observed by TRAPPIST-North (215 stars in red dots) from 02 September, 2019 to 28 February, 2024, and with TRAPPIST-South (42 stars in blue dots).

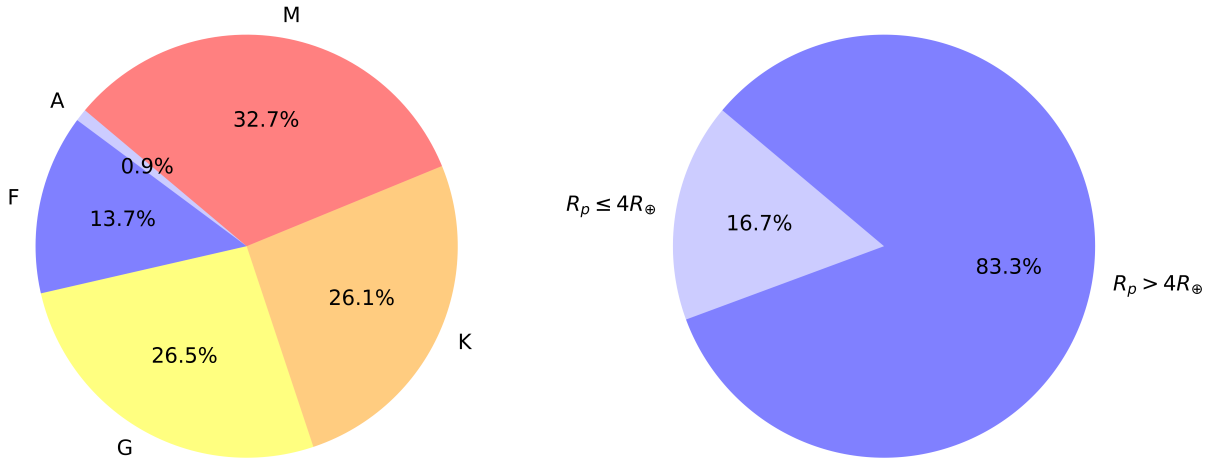

Figure 3.15: Percentages of spectral types of stars (*left*) and radii of the planets (*right*) monitored by TRAPPIST-North.

Chapter 4

Results

.

4.1 TOI-1680 system

TOI-1680 b is a super-Earth planet orbiting a mid-type M-dwarf star located 37.14 pc away, in the northern continuous viewing zone of *TESS*. It was fist detected by *TESS* and validated by ground-based follow-up photometry from various facilities including TRAPPIST-North telescope, and high resolution imaging. Our analyses showed that the host star, TOI-1680, has a radius of 0.2100 ± 0.0064 $R_{\odot}$, a mass of mass of 0.1800 ± 0.0044 $M_{\odot}$, and an effective temperature of 3211 ± 100 K.

Joint analyses of the *TESS* and ground-based photometric data, using `EXOFASTv2`, showed that the planet TOI-1680 b has a radius of $1.466^{+0.063}_{-0.049}$ $R_{\oplus}$, an orbital period of $4.8026345^{+0.0000040}_{-0.0000039}$ days, and an equilibrium temperature of 404 ± 14K, assuming no albedo and perfect heat redistribution. The mass of the planet is not determined yet because there are no RV observations. According to its location in the *radius* and *density valleys*, TOI-1680 b is assumed to have a rocky composition. Still, using the relation of Chen & Kipping (2017), its mass is estimated to be $3.18^{+1.1}_{-0.69}$ $R_{\oplus}$. This mass would result in a reflex motion of the host star with a semi-amplitude of $3.78^{+1.1}_{-0.82}$ ms^{-1}. Such reflex motion could be detected with the MAROON-X instrument installed on the 8.1-m Gemini North telescope (Seifahrt et al., 2020), which will determine the mass of the planet and then confirm its bulk composition. This planet has a transmission spectroscopy metric (TSM) of 7.82, with 10 being the threshold for this size range of this planets. Thus, TOI-1680 b, could be a promising candidate for atmospheric characterization with the James Webb Space Telescope (JWST), especially as the system is located near the JWST CVZ.

A&A 677, A31 (2023)
https://doi.org/10.1051/0004-6361/202347040

Astronomy & Astrophysics

TESS discovery of a super-Earth orbiting the M-dwarf star TOI-1680

M. Ghachoui[1,2], A. Soubkiou[2,3,4], R. D. Wells[5], B. V. Rackham[6,7,⋆], A. H. M. J. Triaud[8], D. Sebastian[8], S. Giacalone[9], K. G. Stassun[10], D. R. Ciardi[11], K. A. Collins[12], A. Liu[6], Y. Gómez Maqueo Chew[13], M. Gillon[1], Z. Benkhaldoun[2], L. Delrez[1,14], J. D. Eastman[12], O. Demangeon[3,4], K. Barkaoui[1,6,15], A. Burdanov[6], B.-O. Demory[5], J. de Wit[6], G. Dransfield[8], E. Ducrot[16,⋆⋆], L. Garcia[1], M. A. Gómez-Muñoz[17], M. J. Hooton[18], E. Jehin[14], C. A. Murray[18], P. P. Pedersen[18], F. J. Pozuelos[19], D. Queloz[18], L. Sabin[17], N. Schanche[5], M. Timmermans[1], E. J. Gonzales[20], C. D. Dressing[9], C. Aganze[21], A. J. Burgasser[21], R. Gerasimov[21], C. Hsu[21,22], C. A. Theissen[21], D. Charbonneau[12], J. M. Jenkins[23], D. W. Latham[12], G. Ricker[7,24], S. Seager[6,25,26], A. Shporer[26], J. D. Twicken[27], R. Vanderspek[26], J. N. Winn[28], K. I. Collins[29], A. Fukui[30,31], T. Gan[32], N. Narita[30,33,31], and R. P. Schwarz[12]

(Affiliations can be found after the references)

Received 29 May 2023 / Accepted 3 July 2023

ABSTRACT

We report the discovery by the TESS mission of a super-Earth on a 4.8-days orbit around an inactive M4.5 dwarf (TOI-1680), validated by ground-based facilities. The host star is located 37.14 pc away, with a radius of 0.2100 ± 0.0064 $R_\odot$, mass of 0.1800 ± 0.0044 $M_\odot$, and an effective temperature of 3211 ± 100 K. We validated and characterized the planet using TESS data, ground-based multi-wavelength photometry from TRAPPIST, SPECULOOS, and LCO, as well as high-resolution AO observations from Keck/NIRC2 and *Shane*. Our analyses have determined the following parameters for the planet: a radius of $1.466^{+0.063}_{-0.049}$ $R_\oplus$ and an equilibrium temperature of 404 ± 14 K, assuming no albedo and perfect heat redistribution. Assuming a mass based on mass-radius relations, this planet is a promising target for atmospheric characterization with the *James Webb* Space Telescope (JWST).

Key words. techniques: photometric – planets and satellites: detection

1. Introduction

The science of exoplanets has dramatically flourished in the last decade, especially thanks to dedicated space missions. Following the completion of NASA's *Kepler* mission survey, where it was revealed that small transiting planets with sizes between those of Earth and Neptune (i.e., $1 < R_p < 4\,R_\oplus$) are common in close-in orbits around other stars (Howard et al. 2012; Fressin et al. 2013), the Transiting Exoplanet Survey Satellite (TESS: Ricker et al. 2015) mission took over to search for such planets orbiting bright and nearby stars (Jenkins et al. 2019). This mission concept was chosen for easy subsequent spectroscopic investigation of the planets' masses and atmospheres, notably with the *James Webb* Space Telescope (JWST; Deming & Sheppard 2017). TESS observed 85% of the sky in its nominal mission and is now in its extended mission (Wong & Shporer 2022). Up to now, TESS has detected more than 6000 planet candidates (TESS Objects of Interest, TOIs), including more than 1300 that could be smaller than 4 $R_\oplus$.

The exploration of planets larger than Earth and smaller than Neptune is an area of great interest. Since such planets are not present in our Solar System, our understanding of their origins and formation mechanisms is limited. Interestingly, demographic studies performed by Fulton et al. (2017) on the basis of California – *Kepler* Survey exoplanets sample – a subset of transiting planets from *Kepler* with high-resolution spectroscopic follow-up of their host stars (CKS: Petigura et al. 2017; Johnson et al. 2017) – uncovered a gap, usually known as the "radius valley," in the radius distribution of small planets in close orbits (<100 days) around FGK stars. This radius valley separates super-Earths and sub-Neptunes. This finding presents a key phenomenon for understanding planet formation mechanisms.

Two main theories have been proposed to explain the radius valley: thermally driven mass-loss (Lopez & Fortney 2013; Owen & Wu 2013; Jin et al. 2014; Chen & Rogers 2016) and gas-poor formation (Luque et al. 2021; Lee et al. 2014; Lee & Chiang 2016; Lee & Connors 2021). Each of the two predict different origins for the radius valley. Moreover, a recent study conducted by Luque & Pallé (2022) on a sample of 34 well-characterized exoplanets around M dwarfs has instead indicated the presence of a density gap separating rocky and water-rich exoplanets. However, the small size of exoplanet samples used in these studies precludes definitive constraints. Thus, having a significantly large sample of exoplanets with accurate density estimates is strongly needed.

In this paper, we present the discovery and characterization of a super-Earth planet ($1.466^{+0.063}_{-0.049}\,R_\oplus$) which was first discovered by TESS to orbit an M-dwarf star located near the continuous viewing zone (CVZ) of JWST. We validate its planetary nature using ground-based observations, including time-series photometry, high-angular-resolution imaging and spectroscopy. Although we do not present a mass measurement in this paper, this could be done with high-precision radial velocity observation, as discussed in Sect. 4. This measurement would allow for detailed studies on planet formation in the future.

⋆ 51 Pegasi b Fellow.
⋆⋆ Paris Region Fellow, Marie Sklodowska-Curie Action.

Table 1. Ground-based time-series photometric observations of TOI-1680, and the detrending parameters that maximize the log-likelihood of each light curve.

Date (UT)	Filter	Facility	Exp. time (s)	Notes	Detrending parameters
13 Jun. 2020	Ic	LCO-McD-1m	150	full	Airmass
22 Jun. 2021	z'	TRAPPIST-N-0.6m	80	egress	Airmass
07 Jul. 2020	i'	LCO-McD-1m	150	full	Airmass
16 Jul. 2021	z'	TRAPPIST-N-0.6m	80	full	Airmass + Background
09 Aug. 2021	r'	Artemis-1m	100	full	Airmass
02 Sep. 2021	$I+z$	Artemis-1m	20	full	Airmass + Background
21 Sep. 2021	$I+z$	SAINT-EX-1m	19	full	Airmass + Background
08 Nov. 2021	r'	SAINT-EX-1m	105	No post-egress	Airmass
21 Apr. 2022	g', r', i', zs	LCO-Hal-M3-2m	200, 116, 58, 56	full	Airmass

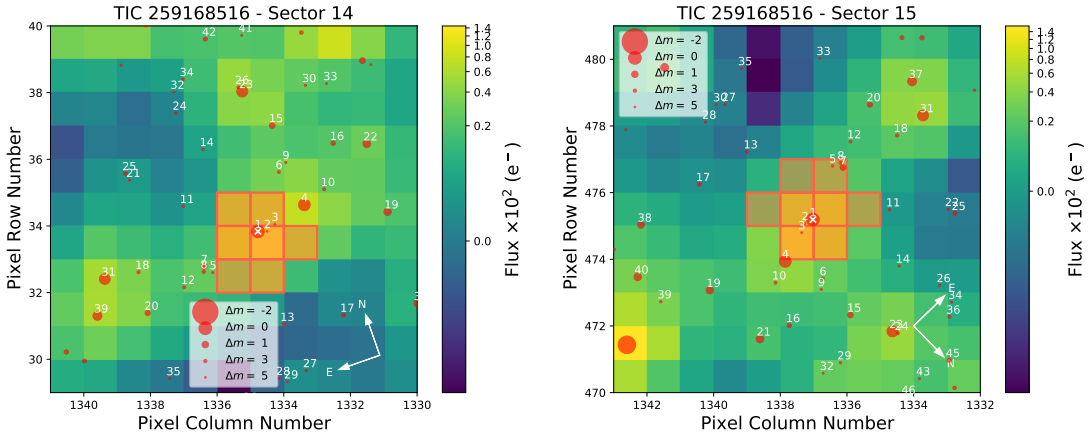

Fig. 1. Target pixel files (TPFs) of TOI-1680 in TESS Sector 14 and 15, created with `tpfplotter` (Aller et al. 2020). The orange shaded region represents the aperture used to extract the SPOC photometry. The red circles are the *Gaia* DR2 sources. Sizes represent magnitude contrasts with respect to TOI-1680. Figure continued in Appendix A.

The paper is structured as follows. Section 2 presents the data from TESS and all ground-based observations. Stellar characterization, validation of the transit signals, and transit analyses are presented in Sect. 3. We discuss our findings in Sect. 4 and give our conclusions in Sect. 5.

2. Observations

In this section, we present all the observations of TOI-1680 obtained with TESS and ground-based facilities. Table 1 summarizes all the ground-based, time-series photometric observations.

2.1. TESS photometry

Over its two-year primary mission, TESS (Ricker et al. 2015) performed an all-sky survey in a series of contiguous overlapping 96 × 24 deg sectors, each observed for 27 days. Depending on the ecliptic latitude, the overlapping regions of the sectors were observed for up to ∼351 days. Given its high ecliptic latitude (β = +81.05 deg), TOI-1680 (TIC 259168516) is well placed in the TESS CVZ. It was then observed by TESS in all the northern sectors (from 14 to 26) in the second year of TESS primary mission, from 18 July 2019 to 4 July 2020. It was also observed in the TESS extended mission in sectors 40–41 from 25 June to 20 August 2021. Most recently, it was observed in sectors 47–59 from 31 December 2021 to 23 December 2022. The target pixel files (TPFs) and simple aperture photometry (SAP) apertures used in each sector are shown in Fig. 1, along with the superplotted locations of nearby *Gaia* DR2 (Gaia Collaboration 2018) sources. The astrometric and photometric properties of TOI-1680 from the literature are reported in Table 2. The time series observations were processed in the TESS Science Processing Operations Center (SPOC) pipeline, originally developed for the *Kepler* mission at NASA Ames Research Center (Jenkins et al. 2016, 2020). The SPOC pipeline conducted a transit search of the combined light curve from sectors 14–16 on 26 October 2019 with an adaptive, noise-compensating matched filter (Jenkins 2002; Jenkins et al. 2010, 2020), producing a threshold crossing event (TCE) with 4.8-day period for which an initial limb-darkened transit model was fitted (Li et al. 2019) and a suite of diagnostic tests were conducted to help make or break the planetary nature of the signal (Twicken et al. 2018). The 5.1 ppt transit signature passed all diagnostic tests presented in the SPOC data validation reports, and the source of the transit signal was localized within 4.03 ± 4.58″. The TESS Science Office (TSO) reviewed the vetting information and issued an alert for TOI-1680 b on 30 January 2020 (Guerrero et al. 2021).

For subsequent analysis, we retrieved the 2-min presearch data conditioning light curves (PDC-SAP, Stumpe et al. 2012, 2014; Smith et al. 2012) from the Mikulski Archive for Space Telescopes (MAST). We were limited to sectors 13–26 of the primary mission and sectors 47–50 of the extended mission. We removed all the bad data points flagged as "bad quality." We then detrended the light curves to remove stellar variability using a biweight time-windowed slider via `wotan` (Hippke et al. 2019). We excluded the transit signal by applying a filter

Table 2. TOI-1680 stellar astrometric and photometric properties.

Parameter	Value	Source
	Target designations	
TIC	259168516	1
2MASS	J19291521+6558279	2
UCAC 4	780-032486	3
Gaia EDR3	2242756094328104576	4
	Photometry	
TESS	11.040 ± 0.007	1
BP	16.27 ± 0.02	4
Gaia	14.61 ± 0.002	4
RP	13.38 ± 0.02	4
J	11.637 ± 0.020	2
H	11.137 ± 0.023	2
K	10.821 ± 0.020	2
WISE 3.4 µm	0.627 ± 0.023	5
WISE 4.6 µm	10.449 ± 0.021	5
WISE 12 µm	10.275 ± 0.047	5
WISE 22 µm	8.23 ± 0.446	5
	Astrometry	
RA (J2000)	19 29 15.21	4
Dec (J2000)	+65 58 27.72	4
RA PM (mas yr^{-1})	56.490 ± 0.022	4
Dec PM (mas yr^{-1})	–131.659 ± 0.020	4
Parallax (mas)	26.8860 ± 0.0158	4

References. 1. Stassun et al. (2018), 2. Cutri et al. (2003), 3. Zacharias et al. (2012), 4. Gaia Collaboration (2020), 5. Cutri et al. (2013).

window that is three times longer than the transit duration of $71.150^{+0.993}_{-0.936}$ min.

2.2. Ground-based photometry

The pixel scale of TESS spacecraft is 21″ per pixel (Ricker et al. 2015). A targeted star might not be alone in a single pixel. Other stars in the same pixel might be suspected to be the source of the TESS detection. Even if the transit signal is on target, the depth might appear shallower because of the contaminating nearby stars. To confirm the signal on target and validate its planetary nature, a series of precise ground-based observations were collected using five observatories as part of the TESS Follow-up Observing Program (TFOP[1]). We made use of TESS Transit Finder (`TTF`) tool, which is a customized version of the `Tapir` software package (Jensen 2013), to schedule our observations described hereafter.

2.2.1. LCOGT 1m

The first two full transits of TOI-1680 b were observed from Las Cumbres Observatory Global Telescope (LCOGT; Brown et al. 2013) 1.0-m network node at McDonald Observatory. The 1-meter telescopes are equipped with 4096×4096 pixels SINISTRO cameras having a pixel scale of 0.389″ per pixel, offering a field of view of 26′×26′. The first transit was observed on 13 June 2020 in the *Ic* band for 210 min, over which we gathered 64 images with an exposure time of 150 seconds. The second transit was observed on 07 July 2020 in Sloan *i*′ band during an observational window of 198 min, where we collected 63 images with an exposure time of 150 s. The data reduction and photometric data extraction were performed using the `AstroImageJ` (AIJ: Collins et al. 2017) software package with an uncontaminated aperture of 8.0 pixels (3.11″) for both observations.

2.2.2. TRAPPIST-North photometry

We observed a partial and a full transit of TOI-1680 b with the 0.6-m TRAPPIST-North telescope located at Oukaimeden Observatory in Morocco (Jehin et al. 2011; Gillon et al. 2013; Barkaoui et al. 2019) on 22 June and 16 July 2021, respectively. TRAPPIST-North is equipped with a thermoelectrically cooled 2K×2K Andor iKon-L BEX2-DD CCD camera with a pixel scale of 0.6″ per pixel, offering a field of view of 20′×20′. Both observations were performed in Sloan z' band with an exposure time of 80 s. The first observation consisted of 113 images for 182 min and the second consisted of 99 images for 166 min duration. For both datasets, we performed the data reduction and differential aperture photometry using `prose`[2] (Garcia et al. 2022), which selected the optimum apertures for the photometric data extraction to be 6.94 pixels (4.16″) for the first observation and 8.32 pixels (5″) for the second.

2.2.3. SPECULOOS-North Artemis photometry

Two full transits of TOI-1680 b were observed by the telescope Artemis of the SPECULOOS Northern Observatory (SNO, Burdanov et al. 2022), located at the Teide Observatory (Canary Islands, Spain). Artemis is operated in a fully automated manner and equipped with Andor iKon-L camera with a 2K×2K deep-depletion CCD, which has a pixel scale of 0.35″ per pixel. The first transit was observed on 09 August 2021 in the Sloan r' filter with an exposure time of 100 s. We gathered 156 images over 319 min. The second transit was observed on 02 September 2021 in an $I + z$ filter (Johnson/Cousins I + Sloan z') with an exposure time of 20 s. We gathered 641 images during an observational window of 325 min. Both datasets were calibrated, and the differential aperture photometry were performed using the `PRINCE` pipeline (Demory et al. 2020). The aperture radii used were 5.0 pixels (1.75″) for the first observation and 8.5 pixels (2.97″) for the second.

2.2.4. SAINT-EX photometry

More ground-based photometric time-series observations of TOI-1680 b were obtained from the SAINT-EX observatory (Search And characterIsatioN of Transiting EXoplanets). SAINT-EX is a 1-m telescope in the $F/8$ Ritchey–Chrétien configuration and operated in fully robotic manner. It is equipped with an 2k×2k deep-depletion CCD camera with a pixel scale of 0.34″ per pixel offering a field of view of 12′×12′. The telescope is allied to an ASTELCO equatorial NTM-1000 German mount associated with direct-drive motors that permits observation without a meridian flip. It is in fact a twin of the SPECULOOS-South and SPECULOOS-North telescopes, and it operates as part of the SPECULOOS survey (Delrez et al. 2018; Sebastian et al. 2021).

Two full transits were observed by SAINT-EX. The first on 21 September 2021 in an $I + z$ filter for 314 min, in which we gathered 520 raw images with an exposure time of 19 s. And the second on 08 November 2021 in Sloan r' filter for 206 min, with an exposure time of 105 seconds where we gathered 104 images.

[1] https://tess.mit.edu/followup

[2] https://github.com/lgrcia/prose

The data reduction and differential aperture photometry were performed automatically using the PRINCE pipeline. For more information on the SAINT-EX telescope and PRINCE pipeline, we refer to Demory et al. (2020). The aperture radii used were 6.5 pixels (2.28″) for the first observation and 11.0 pixels (3.85″) for the second.

2.2.5. LCOGT MUSCAT3 photometry

A full transit of TOI-1680 b was observed simultaneously in Sloan-g', r', i', and Pan-STARRS z-short bands on UTC April 21, 2022 using the LCOGT 2 m Faulkes Telescope North at Haleakala Observatory on Maui, Hawaii. The telescope is equipped with the MuSCAT3 multi-band imager (Narita et al. 2020). The raw images were calibrated using the standard LCOGT BANZAI pipeline (McCully et al. 2018), and photometric measurements were extracted using AstroImageJ (Collins et al. 2017). The light curve in the Sloan-g' filter was not selected to be included in the analyses because of the low signal-to noise ratio (S/N) that is due to the faintness of the star in this band.

2.3. Spectroscopic observations

With the aim of better constraining the stellar properties, we also performed spectroscopic observation detailed hereafter. The analyses are presented in Sect. 3.1.1.

2.3.1. IRTF/SpeX

We gathered a near-infrared spectrum of TOI-1680 with the SpeX spectrograph (Rayner et al. 2003) on the 3.2-m NASA Infrared Telescope Facility (IRTF) on 19 Oct 2021 (UT). The conditions were clear with a seeing of 1.″0–1.″2. We followed the same observational design as other recent IRTF/SpeX observations of M-dwarf TOIs (Wells et al. 2021; Delrez et al. 2022). We used the short-wavelength cross-dispersed (SXD) mode with the 0.3″ × 15″ slit aligned to the parallactic angle, which gives a set of spectra covering 0.75–2.42 µm with a resolving power of R∼2000. Nodding in an ABBA pattern, we collected 18 exposures of 64.9 s each, totaling 19.5 min on source. We collected a set of standard SXD flat-field and arc-lamp exposures immediately after the science frames, followed by a set of six, 2.8-s exposures of the A0 V star HD 172728 (V = 5.7). We reduced the data using Spextool v4.1 (Cushing et al. 2004), following the instructions for standard usage in the Spextool User's Manual[3]. The final spectrum has a median S/N per pixel of 68 with peaks in the J, H, and K bands of 98, 101, and 91, respectively, along with an average of 2.5 pixels per resolution element.

2.3.2. *Shane*/Kast

We obtained a low-resolution optical spectrum of TOI-1680 on 27 Nov 2021 (UT) using the Kast double spectrograph (Miller & Stone 1994) on the 3-m *Shane* Telescope at Lick Observatory. Conditions were partly cloudy with a seeing of 1″. We obtained two sequential exposures of 1200 s (40 min total) through the red channel of Kast using the 600/7500 grism and 2″-wide slit, providing spectra covering 5900–9200 Å at an average resolving power of $R \approx 1900$. We observed the spectrophotometric calibrator Feige 110 (Hamuy et al. 1992, 1994) earlier that night for flux calibration, and the G2 V star HD 205113 (V = 6.87) immediately after TOI-1680 for telluric absorption calibration. Flat-field and arc line lamps were obtained at the start of the night for flux and wavelength calibration. Data were reduced and analyzed using the kastredux package[4], with standard settings for image reduction and calibration, boxcar extraction of the spectrum, wavelength calibration, flux calibration, and telluric absorption calibration. The final spectrum has a S/N = 150 at 7500 Å and wavelength accuracy of 0.51 Å (22 km s^{-1}).

2.4. High-resolution imaging

As part of our standard process for validating transiting exoplanets to assess the possible contamination of bound or unbound companions on the derived planetary radii (Ciardi et al. 2015), we observed the TOI-1680 with near-infrared adaptive optics (AO) imaging at Keck and *Shane* Observatories. *Gaia* DR3 is also used to provide additional constraints on the presence of undetected stellar companions as well as wide companions.

2.4.1. Keck-II near-infrared adaptive optics imaging

The Keck Observatory observations were made with the NIRC2 instrument on Keck-II behind the natural guide star AO system (Wizinowich et al. 2000) on 28 Aug 2021 UT in the standard three-point dither pattern that is used with NIRC2 to avoid the left lower quadrant of the detector, which is typically noisier than the other three quadrants. The dither pattern step size was 3″ and was repeated twice, with each dither offset from the previous dither by 0.5″. NIRC2 was used in the narrow-angle mode with a full field of view of ∼10″ and a pixel scale of approximately 0.0099442″ per pixel. The Keck observations were made in the K filter (λ_o = 2.196; $\Delta\lambda$ = 0.336 µm) with an integration time of 1 second for a total of 9 s on target.

The AO data were processed and analyzed with a custom set of IDL tools. The science frames were flat-fielded and sky-subtracted. The flat fields were generated from a median average of dark-subtracted flats taken on-sky. The flats were normalized such that the median value of the flats is unity. The sky frames were generated from the median average of the dithered science frames; each science image was then sky-subtracted and flat-fielded. The reduced science frames were combined into a single combined image using an intra-pixel interpolation that conserves flux, shifts the individual dithered frames by the appropriate fractional pixels, and median-coadds the frames. The final resolutions of the combined dithers were determined from the full-width half-maximum of the point spread functions (0.056″ for the Keck observations).

The sensitivities of the final combined AO image were determined by injecting simulated sources azimuthally around the primary target every 20° at separations of integer multiples of the central source's FWHM (Furlan et al. 2017). The brightness of each injected source was scaled until standard aperture photometry detected it with 5σ significance. The resulting brightness of the injected sources relative to TOI-1680 set the contrast limits at that injection location. The final 5σ limit at each separation was determined from the average of all of the determined limits at that separation and the uncertainty on the limit was set by the rms dispersion of the azimuthal slices at a given radial distance. The Keck data have a sensitivity close-in of δmag = 2.9 mag at 0.06″, and deeper sensitivity at wider separations (δmag = 6.5 mag at $\gtrsim$0.4″). The final sensitivity curve for the Keck is shown in Fig. 2. No close-in ($\lesssim$1″) stellar companions were detected by Keck.

[3] Available at http://irtfweb.ifa.hawaii.edu/~spex/observer/

[4] https://github.com/aburgasser/kastredux

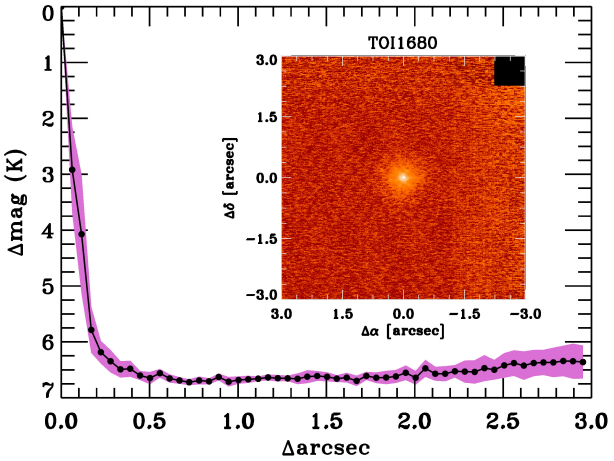

Fig. 2. Keck NIR AO imaging and sensitivity curve for TOI-1680 taken in the K filter. The image reaches a contrast of ∼7 magnitudes fainter than the host star beyond 0.″5. Inset: image of the central portion of the data.

2.4.2. *Shane* near-infrared adaptive optics imaging

We observed TIC 259168516 on UT 2021 June 2 using the ShARCS camera on the *Shane* 3-meter telescope at Lick Observatory (Kupke et al. 2012; Gavel et al. 2014; McGurk et al. 2014). The observation was taken with the *Shane* adaptive optics system in natural guide star mode. The final images were constructed using sequences of images taken in a four-point dither pattern with a separation of 4″ between each dither position. Two image sequences were taken of this star: one with a Ks filter (λ_0 = 2.150 µm, $\Delta\lambda$ = 0.320 µm) and one with a J filter (λ_0 = 1.238 µm, $\Delta\lambda$ = 0.271 µm). A more detailed description of the observing strategy and reduction procedure can be found in Savel et al. (2020). The contrast curves extracted from these observations are shown in Fig 3. With the Ks filter, we achieve contrasts of 2.5 at 1″ and 4.4 at 2″. With the J filter, we achieve contrasts of 2.8 at 1″ and 4.0 at 2″. We detect one companion about 5.″8 west of TIC 259168516 that is 5.0 magnitudes fainter in Ks and 5.7 magnitudes fainter in J. Based on this, the star is likely the known neighbor TIC 1884271108. *Gaia* EDR3 parallax and proper motion indicate that it is another line-of-sight star.

2.5. Gaia assessment

In addition to the high resolution imaging, we have used *Gaia* to identify any wide stellar companions that may be bound members of the system. Typically, these stars are already in the TESS Input Catalog and their flux dilution to the transit has already been accounted for in the transit fits and associated derived parameters from the TESS PDC-SAP photometry. There are no additional widely separated companions identified by *Gaia* that have the same distance and proper motion as TOI-1680 (see also Mugrauer & Michel 2020, 2021).

Additionally, the *Gaia* DR3 astrometry provides additional information on the possibility of inner companions that may have gone undetected by either *Gaia* or the high resolution imaging. The *Gaia* renormalised unit weight Error (RUWE) is a metric, similar to a reduced chi-square, where values that are $\lesssim$1.4 indicate that the *Gaia* astrometric solution is consistent with the star being single whereas RUWE values $\gtrsim$1.4 may indicate an astrometric excess noise, possibly caused by the presence of an unseen massive (stellar) companion (e.g., Ziegler et al. 2020). TOI-1680 has a *Gaia* DR3 RUWE value of 1.05 indicating that the astrometric fits are consistent with the single star model.

3. Analyses

3.1. Stellar characterization

3.1.1. Spectroscopic analysis

The *Shane*/Kast optical and IRTF/SpeX near-infrared spectra allow us to assess TOI-1680's fundamental stellar properties. Using tools in the `kastredux` package, we compared the optical spectrum to the SDSS M dwarf templates of Bochanski et al. (2007), and found a best overall match to the M5 template (Fig. 4). Spectral indices from Reid et al. (1995), Martín et al. (1999), Lépine et al. (2003), and Riddick et al. (2007) are more consistent with an M4 classification, suggesting an intermediate type of M4.5 ± 0.5. The ζ metallicity index of Lépine et al. (2007); Mann et al. (2013), based on relative strengths of TiO and CaH features, is measured to be 1.025 ± 0.002, consistent with a metallicity of [Fe/H] = +0.04 ± 0.20 based on the calibration of Mann et al. (2013). We see no evidence of Hα emission in the Balmer line at 6563 Å (equivalent width limit of <0.3 Å), suggesting an age $\gtrsim$4–7 Gyr (West et al. 2008).

The SpeX SXD spectrum of TOI-1680 is shown in Fig. 4. We used the SpeX Prism Library Analysis Toolkit (SPLAT, Burgasser & Splat Development Team 2017) to compare the spectrum to that of single-star spectral standards in the IRTF Spectral Library (Cushing et al. 2005; Rayner et al. 2009), finding the best single match to the M3.5 standard Gl 273. We note that the shape of the spectrum of TOI-1680 suggests it is cooler than the M3.5 standard, though the M4.0 standards in the library give poorer fits. We adopt an infrared spectral type of M3.5 ± 0.5, earlier but consistent with the optical classification. After adjusting for a barycentric velocity of $-1.64\,\mathrm{km\,s^{-1}}$, we cross-correlated the SpeX spectrum of TOI-1680 with the rest-frame velocity of the M3.5 standard to determine the radial velocity. Determining the uncertainty of the cross-correlation with a Monte Carlo approach, we estimate a radial velocity of $-34.3 \pm 3.3\,\mathrm{km\,s^{-1}}$. After applying a radial-velocity correction, we confirmed that the best-fit spectral standard did not change.

The SpeX spectrum also provides an estimate of stellar metallicity. Using SPLAT, we measured the equivalent widths of the K-band Na I and Ca I doublets and the H2O–K2 index (Rojas-Ayala et al. 2012). We then used the Mann et al. (2013) relation between these observables and [Fe/H] to estimate the stellar metallicity, propagating uncertainties using a Monte Carlo approach (see Delrez et al. 2022). We determined a metallicity of [Fe/H] = −0.32 ± 0.13, which is lower than but formally consistent with the optical measurement and more in line with the apparent old magnetic activity age of the star.

3.1.2. Empirical relations

We used available empirical relationships appropriate for M dwarfs to determine the stellar parameters of TOI-1680. We first used *Gaia* EDR3 parallax and 2MASS m_K visual magnitude to calculate the M_K absolute magnitude and found M_K = 7.9720 ± 0.0203. We then used the empirical relationship between the mass and M_K absolute magnitude of Mann et al. (2019) to estimate the mass of TOI-1680, which we found to be $M_\star = 0.1800 \pm 0.0043\,M_\odot$. This is in good agreement with the mass value of $M_\star = 0.1765 \pm 0.02\,M_\odot$, estimated using the mass–luminosity relation in the K-band from

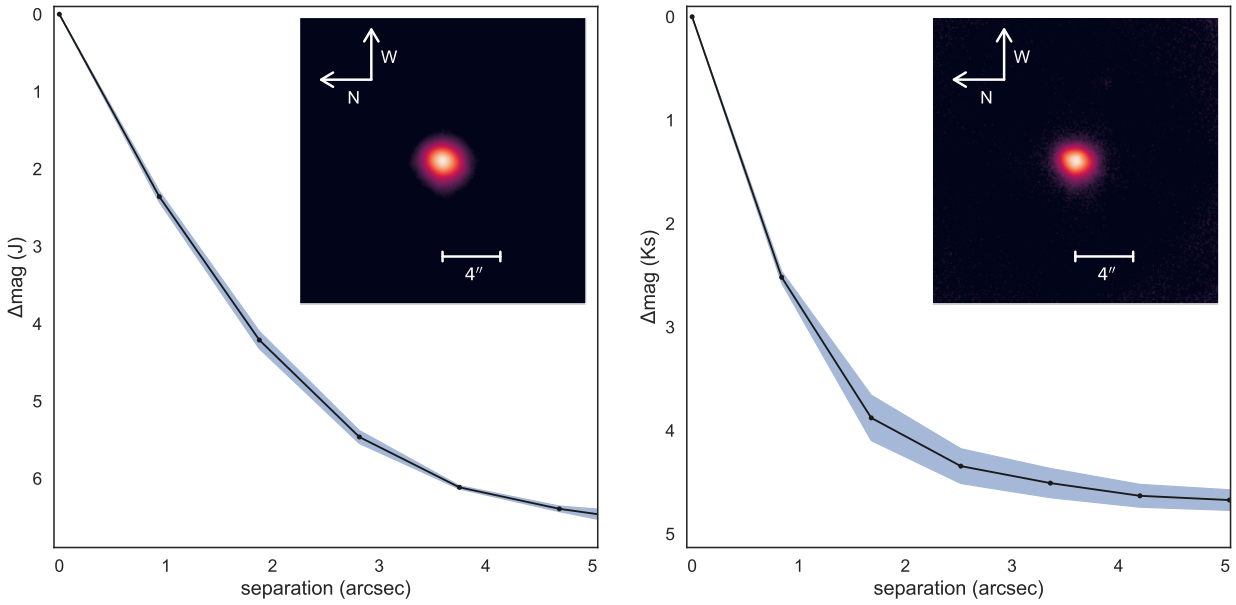

Fig. 3. High-resolution imaging and contrast curves of TOI-1680 obtained with the ShARCS camera on the *Shane* 3-m telescope, with the J (left) and Ks filter (right). No secondary sources were detected.

Benedict et al. (2016), where the uncertainty is dominated by the scatter in the mass-Ks relation.

Using the empirical polynomial relation between the stellar radius R_* and M_K derived by Mann et al. (2015), we estimated R_* to be $0.2130 \pm 0.0064\,R_\odot$, with a typical uncertainty of 3% as reported in Table 1 of Mann et al. (2015). As an independent check, we used the mass–radius relationship of Boyajian et al. (2012) to determine the radius from the masses we previously estimated. We found $R_* = 0.2075 \pm 0.0039\,R_\odot$, which is consistent with the aforementioned radius determination. This leads to a stellar density of 27.4 ± 2.6 g cm^{-3}.

As for the effective temperature determination, we first estimated the bolometric correction in the K-band to be $\mathrm{BC}_K = 2.7414 \pm 0.0822$ mag, by making use of the empirical polynomial relation between BC_K and $V - J$ of Mann et al. (2015). Then, we determined a bolometric magnitude of $M_{\rm bol} = 10.72 \pm 0.085$ mag, which gives a bolometric luminosity of $L_* = 0.004353 \pm 0.000340\,L_\odot$. The Stefan-Boltzmann Law, along with the aforementioned stellar radius and bolometric luminosity, gives an effective temperature $T_{\rm eff} = 3210 \pm 62$ K. Independently, we also determined the effective temperature based on the empirical relation of Mann et al. (2015) using the color indexes $V - J$ and $J - H$, and found $T_{\rm eff} = 3224 \pm 100$ K. The two values are consistent within 1σ.

3.1.3. SED fitting

As an independent check, we used the `EXOFASTv2` analyses package (Eastman et al. 2019) to perform an analysis of the broadband spectral energy distribution (SED) of TOI-1680 using MIST stellar models (Dotter 2016; Choi et al. 2016) to determine the stellar parameters. We pulled the $JHK_{\rm s}$ magnitudes from the 2MASS catalog (Cutri et al. 2003), WISE1-WISE4 magnitudes from the AllWISE catalog (Cutri et al. 2003) and the $GG_{\rm BP}G_{\rm RP}$ magnitudes from *Gaia* EDR3 (see Table 2). We performed the fit shown in Fig. 5 with $T_{\rm eff}$, R_* and M_* as free parameters with a Gaussian prior on the *Gaia* EDR3 parallax which we corrected for systematics by subtracting -0.041867248 mas from the nominal value according to the Lindegren (2020) prescription. We set an upper limit on the extinction of $A_V = 0.29233$ from the dust maps of Schlafly & Finkbeiner (2011) and a Gaussian prior on the stellar metallicity from IRTF/SpeX (see Table 3). The SED fit results, reported in Table 3, are in excellent agreement with our previous determinations.

3.2. Statistical validation

To statistically validate TOI-1680 b, we used `TRICERATOPS`[5] (Giacalone et al. 2021), which validates planets by simulating astrophysical false positives arising from gravitationally bound stellar companions, chance-aligned foreground or background stars, and known nearby stars that are blended with the target in the TESS data. It uses a Bayesian tool that incorporates prior knowledge of the target star, planet occurrence rates, and stellar multiplicity to calculate the false positive probability (FPP) and nearby false positive probability (NFPP). The FPP quantity represents the probability that the observed transit is due to something other than a transiting planet around the target star and the NFPP quantity represents the probability that the observed transit originates from a resolved nearby star rather than the target star. Giacalone et al. (2021) state that for a planet to be statistically validated it must have FPP < 0.015 and NFPP < 0.001.

We first applied `TRICERATOPS` to the TESS 2-min-cadence light curve supplied with the contrast curve obtained by the NIRC2 speckle imaging in Sect. 2.4.1. The resulting FPP and NFPP values are 0.0018 ± 0.0001 and 0.0017 ± 0.0001 respectively. The FPP is good enough but NFPP is above the threshold to classify a validated planet (Giacalone et al. 2021). Only three nearby stars were bright enough and close enough to the target star to cause nearby false positives: TIC 1884271108 ($\Delta T = 6.4$, sep = 6″), TIC 259168518 ($\Delta T = 1.3$, sep = 30″), and TIC 259168513 ($\Delta T = 2.6$, sep = 37″). However, because the event observed by TESS was confirmed to be on-target by our ground-based observations, we were able to rule out these stars

[5] https://github.com/stevengiacalone/triceratops

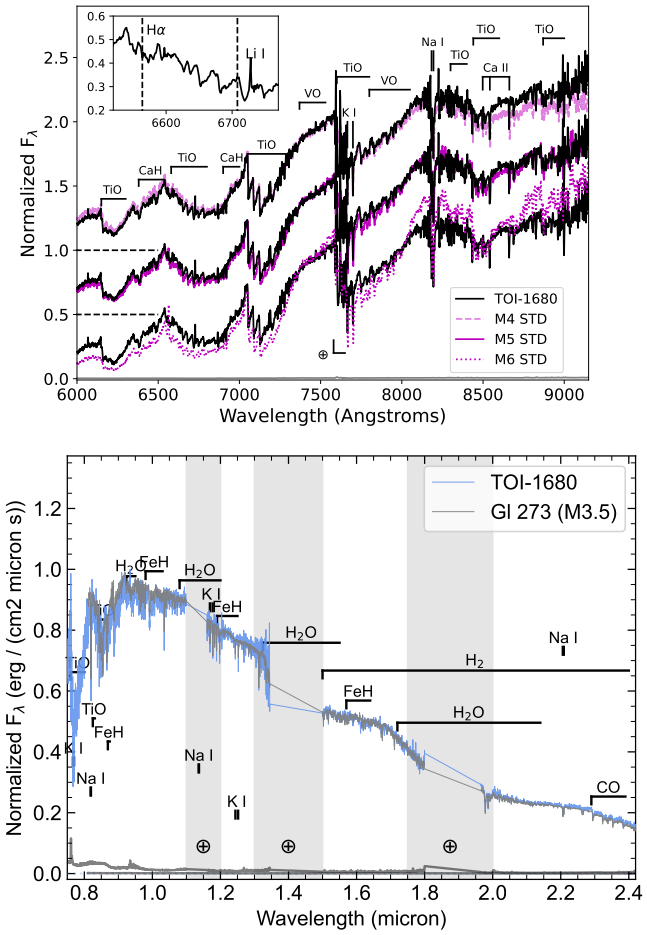

Fig. 4. Kast optical spectrum of TOI-1680 (black lines) compared to M4, M5, and M6 SDSS optical templates (magenta lines from top to bottom) from Bochanski et al. (2007) shown at the top. Each spectral comparison is normalized at 7500 Å and offset by a constant of 0.5. Key atomic and molecular absorption features are labeled, including residual O_2 telluric absorption at 7600 Å (⊕ symbol). The inset box shows a close-up of the region around the 6563 Å Hα and 6708 Å Li I lines, neither of which are detected. Bottom panel displays SpeX SXD spectrum of TOI-1680 (blue) compared to SpeX SXD spectrum of the M3.5 standard Gl 273 (grey; Rayner et al. 2009). Prominent spectral features of M dwarfs are highlighted, and regions of strong telluric absorption are shaded. The grey lines at the bottom of the plot show the measurement uncertainties for TOI-1680 and Gl 273 (higher and lower, respectively).

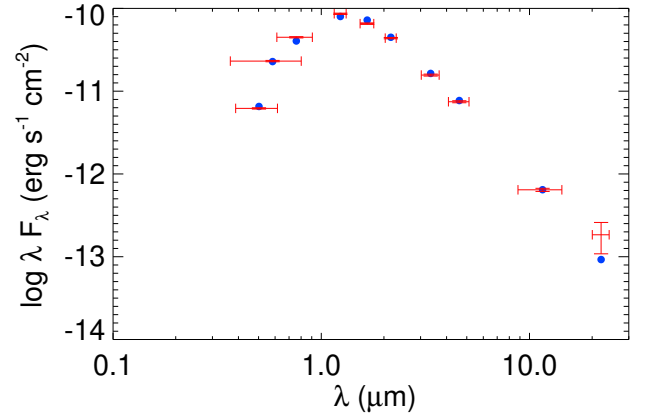

Fig. 5. Spectral energy distribution (SED) of TOI-1680. The red crosses show the broadband observations and the error bars show the width of the filters. The blue circles represent the model fluxes.

Table 3. Stellar parameters.

Parameter	Value	Source
Sp. type	M4.5 ± 0.5	*Shane*/Kast [(a)]
	M3.5 ± 0.5	IRTF/SpeX [(b)]
$T_{\rm eff}$/K	3191^{+81}_{-79}	SED
	3224 ± 100	Mann et al. (2015)
	3210 ± 100	Stefan–Boltzmann
[Fe/H]	+0.04 ± 0.20	*Shane*/Kast [(c)]
	−0.32 ± 0.13	IRTF/SpeX [(d)]
$M_\star$ / $M_\odot$	**0.1800 ± 0.0044**	Mann et al. (2019)
	0.208 ± 0.010	Mann et al. (2015)
	0.1801 ± 0.021	SED
$R_\star$ / $R_\odot$	**0.2130 ± 0.0064**	Mann et al. (2015)
	0.209 ± 0.011	SED
$L_\star.10^{-3}$ / $L_\odot$	$4.07^{+0.25}_{-0.32}$	SED
	4.353 ± 0.340	BC$_K$ (Mann et al. 2015)
$\log g_\star$/dex	$5.063^{+0.047}_{-0.048}$	SED
$\rho_\star$ / g cm^{-3}	27.40 ± 2.82	$M_\star, R_\star$
	$28.4^{+4.5}_{-3.8}$	SED
	$27.3^{+2.3}_{-2.4}$	Global fit

Notes. Parameters in bold are the adopted stellar values in the analyses. [(a)]Classification based on spectral templates from Bochanski et al. (2007) and spectral type/index relations from Reid et al. (1995), Martín et al. (1999), Lépine et al. (2003) and Riddick et al. (2007). [(b)]Classification based on comparison to spectral standards (Cushing et al. 2005; Rayner et al. 2009) and spectral type/index relations from Kirkpatrick et al. (2010). [(c)]Metallicity based on measurement of the ζ index Lépine et al. (2007); Mann et al. (2013) and calibrations from Mann et al. (2013). [(d)]Metallicity based on measurement of K-band Na I and Ca I doublets and the H2O–K2 index (Rojas-Ayala et al. 2012), and the calibrations of Mann et al. (2014).

as sources of false positives and set NFPP = 0 from the outset. The FPP is then reduced to 0.0001 ± 0.0001, which is low enough for validating the planet. Independently, we also used the light curves obtained by the Artemis 1-m and LCO-Hal 2-m telescopes as they present tighter photometric constraints than the TESS data. This was supplied with the same contrast curve mentioned above and without removing any nearby star. This yields FPP and NFPP values generally lower than 0.01 and 0.001 respectively. Therefore, we consider this TESS candidate to be a validated planet.

3.3. Stellar activity

With an ecliptic latitude of β = +81.05 deg, TOI-1680 is located near the northern ecliptic pole in the TESS CVZ. Targets in the CVZ are highly valuable for extracting long-period rotation rates. We first visually inspected the TESS PDC-SAP light curves and found no hints of rotational modulation nor evidence of flares. We then used the Systematics-Insensitive Periodogram (`TESS-SIP`[6]) to build a periodogram for photometric data from all the 19 sectors. This tool creates a Lomb–Scargle periodogram, while simultaneously detrending TESS systematics using a similar method to that described in Angus et al. (2016) for detrending systematics in the NASA *Kepler*/K2 dataset.

[6] https://github.com/christinahedges/TESS-SIP

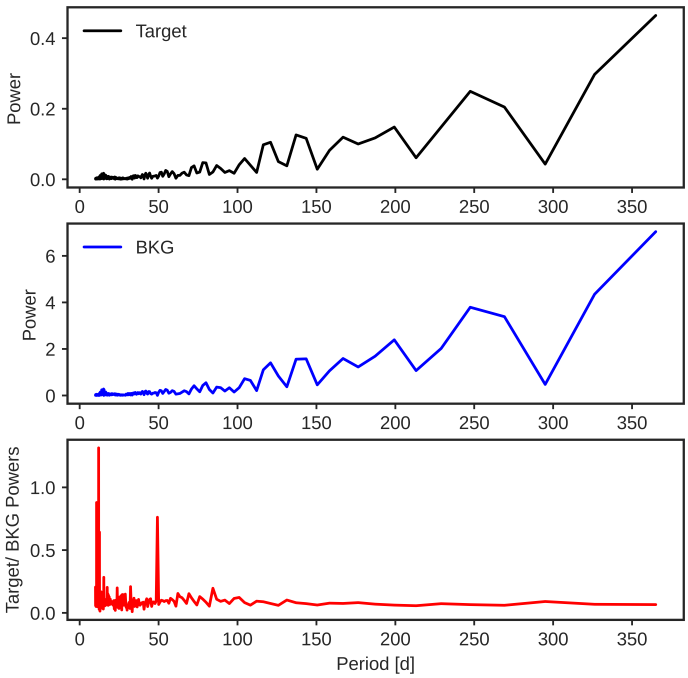

Fig. 6. Systematics-insensitive periodogram (SIP) for TOI-1680 b. The periodogram is calculated for both the corrected light curve (black line in the top panel) and the background (BKG) pixels (blue line in the middle panel). The star and the BKG show the same powers. The bottom panel shows the target to the BKG ratio. We do not see any clear peak for the target.

Since the rotational period of the star might be removed by the PDC pipeline, `TESS-SIP` uses the TESS target pixel file (TPF) data, and apertures assigned by the TESS Pipeline to reproduce a simple aperture photometry (SAP) light curves of the target. We applied this operation on all the 19 observing sectors. Searching for periods between 10 and 365 days, we applied `TESS-SIP` on the target and on all the background pixels outside of the TESS pipeline aperture in the TESS TPFs for TOI-1680. The SIP powers, presented in Fig. 6, show a marked similarity between the periodograms of the target and of the background. For comparison, the lower panel shows the ratio of the target to the background powers. We do not see any significant peaks where the target would display power that would be substantially greater than that of the background.

We also used `TESS-SIP` on each sector alone. We did not find any clear stellar rotation signal nor consistency between the periodograms of any sectors. In short, there is no hint of rotational variability detected for TOI-1680 in the TESS dataset, which is consistent with the lack of detectable Hα emission in its optical spectrum.

Although the TESS CVZ light curves would encompass typical rotation periods for mid-M-dwarfs (0.1 to 140 days; e.g., Newton et al. 2016), we searched for completeness other ground-based photometric archives. Our target TOI-1680 is not part of the MEarth sample (Berta et al. 2012). We analyzed the ASAS-SN light curves (Shappee et al. 2014; Kochanek et al. 2017) for our object that had observations in V and g, spanning from June 2012 to June 2023. We do not find rotational modulation. We note that given the faintness of our target in bluer bands (e.g., $Gaia_{\rm BP}$ = 16.27 mag), only ~65% of the ASAS-SN observations were above the observational limit of each individual observation (with a median limiting magnitude of 16.832 mag in the full light curve). Furthermore, flares cannot be robustly detected in the ASAS-SN data because of its cadence (about two to three days; Jayasinghe et al. 2018).

Table 4. Quadratic limb-darkening coefficients used in the photometric joint analysis for each passband.

Filter	u_1	u_2
TESS	0.2759 ± 0.0300	0.3347 ± 0.0500
z'	0.2367 ± 0.0277	0.3540 ± 0.0529
r'	0.5211 ± 0.0533	0.3247 ± 0.0790
g'	0.5262 ± 0.0457	0.3611 ± 0.0646
Ic	0.2940 ± 0.0280	0.3729 ± 0.0516
i'	0.3121 ± 0.0301	0.3743 ± 0.0550

3.4. Transit modeling

We jointly analyzed the light curves from TESS and ground-based instrumentation described in Sect. 2 using the `EXOFASTv2` (Eastman et al. 2019) software package. We included the TESS photometric data described in Sect. 2.1 from sectors 14 to 50. We detrended the ground-based light curves for the airmass, as well as for either the background or the half width at half maximum (HWHM) of the PSF. The choice of these parameters was based on the likelihood maximization. Some light curves were detrended only for airmass, especially the partial ones. Table 1 shows the detrending parameters of each light curve. The detrending was done simultaneously with the transit fitting to ensure a good propagation of the uncertainties on the derived parameters. We fixed the eccentricity to zero assuming the orbit to be circular (see justification below). We set the `NOMIST` flag to disable the MIST stellar track that constrains the star and, instead, we imposed Gaussian priors on the stellar mass ($0.1800 \pm 0.0044\,M_\odot$), radius ($0.2100 \pm 0.0064\,R_\odot$) and temperature ($3224 \pm 100K$) from our determinations reported in Table 3 as well as uniform priors on the period ($P = 4.8026 \pm 0.1P$ d) and transit epoch ($T_c \pm P/3$) from the values reported in ExoFOP. We set the `NOCLARET` flag to disable the Claret tables (Claret 2017; Claret & Bloemen 2011) that are used to fit the quadratic limb-darkening parameters u_1 and u_2 and we applied our own gaussian priors computed using the `PyLDTk` code (Parviainen & Aigrain 2015) for each passband (see Table 4). TESS light curves are corrected for contamination, but we still fit for dilution of the transit signal in the TESS band due to the neighboring stars using 0±10% of the contamination ratio reported in the TIC 259168516 on ExoFOP as Gaussian prior as recommended by Eastman et al. (2019) to account for any uncertainty in the correction. We ran the EXOFASTv2 analysis until convergence when the Gelman–Rubin statistic (GR) and the number of independent chain draws (Tz) were less than 1.01 and greater than 1000, respectively.

To test the impact of the detrending on our derived parameters, we performed independent analyses of the light curves with another code. We used the `PyTransit` package (Parviainen 2015) and linear models of detrending vectors (FWHM, airmass and background), as done in Wells et al. (2021) and Schanche et al. (2022). We found good agreement between the fits and therefore continued with `EXOFASTv2` for the full analysis. The detrended and modeled light curves are presented in Fig. 7 and the TESS phase-folded light curve is presented in Fig. 8. The results are reported in Table 5. We also fitted for an eccentric orbit to assess the evidence for orbital eccentricity

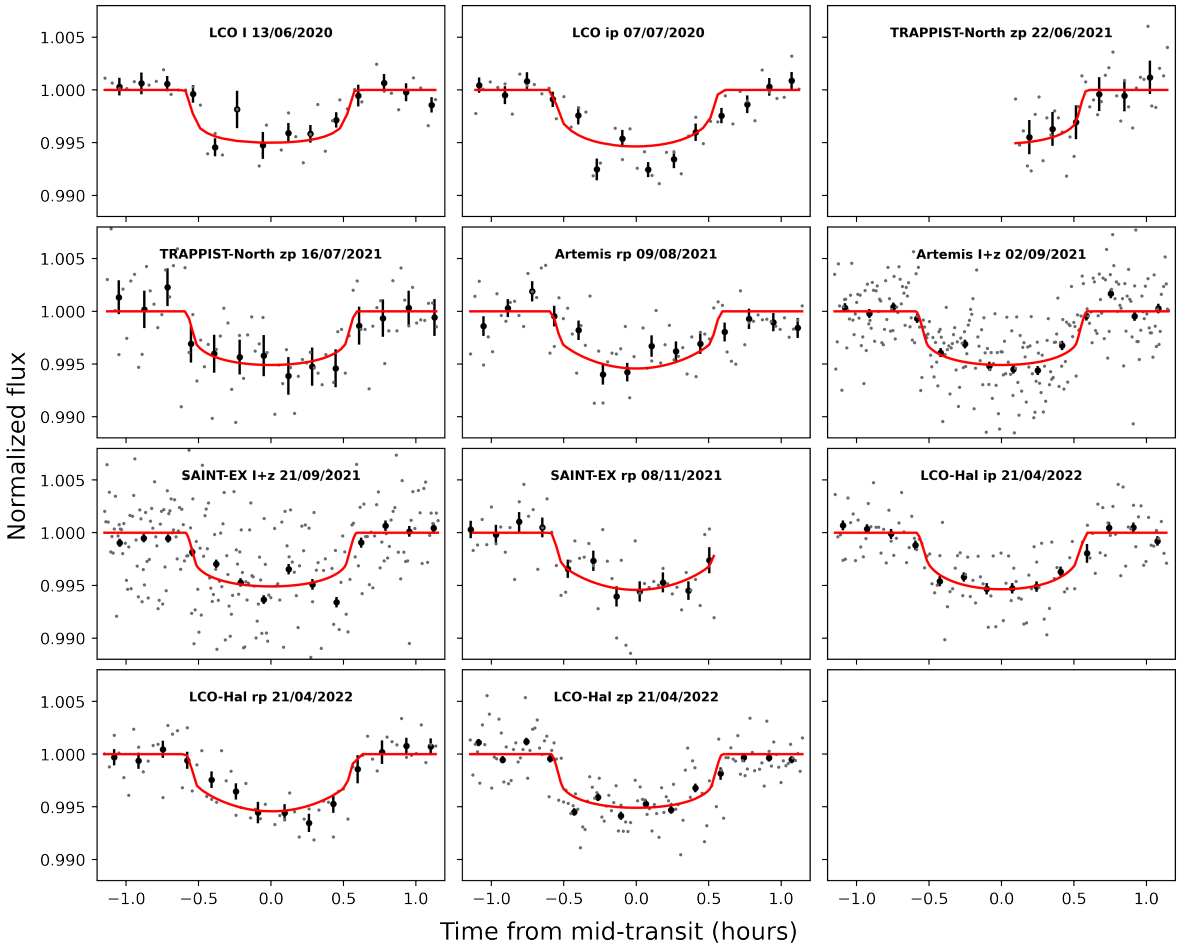

Fig. 7. Phase-folded ground-based transit light curves of TOI-1680 b. The unbinned light curves are shown with gray points. The binned points (bin size=10 min) are shown in black with the corresponding error bars. The red line corresponds to the final `EXOFASTv2` transit model.

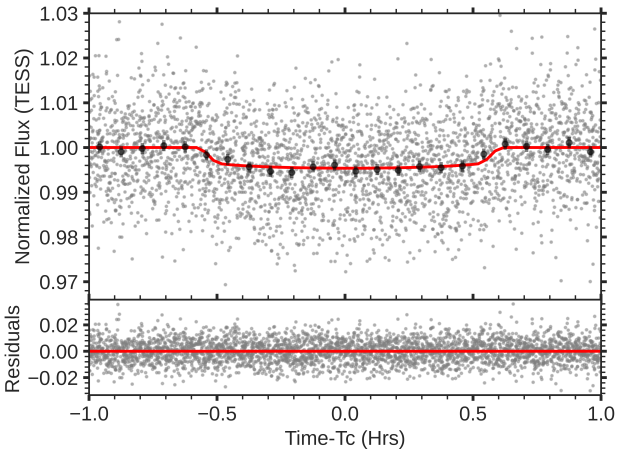

Fig. 8. TESS light curve folded in phase with the time in hours from mid-transit of TOI-1680 b. The red solid line represents the best-fit transit model from the final joint-fit. The gray dots are the 2-min TESS data and the black dots are the binned data every phase interval of 5 min. The residuals are plotted in the bottom panel.

using photometric-only data. A comparision of the loglikelihood of the two fits appears to favor a circular orbit.

We were concerned that the background level was overestimated and overcorrected in the SPOC pipeline in the northern year 2 sectors (14–26). Fitting only data from sectors 14 to 50 would lead to an overestimation of the planet radius by roughly 2%. However, this bias is comparable to the error bars on the planet radius and, the inclusion of the dilution term and additional ground-based data significantly mitigates the problem.

4. Discussion

4.1. TOI-1680 b and the radius valley

Studies performed by Fulton et al. (2017) on the *Kepler* small exoplanets have identified a radius valley roughly from 1.5 to 2 $R_\oplus$, separating rocky super-Earths and gaseous sub-Neptunes around Sun-like stars. A low-radius peak at 1.3 $R_\oplus$ corresponds to high-density super-Earths and a high-radius peak at 2.4 $R_\oplus$ corresponds to low-density sub-Neptunes with significant primordial H/He atmospheres. This gap is considered as possible transition region between rocky and icy "super-Earth" and "mini-Neptunes." Cloutier & Menou (2020) showed that the radius valley persists for low-mass stars (i.e., $M \lesssim 0.65\,R_\odot$).

Two contrasting theories have been presented to explain the radius valley. The first is gas-poor formation model which proposes that the radius valley is a feature intrinsic to the exoplanet population from formation onward (Luque et al. 2021; Lee et al. 2014; Lee & Chiang 2016; Lee & Connors 2021). Specifically, some planets are formed with extended H/He envelopes, whereas the population of rocky planets is formed later in a gas-poor environment after the gas is dissipated from the

Table 5. Median values and 68% confidence intervals for the parameters of TOI-1680 b obtained using EXOFASTv2.

Parameter	Description	Best-fit value
	Stellar parameters	
M_*	Mass ($M_\odot$)	0.1798 ± 0.0044
R_*	Radius ($R_\odot$)	$0.2106^{+0.0061}_{-0.0048}$
L_*	Luminosity ($L_\odot$)	$0.00434^{+0.00062}_{-0.00055}$
ρ_*	Density (cgs)	$27.2^{+2.0}_{-2.3}$
$\log g$	Surface gravity (cgs)	$5.046^{+0.027}_{-0.021}$
$T_{\rm eff}$	Effective temperature (K)	3225^{+99}_{-100}
	Planetary parameters	
P	Orbital period (days)	$4.8026345^{+0.0000040}_{-0.0000039}$
$R_{\rm P}$	Planet radius ($R_\oplus$)	$1.466^{+0.063}_{-0.049}$
T_C	Transit time ($\rm BJD_{TDB}$)	$2\,459\,013.84254^{+0.00037}_{-0.00039}$
a	Semi-major axis (AU)	$0.03144^{+0.00025}_{-0.00026}$
i	Inclination (degrees)	$89.58^{+0.26}_{-0.22}$
$T_{\rm eq}$	Equilibrium temperature[(a)] (K)	404 ± 14
$R_{\rm P}/R_\star$	Planet-to-star radius ratio	0.0638 ± 0.0015
$a/R_\star$	Semi-major axis in stellar radii	$32.04^{+0.74}_{-0.93}$
δ	$(R_{\rm P}/R_\star)^2$	$0.00407^{+0.00019}_{-0.00018}$
$\delta_{\rm I}$	Transit depth in I (fraction)	0.00472 ± 0.00020
$\delta_{\rm i'}$	Transit depth in i' (fraction)	$0.0066^{+0.0023}_{-0.0015}$
$\delta_{\rm r'}$	Transit depth in r' (fraction)	$0.0066^{+0.0020}_{-0.0014}$
$\delta_{\rm z'}$	Transit depth in z' (fraction)	$0.00503^{+0.00098}_{-0.00065}$
$\delta_{\rm TESS}$	Transit depth in TESS (fraction)	$0.00507^{+0.0012}_{-0.00070}$
τ	Ingress/egress transit duration (days)	$0.00312^{+0.00026}_{-0.00016}$
T_{14}	Total transit duration (days)	$0.04941^{+0.00069}_{-0.00065}$
T_{FWHM}	FWHM transit duration (days)	$0.04625^{+0.00072}_{-0.00069}$
b	Transit impact parameter	$0.23^{+0.11}_{-0.14}$
$\langle F \rangle$	Incident flux (10^9 erg s^{-1} cm^{-2})	$0.00600^{+0.00084}_{-0.00075}$
d/R_*	Separation at mid-transit	$32.04^{+0.74}_{-0.93}$
	Predicted parameters	
$M_{\rm P}$	Planet mass[(b)] ($M_\oplus$)	$3.18^{+1.1}_{-0.69}$
K	RV semi-amplitude (m s^{-1})	$3.78^{+1.3}_{-0.82}$
TSM	Transmission spectroscopy metric	7.82
$M_{\rm P}/M_*$	Planet-to-star mass ratio	$0.000053^{+0.000019}_{-0.000011}$
ρ_P	Planet mean density (cgs)	$5.5^{+1.9}_{-1.2}$

Notes. [(a)]The equilibrium temperature corresponds to a case with null albedo and an 100% efficient heat recirculation. [(b)]The planetary mass is estimated from the planetary radius from transit using the Chen & Kipping (2017) mass–radius relation. The radial velocity semi-amplitude (K) is predicted using the estimated mass.

protoplanetary disk. The second is thermally driven atmospheric mass loss (Lopez & Fortney 2013; Owen & Wu 2013; Jin et al. 2014; Chen & Rogers 2016), which proposes that the radius gap is formed through evolution after the gas accretion phase. That is, planets are formed with gaseous envelopes and some of them experience atmospheric escape through two scenarios: 1) photo-evaporation (Lopez & Fortney 2013; Owen & Wu 2013; Jin et al. 2014; Chen & Rogers 2016) triggered by energetic EUV and X-ray flux from the host star in the first ∼100 Myrs (Owen & Wu 2013) of the system and 2) core-powered mass-loss (Ginzburg et al. 2016) triggered by the energy emergent from the cooling planetary core in a Gyr timescale (Ginzburg et al. 2018).

On the contrary, a recent study performed by Luque & Pallé (2022) further suggests that there is a density gap, but not a radius gap, separating rocky planets and water-rich worlds with no planets with intermediate composition. Using a sample of 34 exoplanets with well-characterized densities around M-dwarf stars, they identified three populations: rocky planets ($\rho = 0.94 \pm 0.13\ \rho_\oplus$), water-rich planets ($\rho = 0.47 \pm 0.05\ \rho_\oplus$), and gas-rich planets ($\rho = 0.24 \pm 0.04\ \rho_\oplus$). These study findings favor the pebble accretion model (Venturini et al. 2020; Brügger et al. 2020) as the main mechanism for forming small planets around M dwarfs, where rocky planets are formed within the ice line while water-rich planets are formed beyond the ice line and then migrated inwards. However, as for previous studies, the sample of exoplanets used in this study is not large enough to draw firm conclusions.

Figure 9 shows the current period–radius diagram of all known exoplanets with precise radius measurements orbiting M dwarfs. The empirical locations of the radius valley for FGK stars as predicted by thermally driven photoevaporation (dashed line) given by Van Eylen et al. (2018) and for low-mass stars as

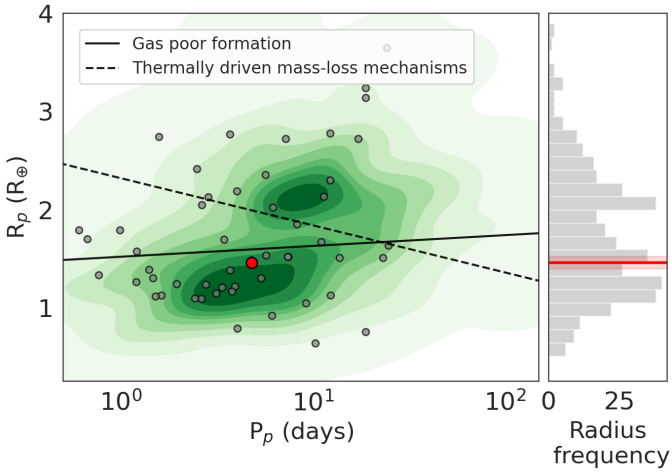

Fig. 9. Distribution of planet radii and orbital periods for all confirmed small planets hosted by low-mass stars ($M_* \lesssim 0.65\,M_\odot$). The solid and dashed lines represent the predicted locations of the radius valley based on the gas-poor formation model and thermally driven photoevaporation models, respectively. The red dot represents the planet TOI-1680 b. The 1D radius distribution, with the location of the planet TOI-1680 b, is shown on the right panel.

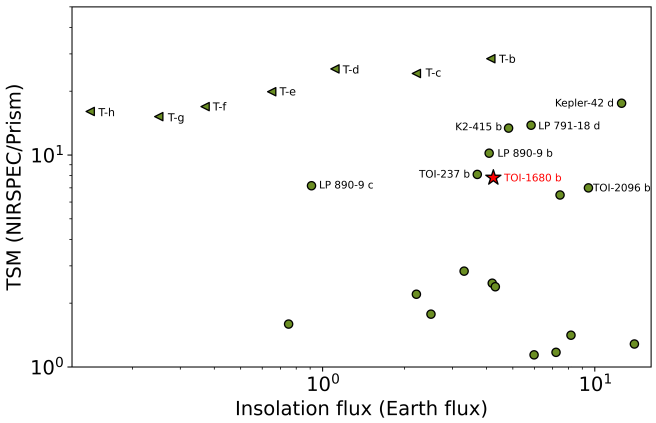

Fig. 10. Transmission Spectroscopy Metric for known planets that can be observed with the JWST NIRSPEC/Prism. The sample is limited to exoplanets with equilibrium temperatures below 500 K and radii smaller than 1.5 $R_\oplus$ and orbiting stars fainter than $J = 10.5$. The x-axis is limited to 16 times Earth insolation flux. TOI-1680 b is labeled and highlighted with a star. Data were taken from NASA Exoplanet Archive on June 25, 2023.

predicted by gas-poor formation (solid line) given by Cloutier & Menou (2020) are also displayed. With a radius of $1.466^{+0.063}_{-0.049}\,R_\oplus$ and orbital period of 4.8026343 ± 0.0000030 days, TOI-1680 b is located close to the center of the super-Earth population where the two models predict the location of small rocky planets. With a future planetary mass determination, TOI-1680 b can join the growing sample of small planets with precise bulk densities around M dwarfs.

4.2. Prospects for a radial velocity follow-up

The precise mass determination of TOI-1680 b would allow us to better constrain the detectability of a possible atmosphere and better locate the planet in the radius-density gap. High-precision radial velocity (RV) measurements will not only allow us to constrain the planetary mass, but also constrain its orbit such as its eccentricity, which may shed some light onto the dynamical history of the system. TOI-1680 b has a radius of $1.466^{+0.063}_{-0.049}\,R_\oplus$. Thus, we expect a RV semi-amplitude of $3.78^{+1.3}_{-0.82}$ m s^{-1}, assuming a circular orbit and a mass of $3.18^{+1.1}_{-0.69}\,M_\oplus$, as predicted from the mass–radius relation of Chen & Kipping (2017).

Not many high-precision spectrographs in the northern hemisphere are capable of detecting such a shallow signal from a faint target ($V = 15.87$ mag and $J = 11.63$ mag). Many typical planet finders, mounted on 2–4 m class telescopes such as CARMENES (Quirrenbach et al. 2020), HARPS-N (Cosentino et al. 2012), NEID (Schwab et al. 2016) or EXPRES (Jurgenson et al. 2016) have limiting magnitudes that are brighter than V=15.87. MAROON-X at the 8.1 m Gemini North telescope (Seifahrt et al. 2020) has shown to reach the necessary precision for faint M-dwarf host stars (Seifahrt et al. 2022). Despite the high declination, it would be possible to reach a S/N of about 40 in the red arm after a 15 min exposure. Assuming a stellar activity level of <1.5 m s^{-1}, this would allow for an overall precision of 0.7 m s^{-1} precision with about 70 spectra. Thus, it will be possible to measure the planet mass with state-of-the-art instrumentation at 5 σ precision by investing about 29 h of telescope time on a 8-m-class telescope.

4.3. Potential for atmospheric characterization

We assess the potential for atmospheric characterization of TOI-1680 b with JWST using the transmission spectroscopy metric (TSM, Kempton et al. 2018). The TSM quantifies the expected S/N in the transmission spectrum of a given planet with a cloud-free atmosphere. Analytically, it is expressed as:

$$\mathrm{TSM} = S \times \frac{R_\mathrm{p}^3 T_\mathrm{eq}}{M_\mathrm{p} R_*^2} \times 10^{\frac{-m_j}{5}},$$

where R_p and M_p are the planetary radius and mass in Earth units, R_* is the stellar radius in Solar radii, T_eq is the equilibrium temperature of the planet in K and m_J is the apparent magnitude of the star in the J band. Also, S is a scale factor whose value depends on the planetary radius range.

TOI-1680 b is a cool ($T_\mathrm{eq} < 500$ K) super-Earth ($R < 1.5\,R_\oplus$). With $J = 11.6$, the host star is within reach of the JWST NIRSpec/PRISM (0.6–5.3 µm) instrument (Jakobsen et al. 2022), which cannot observe stars brighter than $J = 10.5$ without saturation. We used the TSM to assess the suitability of all cool ($T_\mathrm{eq} < 500$ K) planets with radii smaller than $1.5\,R_\oplus$ orbiting stars fainter than $J = 10.5$ for atmospheric studies with this instrument. This sample of exoplanets contains 63 targets. We used the empirical mass–radius relation of Chen & Kipping (2017) to estimate the mass of planets that do not have mass measurements as is the case for TOI-1680 b. TSM values of these planets are shown in Fig. 10. We found that TOI-1680 b has a TSM=7.82 which indicate that it could be a suitable target for transmission studies with the JWST NIRSpec/PRISM instrument. Specifically, amongst 63 targets, TOI-1680 b ranks as the thirteenth most amenable target for these studies. It follows all the TRAPPIST-1 planets (Gillon et al. 2017), Kepler-42 d (Muirhead et al. 2012), K2-415 b (Hirano et al. 2023), LP 791-18 d (Peterson et al. 2023), LP 890-9 b (Delrez et al. 2022) and TOI-237 b (Waalkes et al. 2021). Moreover, the TSM is based on 10 h of JWST observing time and with an ecliptic latitude of $\beta = +81.05$ deg. TOI-1680 b is located near the JWST CVZ, and it has the advantage of being observable for about 250 days per year, which encourages its atmospheric characterization.

5. Conclusion

We have reported the discovery and initial characterization of TOI-1680 b, a super-Earth orbiting a faint mid-M dwarf (V = 15.87). We used the combination of 2-min cadence TESS observations from 19 sectors, ground-based photometry, high-angular-resolution imaging and spectroscopic observations to validate its planetary nature. Joint analyses of TESS and ground-based data yielded a planetary radius of $1.466^{+0.063}_{-0.049}$ $R_\oplus$, an orbital period of $4.8026345^{+0.0000040}_{-0.0000039}$ days and an equilibrium temperature of 404 ± 14 K. According to the transmission spectroscopy metric (TSM) of Kempton et al. (2018), TOI-1680 b could be a promising candidate for atmospheric characterization with the JWST. However, a stronger prediction of the expected S/N waits for direct mass measurement from radial velocity observations, which could be done with the MAROON-X instrument at the 8.1 m Gemini North telescope.

Acknowledgements. This research received funding from the European Research Council (ERC) under the European Union's Horizon 2020 research and innovation programme (grant agreement no. 803193/BEBOP). B.V.R. thanks the Heising-Simons Foundation for support. TRAPPIST is funded by the Belgian Fund for Scientific Research (Fond National de la Recherche Scientifique, FNRS) under the grant FRFC 2.5.594.09.F, with the participation of the Swiss National Science Fundation (SNF). The ULiege's contribution to SPECULOOS has received funding from the European Research Council under the European Union's Seventh Framework Programme (FP/2007–2013) (grant Agreement n° 336480/SPECULOOS), from the Balzan Prize and Francqui Foundations, from the Belgian Scientific Research Foundation (F.R.S.-FNRS; grant no. T.0109.20), from the University of Liege, and from the ARC grant for Concerted Research Actions financed by the Wallonia-Brussels Federation. This work is based upon observations carried out at the Observatorio Astronómico Nacional on the Sierra de San Pedro Mártir (OAN-SPM), Baja California, México. SAINT-EX observations and team were supported by the Swiss National Science Foundation (PP00P2-163967 and PP00P2-190080), the Centre for Space and Habitability (CSH) of the University of Bern, the National Centre for Competence in Research PlanetS, supported by the Swiss National Science Foundation (SNSF), and UNAM PAPIIT-IG101321. The postdoctoral fellowship of KB is funded by F.R.S.-FNRS grant T.0109.20 and by the Francqui Foundation. This work makes use of observations from the LCOGT network. Part of the LCOGT telescope time was granted by NOIRLab through the Mid-Scale Innovations Program (MSIP). MSIP is funded by NSF. This research has made use of the Exoplanet Follow-up Observation Program (ExoFOP; DOI: 10.26134/ExoFOP5) website, which is operated by the California Institute of Technology, under contract with the National Aeronautics and Space Administration under the Exoplanet Exploration Program. Funding for the TESS mission is provided by NASA's Science Mission Directorate. K.A..C. acknowledges support from the TESS mission via subaward s3449 from MIT. Resources supporting this work were provided by the NASA High-End Computing (HEC) Program through the NASA Advanced Supercomputing (NAS) Division at Ames Research Center for the production of the SPOC data products. This paper is based on observations made with the MuSCAT3 instrument, developed by the Astrobiology Center and under financial supports by JSPS KAKENHI (JP18H05439) and JST PRESTO (JPMJPR1775), at Faulkes Telescope North on Maui, HI, operated by the Las Cumbres Observatory. This work is partly supported by JSPS KAKENHI Grant Number JP18H05439 and JST CREST Grant Number JPMJCR1761. This work was partially supported by a grant from the Erasmus+ International Credit Mobility program (M. Ghachoui). M.G. is F.R.S-FNRS Research Director. L.D. is an F.R.S.-FNRS Postdoctoral Researcher. J.d.W. and M.I.T. gratefully acknowledge financial support from the Heising-Simons Foundation, Dr. and Mrs. Colin Masson and Dr. Peter A. Gilman for Artemis, the first telescope of the SPECULOOS network situated in Tenerife, Spain. F.J.P. acknowledges financial support from the grant CEX2021-001131-S funded by MCIN/AEI/10.13039/501100011033. This publication benefits from the support of the French Community of Belgium in the context of the FRIA Doctoral Grant awarded to M.T.

References

Aller, A., Lillo-Box, J., Jones, D., Miranda, L. F., & Barceló Forteza, S. 2020, A&A, 635, A128
Angus, R., Foreman-Mackey, D., & Johnson, J. A. 2016, ApJ, 818, 109
Barkaoui, K., Burdanov, A., Hellier, C., et al. 2019, AJ, 157, 43
Benedict, G. F., Henry, T. J., Franz, O. G., et al. 2016, AJ, 152, 141
Berta, Z. K., Irwin, J., Charbonneau, D., Burke, C. J., & Falco, E. E. 2012, AJ, 144, 145
Bochanski, J. J., West, A. A., Hawley, S. L., & Covey, K. R. 2007, AJ, 133, 531
Boyajian, T. S., von Braun, K., van Belle, G., et al. 2012, ApJ, 757, 112
Brown, T. M., Baliber, N., Bianco, F. B., et al. 2013, PASP, 125, 1031
Brügger, N., Burn, R., Coleman, G. A. L., Alibert, Y., & Benz, W. 2020, A&A, 640, A21
Burdanov, A. Y., de Wit, J., Gillon, M., et al. 2022, PASP, 134, 105001
Burgasser, A. J., & Splat Development Team. 2017, in ASI Conf. Ser., 14, 7
Chen, J., & Kipping, D. 2017, ApJ, 834, 17
Chen, H., & Rogers, L. A. 2016, ApJ, 831, 180
Choi, J., Dotter, A., Conroy, C., et al. 2016, ApJ, 823, 102
Ciardi, D. R., Beichman, C. A., Horch, E. P., & Howell, S. B. 2015, ApJ, 805, 16
Claret, A. 2017, A&A, 600, A30
Claret, A., & Bloemen, S. 2011, A&A, 529, A75
Cloutier, R., & Menou, K. 2020, AJ, 159, 211
Collins, K. A., Kielkopf, J. F., Stassun, K. G., & Hessman, F. V. 2017, AJ, 153, 77
Cosentino, R., Lovis, C., Pepe, F., et al. 2012, Proc. SPIE, 8446, 84461V
Cushing, M. C., Vacca, W. D., & Rayner, J. T. 2004, PASP, 116, 362
Cushing, M. C., Rayner, J. T., & Vacca, W. D. 2005, ApJ, 623, 1115
Cutri, R. M., Skrutskie, M. F., van Dyk, S., et al. 2003, VizieR Online Data Catalog, II/246
Cutri, R. M., Wright, E. L., Conrow, T., et al. 2013, Explanatory Supplement to the AllWISE Data Release Products
Delrez, L., Gillon, M., Queloz, D., et al. 2018, SPIE Conf. Ser., 10700, 107001I
Delrez, L., Murray, C. A., Pozuelos, F. J., et al. 2022, A&A, 667, A59
Deming, D., & Sheppard, K. 2017, ApJ, 841, L3
Demory, B. O., Pozuelos, F. J., Gómez Maqueo Chew, Y., et al. 2020, A&A, 642, A49
Dotter, A. 2016, ApJS, 222, 8
Eastman, J. D., Rodriguez, J. E., Agol, E., et al. 2019, ArXiv e-prints [arXiv:1907.09480]
Fressin, F., Torres, G., Charbonneau, D., et al. 2013, ApJ, 766, 81
Fulton, B. J., Petigura, E. A., Howard, A. W., et al. 2017, AJ, 154, 109
Furlan, E., Ciardi, D. R., Everett, M. E., et al. 2017, AJ, 153, 71
Gaia Collaboration (Brown, A. G. A., et al.) 2018, A&A, 616, A1
Gaia Collaboration 2020, VizieR Online Data Catalog: I/350
Garcia, L. J., Timmermans, M., Pozuelos, F. J., et al. 2022, MNRAS, 509, 4817
Gavel, D., Kupke, R., Dillon, D., et al. 2014, SPIE Conf. Ser., 9148, 914805
Giacalone, S., Dressing, C. D., Jensen, E. L. N., et al. 2021, AJ, 161, 24
Gillon, M., Anderson, D. R., Collier-Cameron, A., et al. 2013, A&A, 552, A82
Gillon, M., Triaud, A. H. M. J., Demory, B.-O., et al. 2017, Nature, 542, 456
Ginzburg, S., Schlichting, H. E., & Sari, R. 2016, ApJ, 825, 29
Ginzburg, S., Schlichting, H. E., & Sari, R. 2018, MNRAS, 476, 759
Guerrero, N. M., Seager, S., Huang, C. X., et al. 2021, ApJS, 254, 39
Hamuy, M., Walker, A. R., Suntzeff, N. B., et al. 1992, PASP, 104, 533
Hamuy, M., Suntzeff, N. B., Heathcote, S. R., et al. 1994, PASP, 106, 566
Hippke, M., David, T. J., Mulders, G. D., & Heller, R. 2019, AJ, 158, 143
Hirano, T., Dai, F., Livingston, J. H., et al. 2023, AJ, 165, 131
Howard, A. W., Marcy, G. W., Bryson, S. T., et al. 2012, ApJS, 201, 15
Jakobsen, P., Ferruit, P., Alves de Oliveira, C., et al. 2022, A&A, 661, A80
Jayasinghe, T., Kochanek, C. S., Stanek, K. Z., et al. 2018, MNRAS, 477, 3145
Jehin, E., Gillon, M., Queloz, D., et al. 2011, The Messenger, 145, 2
Jenkins, J. M. 2002, ApJ, 575, 493
Jenkins, J. M., Chandrasekaran, H., McCauliff, S. D., et al. 2010, SPIE Conf. Ser., 7740, 77400D
Jenkins, J. M., Twicken, J. D., McCauliff, S., et al. 2016, SPIE Conf. Ser., 9913, 99133E
Jenkins, J. S., Pozuelos, F. J., Tuomi, M., et al. 2019, MNRAS, 490, 5585
Jenkins, J. M., Tenenbaum, P., Seader, S., et al. 2020, *Kepler* Data Processing Handbook: Transiting Planet Search, *Kepler* Science Document KSCI-19081-003, ed. J. M. Jenkins, 9
Jensen, E. 2013, Astrophysics Source Code Library [record ascl:1306.007]
Jin, S., Mordasini, C., Parmentier, V., et al. 2014, ApJ, 795, 65
Johnson, J. A., Petigura, E. A., Fulton, B. J., et al. 2017, AJ, 154, 108
Jurgenson, C., Fischer, D., McCracken, T., et al. 2016, SPIE Conf. Ser., 9908, 99086T
Kempton, E. M.-R., Bean, J. L., Louie, D. R., et al. 2018, PASP, 130, 114401
Kirkpatrick, J. D., Looper, D. L., Burgasser, A. J., et al. 2010, ApJS, 190, 100
Kochanek, C. S., Shappee, B. J., Stanek, K. Z., et al. 2017, PASP, 129, 104502
Kupke, R., Gavel, D., Roskosi, C., et al. 2012, SPIE Conf. Ser., 8447, 84473G
Lee, E. J., & Chiang, E. 2016, ApJ, 817, 90
Lee, E. J., & Connors, N. J. 2021, ApJ, 908, 32
Lee, E. J., Chiang, E., & Ormel, C. W. 2014, ApJ, 797, 95
Lépine, S., Rich, R. M., & Shara, M. M. 2003, AJ, 125, 1598
Lépine, S., Rich, R. M., & Shara, M. M. 2007, ApJ, 669, 1235
Li, J., Tenenbaum, P., Twicken, J. D., et al. 2019, PASP, 131, 024506

Lindegren, L. 2020, A&A, 633, A1
Lopez, E. D., & Fortney, J. J. 2013, ApJ, 776, 2
Luque, R., & Pallé, E. 2022, Science, 377, 1211
Luque, R., Serrano, L. M., Molaverdikhani, K., et al. 2021, A&A, 645, A41
Mann, A. W., Brewer, J. M., Gaidos, E., Lépine, S., & Hilton, E. J. 2013, AJ, 145, 52
Mann, A. W., Deacon, N. R., Gaidos, E., et al. 2014, AJ, 147, 160
Mann, A. W., Feiden, G. A., Gaidos, E., Boyajian, T., & von Braun, K. 2015, ApJ, 804, 64
Mann, A. W., Dupuy, T., Kraus, A. L., et al. 2019, ApJ, 871, 63
Martín, E. L., Delfosse, X., Basri, G., et al. 1999, AJ, 118, 2466
McCully, C., Volgenau, N. H., Harbeck, D.-R., et al. 2018, SPIE Conf. Ser., 10707, 107070K
McGurk, R., Rockosi, C., Gavel, D., et al. 2014, SPIE Conf. Ser., 9148, 91483A
Miller, J. S., & Stone, R. P. S. 1994, The Kast Double Spectrograph, Tech. Rep. 66, University of California Lick Observatory Technical Reports
Mugrauer, M., & Michel, K.-U. 2020, Astron. Nachr., 341, 996
Mugrauer, M., & Michel, K.-U. 2021, Astron. Nachr., 342, 840
Muirhead, P. S., Johnson, J. A., Apps, K., et al. 2012, ApJ, 747, 144
Narita, N., Fukui, A., Yamamuro, T., et al. 2020, SPIE Conf. Ser., 11447, 114475K
Newton, E. R., Irwin, J., Charbonneau, D., et al. 2016, ApJ, 821, 93
Owen, J. E., & Wu, Y. 2013, ApJ, 775, 105
Parviainen, H. 2015, MNRAS, 450, 3233
Parviainen, H., & Aigrain, S. 2015, MNRAS, 453, 3821
Peterson, M. S., Benneke, B., Collins, K., et al. 2023, Nature, 617, 701
Petigura, E. A., Howard, A. W., Marcy, G. W., et al. 2017, AJ, 154, 107
Quirrenbach, A., CARMENES Consortium, Amado, P. J., et al. 2020, SPIE Conf. Ser., 11447, 114473C
Rayner, J. T., Toomey, D. W., Onaka, P. M., et al. 2003, PASP, 115, 362
Rayner, J. T., Cushing, M. C., & Vacca, W. D. 2009, ApJS, 185, 289
Reid, I. N., Hawley, S. L., & Gizis, J. E. 1995, AJ, 110, 1838
Ricker, G. R., Winn, J. N., Vanderspek, R., et al. 2015, J. Astron. Telescopes Instrum. Syst., 1, 014003
Riddick, F. C., Roche, P. F., & Lucas, P. W. 2007, MNRAS, 381, 1067
Rojas-Ayala, B., Covey, K. R., Muirhead, P. S., & Lloyd, J. P. 2012, ApJ, 748, 93
Savel, A. B., Dressing, C. D., Hirsch, L. A., et al. 2020, AJ, 160, 287
Schanche, N., Pozuelos, F. J., Günther, M. N., et al. 2022, A&A, 657, A45
Schlafly, E. F., & Finkbeiner, D. P. 2011, ApJ, 737, 103
Schwab, C., Rakich, A., Gong, Q., et al. 2016, SPIE Conf. Ser., 9908, 99087H
Sebastian, D., Gillon, M., Ducrot, E., et al. 2021, A&A, 645, A100
Seifahrt, A., Bean, J. L., Stürmer, J., et al. 2020, SPIE Conf. Ser., 11447, 114471F
Seifahrt, A., Bean, J. L., Kasper, D., et al. 2022, SPIE Conf. Ser., 12184, 121841G
Shappee, B. J., Prieto, J. L., Grupe, D., et al. 2014, ApJ, 788, 48
Smith, J. C., Stumpe, M. C., Van Cleve, J. E., et al. 2012, PASP, 124, 1000
Stassun, K. G., Oelkers, R. J., Pepper, J., et al. 2018, AJ, 156, 183
Stumpe, M. C., Smith, J. C., Van Cleve, J. E., et al. 2012, PASP, 124, 985
Stumpe, M. C., Smith, J. C., Catanzarite, J. H., et al. 2014, PASP, 126, 100
Twicken, J. D., Catanzarite, J. H., Clarke, B. D., et al. 2018, PASP, 130, 064502
Van Eylen, V., Agentoft, C., Lundkvist, M. S., et al. 2018, MNRAS, 479, 4786
Venturini, J., Guilera, O. M., Haldemann, J., Ronco, M. P., & Mordasini, C. 2020, A&A, 643, A1
Waalkes, W. C., Berta-Thompson, Z. K., Collins, K. A., et al. 2021, AJ, 161, 13
Wells, R. D., Rackham, B. V., Schanche, N., et al. 2021, A&A, 653, A97
West, A. A., Hawley, S. L., Bochanski, J. J., et al. 2008, AJ, 135, 785
Wizinowich, P., Acton, D. S., Shelton, C., et al. 2000, PASP, 112, 315
Wong, I., & Shporer, A. 2022, in Bull. Am. Astron. Soc., 54, 102.320
Zacharias, N., Finch, C. T., Girard, T. M., et al. 2012, VizieR Online Data Catalog: I/322A
Ziegler, C., Tokovinin, A., Briceño, C., et al. 2020, AJ, 159, 19

[1] Astrobiology Research Unit, Université de Liège, Allée du 6 Août 19C, 4000 Liège, Belgium
e-mail: mr.ghachoui@gmail.com
[2] Oukaimeden Observatory, High Energy Physics and Astrophysics Laboratory, Cadi Ayyad University, Marrakech, Morocco
[3] Departamento de Fisica e Astronomia, Faculdade de Ciencias, Universidade do Porto, Rua do Campo Alegre, 4169-007 Porto, Portugal
[4] Instituto de Astrofisica e Ciencias do Espaco, Universidade do Porto, CAUP, Rua das Estrelas, 150-762 Porto, Portugal
[5] Center for Space and Habitability, University of Bern, Gesellschaftsstrasse 6, 3012, Bern, Switzerland
[6] Department of Earth, Atmospheric and Planetary Science, Massachusetts Institute of Technology, 77 Massachusetts Avenue, Cambridge, MA 02139, USA
[7] Kavli Institute for Astrophysics and Space Research, Massachusetts Institute of Technology, Cambridge, MA 02139, USA
[8] School of Physics & Astronomy, University of Birmingham, Edgbaston, Birmimgham B15 2TT, UK
[9] Department of Astronomy, University of California Berkeley, Berkeley, CA 94720, USA
[10] Department of Physics and Astronomy, Vanderbilt University, Nashville, TN 37235, USA
[11] NASA Exoplanet Science Institute-Caltech/IPAC, 1200 E. California Blvd, Pasadena, CA 91125 USA
[12] Center for Astrophysics | Harvard & Smithsonian, 60 Garden Street, Cambridge, MA 02138, USA
[13] Universidad Nacional Autónoma de México, Instituto de Astronomía, AP 70-264, Ciudad de México, 04510, Mexico
[14] Space Sciences, Technologies and Astrophysics Research (STAR) Institute, Université de Liège, Allée du 6 Août 19C, 4000 Liège, Belgium
[15] Instituto de Astrofísica de Canarias (IAC), Calle Vía Láctea s/n, 38200 La Laguna, Tenerife, Spain
[16] AIM, CEA, CNRS, Université Paris-Saclay, Université de Paris, F91191 Gif-sur-Yvette, France
[17] Universidad Nacional Autónoma de México, Instituto de Astronomía, AP 106, Ensenada 22800, BC, Mexico
[18] Cavendish Laboratory, JJ Thomson Avenue, Cambridge, CB3 0HE, UK
[19] Instituto de Astrofísica de Andalucía (IAA-CSIC), Glorieta de la Astronomía s/n, 18008 Granada, Spain
[20] Department of Astronomy and Astrophysics, University of California, Santa Cruz, 1156 High St. Santa Cruz, CA 95064, USA
[21] Center for Astrophysics and Space Science, University of California San Diego, La Jolla, CA 92093, USA
[22] Center for Interdisciplinary Exploration and Research in Astrophysics (CIERA), Northwestern University, 1800 Sherman, Evanston, IL 60201, USA
[23] NASA Ames Research Center, Moffett Field, CA 94035, USA
[24] Department of Physics, Massachusetts Institute of Technology, Cambridge, MA 02139, USA
[25] Department of Aeronautics and Astronautics, MIT, 77 Massachusetts Avenue, Cambridge, MA 02139, USA
[26] Department of Physics and Kavli Institute for Astrophysics and Space Research, Massachusetts Institute of Technology, Cambridge, MA 02139, USA
[27] SETI Institute, Mountain View, CA 94043, USA
[28] Department of Astrophysical Sciences, Princeton University, Princeton, NJ 08544, USA
[29] George Mason University, 4400 University Drive, Fairfax, VA 22030, USA
[30] Komaba Institute for Science, The University of Tokyo, 3-8-1 Komaba, Meguro, Tokyo 153-8902, Japan
[31] Instituto de Astrofisica de Canarias (IAC), 38205 La Laguna, Tenerife, Spain
[32] Department of Astronomy and Tsinghua Centre for Astrophysics, Tsinghua University, Beijing 100084, PR China
[33] Astrobiology Center, 2-21-1 Osawa, Mitaka, Tokyo 181-8588, Japan

Appendix A: Target pixel files of TOI-1680

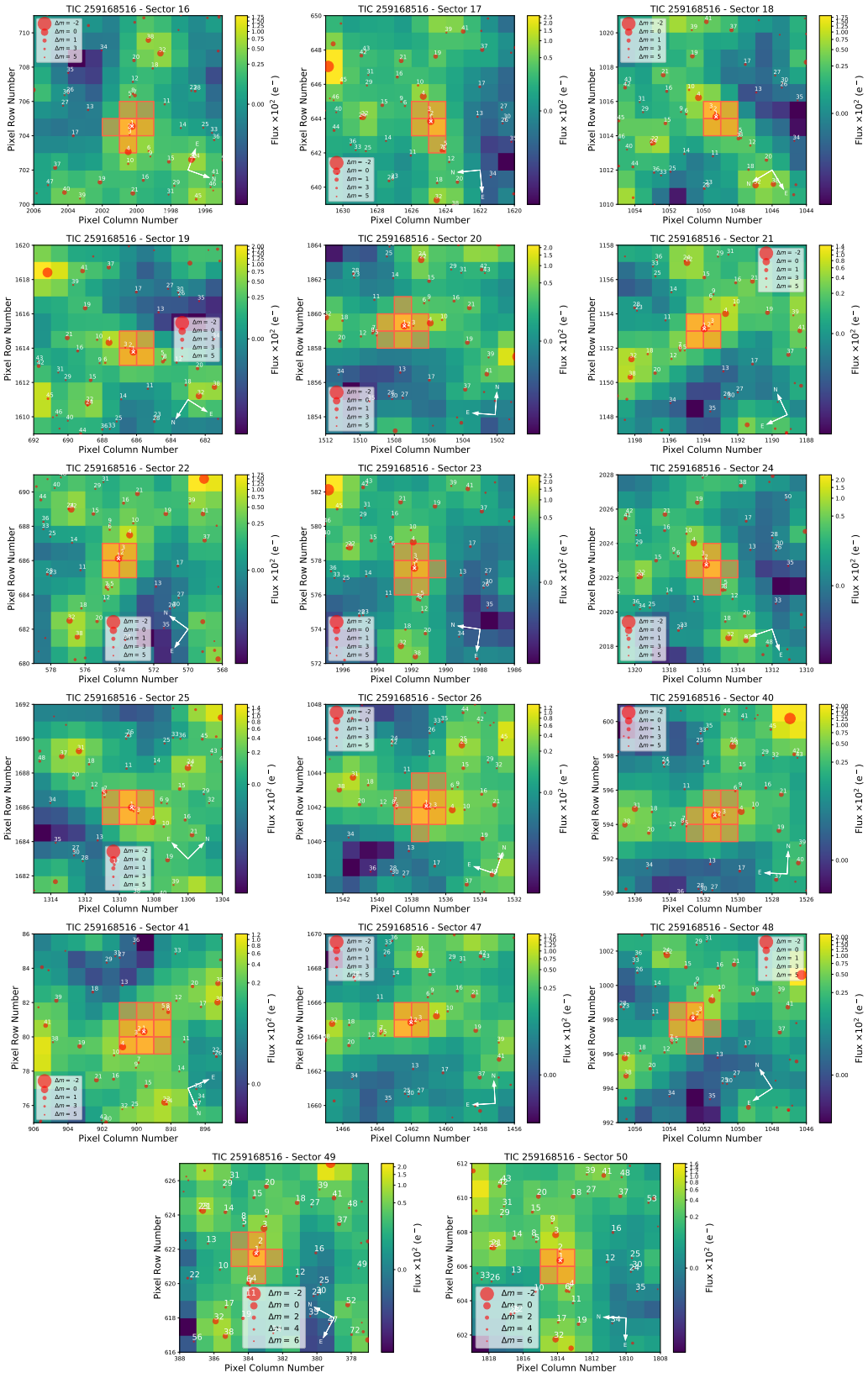

Fig. A.1. TESS target pixel file images of TOI-1680 observed in Sectors 16, 17, 18, 19, 20, 21, 22, 23, 24, 25, 26, 40, 41, 47, 49, and 50, shown on the left. The red circles show the sources in the field identified by the *Gaia* DR2 catalogue with scaled magnitudes. The position of the targets is indicated by white crosses and the mosaic of orange squares show the mask used by the pipeline to extract the SPOC photometry. These plots were created with `tpfplotter` (Aller et al. 2020).

Chapter 5

Conclusion and future work

5.1 Conclusion

During my thesis, I took charge of the entire transiting exoplanet program of the TRAPPIST-North robotic telescope, for more than three years. This program is dedicated to the follow-up of *TESS* objects of interest (TOIs), which are transiting planet candidates. The main goal was to confirm whether the transit-like signals detected by *TESS* are indeed due to transiting exoplanets, or due to other astrophysical phenomena, called "false positives". My main work included the selection of interesting *TESS* planet candidates to observe, scheduling of observations, reduction and analysis of the collected photometric data, and interpretation of results. All this work was conducted in coordination with the *TESS* Follow-up Observing Program Working Group (TFOP-WG), especially Sub-Group 1 (SG1) which is dedicated to the seeing-limited photometric follow-up of *TESS* candidates. After each successful observation, a summarizing report was submitted to SG1.

I contributed to the photometric follow-up of more than 257 *TESS* planet candidates, most of them with the TRAPPIST-North telescope. This work contributed to the *'validation'* of 9 transiting exoplanets. The *'validation'* of exoplanets is a process to confirm the planetary nature of the transit signals through multi-color photometric observations of the transit signal, adaptive optic observations to confirm that the host stars are single, spectroscopic observations to further characterize the host stars (e.g. spectral type, metallicity), as well as statistical validation checking that the transits present a significantly higher probability to be produced by transiting planets than by other astrophysical phenomena. About 11 other planets have been *'validated'* with the measurement of their masses through radial velocity observations. Their masses have been found consistent with planetary-mass companions, which led to classify them as *'confirmed'* planets. *Validated* and *confirmed* planets are presented in peer-reviewed publications. Out of 198 TOIs (of the 275 TOIs) have been found to present signals consistent with transiting planet using only photometric multi-color photometric observations. Such cases are called *'verified planet candidates'* (VPC) and will pass though the *'validation'* process in future. This work also led to the identification of 2 nearby planet candidates (NPC, i.e planets transiting stars close to the targeted stars), 4 eclipsing binaries (EB/SB1), 10 nearby eclipsing binaries (NEB), 9 blended eclipsing binary (BEB/SB2) and 4 false alarm (FA) detections. $\sim$ 10 TOIs remain as planet candidates that

need more photometric follow-up observations.

I led the observations, analyses and publication of a *'validation'* paper of the super-Earth planet TOI-1680 b (Ghachoui et al., 2023). My *MCMC* analyses of the data collected by *TESS* and ground-based telescopes yielded that TOI-1680 b has a radius of $1.460^{+0.063}_{-0.049}\,R_\oplus$ and equilibrium temperature of 404 ± 14 K. It is on a 4.8-days orbit around a mid-type M-dwarf star (TOI-1680, $R_* = 0.2100 \pm 0.0064$ $R_\odot$, $M_* = 0.1800 \pm 0.0044$ $M_\odot$, and $T_{eff} = 3211 \pm 100\,K$, V = 15.87 mag and J = 11.63 mag) located near the northern continuous viewing zone of *JWST* and 37.14 pc away. I also investigated the potential of the planet for mass determination and atmospheric characterization. The mass could be determined with state-of-art instrument such as MAROON-X on 8-m telescope. Once its mass will be determined, TOI-1680 b will join the small sample of keystone planets that could teach us more on the features of the *radius valley* (see e.g. Fulton et al., 2017; Cloutier & Menou, 2020) and the *density valley* (Luque & Pallé, 2022) and, eventually, help us to understand the formation and evolution of super-Earths and mini-Neptunes. Also, I found that TOI-1680 b is a good target for atmospheric characterization, via transmission spectroscopy, with the *JWST* NIRSpec/PRISM instrument. Such observations are encouraged given the star's location near the CVZ of *JWST*.

5.2 Future work

A project of validation paper for TOI-6002 b and TOI-5713 b

I am leading a project of *'validation'* paper for two super-Earth planets, TOI-6002 b and TOI-5713 b (Ghachoui et al., 2024). We used the *TESS* data and ground-based multi-wavelength photometry from various ground-based facilities, as well as high-resolution AO observations to validate the planetary nature of the transit signals for both planets. I used the newer branch of `EXOFASTv2` (Eastman et al., 2013, 2019) to globally model each planet, using all available photometric data, along with the SED fit and the relationships of Mann et al. (2015) and Mann et al. (2019) to characterize the host stars. I found that TOI-6002 b has a radius of $1.65^{+0.22}_{-0.19}\,R_\oplus$ and is on 10.90-days orbit around a mid-type M-dwarf star (TOI-6002, $R_* = 0.2409^{+0.0066}_{-0.0065}$ $R_\odot$, $M_* = 0.2105^{+0.0049}_{-0.0048}$ $M_\odot$, $T_{eff} = 3241^{+82}_{-60}$ K, V = 14.6 mag and J = 11 mag) located 32.04 pc away. On its side, TOI-5713 b has a radius of $1.77^{+0.13}_{-0.11}\,R_\oplus$ and is on a 10.44-days orbit around a mid-type M-dwarf star too (TOI-5713, $0.2985^{+0.0073}_{-0.0072}$ $R_\odot$, $M_* = 0.2654 \pm 0.0061$ $M_\odot$, $T_{eff} = 3228^{+41}_{-40}$ K, V = 15.35 mag and J = 11.07 mag) located 40.94 pc from us. The host star TOI-5713 has been found active, as it showed some clear flares in the *TESS* light curves.

Both planets do not have yet their masses determined via RV observations. To test their potential for this, I used the mass-radius relationship of Chen & Kipping (2017) to estimate their masses, where I found $M_p = 3.8^{+1.6}_{-1.0}\,M_\oplus$ for TOI-6002 b and $M_p = 4.3^{+1.7}_{-1.1}\,M_\oplus$ for TOI-5713 b. Given the masses of the host stars, this would result in reflex motions

with semi-amplitudes in the order of $3\,\mathrm{ms}^{-1}$ for both host stars. Due to the faintness of the stars, achieving such precision with instruments on 4-m class telescopes such as HARPS-N (Cosentino et al., 2012) or CARMENES (Quirrenbach et al., 2020) is challenging. However, it should be possible with the MAROON-X instrument (Seifahrt et al., 2020) at the 8.1-m Gemini North telescope.

Looking at the radii distribution and their corresponding densities in the study of Luque & Pallé (2022) (see Figure 2.2 in Chapter 2), TOI-5713 b falls slightly towards the range of water-rich planets and TOI-6002 b falls in the region where we can find both rocky and water-rich planets. Hence, it is unclear whether the two planets have rocky or water-rich compositions. If they are not of intermediate composition, they might then be either some of the largest rocky planets or some of the smallest water-rich worlds known to date. Also, both planets are located near the opposing sides of the '*keystone planets*' zone of the *radius valley* (Fulton et al., 2017; Cloutier & Menou, 2020) (see Figure 5.1 below), it is then unclear whether they have lost their gaseous envelopes or not. In all cases, when their masses are determined, these planets will be important additional targets to the sample of *'keystone planets'*. This sample is important to conduct strong statistical inferences on the *radius/density valley*. This will ease the refinement of the relative dominance of the various mechanisms thought to lie behind the formation and evolution of super-Earths and sub-Neptunes around M dwarf stars, as elaborated in Chapter 2 (see e.g. Cloutier & Menou, 2020; Cherubim et al., 2023; Luque & Pallé, 2022).

To evaluate the atmospheric study potential for both planets, I initially used the transmission spectroscopy metric (TSM) by Kempton et al. (2018) to prioritize the transiting planets most amenable for atmospheric investigations through transmission spectroscopy with the *JWST*. Given their estimated masses, both planets have TSM values between 40 and 60, with 90 being the threshold for planets in their sizes to be most suitable for atmospheric studies. However, this does not mean that these planets are not important targets. Interestingly, TOI-6002 b and TOI-5713 b receive insolation fluxes of $1.77^{+0.16}_{-0.11} S_{\oplus}$ and $2.42 \pm 0.11 S_{\oplus}$, respectively, which place them near the inner edge of the habitable zones of their host stars (see e.g. Kopparapu et al., 2013; Kaltenegger, 2017). This region is known as the "Venus-zone", referring to the orbit of Venus in our Solar System (see e.g. Kaltenegger et al., 2023). Venus is an Earth-analog in terms of its radius and bulk composition, but it could not save its water as long as Earth. The process presumed to be responsible for this is the so-called "*runaway greenhouse effect*" (see e.g. Goldblatt & Watson, 2012; Kasting et al., 1984; Delrez et al., 2022) caused by water vapor and CO_2, where water evaporation is accelerated. Both planets, TOI-6002 b and TOI-5713 b, are important targets for future atmospheric studies to observe wether they suffered this effect. These studies will help in understanding how potentially habitable planets transition to Venus-like planets as it happened with Venus in our Solar System (see e.g. Delrez et al., 2022; Kaltenegger et al., 2023).

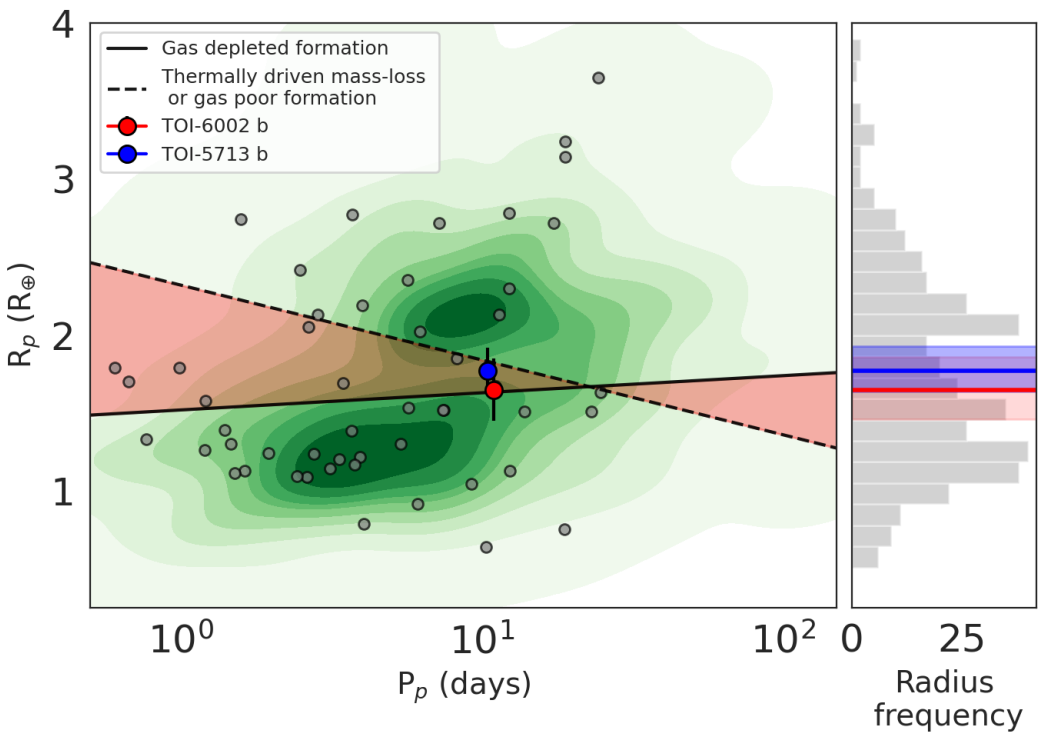

Figure 5.1: Distribution of planet radii and orbital periods for all confirmed small planets hosted by low-mass stars ($M_* \lesssim 0.65\,M_\odot$). The solid line represents the predicted location of the *radius valley* based on the gas-depleted formation model (Cloutier & Menou, 2020). The dashed line shows the predicted location of the valley for the thermally-driven photoevaporation and gas-poor formation models (VanEylen et al., 2018). The red and blue dots represents the planets TOI-6002b and TOI-5713b, respectively. The 1D radius distribution, with the location of the two planets, is shown on the right panel.

Towards the study of super-Earths and sub-Neptunes

The mission *TESS*, supported with seeing-limited ground-based follow-up observations, is on its way to enlarge the sample of super-Earth and sub-Neptune planets in orbits around low mass stars (typically M dwarfs). Many of these planets are amenable to an accurate measurement of their masses through radial velocity observations. These planets will enable the scientific community to conduct in-depth statistical inferences on their formation and evolution mechanisms. One of the pathways followed for this purpose is the *radius/density valley* as explained in details in Chapter 2. I aim to continue the follow-up of promising *TESS* exoplanet candidates for validation along with the selection of those that are amenable to mass determination via radial velocity observations. I will also focus on the study of how super-Earths and sub-Neptunes form and evolve by investigating the *radius/density valley*. A special focus will be placed on the *keystone planets* (see Section 2.1 in Chapter 2) to statistically exploit the diversity of their bulk compositions to test the potential of the various mechanisms thought to be at work in their formation and evolution. This effort is encouraged by the increasing number of these planets.

Appendix A

NEB check for TOI-5663 b

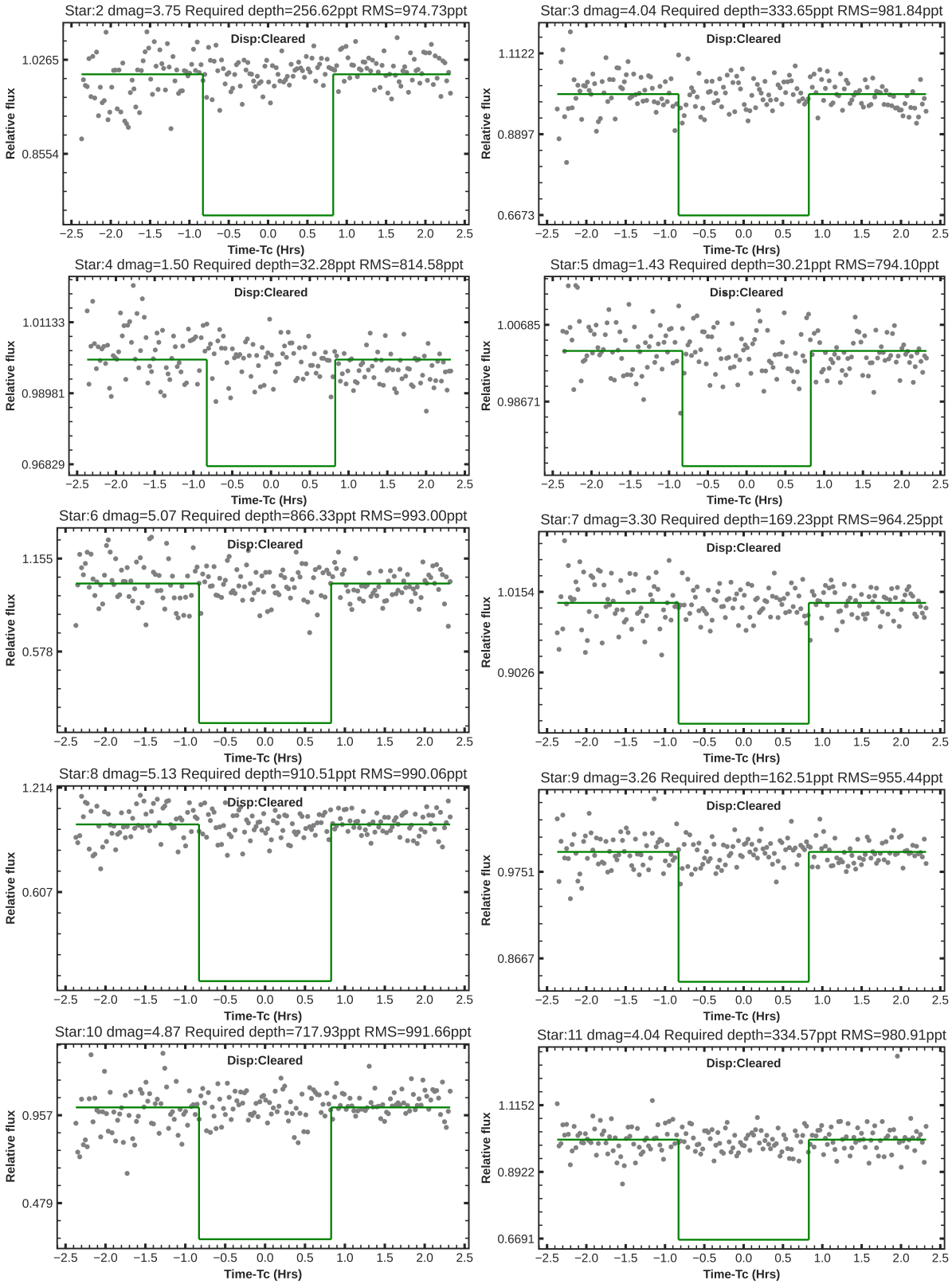
Star:2 dmag=3.75 Required depth=256.62ppt RMS=974.73ppt
Disp:Cleared
Relative flux
1.0265
0.8554
Time-Tc (Hrs)
Star:3 dmag=4.04 Required depth=333.65ppt RMS=981.84ppt
Disp:Cleared
Relative flux
1.1122
0.8897
0.6673
Time-Tc (Hrs)
Star:4 dmag=1.50 Required depth=32.28ppt RMS=814.58ppt
Disp:Cleared
Relative flux
1.01133
0.98981
0.96829
Time-Tc (Hrs)
Star:5 dmag=1.43 Required depth=30.21ppt RMS=794.10ppt
Disp:Cleared
Relative flux
1.00685
0.98671
Time-Tc (Hrs)
Star:6 dmag=5.07 Required depth=866.33ppt RMS=993.00ppt
Disp:Cleared
Relative flux
1.155
0.578
Time-Tc (Hrs)
Star:7 dmag=3.30 Required depth=169.23ppt RMS=964.25ppt
Disp:Cleared
Relative flux
1.0154
0.9026
Time-Tc (Hrs)
Star:8 dmag=5.13 Required depth=910.51ppt RMS=990.06ppt
Disp:Cleared
Relative flux
1.214
0.607
Time-Tc (Hrs)
Star:9 dmag=3.26 Required depth=162.51ppt RMS=955.44ppt
Disp:Cleared
Relative flux
0.9751
0.8667
Time-Tc (Hrs)
Star:10 dmag=4.87 Required depth=717.93ppt RMS=991.66ppt
Disp:Cleared
Relative flux
0.957
0.479
Time-Tc (Hrs)
Star:11 dmag=4.04 Required depth=334.57ppt RMS=980.91ppt
Disp:Cleared
Relative flux
1.1152
0.8922
0.6691
Time-Tc (Hrs)

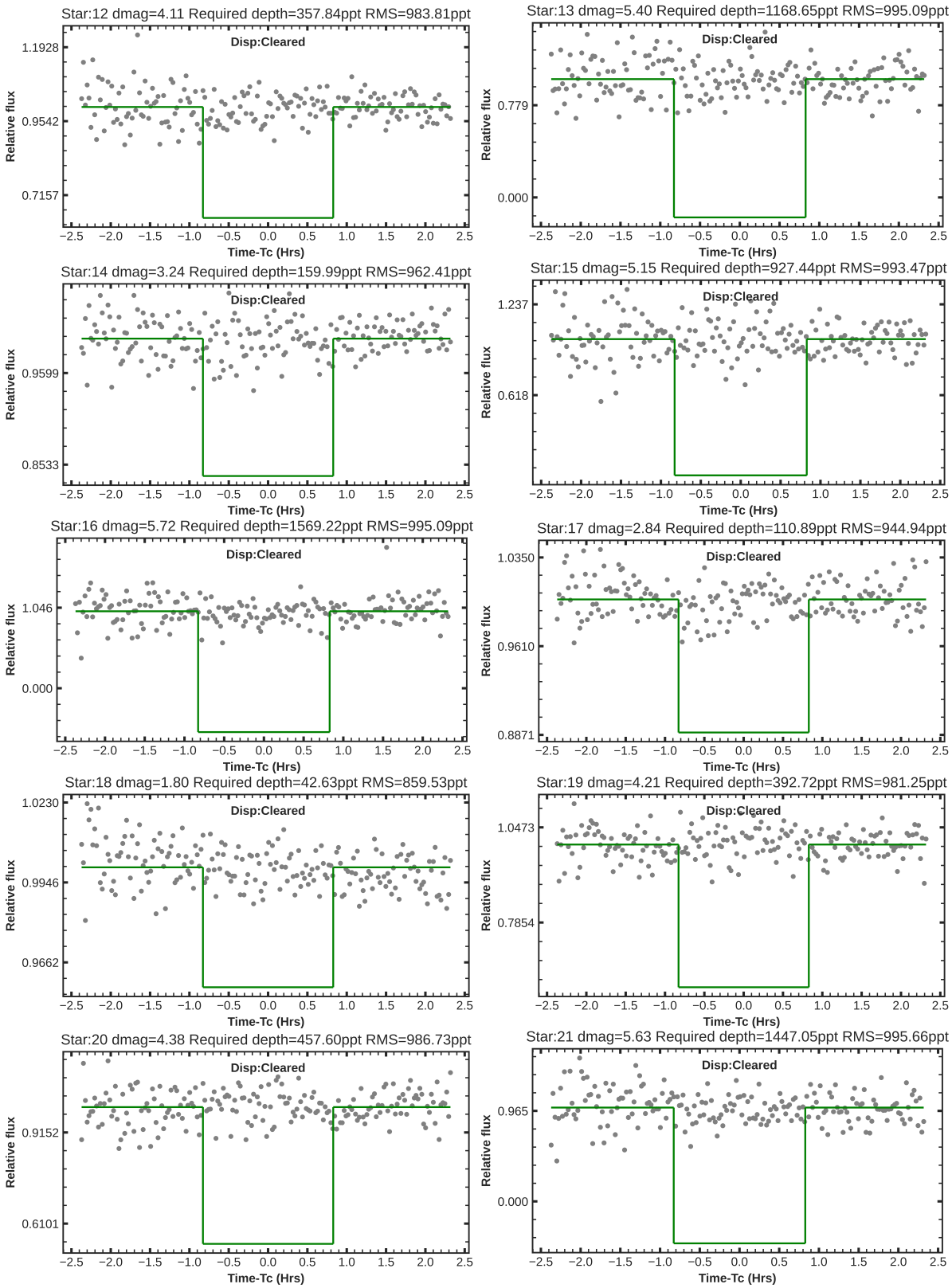

[*Appendix A continued*]

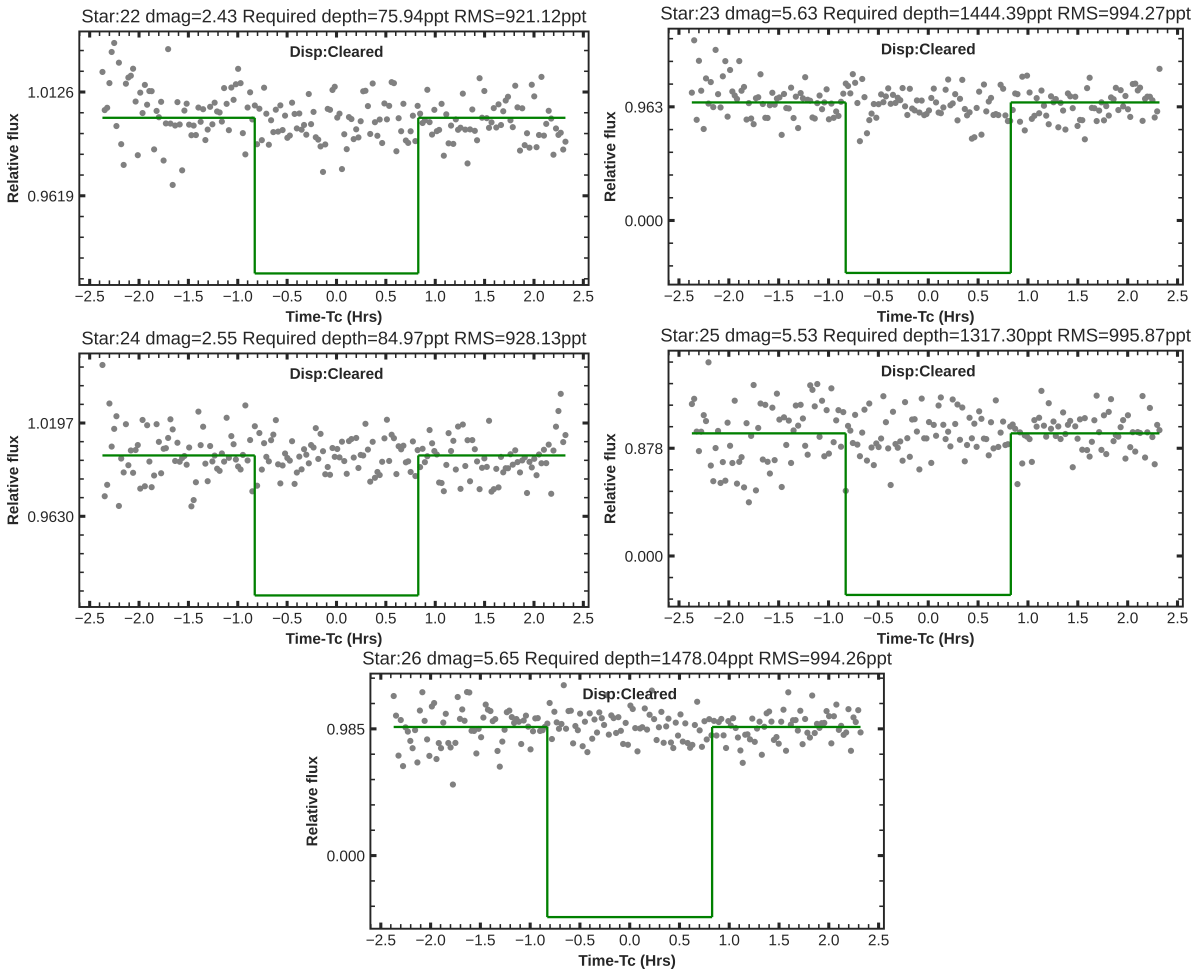

[Appendix A continued]

Appendix B

List of publications

First author publications

- TESS discovery of a super-Earth orbiting the M-dwarf star TOI-1680: ***M. Ghachoui*** *et al. 2023, doi:10.1051/0004-6361/202347040*
- TESS discovery of of two super-Earths orbiting the M-dwarf stars TOI-6002 and TOI-5713: ***M. Ghachoui*** *et al. 2024, doi:10.1051/0004-6361/202451120*

Co-author publications

- Color validation of TESS candidates: a Super-Earth Transiting the Nearby M Dwarf TOI-1846: *A.Soubkiou, K.Barkaoui,* ***M.Ghachoui*** *and al (in prep.)*
- TOI-4336 A b: A temperate sub-Neptune ripe for atmospheric characterization in a nearby triple M-dwarf system: *Timmermans et al. incl* ***M.Ghachoui****. 2024. 10.48550/arXiv.2404.12722*
- Detection of an Earth-sized exoplanet orbiting the nearby ultracool dwarf star SPECULOOS-3: *Michaël Gillon et al. incl* ***M. Ghachoui****, 2024, Nature Astronomy, doi:10.1038/s41550-024-02271-2*
- Identification of the Top TESS Objects of Interest for Atmospheric Characterization of Transiting Exoplanets with JWST: *Hord et al. incl incl* ***M.Ghachoui****. 2024, The Astronomical Journal, 167, 233. 10.3847/1538-3881/ad3068*
- A hot mini-Neptune and a temperate, highly eccentric sub-Saturn around the bright K-dwarf TOI-2134: *Rescigno et al. incl.* ***M.Ghachoui****. 2024, Mon. Not. R. Astron. Soc., 527, 5385. doi:10.1093/mnras/stad3255*
- An M dwarf accompanied by a close-in giant orbiter with SPECULOOS: *Triaud et al. incl.* ***M.Ghachoui****. 2023, Mon. Not. R. Astron. Soc., 525, L98. doi:10.1093/mnrasl/slad097*
- TOI-2084 b and TOI-4184 b: Two new sub-Neptunes around M dwarf stars: *Barkaoui et al. incl* ***M.Ghachoui****. 2023a, Astron. Astrophys., 677, A38. doi:10.1051/0004-6361/202346838*
- Identification of the Top TESS Objects of Interest for Atmospheric Characterization of Transiting Exoplanets with JWST: *Hord et al. incl.* ***M.Ghachoui****. 2023, doi:10.48550/arXiv.2308.09617*
- WASP-193b: An extremely low-density super-Neptune: *Barkaoui et al. incl* ***M.Ghachoui****. 2023b, doi:10.48550/arXiv.2307.08350*

- VaTEST. II. Statistical Validation of 11 TESS-detected Exoplanets Orbiting K-type Stars: *Mistry et al. incl.* ***M. Ghachoui****. 2023, Astron. J., 166, 9. doi:10.3847/1538-3881/acd548*
- Another shipment of six short-period giant planets from TESS: *Rodriguez et al. incl.* ***M. Ghachoui****. 2023, Mon. Not. R. Astron. Soc., 521, 2765. doi:10.1093/mnras/stad595*
- TOI-1442 b and TOI-2445 b: Two potentially rocky ultra-short period planets around M dwarfs: *Morello et al. incl.* ***M. Ghachoui****. 2023, Astron. Astrophys., 673, A32. doi:10.1051/0004-6361/202243592*
- VizieR Online Data Catalog: TESS Grand Unified Hot Jupiter Surveys. II: *Yee et al. incl.* ***M. Ghachoui****. 2023b, VizieR Online Data Catalog, J/ApJS/265/1.*
- A super-Earth and a mini-Neptune near the 2:1 MMR straddling the radius valley around the nearby mid-M dwarf TOI-2096: *Pozuelos et al. incl.* ***M. Ghachoui****. 2023, aap, 672, A70. doi:10.1051/0004-6361/202245440*
- The TESS Grand Unified Hot Jupiter Survey. II. Twenty New Giant Planets: *Yee et al. incl.* ***M. Ghachoui****. 2023a, VizieR Online Data Catalog, J/ApJS/265/1. 10.3847/1538-4365/aca286*
- TOI-3235 b: A Transiting Giant Planet around an M4 Dwarf Star: *Hobson et al. incl.* ***M. Ghachoui****. 2023, Astrophys. J., Letters, 946, L4. 10.3847/2041-8213/acbd9a*
- TESS discovery of a sub-Neptune orbiting a mid-M dwarf TOI-2136: *Gan et al. incl* ***M. Ghachoui****. 2022, Mon. Not. R. Astron. Soc., 514, 4120. doi:10.1093/mnras/stac1448*
- HATS-74Ab, HATS-75b, HATS-76b, and HATS-77b: Four Transiting Giant Planets Around K and M Dwarfs: *Jordan et al. incl.* ***M. Ghachoui****. 2022b, Astron. J., 163, 125. doi:10.3847/1538-3881/ac4a77*
- Validation of 13 Hot and Potentially Terrestrial TESS Planets: *Giacalone et al. incl.* ***M. Ghachoui****. 2022, Astron. J., 163, 99. doi:10.3847/1538-3881/ac4334*
- TOI-2257 b: A highly eccentric long-period sub-Neptune transiting a nearby M dwarf: *Schanche et al. incl.* ***M. Ghachoui****. 2022, Astron. Astrophys., 657, A45. doi:10.1051/0004-6361/202142280*
- VizieR Online Data Catalog: Warm Jupiters in TESS FFIs 1st year (2018-2019 July): *Dong et al. incl.* ***M. Ghachoui****. 2021, VizieR Online Data Catalog, J/ApJS/255/6. doi:10.26093/cds/vizier.22550006*
- A large sub-Neptune transiting the thick-disk M4 V TOI-2406: *Wells et al. incl.* ***M. Ghachoui****. 2021, Astron. Astrophys., 653, A97. doi:10.1051/0004-6361/202141277*

- TOI-1830 and TOI-1312: Two EBs hosting very low-mass stellar companions in eccentric orbits: *Rabus et al. incl.* ***M. Ghachoui****. 2021, in Posters from the TESS Science Conference II (TSC2), 179. doi:10.5281/zenodo.5131541*

- Warm Jupiters in TESS Full-frame Images: A Catalog and Observed Eccentricity Distribution for Year 1: *Dong et al. incl.* ***M. Ghachoui****. 2021, VizieR Online Data Catalog, J/ApJS/255/6. doi:10.3847/1538-4365/abf73c*

- VizieR Online Data Catalog: TRICERATOPS predictions for 384 TOIs: *Giacalone et al. incl.* ***M. Ghachoui****. 2021a, VizieR Online Data Catalog, J/AJ/161/24. doi:10.26093/cds/vizie*

- Vetting of 384 TESS Objects of Interest with TRICERATOPS and Statistical Validation of 12 Planet Candidates: *Giacalone et al. incl.* ***M. Ghachoui****. 2021b, Astron. J., 161, 24. doi:10.3847/1538-3881/abc6af*

- A super-Earth and a sub-Neptune orbiting the bright, quiet M3 dwarf TOI-1266: *Demory et al. incl.* ***M. Ghachoui****. 2020, Astron. Astrophys., 642, A49. doi:10.1051/0004-6361/202038616*

Proceedings

- Using the OWL@OUKA telescope to follow-up the TESS planet candidates: first results: *Ghachoui et al. 2020, in Society of Photo-Optical Instrumentation Engineers (SPIE) Conference Series, Vol. 11447, Society of Photo-Optical Instru- mentation Engineers (SPIE) Conference Series, 114479Z. doi:10.1117/12.2562184*

Appendix C

Proceeding

Using the OWL@OUKA telescope to follow-up the TESS planet candidates: first results

Ghachoui, Mourad, Benkhaldoun, Zouhair, Soubkiou, Abderahmane, Barkaoui, Khalid, Daassou, Ahmed, et al.

Mourad Ghachoui, Zouhair Benkhaldoun, Abderahmane Soubkiou, Khalid Barkaoui, Ahmed Daassou, Hong-Suh Yim, Myung-Jin Kim, Dong-Goo Roh, Youssef El Azhari, Abdelhadi Jabiri, "Using the OWL@OUKA telescope to follow-up the TESS planet candidates: first results," Proc. SPIE 11447, Ground-based and Airborne Instrumentation for Astronomy VIII, 114479Z (13 December 2020); doi: 10.1117/12.2562184

SPIE.

Event: SPIE Astronomical Telescopes + Instrumentation, 2020, Online Only

Using the OWL@OUKA telescope to follow-up the TESS planet candidates: First results

Mourad Ghachoui[a], Zouhair Benkhaldoun[a], Abderahmane Soubkiou[a], Khalid Barkaoui[a,b], Ahmed Daassou[a,c], Hong-Suh Yim[d], Myung-Jin Kim[d], Dong-Goo Roh[d], Youssef El Azhari[a], and abdelhadi jabiri[a]

[a]Oukaimeden Observatory, High Energy Physics and Astrophysics Laboratory, Cadi Ayyad University, Marrakesh, Morocco.
[b]Astrobiology Research Unit, Université de Liège, Allée du 6 Août19C, B-4000 Liège, Belgium.
[c]Fundamental and Applied Physics Laboratory -Safi, Physics Department, Polydisciplinary Faculty, Cadi Ayyad University, Marrakesh, Morocco.
[d]Korean Astronomy and Space Science Institute (KASI), Daejeon, Korea.

ABSTRACT

The OWL@OUKA is the Optical Wide-field patroL (OWL) facility designed and built by Korea Astronomy and Space Science Institute (KASI) and installed in 2015 at Oukaimeden Observatory. For the first time we used the opportunities offered by this instrument for the detection and monitoring the exoplanets by the transit method. In this work, we present, first, the validation of the OWL@OUKA for the transit method by reporting the observations we have done to calibrate the instrument in order to chose the best exposure time for a given star. We report on the results obtained form the first observations, in V filter, of a known transit event of the planet Qatar-1b, a hot Jupiter orbiting a metal-rich K dwarf star ($T_{eff} = 5013.0, V_{mag} = 12.84$). We have used the software AstroImagJ to reduce the data and the software EXOFASTv2 to fit the transit and extract the planetary parameters, where we obtained a transit depth $0.0207^{+0.0044}_{-0.0040}$ and a planetary radius of 1.09 ± 0.11 R_J, that are in good consistence with the discovery paper. Given the good results obtained, we moved to the second stage of our program, which consists of tracking TESS candidates.

Keywords: Telescope, Exoplanet, Transit method, TESS.

1. INTRODUCTION

The discovery of the first exoplanet[1] – planet outside our solar system– opened up the opportunity to one of the most exciting fields of science, exoplanetology. Since that first discovery, more than 4171 exoplanets have been detected and confirmed according to the NASA Exoplanet Archive catalog. Many technique methods are used to detect exoplanets and the transit method is mostly used thanks to its facility and the information it can provides about the object. For such a transiting planet, it is possible to determine its mass, radius, orbital parameters and its atmospheric properties.

To further understand the exo-worlds, many NASA's space missions have been launched alongside many ground based instrumentation. The NASA's Transiting Exoplanets Survey Satellite (TESS[2]) is further revolutionizing the exoplanets field by detecting transiting planets of all sizes in orbit around bright and nearby stars that are mainly chosen for easy spectroscopic investigations on the planetary masses and atmospheres, by the upcoming James Web Space Telescope (JWST). TESS is well underway to reach its goal of detecting upwards thousand planets smaller than Neptune by focusing on at least 200 000 pre-selected main-sequence stars.[2]

In this paper, we present the validation of OWL@OUKA instrument to follow-up TESS candidates. OWL@OUKA is a 50-cm diameter robotic telescope designed and built by the Korean Astronomy and Space Science Institute (KASI) and installed since 2015 at Oukaimeden observatory . We present, first, the protocol we followed to calibrate the instrument in order to choose the best exposure time for a given star. Then, we report on the results obtained from the first observation we have performed for a known transit event of the planet Qatar-1b.

E-mail: mr.ghachoui@gmail.com

Ground-based and Airborne Instrumentation for Astronomy VIII, edited by Christopher J. Evans, Julia J. Bryant, Kentaro Motohara, Proc. of SPIE Vol. 11447, 114479Z · © 2020 SPIE · CCC code: 0277-786X/20/$21 · doi: 10.1117/12.2562184

2. OWL-NET PROJECT

OWL-Net (Optical Wild-field patroL Network) is a South-Korean project funded and led by the Korean Astronomy and Space Science Institute (KASI). The project consists of five similar observatories uniformly spread around the world (Mongolia, Morocco, Israel, South Korea and USA). Each observatory consists of a 0.5-m diameter robotic telescope controlled by the headquarters located in Daejeon, Korea. The project is devoted to follow-up South-Korean LEO and GEO satellites with the aim of obtaining their orbital information and maintain their orbital elements.[3]

3. TELESCOPE AND INSTRUMENTATION

The OWL@OUKA telescope (figure 1) is one of the five similar stations of OWL-net project. With a field of view of $1.1deg \times 1.1deg$ on the CCD sensor. The telescope consists of a 0.5-m primary mirror in the Ritchey-Chretien configuration and a 0.2-m secondary mirror.[4] It is installed at the Oukaimeden Observatory in collaboration with Cadi Ayyad University in Marrakesh, Morocco. It is equipped with an alt-azimuthal mount. The telescope maximum speed is of 10 deg/sec and its acceleration is 2 deg/sec. Regarding its relatively simple structure and quite wide sight, a clamshel type dome was adopted to the telescope. It is controlled in a fully robotic manner. An environment monitoring system is adopted to the observatory to record the weather conditions.[3]

(a) (b)

Figure 1. (a): close-up of the 50-cm OWL@OUKA telescope. (b): The dome of OWL@OUKA at the Oukaimeden Observatory

OWL@OUKA is equipped with an electrically cooled ProLine PL 16803 CCD camera* with 4096×4096 9-μm pixels on the CCD sensor and a pixel scale of 1 arcsecond per pixel. The camera is fitted with a wheel of four filters (B, V, R and I) and one clear position. The tracking accuracy allows an exposure time of five minutes maximum. The quantum efficiency (figure 2) of the CCD detector presents a maximum of 60% near 560 nm. There are two readout modes: low noise readout mode with $10e^-$ @ 1 MHz and fast readout mode with $14e^-$ @ MHz. The cooling is 55 Cdeg below ambient. Usually, during the observations, the temperature of the CCD detector is set to -20 deg.

4. OBSERVATIONS

In order to find a transit event observable from the Oukaimeden Observatory, we have used the Exoplanet Transit Database ETD[5] and we found the transit event of the hot Jupiter Qatar-1b.[6,7] Before performing the first observations, we had to perform many trial observations, in the filter being used, for the purpose of

*http://www.flicamera.com/spec_sheets/PL16803.pdf

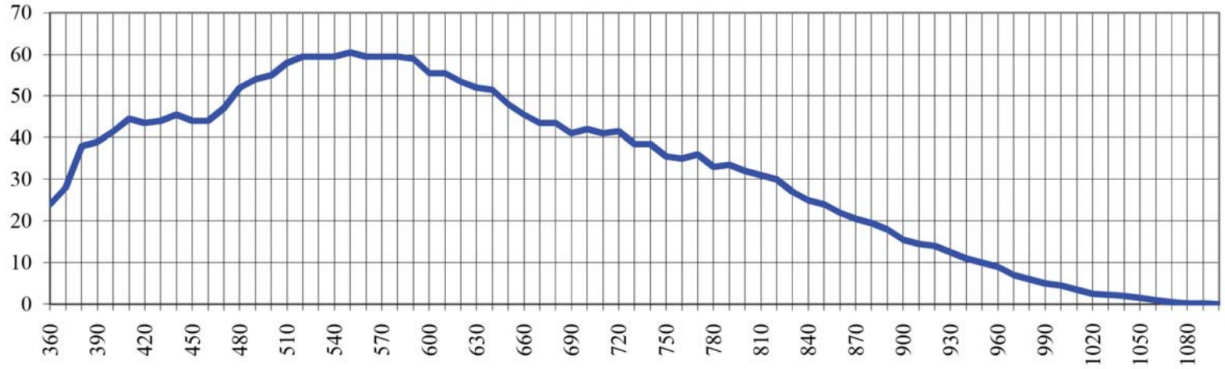

Figure 2. The quantum efficiency of OWL@OUKA CCD camera ProLine PL 16803. .

choosing the best exposure time for a given star taking into account its V magnitude. The idea was to gather many sequences of images with the one filter (filter being used) but with different exposure times. The best exposure time has been chosen on the basis of minimizing the signal-to-noise without saturating the CCD camera. Then, we passed to perform photometric time series observation separately in the V and R filters while target has an elevation greeter than 30 degrees from the local horizon. Generally, we start the observations about one hour before the predicted start of the transit and end one hour after the predicted end of the transit to take into account the out-of-transit data.

To evaluate the best exposure time for our target stars, we have used a Exposure Time Calculator (ETC) written in Fortran by Michaël Gillon and used for TRAPPIST[8,9] telescopes. This ETC takes into account all the necessary parameters (e.g spectral type, filter, Vmag, primary mirror, secondary mirror, elevation,...) that have an effect on the exposure time for a given star. For this ETC code to be convenient for our telescope instrumentation, we have introduced the necessary modifications especially on the primary and secondary mirrors, focal ratio.

5. DATA REDUCTION

To reduce our data, we have used the software AstroImageJ (AIJ[10]). AIJ software creates first the Master Bias file by average combining the raw bias images, creates the Master Dark files by average combining the raw Dark images and Bias subtracts the Master Dark file. Then, AIJ software both Bias and Dark subtracts each raw flat file and, creates the Master flat. Each science exposure is both Master Bias and Master Dark subtracted and flat-field divided. Following the instructions detailed in the AIJ user guide, we used AIJ to extract the flux and perform multi-apertures differential photometry providing us the differential light curves of the target as well as the comparison stars. Although AIJ can be used to analyze the data, we have used the EXOFASTv2[11] software to perform the analyses on the flux file provided by AIJ.

6. DATA ANALYSIS AND RESULTS

To fully characterize the Qatar-1 system, we used the EXOFASTv2 software package,[12,13] which uses a differential evolution Markov chain Monte Carlo to model the stellar system by simultaneously fitting our OWL@OUKA transits, the spectral energy distribution, and the MIST stellar evolutionary models.[14]

To constrain the SED, We pulled $BVgri$ magnitudes from APASS,[15] the JHK_s magnitudes from 2MASS,[16] and W1,W2,W3 from the AllWISE catalog,[17] and the Gaia DR2.[18] For the fit, we used Gaussian priors on T_{eff} and [Fe/H] from the spectral analysis of the discovery paper of Qatar-1b,[6] as well as Gaussian priors on the parallax from Gaia DR2,[18] adding 82μas to correct for the systematic offset reported in Stassun and Torres paper[19] and adding the 33μas uncertainty in their offset in quadrature to the Gaia-reported uncertainty. We defined the orbit of planet b as circular and we applied a Gaussian prior on the orbital period and an upper limit on the V-band extinction from the Schlafly and Finkbeiner dust maps.[20] The resulting EXOFASTv2 fit of transits (figure 4 and 5), SED (figures 3) and MIST provides parameters reported in table 1.

Parameter		OWL@OUKA	Discovery paper[6]
Stellar parameters:			
M_*	Mass ($M_\odot$)	$0.812^{+0.035}_{-0.030}$	0.85 ± 0.03
R_*	Radius($R_\odot$)	0.793±0.019	0.82 ± 0.025
ρ_*	Density (cgs)	$2.30^{+0.14}_{-0.13}$	2.14 ± 0.16
log$g$	Surface gravity (cgs)	4.550±0.018	4.536 ± 0.024
T_{eff}	Effective Temperature (K)	4920^{+83}_{-78}	4861 ± 125
$[Fe/H]$	Metallicity (dex)	$0.185^{+0.094}_{-0.093}$	0.20 ± 0.10
Planetary parameters:			
Depth	Transit depth (fraction)	$0.0183^{+0.0032}_{-0.0028}$	0.0211±0.00045
R_p	Radius R_J	$1.044^{+0.083}_{-0.078}$	1.164 ±0.045
T_{eq}	Equilibrium temperature (K)	1379^{+26}_{-24}	1399 ±42
T_{14}	Total transit duration (days)	$0.0683^{+0.0013}_{-0.0012}$	0.067 16 ± 0.000 77
b	Transit Impact parameter	$0.619^{+0.027}_{-0.029}$	$0.696^{+0.021}_{-0.024}$
τ	Ingress/egress transit duration (days)	$0.0125^{+0.0012}_{-0.0011}$	
P	Period(days)	1.42002405±0.00000021	1.4200 33±0.000 016
a	Semi-major axis (AU)	0.02344±0.00037	$0.02343^{+0.00026}_{-0.00025}$

Table 1. Stellar and planetary parameters obtained from the best fit of transits, SED and MIST.

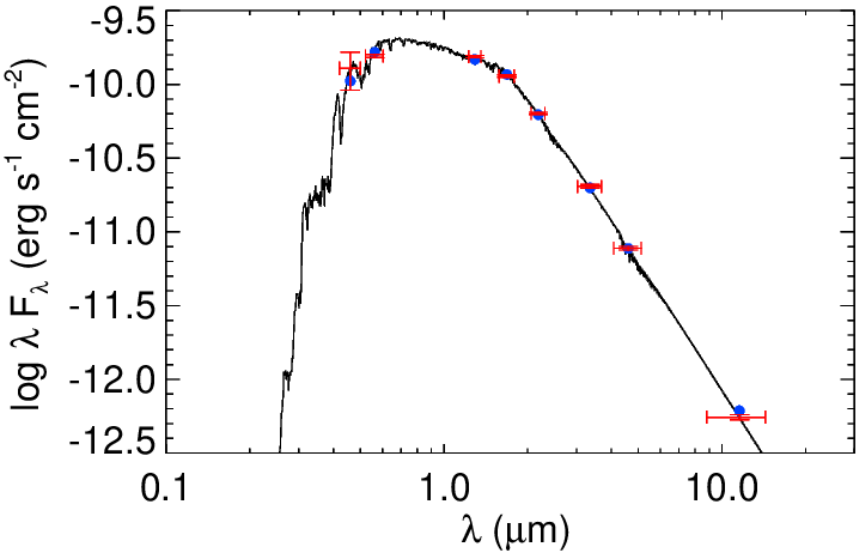

Figure 3. Spectral energy distribution (SED) of Qatar-1. Red symbols correspond to the observed photometric measurements, where the horizontal bars correspond to the effective width of the passband. Blue symbols are the model fluxes from the best-fit NextGen atmosphere model (black).

7. CONCLUSIONS AND FUTURE WORK

We have presented observations of Qatar-1b, where we have used for the first time the OWL@OUKA instrument of which we have presented a detailed description as well as the the OWL-Net project. We have reported the differential photometry time series of the transits of Qatar-1b. Combining all the transits together, we have obtained a transit depth with a precision of about 11ppt. Given this precision and regarding our experiments, OWL@OUKA can be used for potential detection and characterization of hot Jupiters with transit depth >8ppt.

We have reported the analyses we performed for both planet and host star using EXOFASTv2 software. The planetary parameters we have obtained are in good consistence with the literature, which encouraged us to move to the next step of our program that aims at the following up of TESS planet candidates. Actually,

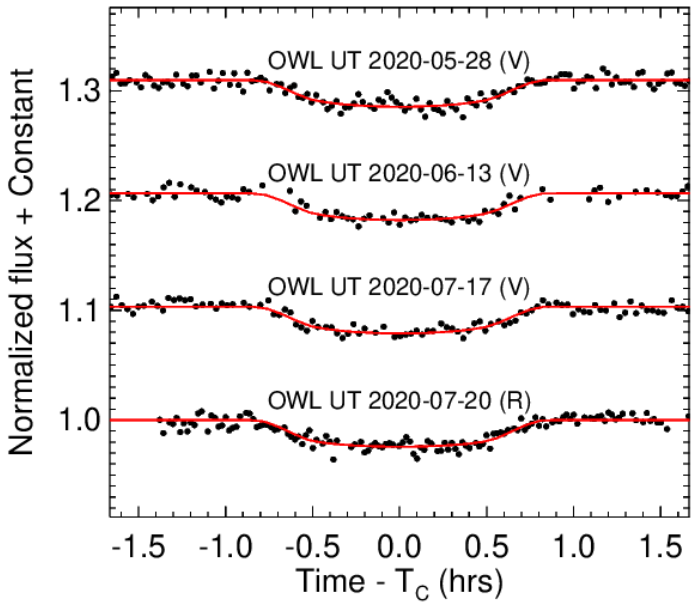

Figure 4. Phase-folded light transits (black dots) obtained for each observation. The red line shows the best fit transit model.

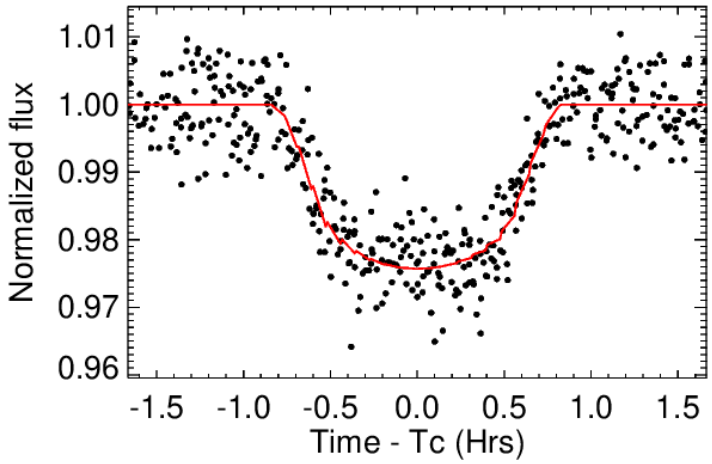

Figure 5. Combined and phase-folded light curve of Qatar-1b (black dots). The red line shows the best fit transit model.

OWL@OUKA is recognized as one of the ground-based facilities contributing to the TESS Follow-up Observing Program Working Groupe (TFOP-WG) Sub Groupe 1 (SG1).

REFERENCES

[1] Mayor, M. and Queloz, D. *Nature* **378**, 355–359 (Nov. 1995).

[2] Ricker, G. R., Winn, J. N., and Vanderspek, e. a. *Journal of Astronomical Telescopes, Instruments, and Systems* **1**, 014003 (Jan. 2015).

[3] Park, J.-H., Yim, H.-S., and Choi, e. a. *Advances in Space Research* **62**, 152–163 (July 2018).

[4] Park, J., Choi, Y., Jo, J., and Moon, e. a. in [*Advanced Maui Optical and Space Surveillance Technologies Conference*], E14 (Sept. 2014).

[5] Poddaný, S., Brát, L., and Pejcha, O. *na* **15**, 297–301 (Mar. 2010).
[6] Alsubai, K. A., Parley, N. R., and Bramich, e. a. *mnras* **417**, 709–716 (Oct. 2011).
[7] Collins, K. A., Kielkopf, J. F., and Stassun, K. G. *aj* **153**, 78 (jan 2017).
[8] Jehin, E., Gillon, M., Queloz, D., Magain, P., Manfroid, J., Chantry, V., Lendl, M., Hutsemékers, D., and Udry, S. *The Messenger* **145**, 2–6 (Sept. 2011).
[9] Jehin, E., Gillon, M., and Opitom, e. a. in [*European Planetary Science Congress*], EPSC2013–968 (Sept. 2013).
[10] Collins, K. A., Kielkopf, J. F., and Stassun, e. a. *aj* **153**, 77 (Feb 2017).
[11] Eastman, J. D., Rodriguez, J. E., and Agol, e. a. *arXiv e-prints* , arXiv:1907.09480 (Jul 2019).
[12] Eastman, J. (Oct. 2017).
[13] et al, J. D. E. (2019).
[14] Dotter, A. *apjs* **222**, 8 (Jan. 2016).
[15] Henden, A. A., Templeton, M., and Terrell, e. a. *VizieR Online Data Catalog* , II/336 (Jan. 2016).
[16] Cutri, R. M., Skrutskie, M. F., and van Dyk, e. a. *VizieR Online Data Catalog* , II/246 (June 2003).
[17] Cutri, R. M. and et al. *VizieR Online Data Catalog* , II/328 (Nov. 2013).
[18] Gaia Collaboration, Brown, A. G. A., and Vallenari, e. a. *aap* **616**, A1 (Aug. 2018).
[19] Stassun, K. G. and Torres, G. *apj* **862**, 61 (July 2018).
[20] Schlafly, E. F. and Finkbeiner, D. P. *apj* **737**, 103 (Aug. 2011).

Appendix D

List of TOIs observed by TRAPPIST-North telescope and submitted to ExoFOP. The TOIs I worked on are highlighted in yellow

TIC ID	TOI	Planet radius	date	Transit coverage	filter	Disposition
320208949	3867.01	11.85	2024-02-28	Full	zp	VPC+
252913663	6909.01	--	2024-02-25	Full	I+z	VPC
318209162	5746.01	12.63	2024-02-23	Full	B	SEB1
416542079	3860.01	14.47	2024-02-19	Full	zp	VPC+
27414976	6694.01	13.45	2024-02-18	Full	B	VPC+
455153906	4772.01	13.04	2024-02-17	Full	zp	VPC+
27414976	6694.01	13.45	2024-02-02	Full	I+z	VPC+
67444896	5479.01	11.92	2024-01-31	Full	zp	VPC
32004914	4814.01	15.82	2024-01-23	Full	zp	VPC+
302381442	5570.01	9.49	2024-01-22	Full	zp	VPC
318796593	2886.01	18.65	2024-01-21	Full	zp	VPC+
438073782	5091.01	16.50	2024-01-12	Full	zp	VPC+
39724477	2729.01	12.53	2024-01-11	Full	zp	VPC+
94823134	5501.01	8.65	2024-01-10	Full	zp	VPC
168936945	6449.01	12.14	2024-01-08	Full	zp	VPC+?
122798633	6446.01	11.52	2024-01-07	Full	zp	VPC+
373612558	3801.01	12.84	2024-01-06	Full	I+z	VPC-
248689510	4681.01	14.55	2024-01-04	Full	zp	VPC+
373614579	3799.01	14.67	2024-01-01	Full	zp	VPC
196474344	6320.01	18.92	2023-12-31	Full	zp	VPC
29105766	3793.01	17.89	2023-12-30	Full	I+z	VPC+
368678195	6027.01	24.29	2023-12-29	Full	B	VPC+
38399060	2692.01	12.17	2023-12-27	Full	B	VPC
142381532	1823.01	8.03	2023-12-27	Egress	B	VPC
248689510	4681.01	14.55	2023-12-26	Full	zp	VPC+
277833423	3426.01	18.58	2023-12-26	Full	zp	VPC+
9346507	3826.01	17.25	2023-12-25	Ingress	zp	VPC+
428317266	6216.01	10.95	2023-12-25	Ingress	zp	VPC
217980791	6141.01	16.21	2023-12-24	Full	zp	VPC+
237603062	4202.01	nan	2023-12-24	Full	zp	VPC
312345863	3671.01	20.20	2023-12-22	Full	I+z	VPC
452867348	6408.01	11.10	2023-12-22	Full	I+z	VPC-+
122798633	6446.01	11.52	2023-12-21	Full	I+z	VPC+

200775844	6325.01	6.79	2023-12-17	Full	I+z	VPC
32004914	4814.01	15.82	2023-12-15	Full	B	VPC+
357244603	5583.01	11.14	2023-12-15	Full	I+z	VPC+
186715217	6338.01	10.79	2023-12-13	Full	zp	VPC
33397739	5292.01	13.44	2023-12-11	Full	zp	VPC
75697959	5433.01	12.17	2023-12-11	Full	I+z	VPC+
9136777	6356.01	16.25	2023-12-10	Full	zp	VPC
33397739	5292.01	13.44	2023-12-09	Egress	I+z	VPC
104195270	6696.01	23.32	2023-12-06	Full	B	SEB1
68850908	3775.01	15.85	2023-12-03	Full	zp	VPC+
46772529	6486.01	15.99	2023-11-28	Full	I+z	VPC
102808276	6056.01	12.61	2023-11-28	Full	I+z	VPC+
368678195	6027.01	24.29	2023-11-22	Full	zp	VPC+
381591826	6337.01	9.85	2023-11-18	Full	I+z	VPC
186715217	6338.01	10.79	2023-11-17	Full	I+z	VPC
274002141	6368.01	11.43	2023-11-13	Full	zp	VPC
202869426	6307.01	12.63	2023-11-12	Full	zp	VPC+
184739529	6342.01	13.67	2023-11-11	Full	B	VPC+
328513434	6383.01	11.41	2023-11-11	Full	zp	VPC+
258037656	5879.01	9.63	2023-11-10	Full	gp	VPC+
328513434	6383.01	11.41	2023-11-08	Full	I+z	VPC+
202869426	6307.01	12.63	2023-11-07	Full	I+z	VPC+
3027681	3723.01	14.65	2023-11-05	Full	I+z	VPC
280315875	4012.01	11.75	2023-11-04	Full	B	VPC+
44295981	6137.01	21.82	2023-11-03	Full	I+z	VPC
322046084	4449.01	12.99	2023-10-21	Full	V	VPC+
437736517	6229.01	10.61	2023-10-12	Full	zp	VPC+
53874375	6227.01	15.73	2023-10-04	Full	I+z	VPC
298776943	6176.01	12.93	2023-10-02	Full	zp	VPC
411343008	6153.01	14.49	2023-10-01	Full	zp	VPC
322498101	6119.01	16.59	2023-09-24	Full	zp	VPC
274002141	6368.01	11.43	2023-08-27	Full	I+z	VPC
171312653	5284.01	21.55	2023-07-29	Egress	zp	VPC-+
404456775	6158.01	9.04	2023-07-27	Full	zp	VPC
258037656	5879.01	9.63	2023-07-16	Full	I+z	VPC+

388076422	6034.01	12.15	2023-07-15	Full	zp	VPC+
247172524	5878.01	14.80	2023-07-07	Full	B	VPC-+
72889156	5756.01	9.44	2023-07-06	Full	zp	BEB
336840314	4085.01	10.28	2023-07-05	Full	zp	VPC+
120115768	6115.01	17.95	2023-07-03	Full	zp	VPC+
388076422	6034.01	12.15	2023-07-02	Full	I+z	VPC+
373816781	5871.01	18.37	2023-06-24	Ingress	zp	VPC+
66726479	6224.01	13.12	2023-06-23	Full	I+z	VPC+?
103865797	5695.01	9.36	2023-06-22	Full	I+z	VPC+
219041246	5713.01	1.86	2023-06-17	Full	I+z	VPC+?
357373216	3901.01	12.47	2023-06-15	Full	zp	VPC
455947620	6022.02	2.48	2023-06-14	Full	I+z	VPC?
269488987	6124.01	12.73	2023-06-13	Full	I+z	VPC-+
305790119	5918.01	11.70	2023-06-12	Ingress	zp	VPC
380517859	5867.01	10.28	2023-06-11	Ingress	I+z	PC
345205395	5863.01	13.92	2023-06-08	Full	zp	VPC+
404456775	6158.01	9.04	2023-05-20	Full	I+z	VPC
459982699	6387.01	12.75	2023-05-20	Full	I+z	VPC+
158617175	3910.01	12.32	2023-05-15	Full	zp	VPC+
222485202	5838.01	13.03	2023-05-14	Full	B	VPC+
416542079	3860.01	14.47	2023-05-13	Full	B	VPC+
39143128	5389.01	8.81	2023-05-12	Full	zp	VPC
255928426	5686.01	15.70	2023-05-08	Full	I+z	VPC+
376688393	3865.01	nan	2023-05-07	Full	B	VPC+
23179035	5770.01	12.18	2023-05-06	Full	zp	VPC+
37150278	5692.01	12.43	2023-05-02	Full	zp	VPC+
236785891	5956.01	10.61	2023-05-01	Full	zp	VPC+
81247877	3915.01	13.61	2023-04-25	Full	BC	VPC+
75784122	5846.01	15.22	2023-04-22	Full	zp	VPC
255928426	5686.01	15.70	2023-04-21	Full	zp	VPC+
86005116	6157.01	11.78	2023-04-15	Full	I+z	NPC
198161914	5663.01	7.92	2023-04-15	Full	I+z	VPC
55266835	5175.01	15.65	2023-04-13	Full	I+z	VPC
1870990135	3514.01	17.38	2023-04-13	Egress	I+z	VPC-
399956872	5283.12	--	2023-04-11	Full	zp	VPC+

12938488	5977.01	8.49	2023-04-06	Full	I+z	APC
165414210	5620.01	12.58	2023-04-06	Full	zp	VPC+
172222885	5468.01	12.24	2023-04-01	Full	I+z	VPC
193634953	5688.01	9.41	2023-04-01	Full	zp	VPC+
207439380	5681.01	10.63	2023-03-31	Full	zp	BEB
321436679	3733.01	28.76	2023-03-31	Full	zp	EB
445807396	3830.01	10.36	2023-03-30	Full	zp	VPC+
219728669	1852.01	13.47	2023-03-28	Full	zp	VPC+
219506608	5757.01	11.62	2023-03-25	nan	I+z	VPC
81247877	3915.01	13.61	2023-03-23	Full	zp	VPC+
114947483	5859.01	6.36	2023-03-23	Full	I+z	VPC
32260988	5684.01	16.02	2023-03-21	Full	zp	VPC+
33091590	2495.01	1.89	2023-03-21	Full	I+z	VPC
9701368	5774.01	14.73	2023-03-19	Full	I+z	VPC+
135100529	5628.01	nan	2023-03-19	Full	I+z	VPC+
23725901	4743.01	19.45	2023-03-15	Full	I+z	VPC
323250919	5689.01	14.99	2023-03-15	Full	zp	VPC+
161003569	3909.01	12.81	2023-03-14	Full	BC	VPC+
393853275	3831.01	nan	2023-03-12	Full	zp	VPC+
63190194	5514.01	12.80	2023-02-27	Full	BC	VPC+
156007004	3974.01	12.70	2023-02-27	Full	I+z	VPC+
85284138	5597.01	22.54	2023-02-24	Full	B	VPC+
119585136	5634.01	9.67	2023-01-24	Full	I+z	VPC+
455947620	6022.01	17.79	2023-01-23	Full	zp	VPC+
458686969	5073.01	16.05	2023-01-23	Full	I+z	VPC+
171646471	5464.01	9.92	2023-01-22	Full	zp	VPC+
335590096	4860.01	8.99	2023-01-21	Full	I+z	P
166648874	1806.02	2.77	2023-01-17	Ingress	I+z	VPC+
306401382	5311.01	13.53	2023-01-16	Ingress	I+z	VPC
119585136	5634.01	9.67	2023-01-13	Ingress	I+z	VPC+
68443254	5419.01	15.22	2023-01-12	Full	I+z	VPC
126982221	5315.01	17.17	2023-01-10	Full	Exo	VPC+
141202786	5641.01	7.67	2023-01-08	Full	I+z	VPC+
248655096	2718.01	10.81	2023-01-08	Full	zp	VPC+
39143128	5389.01	8.81	2023-01-07	Full	I+z	VPC

468777766	3750.01	8.49	2023-01-04	Full	I+z	VPC
270716565	4728.01	12.81	2023-01-03	Full	I+z	VPC
99097200	3818.01	13.85	2023-01-02	Full	I+z	VPC+
171646471	5464.01	9.92	2023-01-01	Full	I+z	VPC+
165985431	3842.01	13.59	2022-12-30	Full	zp	VPC+
181804752	736.01	2.28	2022-12-29	Full	I+z	VP
455947620	6022.01	17.79	2022-12-27	Full	I+z	VPC+
141202786	5641.01	7.67	2022-12-26	Full	Exo	VPC+
126325149	3855.01	12.65	2022-12-23	Full	I+z	VPC+
155949264	5683.01	17.14	2022-12-22	Full	Exo	VPC+
311441461	3739.01	16.62	2022-12-21	Full	zp	VPC+
281837575	5143.01	11.48	2022-12-19	Full	zp	VPC+
306903715	2782.01	nan	2022-12-13	Full	B	VPC+
438149332	4733.01	17.47	2022-12-12	Full	I+z	VPC
444558604	4079.01	15.61	2022-12-12	Full	zp	VPC+
75697959	5433.01	12.17	2022-12-03	Full	I+z	VPC+
330637910	5561.01	7.16	2022-12-03	Full	I+z	VPC+
123462119	2826.01	nan	2022-11-30	Full	zp	VPC-+
467615239	5338.01	13.97	2022-11-29	Full	I+z	VPC
305506996	5916.01	10.92	2022-11-28	Full	I+z	VPC+
88529975	5592.01	13.91	2022-11-27	Full	I+z	VPC+
29105766	3793.01	17.89	2022-11-15	Full	I+z	VPC+
85284138	5597.01	22.54	2022-11-11	Full	I+z	VPC+
443534757	2769.01	nan	2022-11-10	Full	I+z	VPC+
85284138	5597.01	22.54	2022-11-09	Full	I+z	VPC+
90767677	5359.01	9.29	2022-11-04	Full	Exo	VPC
410552165	3653.01	13.56	2022-11-03	Full	I+z	VPC+
155867025	3714.01	11.61	2022-10-30	Full	zp	P
193634953	5688.01	9.41	2022-10-27	Full	I+z	VPC+
280315875	4012.01	11.75	2022-10-26	Full	zp	VPC+
94727308	4622.01	11.29	2022-10-23	Full	Exo	FA?
26054627	5349.01	9.43	2022-10-20	Full	I+z	VPC+
246965431	5319.01	3.75	2022-10-06	Full	I+z	VPC
72889156	5756.01	9.44	2022-10-04	Full	I+z	BEB
15460993	3544.01	nan	2022-09-29	Full	zp	VPC-+

328081248	5799.01	1.99	2022-09-28	Full	zp	VPC+
90767677	5359.01	9.29	2022-09-24	Full	I+z	VPC
434105094	4506.01	2.89	2022-09-22	Full	I+z	VPC
155867025	3714.01	11.61	2022-09-21	Full	I+z	P
250111245	5293.01	11.89	2022-09-18	Full	I+z	P
4619242	5295.01	10.27	2022-09-14	Full	zp	BEB
467265105	3923.01	nan	2022-09-07	Full	I+z	VPC-
403340402	3993.01	9.68	2022-09-06	Full	zp	VPC-
346081845	3940.01	12.95	2022-09-04	Full	I+z	VPC+
126982221	5315.01	17.17	2022-08-27	Out of Transit	I+z	VPC+
16005254	5344.01	9.66	2022-08-26	nan	I+z	VPC+
75878355	2134.02	7.85	2022-08-22	Egress	BC	PC
233654042	3973.01	nan	2022-02-16	Egress	I+z	VPC+
168191686	2753.01	15.34	2022-02-15	Ingress	I+z	VPC+
368287008	2015.01	5.38	2022-02-14	Full	I+z	VPC+
18067025	3888.01	8.01	2022-02-13	Full	I+z	VPC+
143059017	4865.01	11.40	2022-02-12	Full	I+z	BEB
166648874	1806.01	2.84	2022-02-10	Full	zp	VPC+
125552076	3856.01	13.36	2022-02-02	Full	zp	VPC+
137157546	4148.01	3.74	2022-01-19	Ingress	I+z	NEB
468329664	3978.01	16.29	2021-07-17	Full	I+z	VPC
259168516	1680.01	1.42	2021-07-16	Full	zp	VP
389900760	2120.01	2.63	2021-07-14	Full	zp	VPC+
417047499	3523.01	16.97	2021-07-07	Egress	zp	VPC+
336128819	2136.01	2.17	2021-07-06	Full	zp	VP
455784423	3629.01	8.10	2021-07-02	Full	I+z	P
271167979	3548.01	15.72	2021-07-01	Full	I+z	NEB
407694390	3574.01	nan	2021-06-29	Full	zp	VPC-
336128819	2136.01	2.17	2021-06-28	Full	zp	VP
272672133	1765.01	5.66	2021-06-23	Full	zp	VPC+
259168516	1680.01	1.42	2021-06-22	Egress	zp	VP
462615350	2288.01	2.79	2021-06-16	Egress	I+z	VPC+
418012030	2533.01	9.65	2021-05-19	Full	I+z	VPC
422385684	2561.01	15.28	2021-05-17	Egress	I+z	VPC+
336128819	2136.01	2.17	2021-05-12	Full	zp	VP

207425167	1812.03	5.09	2021-05-09	Egress	I+z	VPC
207425167	1812.03	5.09	2021-05-09	Egress	I+z	VPC
7548817	2583.01	13.73	2021-05-07	Egress	I+z	P
229586455	1887.01	2.50	2021-04-22	nan	I+z	VPC+
198485881	2257.01	2.23	2021-04-19	Ingress	zp	VP
39200363	2133.01	2.45	2021-04-17	Full	zp	PPC
219766989	2354.01	9.55	2021-04-02	Full	zp	EB
219852882	1346.01	2.70	2021-03-24	Full	zp	PC
153949511	1277.02	2.61	2021-03-11	Full	zp	PC
8348911	2266.01	1.98	2021-03-02	Full	zp	VPC+
8348911	2266.01	1.98	2021-02-23	Full	zp	VPC+
172900988	2.16	--	2021-02-17	Ingress	zp	PC
172900988	2.16	--	2021-02-16	Out of Transit	zp	PC
172900988	2.16	--	2021-02-15	Out of Transit	zp	PC
172900988	2.16	--	2021-02-14	Out of Transit	zp	PC
441738827	2084.01	2.07	2021-01-30	Egress	I+z	VP
367630162	2104.02	1.46	2021-01-28	Full	zp	PC
8348911	2266.01	1.98	2021-01-26	Full	I+z	VPC+
166648874	1806.01	2.84	2021-01-12	Full	I+z	VPC+
22705558	1699.01	3.01	2021-01-05	Full	zp	VPC-
299798795	1224.01	2.18	2021-01-02	Full	zp	VPC+?
39218269	2366.01	12.93	2021-01-01	Full	zp	BEB
280031353	2300.01	3.30	2020-12-18	Full	I+z	VPC+
266500992	1655.01	3.63	2020-12-12	Full	zp	VPC+
47601197	2350.01	7.55	2020-12-11	Full	zp	VPC+
248391319	2410.01	4.01	2020-12-08	Full	I+z	BEB
39414571	2364.01	9.58	2020-11-28	Full	zp	P
459837008	2267.01	1.27	2020-11-18	nan	I+z	VPC-
405904232	1312.01	12.81	2020-10-30	Ingress	zp	VPC
142748283	2096.01	1.62	2020-10-26	Full	I+z	VP
104208182	1738.01	4.38	2020-10-24	Full	I+z	VPC
142748283	2096.02	2.04	2020-10-11	Full	I+z	VP
165551882	1633.01	1.92	2020-10-03	Full	I+z	FA
232568235	2260.01	1.65	2020-09-28	Full	zp	VP
200593988	526.01	6.21	2020-09-24	Ingress	zp	NEB

219860288	1743.01	3.31	2020-09-21	Full	I+z	VPC+
27846348	11.12	--	2020-08-18	Egress	I+z	P
219860288	1743.01	3.31	2020-07-19	Full	I+z	VPC+
11996814	2022.01	5.81	2020-07-03	Full	zp	NEB
207425167	1812.01	7.04	2020-06-23	Out of Transit	zp	VPC
467179528	1266.01	2.47	2020-04-01	Full	V	P
467179528	1266.01	2.47	2020-03-21	Ingress	zp	P
142394656	1268.01	9.32	2020-03-06	Full	B	P
181804752	736.01	2.28	2020-03-03	Full	I+z	VP
51024887	1632.01	8.05	2020-02-16	Egress	I+z	NEB
259168516	1680.01	1.42	2020-02-13	Ingress	I+z	VP
312862941	1638.01	5.39	2020-01-26	Full	I+z	VPC+
148914726	1179.01	4.72	2020-01-18	Full	zp	BEB
243185500	1468.02	1.45	2019-12-13	Full	zp	P
36724087	732.02	2.30	2019-12-10	Full	zp	P
43064903	1276.01	1.35	2019-10-24	Full	I+z	FA
33911302	341.01	11.58	2019-09-20	Full	I+z	VPC+

List of TOIs I worked on and submitted to ExoFOP from TRAPPIST-South telescope

TIC ID	TOI	Planet radius	date	Transit coverage	filter	Disposition
31697707	3290.01	10.69	2021-09-04	Full	I+z	NEB
92833442	12.42	--	2020-10-31	Full	zp	NEB
161032923	1080.01	2.03	2021-06-05	Full	I+z	VPC+?
161479081	2685.01	11.18	2021-10-04	Full	I+z	VPC
165827520	3494.01	2.22	2021-08-22	Ingress	I+z	VPC+
170789802	4508.01	2.11	2021-12-29	Full	zp	VPC+
202185707	4325.01	2.40	2021-11-09	Full	I+z	VPC+
204698337	2535.01	9.86	2021-04-28	Full	I+z	VPC+
219366908	2680.01	4.47	2021-10-23	Full	I+z	NEB
237751146	538.01	4.50	2020-10-24	Full	I+z	NEB
310267134	3319.01	6.47	2021-05-21	Full	I+z	NEB
340228388	3458.01	11.91	2021-06-26	Egress	zp	VPC+
369861731	3306.01	8.58	2021-06-09	Full	I+z	NPC
388202128	2621.01	13.79	2021-04-24	Full	I+z	VPC
410314178	3269.01	3.74	2021-08-16	Full	I+z	VPC+
415969908	233.01	2.02	2021-06-02	Full	zp	VPC+
38965512	2615.01	12.78	2021-09-01	Full	I+z	VPC+
47601197	2350.01	7.55	2021-01-11	Full	zp	VPC+
100683605	2698.01	nan	2021-10-13	Full	I+z	VPC-
119448220	2873.01	nan	2021-10-17	Full	zp	VPC+
153078576	2407.01	3.79	2021-01-01	Full	V	VPC+?
160004025	2657.01	12.37	2021-10-03	Full	I+z	VPC
167597352	3247.01	15.54	2021-08-08	Full	I+z	PC
202185707	4325.01	2.40	2021-10-30	Full	I+z	VPC+
212957629	2406.01	2.78	2020-11-29	Full	Exo	VP
219175972	2441.01	2.92	2021-02-04	Full	I+z	VPC
232052748	2795.01	11.46	2021-10-16	Full	I+z	VPC+
234282389	2611.01	5.16	2021-05-29	Full	I+z	FA
237885040	2387.01	12.38	2020-12-03	Full	zp	BEB
238932509	841.01	11.47	2021-01-30	Full	B	VPC+
253126207	6568.01	18.68	2021-02-20	Full	B	VPC+
260541432	2628.01	10.55	2021-05-14	Full	I+z	VPC
260797169	2188.01	14.56	2021-05-23	Full	I+z	VPC+

262829328	2627.01	12.48	2021-05-22	Full	I+z	VPC+
271891552	2225.01	nan	2021-01-23	Full	B	VPC
295233473	3226.01	7.05	2021-06-13	Full	I+z	PC
299176311	4194.01	6.52	2021-09-07	Full	I+z	BEB
332660287	2713.01	5.66	2021-10-02	Full	I+z	VPC
369960846	1077.01	12.63	2021-02-05	Full	V	VPC+
378227267	3179.01	15.38	2021-06-08	Full	zp	VPC-
391900348	2630.01	12.32	2021-04-27	Full	zp	VPC
453100296	2650.01	11.82	2021-05-25	Full	I+z	VPC
466222485	4278.01	9.24	2021-09-03	Full	I+z	VPC-

Appendix E

List of activities

1. 16 - 22/10/2021: Organization of a workshop on detecting and characterizing transiting exoplanets in the First Advanced ArAS School for Astrophysics/ Kottamia observatory /Egypt

2. 15 - 21/11/2021: Participation with Dr. *Emmanuel Jehin* and *Mathieu Vander Donckt* in the maintenance of the telescope TRAPPIST-Nord at the Oukaimeden Observatory.

3. 12/2021 - 03/2022: 30 hours teaching practical work courses on the exoplanets detection, data reduction and analyses to the students of High Energy physics, Astronomy and computational physics Master at the Faculty of Science Semlalia Marrakesh (Cadi Ayyad University, Morocco). This includes also directed works in celestial mechanics with Prof. Abdelhadi Jabiri.

4. 12 - 18/03/2022: Organization of a workshop in the Sixth ArAS School for Astrophysics (ArAS SfA-6)/ Qatar University/ Qatar.

5. 25 - 28/05/2022: Science dissemination activities for the benefit of primary school students in the city of Rabat and its regions (Morocco).

6. 06 - 10/06/2022: Participation (on-line) to "NBIA Workshop on Radiation Transfer in Astrophysics" /Copenhagen, Denmark.

7. 01 - 08/07/2022: Participation in the Oukaimeden International School of Astrophysics (OISA).

8. 18 - 22/07/2022: Participation in the ICESCO[1]'s first international model satellite (cansat) training workshop & aerospace symposium. /Rabat - Oukaimeden, Morocco.

9. 01/07 - 31/08/2022: Supervising the Bachelor student Oumaina Kaouacha: Project: Tracking Satellites and SpaceDebris. Oukaimeden observatory, Morocco.

10. 12 - 16/09/2022: Participation to the Exoplanets and Astrostatistical Analysis techniques Summer School / Geneva, Switzerland.

11. 26/09 - 05/10/2022: TRAPPIST-North maintenance mission at Oukaimeden.

12. 08/12/2022: Participation in the ESO Belgian Day/ Brussels, Belgium.

13. 16/12/2022: Presentation of a lesson of 3 hours on the transit method and data analyses of transiting planets for master students.

[1] Islamic World Educational, Scientific and Cultural Organization

14. 08 - 14/03/2023: Participation in the observation mission to Oukaimeden observatory by the supervision of master students working on exoplanet projects.

15. 15 - 20/04/2024: Participation in the 4th annual conference of the African Astronomical Society (AfAS)/ Marrakesh, Morocco.

Bibliography

Affolter, L., Mordasini, C., Oza, A. V., Kubyshkina, D., & Fossati, L., Planetary evolution with atmospheric photoevaporation. II. Fitting the slope of the radius valley by combining boil-off and XUV-driven escape. 2023, Astron. Astrophys., 676, A119

Agol, E., & Fabrycky, D. C. 2018, in Handbook of Exoplanets, ed. H. J. Deeg & J. A. Belmonte, 7

Agol, E., Luger, R., & Foreman-Mackey, D., Analytic Planetary Transit Light Curves and Derivatives for Stars with Polynomial Limb Darkening. 2020, The Astronomical Journal, 159, 123. https://dx.doi.org/10.3847/1538-3881/ab4fee

Agol, E., Steffen, J., Sari, R., & Clarkson, W., On detecting terrestrial planets with timing of giant planet transits. 2005, Mon. Not. R. Astron. Soc., 359, 567

Agol, E., Dorn, C., Grimm, S. L., Turbet, M., Ducrot, E., et al., Refining the Transit-timing and Photometric Analysis of TRAPPIST-1: Masses, Radii, Densities, Dynamics, and Ephemerides. 2021, Planetary Science. J., 2, 1

Albrecht, S. H., Dawson, R. I., & Winn, J. N., Stellar Obliquities in Exoplanetary Systems. 2022, pasp, 134, 082001

Allard, F., Homeier, D., & Freytag, B., Models of very-low-mass stars, brown dwarfs and exoplanets. 2012, Philosophical Transactions of the Royal Society of London Series A, 370, 2765

Aller, A., Lillo-Box, J., Jones, D., Miranda, L. F., & Barceló Forteza, S., Planetary nebulae seen with TESS: Discovery of new binary central star candidates from Cycle 1. 2020, Astron. Astrophys., 635, A128

Barnes, R., Tidal locking of habitable exoplanets. 2017, Celestial Mechanics and Dynamical Astronomy, 129, 509

Bayes, M., & Price, M., An Essay towards Solving a Problem in the Doctrine of Chances. By the Late Rev. Mr. Bayes, F. R. S. Communicated by Mr. Price, in a Letter to John Canton, A. M. F. R. S. 1763, Philosophical Transactions of the Royal Society of London Series I, 53, 370

Beaulieu, J. P., Bennett, D. P., Fouqué, P., Williams, A., Dominik, M., et al., Discovery of a cool planet of 5.5 Earth masses through gravitational microlensing. 2006, nat, 439, 437

Bell, T. J., Welbanks, L., Schlawin, E., Line, M. R., Fortney, J. J., et al., Methane throughout the atmosphere of the warm exoplanet WASP-80b. 2023, Nature, 623, 709–712. http://dx.doi.org/10.1038/s41586-023-06687-0

Bluhm, P., Pallé, E., Molaverdikhani, K., Kemmer, J., Hatzes, A. P., et al., An ultra-short-period transiting super-Earth orbiting the M3 dwarf TOI-1685. 2021, Astron. Astrophys., 650, A78

Bonfanti, A., Brady, M., Wilson, T. G., Venturini, J., Egger, J. A., et al., Characterising TOI-732 b and c: New insights into the M-dwarf radius and density valley. 2024, Astron. Astrophys., 682, A66

Borucki, W. J., Koch, D., Basri, G., Batalha, N., Brown, T., et al., Kepler Planet-Detection Mission: Introduction and First Results. 2010, Science, 327, 977

Borucki, W. J., Koch, D. G., Basri, G., Batalha, N., Brown, T. M., et al., Characteristics of Planetary Candidates Observed by Kepler. II. Analysis of the First Four Months of Data. 2011, apj, 736, 19

Bracewell, R. N., Detecting nonsolar planets by spinning infrared interferometer. 1978, Nature, 274, 780

Brinkman, C. L., Weiss, L. M., Dai, F., Huber, D., Kite, E. S., et al., TOI-561 b: A Low-density Ultra-short-period "Rocky" Planet around a Metal-poor Star. 2023, Astron. J., 165, 88

Broeg, C., Fernández, M., & Neuhäuser, R., A new algorithm for differential photometry: computing an optimum artificial comparison star. 2005, Astronomische Nachrichten, 326, 134

Brown, T. M., Charbonneau, D., Gilliland, R. L., Noyes, R. W., & Burrows, A., Hubble Space Telescope Time-Series Photometry of the Transiting Planet of HD 209458. 2001, apj, 552, 699

Brown, T. M., & Latham, D. W., es for the Transiting Exoplanet Survey Satellite. 2008, arXiv e-prints, arXiv:0812.1305

Brügger, N., Burn, R., Coleman, G. A. L., Alibert, Y., & Benz, W., Pebbles versus planetesimals. The outcomes of population synthesis models. 2020, Astron. Astrophys., 640, A21

Burdanov, A., Delrez, L., Gillon, M., & Jehin, E. 2018, in Handbook of Exoplanets, ed. H. J. Deeg & J. A. Belmonte, 130

Cadieux, C., Doyon, R., Plotnykov, M., Hébrard, G., Jahandar, F., et al., TOI-1452 b: SPIRou and TESS Reveal a Super-Earth in a Temperate Orbit Transiting an M4 Dwarf. 2022, Astron. J., 164, 96

Cambridge, . 2017 (Cambridge University Press), 103–113. http://dx.doi.org/10.1017/9781316694435.013

Carter, A. L., Hinkley, S., Kammerer, J., Skemer, A., Biller, B. A., et al., The JWST Early Release Science Program for Direct Observations of Exoplanetary Systems I: High-contrast Imaging of the Exoplanet HIP 65426 b from 2 to 16 μm. 2023, apjl, 951, L20

Chambers, K. C., Magnier, E. A., Metcalfe, N., Flewelling, H. A., Huber, M. E., et al., The Pan-STARRS1 Surveys. 2016, arXiv e-prints, arXiv:1612.05560

Charbonneau, D., Brown, T. M., Latham, D. W., & Mayor, M., Detection of Planetary Transits Across a Sun-like Star. 2000, apjl, 529, L45

Charbonneau, D., Allen, L. E., Megeath, S. T., Torres, G., Alonso, R., et al., Detection of Thermal Emission from an Extrasolar Planet. 2005, apj, 626, 523

Charbonneau, D., Berta, Z. K., Irwin, J., Burke, C. J., Nutzman, P., et al., A super-Earth transiting a nearby low-mass star. 2009, Nature, 462, 891–894. http://dx.doi.org/10.1038/nature08679

Chauvin, G., Lagrange, A. M., Dumas, C., Zuckerman, B., Mouillet, D., et al., A giant planet candidate near a young brown dwarf. Direct VLT/NACO observations using IR wavefront sensing. 2004, aap, 425, L29

Chauvin, G., Desidera, S., Lagrange, A. M., Vigan, A., Gratton, R., et al., Discovery of a warm, dusty giant planet around HIP 65426. 2017, aap, 605, L9

Chen, H., & Rogers, L. A., EVOLUTIONARY ANALYSIS OF GASEOUS SUB-NEPTUNE-MASS PLANETS WITH MESA. 2016, The Astrophysical Journal, 831, 180. https://dx.doi.org/10.3847/0004-637X/831/2/180

Chen, J., & Kipping, D., Probabilistic Forecasting of the Masses and Radii of Other Worlds. 2017, apj, 834, 17

Cherubim, C., Cloutier, R., Charbonneau, D., Stockdale, C., Stassun, K. G., et al., TOI-1695 b: A Water World Orbiting an Early-M Dwarf in the Planet Radius Valley. 2023, Astron. J., 165, 167

Claret, A., Limb and gravity-darkening coefficients for the TESS satellite at several metallicities, surface gravities, and microturbulent velocities. 2017, aap, 600, A30

Claret, A., & Bloemen, S., Gravity and limb-darkening coefficients for the Kepler, CoRoT, Spitzer, uvby, UBVRIJHK, and Sloan photometric systems. 2011, aap, 529, A75

Cloutier, R., & Menou, K., Evolution of the Radius Valley around Low-mass Stars from Kepler and K2. 2020, Astron. J., 159, 211

Cloutier, R., Rodriguez, J. E., Irwin, J., Charbonneau, D., Stassun, K. G., et al., TOI-1235 b: A Keystone Super-Earth for Testing Radius Valley Emergence Models around Early M Dwarfs. 2020, Astron. J., 160, 22

Cloutier, R., Charbonneau, D., Stassun, K. G., Murgas, F., Mortier, A., et al., TOI-1634 b: An Ultra-short-period Keystone Planet Sitting inside the M-dwarf Radius Valley. 2021, Astron. J.

Collins, K. A., Kielkopf, J. F., Stassun, K. G., & Hessman, F. V., AstroImageJ: Image Processing and Photometric Extraction for Ultra-precise Astronomical Light Curves. 2017, Astron. J., 153, 77

Cosentino, R., Lovis, C., Pepe, F., Collier Cameron, A., Latham, D. W., et al. 2012, in Society of Photo-Optical Instrumentation Engineers (SPIE) Conference Series, Vol. 8446, Ground-based and Airborne Instrumentation for Astronomy IV, ed. I. S. McLean, S. K. Ramsay, & H. Takami, 84461V

Crossfield, I. J. M., Observations of Exoplanet Atmospheres. 2015, Publ. Astron. Soc. Pacific, 127, 941

Croswell, K., Does Barnard's star have planets? 1988, Astronomy, 16, 6

Cutri, R. M., Wright, E. L., Conrow, T., Fowler, J. W., Eisenhardt, P. R. M., et al. 2013, Explanatory Supplement to the AllWISE Data Release Products, Explanatory Supplement to the AllWISE Data Release Products, ,

Delrez, L., Gillon, M., Queloz, D., Demory, B.-O., Almleaky, Y., et al. 2018, in Society of Photo-Optical Instrumentation Engineers (SPIE) Conference Series, Vol. 10700, Ground-based and Airborne Telescopes VII, ed. H. K. Marshall & J. Spyromilio, 107001I

Delrez, L., Murray, C. A., Pozuelos, F. J., Narita, N., Ducrot, E., et al., Two temperate super-Earths transiting a nearby late-type M dwarf. 2022, Astron. Astrophys., 667, A59

Deming, D., Seager, S., Richardson, L. J., & Harrington, J., Infrared radiation from an extrasolar planet. 2005, nat, 434, 740

do Nascimento, J. D., J., Vidotto, A. A., Petit, P., Folsom, C., Castro, M., et al., Magnetic Field and Wind of Kappa Ceti: Toward the Planetary Habitability of the Young Sun When Life Arose on Earth. 2016, Astrophys. J., Letters, 820, L15

Dorn, C., Harrison, J. H. D., Bonsor, A., & Hands, T. O., A new class of Super-Earths formed from high-temperature condensates: HD219134 b, 55 Cnc e, WASP-47 e. 2018, Monthly Notices of the Royal Astronomical Society, 484, 712. https://doi.org/10.1093/mnras/sty3435

Dorn, C., Venturini, J., Khan, A., Heng, K., Alibert, Y., et al., A generalized Bayesian inference method for constraining the interiors of super Earths and sub-Neptunes. 2017, Astron. Astrophys., 597, A37

Dotter, A., MESA Isochrones and Stellar Tracks (MIST) 0: Methods for the Construction of Stellar Isochrones. 2016, Astrophys. J., Suppl. Ser., 222, 8

Drake, F. D., Project Ozma. 1961, Physics Today, 14, 40

Dressing, C. D., Charbonneau, D., Dumusque, X., Gettel, S., Pepe, F., et al., The Mass of Kepler-93b and The Composition of Terrestrial Planets. 2015, Astrophys. J., 800, 135

Driscoll, P. E. 2018, in Handbook of Exoplanets, ed. H. J. Deeg & J. A. Belmonte, 76

Eastman, J., Gaudi, B. S., & Agol, E., EXOFAST: A Fast Exoplanetary Fitting Suite in IDL. 2013, Publ. Astron. Soc. Pacific, 125, 83

Eastman, J. D., Rodriguez, J. E., Agol, E., Stassun, K. G., Beatty, T. G., et al., EXOFASTv2: A public, generalized, publication-quality exoplanet modeling code. 2019, arXiv e-prints, arXiv:1907.09480

Einstein, A., Lens-Like Action of a Star by the Deviation of Light in the Gravitational Field. 1936, Science, 84, 506. https://doi.org/10.1126/science.84.2188.506

Foreman-Mackey, D., Luger, R., Agol, E., Barclay, T., Bouma, L. G., et al., exoplanet: Gradient-based probabilistic inference for exoplanet data & other astronomical time series. 2021, arXiv e-prints, arXiv:2105.01994

Fortney, J. J., Shabram, M., Showman, A. P., Lian, Y., Freedman, R. S., et al., Transmission Spectra of Three-Dimensional Hot Jupiter Model Atmospheres. 2010, Astrophys. J., 709, 1396

Frank, A., & Sullivan, W. T., I., A New Empirical Constraint on the Prevalence of Technological Species in the Universe. 2016, Astrobiology, 16, 359

Fressin, F., Torres, G., Charbonneau, D., Bryson, S. T., Christiansen, J., et al., The False Positive Rate of Kepler and the Occurrence of Planets. 2013, Astrophys. J., 766, 81

Fried, D. L., Optical Resolution Through a Randomly Inhomogeneous Medium for Very Long and Very Short Exposures. 1966, Journal of the Optical Society of America (1917-1983), 56, 1372

Fulton, B. J., & Petigura, E. A., The California-Kepler Survey. VII. Precise Planet Radii Leveraging Gaia DR2 Reveal the Stellar Mass Dependence of the Planet Radius Gap. 2018, The Astronomical Journal, 156, 264. http://dx.doi.org/10.3847/1538-3881/aae828

Fulton, B. J., Petigura, E. A., Howard, A. W., Isaacson, H., Marcy, G. W., et al., The California-Kepler Survey. III. A Gap in the Radius Distribution of Small Planets. 2017, Astron. J., 154, 109

Fusco, T., Rousset, G., Sauvage, J.-F., Petit, C., Beuzit, J.-L., et al., High-order adaptive optics requirements for direct detection of extrasolar planets: Application to the SPHERE instrument. 2006, Opt. Express, 14, 7515. https://opg.optica.org/oe/abstract.cfm?URI=oe-14-17-7515

Gaia Collaboration, VizieR Online Data Catalog: Gaia EDR3 (Gaia Collaboration, 2020). 2020, VizieR Online Data Catalog, I/350

Gaia Collaboration, Prusti, T., de Bruijne, J. H. J., Brown, A. G. A., Vallenari, A., et al., The Gaia mission. 2016, Astron. Astrophys., 595, A1

Gaia Collaboration, Brown, A. G. A., Vallenari, T., Wyrzykowski, ., Yoldas, A., et al., Gaia Data Release 2. Summary of the contents and survey properties. 2018, aap, 616, A1

Garcia, L. J., Timmermans, M., Pozuelos, F. J., Ducrot, E., Gillon, M., et al., PROSE: a PYTHON framework for modular astronomical images processing. 2022, Mon. Not. R. Astron. Soc., 509, 4817

Gatewood, G., & Eichhorn, H., An unsuccessful search for a planetary companion of Barnard's star BD +4 3561. 1973, Astron. J., 78, 769

Gatewood, G. D., The multichannel astrometric photometer and atmospheric limitations in the measurement of relative positions. 1987, aj, 94, 213

Gaudi, B. S., & Winn, J. N., Prospects for the Characterization and Confirmation of Transiting Exoplanets via the Rossiter-McLaughlin Effect. 2007, apj, 655, 550

Gelman, A., & Rubin, D. B., Inference from Iterative Simulation Using Multiple Sequences. 1992, Statistical Science, 7, 457

Ghachoui, M., Benkhaldoun, Z., Soubkiou, A., Barkaoui, K., Daassou, A., et al. 2020, in Society of Photo-Optical Instrumentation Engineers (SPIE) Conference Series, Vol. 11447, Society of Photo-Optical Instrumentation Engineers (SPIE) Conference Series, 114479Z

Ghachoui, M., Soubkiou, A., Wells, R. D., Rackham, B. V., Triaud, A. H. M. J., et al., TESS discovery of a super-Earth orbiting the M-dwarf star TOI-1680. 2023, Astron. Astrophys., 677, A31

Ghachoui, M., Rackham, B. V., Dévora-Pajares, M., Chouqar, J., Timmermans, M., et al., TESS discovery of two super-Earths orbiting the M-dwarf stars TOI-6002 and TOI-5713 near the radius valley. 2024, Astron. Astrophys., 690, A263

Gilliland, R. L., Brown, T. M., Kjeldsen, H., McCarthy, J. K., Peri, M. L., et al., A Search for Solar-Like Oscillations in the Stars of M67 With CCD Ensemble Photometry on a Network of 4m Telescopes. 1993, Astron. J., 106, 2441

Gillon, M., Searching for red worlds. 2018, Nature Astronomy, 2, 344

Gillon, M., Doyle, A. P., Lendl, M., Maxted, P. F. L., Triaud, A. H. M. J., et al., WASP-50 b: a hot Jupiter transiting a moderately active solar-type star. 2011, Astron. Astrophys., 533, A88

Gillon, M., Triaud, A. H. M. J., Demory, B.-O., Jehin, E., Agol, E., et al., Seven temperate terrestrial planets around the nearby ultracool dwarf star TRAPPIST-1. 2017, Nature, 542, 456

Ginzburg, S., Schlichting, H. E., & Sari, R., Super-Earth Atmospheres: Self-consistent Gas Accretion and Retention. 2016, Astrophys. J., 825, 29

—, Core-powered mass-loss and the radius distribution of small exoplanets. 2018, Mon. Not. R. Astron. Soc., 476, 759

Goldblatt, C., & Watson, A. J., The runaway greenhouse: implications for future climate change, geoengineering and planetary atmospheres. 2012, Philosophical Transactions of the Royal Society A: Mathematical, Physical and Engineering Sciences, 370, 4197–4216. http://dx.doi.org/10.1098/rsta.2012.0004

Gould, A., & Loeb, A., Discovering Planetary Systems through Gravitational Microlenses. 1992, Astrophys. J., 396, 104

Greene, T. P., Line, M. R., Montero, C., Fortney, J. J., Lustig-Yaeger, J., et al., CHARACTERIZING TRANSITING EXOPLANET ATMOSPHERES WITH JWST. 2016, The Astrophysical Journal, 817, 17. https://dx.doi.org/10.3847/0004-637X/817/1/17

Gregory, P. C. 2005, Bayesian Logical Data Analysis for the Physical Sciences: A Comparative Approach with 'Mathematica' Support

Guillot, T., Burrows, A., Hubbard, W. B., Lunine, J. I., & Saumon, D., Giant Planets at Small Orbital Distances. 1996, Astrophys. J., Letters, 459, L35

Gupta, A., & Schlichting, H. E., Signatures of the core-powered mass-loss mechanism in the exoplanet population: dependence on stellar properties and observational predictions. 2020, Mon. Not. R. Astron. Soc., 493, 792

Hadden, S., & Lithwick, Y., Densities and Eccentricities of 139 Kepler Planets from Transit Time Variations. 2014, Astrophys. J., 787, 80

Harrington, J., Transiting exoplanets. 2011, Meteoritics and amp Planetary Science, 46, 767–768. http://dx.doi.org/10.1111/j.1945-5100.2011.01194.x

Hastings, W. K., Monte Carlo Sampling Methods using Markov Chains and their Applications. 1970, Biometrika, 57, 97

Haswell, C. 2021, in 43rd COSPAR Scientific Assembly. Held 28 January - 4 February, Vol. 43, 509

Heng, K., Frierson, D. M. W., & Phillipps, P. J., Atmospheric circulation of tidally locked exoplanets: II. Dual-band radiative transfer and convective adjustment. 2011, Mon. Not. R. Astron. Soc., 418, 2669

Henry, G. W., Marcy, G. W., Butler, R. P., & Vogt, S. S., A Transiting "51 Peg-like" Planet. 2000, apjl, 529, L41

Henry, T. J., Jao, W.-C., Winters, J. G., Dieterich, S. B., Finch, C. T., et al., The Solar Neighborhood XLIV: RECONS Discoveries within 10 parsecs. 2018, Astron. J., 155, 265

Hirano, T., Livingston, J. H., Fukui, A., Narita, N., Harakawa, H., et al., Two Bright M Dwarfs Hosting Ultra-Short-Period Super-Earths with Earth-like Compositions. 2021, Astron. J., 162, 161

Holman, M. J., Winn, J. N., Latham, D. W., O'Donovan, F. T., Charbonneau, D., et al., The Transit Light Curve (TLC) Project. VI. Three Transits of the Exoplanet TrES-2. 2007, Astrophys. J., 664, 1185

Howard, A. W., Marcy, G. W., Bryson, S. T., Jenkins, J. M., Rowe, J. F., et al., Planet Occurrence within 0.25 AU of Solar-type Stars from Kepler. 2012, Astrophys. J., Suppl. Ser., 201, 15

Howell, S. B. 2006, Handbook of CCD Astronomy, Vol. 5

Howell, S. B., Sobeck, C., Haas, M., Still, M., Barclay, T., et al., The K2 Mission: Characterization and Early Results. 2014, Publ. Astron. Soc. Pacific, 126, 398

Huang, C. X., Vanderburg, A., Pál, A., Sha, L., Yu, L., et al., Photometry of 10 Million Stars from the First Two Years of TESS Full Frame Images: Part I. 2020, Research Notes of the American Astronomical Society, 4, 204

Isaak, K. G. 2015, in European Planetary Science Congress, EPSC2015–361

Jackson, T. J. J., Researches on the orbit of 70 Ophiuchi, and on a periodic perturbation in the motion of the system arising from the action of an unseen body. 1896, Astron. J., 16, 17

Jacob, W. S., On certain Anomalies presented by the Binary Star 70 Ophiuchi. 1855, Mon. Not. R. Astron. Soc., 15, 228

Jehin, E., Gillon, M., Queloz, D., Magain, P., Manfroid, J., et al., TRAPPIST: TRAnsiting Planets and PlanetesImals Small Telescope. 2011, The Messenger, 145, 2

Jenkins, J. M., Tenenbaum, P., Seader, S., Burke, C. J., McCauliff, S. D., et al. 2020, Kepler Data Processing Handbook: Transiting Planet Search, Kepler Science Document KSCI-19081-003, ,

Jenkins, J. M., Twicken, J. D., McCauliff, S., Campbell, J., Sanderfer, D., et al. 2016, in Society of Photo-Optical Instrumentation Engineers (SPIE) Conference Series, Vol. 9913, Software and Cyberinfrastructure for Astronomy IV, ed. G. Chiozzi & J. C. Guzman, 99133E

Jensen, E. 2013, Tapir: A web interface for transit/eclipse observability, Astrophysics Source Code Library, record ascl:1306.007, , , ascl:1306.007

Johnson, J. A., Payne, M., Howard, A. W., Clubb, K. I., Ford, E. B., et al., Retired A Stars and Their Companions. VI. A Pair of Interacting Exoplanet Pairs Around the Subgiants 24 Sextanis and HD 200964. 2011, Astron. J., 141, 16

Johnson, J. A., Petigura, E. A., Fulton, B. J., Marcy, G. W., Howard, A. W., et al., The California-KeplerSurvey. II. Precise Physical Properties of 2025KeplerPlanets and Their Host Stars. 2017, The Astronomical Journal, 154, 108. http://dx.doi.org/10.3847/1538-3881/aa80e7

Joshi, M. M., Haberle, R. M., & Reynolds, R. T., Simulations of the Atmospheres of Synchronously Rotating Terrestrial Planets Orbiting M Dwarfs: Conditions for Atmospheric Collapse and the Implications for Habitability. 1997, Icarus, 129, 450

Kaltenegger, L., How to Characterize Habitable Worlds and Signs of Life. 2017, Annual Review of Astronomy and Astrophysics, 55, 433

Kaltenegger, L., Payne, R. C., Lin, Z., Kasting, J., & Delrez, L., Hot Earth or Young Venus? A nearby transiting rocky planet mystery. 2023, Monthly Notices of the Royal Astronomical Society: Letters, 524, L10. https://doi.org/10.1093/mnrasl/slad064

Kasting, J. F., Pollack, J. B., & Ackerman, T. P., Response of Earth's atmosphere to increases in solar flux and implications for loss of water from Venus. 1984, Icarus, 57, 335

Kataria, T., Showman, A. P., Lewis, N. K., Fortney, J. J., Marley, M. S., et al., Three-dimensional Atmospheric Circulation of Hot Jupiters on Highly Eccentric Orbits. 2013, Astrophys. J., 767, 76

Kegerreis, J. A., Eke, V. R., Catling, D. C., Massey, R. J., Teodoro, L. F. A., et al., Atmospheric Erosion by Giant Impacts onto Terrestrial Planets: A Scaling Law for any Speed, Angle, Mass, and Density. 2020, The Astrophysical Journal Letters, 901, L31. https://dx.doi.org/10.3847/2041-8213/abb5fb

Kempton, E. M. R., Bean, J. L., Louie, D. R., Deming, D., Koll, D. D. B., et al., A Framework for Prioritizing the TESS Planetary Candidates Most Amenable to Atmospheric Characterization. 2018, Publ. Astron. Soc. Pacific, 130, 114401

Knutson, H. A., Charbonneau, D., Noyes, R. W., Brown, T. M., & Gilliland, R. L., Using Stellar Limb-Darkening to Refine the Properties of HD 209458b. 2007a, apj, 655, 564

Knutson, H. A., Charbonneau, D., Allen, L. E., Fortney, J. J., Agol, E., et al., A map of the day-night contrast of the extrasolar planet HD 189733b. 2007b, Nature, 447, 183

Konacki, M., Torres, G., Jha, S., & Sasselov, D. D., An extrasolar planet that transits the disk of its parent star. 2003, nat, 421, 507

Kopparapu, R. k., Wolf, E. T., Haqq-Misra, J., Yang, J., Kasting, J. F., et al., The Inner Edge of the Habitable Zone for Synchronously Rotating Planets around Low-mass Stars Using General Circulation Models. 2016, Astrophys. J., 819, 84

Kopparapu, R. K., Ramirez, R., Kasting, J. F., Eymet, V., Robinson, T. D., et al., Habitable Zones around Main-sequence Stars: New Estimates. 2013, apj, 765, 131

Kreidberg, L. 2018, in Handbook of Exoplanets, ed. H. J. Deeg & J. A. Belmonte, 100

Kunimoto, M., Huang, C., Tey, E., Fong, W., Hesse, K., et al., Quick-look Pipeline Lightcurves for 9.1 Million Stars Observed over the First Year of the TESS Extended Mission. 2021, Research Notes of the American Astronomical Society, 5, 234

Landsman, W. B. 1993, in Astronomical Society of the Pacific Conference Series, Vol. 52, Astronomical Data Analysis Software and Systems II, ed. R. J. Hanisch, R. J. V. Brissenden, & J. Barnes, 246

Latham, D. W., Borucki, W. J., Koch, D. G., Brown, T. M., Buchhave, L. A., et al., KEPLER-7b: A TRANSITING PLANET WITH UNUSUALLY LOW DENSITY*. 2010, The Astrophysical Journal Letters, 713, L140. https://dx.doi.org/10.1088/2041-8205/713/2/L140

Lee, E. J., & Connors, N. J., Primordial Radius Gap and Potentially Broad Core Mass Distributions of Super-Earths and Sub-Neptunes. 2021, The Astrophysical Journal, 908, 32. http://dx.doi.org/10.3847/1538-4357/abd6c7

Lee, E. J., Karalis, A., & Thorngren, D. P., Creating the Radius Gap without Mass Loss. 2022, The Astrophysical Journal, 941, 186. http://dx.doi.org/10.3847/1538-4357/ac9c66

Liu, S.-F., Hori, Y., Lin, D. N. C., & Asphaug, E., GIANT IMPACT: AN EFFICIENT MECHANISM FOR THE DEVOLATILIZATION OF SUPER-EARTHS. 2015, The Astrophysical Journal, 812, 164. https://dx.doi.org/10.1088/0004-637X/812/2/164

Lopez, E. D., & Fortney, J. J., The Role of Core Mass in Controlling Evaporation: The Kepler Radius Distribution and the Kepler-36 Density Dichotomy. 2013, Astrophys. J., 776, 2

Lopez, E. D., & Rice, K., How formation time-scales affect the period dependence of the transition between rocky super-Earths and gaseous sub-Neptunesand implications for. 2018, Monthly Notices of the Royal Astronomical Society, 479, 5303. https://doi.org/10.1093/mnras/sty1707

Luque, R., & Pallé, E., Density, not radius, separates rocky and water-rich small planets orbiting M dwarf stars. 2022, Science, 377, 1211

Luque, R., Serrano, L. M., Molaverdikhani, K., Nixon, M. C., Livingston, J. H., et al., A planetary system with two transiting mini-Neptunes near the radius valley transition around the bright M dwarf TOI-776. 2021, Astron. Astrophys., 645, A41

Luque, R., Nowak, G., Hirano, T., Kossakowski, D., Pallé, E., et al., Precise mass determination for the keystone sub-Neptune planet transiting the mid-type M dwarf G 9-40. 2022, Astron. Astrophys., 666, A154

Lyot, B., Étude de la couronne solaire en dehors des éclipses. Avec 16 figures dans le texte. 1932, zap, 5, 73

Mandel, K., & Agol, E., Analytic Light Curves for Planetary Transit Searches. 2002, apjl, 580, L171

Mann, A. W., Feiden, G. A., Gaidos, E., Boyajian, T., & von Braun, K., How to Constrain Your M Dwarf: Measuring Effective Temperature, Bolometric Luminosity, Mass, and Radius. 2015, apj, 804, 64

Mann, A. W., Dupuy, T., Kraus, A. L., Gaidos, E., Ansdell, M., et al., How to Constrain Your M Dwarf. II. The Mass-Luminosity-Metallicity Relation from 0.075 to 0.70 Solar Masses. 2019, apj, 871, 63

Mao, S., & Paczynski, B., Gravitational Microlensing by Double Stars and Planetary Systems. 1991, Astrophys. J., Letters, 374, L37

Marcy, G. W., & Butler, R. P., Precision Radial Velocities with an Iodine Absorption cell. 1992, Publ. Astron. Soc. Pacific, 104, 270

Martinez, C. F., Cunha, K., Ghezzi, L., & Smith, V. V., A Spectroscopic Analysis of the California-Kepler Survey Sample. I. Stellar Parameters, Planetary Radii, and a Slope in the Radius Gap. 2019, The Astrophysical Journal, 875, 29. https://dx.doi.org/10.3847/1538-4357/ab0d93

Matsumura, S., Peale, S. J., & Rasio, F. A., Tidal Evolution of Close-in Planets. 2010, Astrophys. J., 725, 1995

Mayor, M., & Queloz, D., A Jupiter-mass companion to a solar-type star. 1995, Nature, 378, 355

Mazeh, T. 2008, in EAS Publications Series, Vol. 29, EAS Publications Series, ed. M. J. Goupil & J. P. Zahn, 1–65

McLaughlin, D. B., Some results of a spectrographic study of the Algol system. 1924, apj, 60, 22

Mendonça, J. M., Angular momentum and heat transport on tidally locked hot Jupiter planets. 2020, Mon. Not. R. Astron. Soc., 491, 1456

Metropolis, N., Rosenbluth, A. W., Rosenbluth, M. N., Teller, A. H., & Teller, E., Equation of State Calculations by Fast Computing Machines. 1953, Journal of Chemical Physics, 21, 1087

Moulton, F. R., The limits of temporary stability of satellite motion, with an application to the question of the existence of an unseen body in the binary system 70 Ophiuchi. 1899, Astron. J., 20, 33

Murray, C. D., & Correia, A. C. M. 2010a, Keplerian Orbits and Dynamics of Exoplanets, ed. S. Seager, 15–23

—. 2010b, Keplerian Orbits and Dynamics of Exoplanets, ed. S. Seager, 15–23

Muterspaugh, M. W., Lane, B. F., Kulkarni, S. R., Konacki, M., Burke, B. F., et al., The Phases Differential Astrometry Data Archive. V. Candidate Substellar Companions to Binary Systems. 2010, aj, 140, 1657

Nikolov, N., Sing, D. K., Goyal, J., Henry, G. W., Wakeford, H. R., et al., Hubble PanCET: an isothermal day-side atmosphere for the bloated gas-giant HAT-P-32Ab. 2017, Monthly

Notices of the Royal Astronomical Society, 474, 1705–1717. http://dx.doi.org/10.1093/mnras/stx2865

Owen, J. E., & Wu, Y., Kepler Planets: A Tale of Evaporation. 2013, Astrophys. J., 775, 105

Palle, E., Orell-Miquel, J., Brady, M., Bean, J., Hatzes, A. P., et al., GJ 806 (TOI-4481): A bright nearby multi-planetary system with a transiting hot low-density super-Earth. 2023, Astron. Astrophys., 678, A80

Panahi, A., Zucker, S., Clementini, G., Audard, M., Binnenfeld, A., et al., The detection of transiting exoplanets by Gaia. 2022, Astron. Astrophys., 663, A101

Park, J.-H., Yim, H.-S., Choi, Y.-J., Jo, J. H., Moon, H.-K., et al. 2017, in 7th European Conference on Space Debris, 134

Paxton, B., Bildsten, L., Dotter, A., Herwig, F., Lesaffre, P., et al., Modules for Experiments in Stellar Astrophysics (MESA). 2011, Astrophys. J., Suppl. Ser., 192, 3

Paxton, B., Cantiello, M., Arras, P., Bildsten, L., Brown, E. F., et al., Modules for Experiments in Stellar Astrophysics (MESA): Planets, Oscillations, Rotation, and Massive Stars. 2013, Astrophys. J., Suppl. Ser., 208, 4

Paxton, B., Marchant, P., Schwab, J., Bauer, E. B., Bildsten, L., et al., Modules for Experiments in Stellar Astrophysics (MESA): Binaries, Pulsations, and Explosions. 2015, Astrophys. J., Suppl. Ser., 220, 15

Pepe, F., Cristiani, S., Rebolo, R., Santos, N. C., Dekker, H., et al., ESPRESSO at VLT. On-sky performance and first results. 2021, Astron. Astrophys., 645, A96

Perryman, M. A. C., Extra-solar planets. 2000, Reports on Progress in Physics, 63, 1209. https://dx.doi.org/10.1088/0034-4885/63/8/202

Petigura, E. A., Howard, A. W., Marcy, G. W., Johnson, J. A., Isaacson, H., et al., The California-KeplerSurvey. I. High-resolution Spectroscopy of 1305 Stars HostingKeplerTransiting Planets. 2017, The Astronomical Journal, 154, 107. http://dx.doi.org/10.3847/1538-3881/aa80de

Pollacco, D. L., Skillen, I., Cameron, A. C., Christian, D. J., Hellier, C., et al., The WASP Project and the SuperWASP Cameras. 2006, Publications of the Astronomical Society of the Pacific, 118, 1407. https://doi.org/10.1086%2F508556

Quanz, S. P., Ottiger, M., Fontanet, E., Kammerer, J., Menti, F., et al., Large Interferometer For Exoplanets (LIFE). I. Improved exoplanet detection yield estimates for a large mid-infrared space-interferometer mission. 2022, Astron. Astrophys., 664, A21

Queloz, D., Eggenberger, A., Mayor, M., Perrier, C., Beuzit, J. L., et al., Detection of a spectroscopic transit by the planet orbiting the star HD209458. 2000, aap, 359, L13

Quirrenbach, A., CARMENES Consortium, Amado, P. J., Ribas, I., Reiners, A., et al. 2020, in Society of Photo-Optical Instrumentation Engineers (SPIE) Conference Series, Vol. 11447, Society of Photo-Optical Instrumentation Engineers (SPIE) Conference Series, 114473C

Rackham, B. V., Apai, D., & Giampapa, M. S., The Transit Light Source Effect: False Spectral Features and Incorrect Densities for M-dwarf Transiting Planets. 2018, Astrophys. J., 853, 122

Rauer, H., Aerts, C., Deleuil, M., Gizon, L., Goupil, M., et al. 2022, in European Planetary Science Congress, EPSC2022–453

Reylé, C., Jardine, K., Fouqué, P., Caballero, J. A., Smart, R. L., et al., The 10 parsec sample in the Gaia era. 2021, Astron. Astrophys., 650, A201

Ricker, G. R., Winn, J. N., Vanderspek, R., Latham, D. W., Bakos, G. Á., et al., Transiting Exoplanet Survey Satellite (TESS). 2015, Journal of Astronomical Telescopes, Instruments, and Systems, 1, 014003

Ricker, G. R., Vanderspek, R., Winn, J., Seager, S., Berta-Thompson, Z., et al. 2016, in Society of Photo-Optical Instrumentation Engineers (SPIE) Conference Series, Vol. 9904, Space Telescopes and Instrumentation 2016: Optical, Infrared, and Millimeter Wave, ed. H. A. MacEwen, G. G. Fazio, M. Lystrup, N. Batalha, N. Siegler, & E. C. Tong, 99042B

Robinson, T., Characterizing Exoplanet Habitability. 2019, Bulletin of the AAS, 51, 356

Rodriguez, J. E., Quinn, S. N., Vanderburg, A., Zhou, G., Eastman, J. D., et al., Another shipment of six short-period giant planets from TESS. 2023, Mon. Not. R. Astron. Soc., 521, 2765

Rogers, J. G., Gupta, A., Owen, J. E., & Schlichting, H. E., Photoevaporation versus core-powered mass-loss: model comparison with the 3D radius gap. 2021, Monthly Notices of the Royal Astronomical Society, 508, 5886–5902. http://dx.doi.org/10.1093/mnras/stab2897

Rogers, L. A., Most 1.6 Earth-radius Planets are Not Rocky. 2015, Astrophys. J., 801, 41

Rossiter, R. A., On the detection of an effect of rotation during eclipse in the velocity of the brigher component of beta Lyrae, and on the constancy of velocity of this system. 1924, apj, 60, 15

Schlafly, E. F., & Finkbeiner, D. P., Measuring Reddening with Sloan Digital Sky Survey Stellar Spectra and Recalibrating SFD. 2011a, apj, 737, 103

—, Measuring Reddening with Sloan Digital Sky Survey Stellar Spectra and Recalibrating SFD. 2011b, Astrophys. J., 737, 103

Schlichting, H. E., Sari, R., & Yalinewich, A., Atmospheric mass loss during planet formation: The importance of planetesimal impacts. 2015, Icarus, 247, 81. https://www.sciencedirect.com/science/article/pii/S0019103514005284

Schmitz, B., The exoplanet handbook. 2019, Meteoritics and amp Planetary Science, 54, 1642–1643. http://dx.doi.org/10.1111/maps.13308

Seager, S. 2010, Exoplanet Atmospheres: Physical Processes

Seager, S., & Deming, D., Exoplanet Atmospheres. 2010, araa, 48, 631

Seager, S., & Mallén-Ornelas, G. 2003, in Astronomical Society of the Pacific Conference Series, Vol. 294, Scientific Frontiers in Research on Extrasolar Planets, ed. D. Deming & S. Seager, 419–422

Seager, S., Richardson, L. J., Hansen, B. M. S., Menou, K., Cho, J. Y. K., et al., On the Dayside Thermal Emission of Hot Jupiters. 2005, apj, 632, 1122

Seager, S., & Sasselov, D. D., Theoretical Transmission Spectra during Extrasolar Giant Planet Transits. 2000a, apj, 537, 916

—, Theoretical Transmission Spectra during Extrasolar Giant Planet Transits. 2000b, Astrophys. J., 537, 916

Sebastian, D., Pedersen, P. P., Murray, C. A., Ducrot, E., Garcia, L. J., et al. 2020, in Society of Photo-Optical Instrumentation Engineers (SPIE) Conference Series, Vol. 11445, Ground-based and Airborne Telescopes VIII, ed. H. K. Marshall, J. Spyromilio, & T. Usuda, 1144521

Seifahrt, A., Bean, J. L., Stürmer, J., Kasper, D., Gers, L., et al. 2020, in Society of Photo-Optical Instrumentation Engineers (SPIE) Conference Series, Vol. 11447, Ground-based and Airborne Instrumentation for Astronomy VIII, ed. C. J. Evans, J. J. Bryant, & K. Motohara, 114471F

Seifahrt, A., Bean, J. L., Kasper, D., Stürmer, J., Brady, M., et al. 2022, in Society of Photo-Optical Instrumentation Engineers (SPIE) Conference Series, Vol. 12184, Ground-based and Airborne Instrumentation for Astronomy IX, ed. C. J. Evans, J. J. Bryant, & K. Motohara, 121841G

Shields, A. L., Ballard, S., & Johnson, J. A., The habitability of planets orbiting M-dwarf stars. 2016, Physics Reports, 663, 1

Stassun, K. G., Oelkers, R. J., Pepper, J., Paegert, M., Bastien, F. A., et al., Erratum: The TESS Input Catalog and Candidate Target List (¡A href="http://doi.org/10.3847/1538-3881/aad050"¿ 2018, AJ, 156, 102¡/A¿). 2018, Astron. J., 156, 183

Stassun, K. G., Oelkers, R. J., Paegert, M., Torres, G., Pepper, J., et al., The Revised TESS Input Catalog and Candidate Target List. 2019, Astron. J., 158, 138

Steinrueck, M. E., Koskinen, T., Lavvas, P., Parmentier, V., Zieba, S., et al., Photochemical Hazes Dramatically Alter Temperature Structure and Atmospheric Circulation in 3D Simulations of Hot Jupiters. 2023, The Astrophysical Journal, 951, 117. http://dx.doi.org/10.3847/1538-4357/acd4bb

Stelzer, B., Marino, A., Micela, G., Lopez-Santiago, J., & Liefke, C., The UV and X-ray activity of the M dwarfs within 10 pc of the Sun. 2013, Monthly Notices of the Royal Astronomical Society, 431, 2063–2079. http://dx.doi.org/10.1093/mnras/stt225

Struve, O., Proposal for a project of high-precision stellar radial velocity work. 1952, The Observatory, 72, 199

Sudarsky, D., Burrows, A., & Pinto, P., Albedo and Reflection Spectra of Extrasolar Giant Planets. 2000, Astrophys. J., 538, 885

Tasker, E., Tan, J., Heng, K., Kane, S., Spiegel, D., et al., The language of exoplanet ranking metrics needs to change. 2017, Nature Astronomy, 1, 0042

Ter Braak, C. J. F., A Markov Chain Monte Carlo version of the genetic algorithm Differential Evolution: easy Bayesian computing for real parameter spaces. 2006, Statistics and Computing, 16, 239

Torres, G., Andersen, J., & Giménez, A., Accurate masses and radii of normal stars: modern results and applications. 2010, Astron. Astrophys. Reviews, 18, 67

Twicken, J. D., Catanzarite, J. H., Clarke, B. D., Girouard, F., Jenkins, J. M., et al., Kepler Data Validation I—Architecture, Diagnostic Tests, and Data Products for Vetting Transiting Planet Candidates. 2018, Publ. Astron. Soc. Pacific, 130, 064502

Valle, P. J., Fuentes, A., Canales, V. F., Cagigas, M. A., & Cagigal, M. P., Digital coronography: application to space telescope images. 2019, OSA Continuum, 2, 2038. http://dx.doi.org/10.1364/OSAC.2.002038

van de Kamp, P., Astrometric study of Barnard's star from plates taken with the 24-inch Sproul refractor. 1963, Astron. J., 68, 515

—, Alternate dynamical analysis of Barnard's star. 1969, Astron. J., 74, 757

—, The planetary system of Barnard's star. 1982, Vistas in Astronomy, 26, 141

VanEylen, V., Agentoft, C., Lundkvist, M. S., Kjeldsen, H., Owen, J. E., et al., An asteroseismic view of the radius valley: stripped cores, not born rocky. 2018, Mon. Not. R. Astron. Soc., 479, 4786

VanGrootel, V., Fernandes, C. S., Gillon, M., Jehin, E., Manfroid, J., et al., Stellar Parameters for Trappist-1. 2018, Astrophys. J., 853, 30

Venturini, J., Guilera, O. M., Haldemann, J., Ronco, M. P., & Mordasini, C., The nature of the radius valley. Hints from formation and evolution models. 2020, Astron. Astrophys., 643, L1

Wakeford, H. R., Sing, D. K., Deming, D., Lewis, N. K., Goyal, J., et al., The Complete Transmission Spectrum of WASP-39b with a Precise Water Constraint. 2018, aj, 155, 29

Weiss, L. M., & Marcy, G. W., THE MASS-RADIUS RELATION FOR 65 EXOPLANETS SMALLER THAN 4 EARTH RADII. 2014, The Astrophysical Journal, 783, L6. http://dx.doi.org/10.1088/2041-8205/783/1/L6

Williams, D. M., & Pollard, D., Earth-like worlds on eccentric orbits: excursions beyond the habitable zone. 2002, International Journal of Astrobiology, 1, 61

Winn, J. N., Transits and Occultations. 2010, ArXiv e-prints

Winn, J. N., & Fabrycky, D. C., The Occurrence and Architecture of Exoplanetary Systems. 2015, araa, 53, 409

Wolf, E., Kopparapu, R., Airapetian, V., Fauchez, T., Guzewich, S. D., et al., The Importance of 3D General Circulation Models for Characterizing the Climate and Habitability of Terrestrial Extrasolar Planets. 2019, Astro2020: Decadal Survey on Astronomy and Astrophysics, 2020, 177

Wolszczan, A. 1992, in AAS/Division for Planetary Sciences Meeting Abstracts, Vol. 24, AAS/Division for Planetary Sciences Meeting Abstracts #24, 19.01

Wong, I., & Shporer, A. 2022, in Bulletin of the American Astronomical Society, Vol. 54, 102.320

Wong, I., Benneke, B., Shporer, A., Fetherolf, T., Kane, S. R., et al., TESS Phase Curve of the Hot Jupiter WASP-19b. 2020, aj, 159, 104

Wordsworth, R., Atmospheric Heat Redistribution and Collapse on Tidally Locked Rocky Planets. 2015, Astrophys. J., 806, 180

Wright, J. T., & Gaudi, B. S. 2013, in Planets, Stars and Stellar Systems (Springer Netherlands), 489–540. https://doi.org/10.1007/978-94-007-5606-9_10

Wyatt, M. C., Kral, Q., & Sinclair, C. A., Susceptibility of planetary atmospheres to mass-loss and growth by planetesimal impacts: the impact shoreline. 2020, Mon. Not. R. Astron. Soc., 491, 782